



ISSN 1605-2730

MATERIALS PHYSICS AND MECHANICS

Vol. 38, No. 1, 2018

MATERIALS PHYSICS AND MECHANICS

Principal Editors:

Dmitrii Indeitsev

*Institute of Problems of Mechanical Engineering
of the Russian Academy of Science (RAS), Russia*

Andrei Rudskoi

Peter the Great St.Petersburg Polytechnic University, Russia

Founder and Honorary Editor: Ilya Ovid'ko (1961-2017)

*Institute of Problems of Mechanical Engineering
of the Russian Academy of Sciences (RAS), Russia*

Staff Editors:

Anna Kolesnikova

*Institute of Problems of Mechanical Engineering
of the Russian Academy of Sciences (RAS), Russia*

Alexander Nemov

Peter the Great St.Petersburg Polytechnic University, Russia

Editorial Board:

E.C. Aifantis

Aristotle University of Thessaloniki, Greece

K.E. Aifantis

University of Florida, USA

U. Balachandran

Argonne National Laboratory, USA

A. Bellosi

Research Institute for Ceramics Technology, Italy

A.K. Belyaev

Institute of Problems of Mechanical Engineering (RAS), Russia

S.V. Bobylev

Institute of Problems of Mechanical Engineering (RAS), Russia

A.I. Borovkov

Peter the Great St.Petersburg Polytechnic University, Russia

G.-M. Chow

National University of Singapore, Singapore

Yu. Estrin

Monash University, Australia

A.B. Freidin

Institute of Problems of Mechanical Engineering (RAS), Russia

Y. Gogotsi

Drexel University, USA

I.G. Goryacheva

Institute of Problems of Mechanics (RAS), Russia

D. Hui

University of New Orleans, USA

G. Kiriakidis

IESL/FORTH, Greece

D.M. Klimov

Institute of Problems of Mechanics (RAS), Russia

G.E. Kodzhaspirov

Peter the Great St.Petersburg Polytechnic University, Russia

S.A. Kukushkin

Institute of Problems of Mechanical Engineering (RAS), Russia

T.G. Langdon

University of Southampton, U.K.

V.P. Matveenko

Institute of Continuous Media Mechanics (RAS), Russia

A.I. Melker

Peter the Great St.Petersburg Polytechnic University, Russia

Yu.I. Meshcheryakov

Institute of Problems of Mechanical Engineering (RAS), Russia

N.F. Morozov

St.Petersburg State University, Russia

R.R. Mulyukov

Institute for Metals Superplasticity Problems (RAS), Russia

Yu.V. Petrov

St.Petersburg State University, Russia

N.M. Pugno

Politecnico di Torino, Italy

B.B. Rath

Naval Research Laboratory, USA

A.E. Romanov

Ioffe Physico-Technical Institute (RAS), Russia

A.M. Sastry

University of Michigan, Ann Arbor, USA

B.A. Schrefler

University of Padua, Italy

N.V. Skiba

Institute of Problems of Mechanics (RAS), Russia

A.G. Sheinerman

Institute of Problems of Mechanics (RAS), Russia

R.Z. Valiev

Ufa State Aviation Technical University, Russia

K. Zhou

Nanyang Technological University, Singapore

“Materials Physics and Mechanics” Editorial Office:

Phone: +7(812)591 65 28 **E-mail:** mpmjournal@spbstu.ru **Web-site:** <http://www.mpm.spbstu.ru>

International scientific journal "Materials Physics and Mechanics" is published by Peter the Great St.Petersburg Polytechnic University in collaboration with Institute of Problems of Mechanical Engineering of the Russian Academy of Sciences in both hard copy and electronic versions.

The journal provides an international medium for the publication of reviews and original research papers written in English and focused on the following topics:

- Mechanics of nanostructured materials (such as nanocrystalline materials, nanocomposites, nanoporous materials, nanotubes, quantum dots, nanowires, nanostructured films and coatings).
- Physics of strength and plasticity of nanostructured materials, physics of defects in nanostructured materials.
- Mechanics of deformation and fracture processes in conventional materials (solids).
- Physics of strength and plasticity of conventional materials (solids).

Owner organizations: Peter the Great St. Petersburg Polytechnic University; Institute of Problems of Mechanical Engineering RAS.

Materials Physics and Mechanics is indexed in Chemical Abstracts, Cambridge Scientific Abstracts, Web of Science Emerging Sources Citation Index (ESCI) and Elsevier Bibliographic Databases (in particular, SCOPUS).



МЕХАНИКА И ФИЗИКА МАТЕРИАЛОВ

Materials Physics and Mechanics

Vol. 38, No. 1, 2018

**Труды 12-й Международной научно-технической конференции
«Современные металлические материалы и технологии
(СММТ'2017)»**

3–7 июля 2017 г., Санкт-Петербург, Россия

**Министерство образования и науки РФ
Российская Академия наук
Российский фонд фундаментальных исследований
Научный совет РАН по физике конденсированных сред (Россия)
Санкт-Петербургский научный центр РАН
Комитет по науке и высшей школе Правительства Санкт-Петербурга
Санкт-Петербургский политехнический университет Петра Великого**

Под редакцией академика РАН Андрея Рудского

**Proceedings of the 12th International Scientific and Technical Conference
"Advanced Metal Materials and Technologies (AMMT'2017)"**

3-7 July, 2017, St. Petersburg, Russia

**Organized by
Ministry of Education and Science of the Russian Federation
Russian Academy of Sciences
Russian Fund for Basic Research
Saint Petersburg Scientific Center
of the Russian Academy of Science
Scientific Council on Condensed Matter Physics
Committee for science and higher education
of the Saint Petersburg City Government
Peter the Great St. Petersburg Polytechnic University**

Edited by academician of RAS Andrei Rudskoi

Учредители:

**ФГАОУ ВО «Санкт-Петербургский политехнический университет Петра Великого»
ФГБУН «Институт проблем машиноведения Российской Академии Наук»**

Редакционная коллегия журнала

Главные редакторы:

д.ф.-м.н., чл.-корр. РАН **Д.А. Индейцев**
Институт проблем машиноведения Российской Академии Наук
(РАН)

д.т.н., академик РАН **А.И. Рудской**
Санкт-Петербургский политехнический университет
Петра Великого

Основатель и почетный редактор: д.ф.-м.н. **И.А. Овидько (1961-2017)**
Институт проблем машиноведения Российской Академии Наук (РАН)

Ответственные редакторы

д.ф.-м.н. **А.Л. Колесникова**
Институт проблем машиноведения Российской Академии Наук
(РАН)

к.т.н. **А.С. Немов**
Санкт-Петербургский политехнический университет Петра
Великого

Международная редакционная коллегия:

д.ф.-м.н., проф. **А.К. Беляев**
Институт проблем машиноведения РАН, Россия
д.ф.-м.н. **С.В. Бобылев**
Институт проблем машиноведения РАН, Россия
к.т.н., проф. **А.И. Боровков**
Санкт-Петербургский политехнический у-т Петра Великого, Россия
д.ф.-м.н., проф. **Р.З. Валиев**
Уфимский государственный технический университет, Россия
д.ф.-м.н., академик РАН **И.Г. Горячева**
Институт проблем механики РАН, Россия
д.ф.-м.н., академик РАН **Д.М. Климов**
Институт проблем механики РАН, Россия
д.т.н., проф. **Г.Е. Коджаспиров**
Санкт-Петербургский политехнический у-т Петра Великого, Россия
д.ф.-м.н., проф. **С.А. Кукушкин**
Институт проблем машиноведения РАН, Россия
д.ф.-м.н., академик РАН **В.П. Матвеев**
Институт механики сплошных сред РАН, Россия
д.ф.-м.н., проф. **А.И. Мелькер**
Санкт-Петербургский политехнический у-т Петра Великого, Россия
д.ф.-м.н., проф. **Ю.И. Мещеряков**
Институт проблем машиноведения РАН, Россия
д.ф.-м.н., академик РАН **Н.Ф. Морозов**
Санкт-Петербургский государственный университет, Россия
д.ф.-м.н., чл.-корр. РАН **Р.Р. Мулюков**
Институт проблем сверхпластичности металлов РАН, Россия
д.ф.-м.н., чл.-корр. РАН **Ю.В. Петров**
Санкт-Петербургский государственный университет, Россия
д.ф.-м.н., проф. **А.Е. Романов**
Физико-технический институт им. А.Ф. Иоффе РАН, Россия
д.ф.-м.н. **Н.В. Скиба**
Институт проблем машиноведения РАН, Россия
д.ф.-м.н., проф. **А.Б. Фрейдин**
Институт проблем машиноведения РАН, Россия
д.ф.-м.н. **А.Г. Шейнман**
Институт проблем машиноведения РАН, Россия

Prof., Dr. **E.C. Aifantis**
Aristotle University of Thessaloniki, Greece
Dr. **K.E. Aifantis**
University of Florida, USA
Dr. **U. Balachandran**
Argonne National Laboratory, USA
Dr. **A. Bellosi**
Research Institute for Ceramics Technology, Italy
Prof., Dr. **G.-M. Chow**
National University of Singapore, Singapore
Prof., Dr. **Yu. Estrin**
Monash University, Australia
Prof., Dr. **Y. Gogotsi**
Drexel University, USA
Prof., Dr. **D. Hui**
University of New Orleans, USA
Prof., Dr. **G. Kiriakidis**
IESL/FORTH, Greece
Prof., Dr. **T.G. Langdon**
University of Southampton, UK
Prof., Dr. **N.M. Pugno**
Politecnico di Torino, Italy
Dr. **B.B. Rath**
Naval Research Laboratory, USA
Prof., Dr. **A.M. Sastry**
University of Michigan, Ann Arbor, USA
Prof., Dr. **B.A. Schrefler**
University of Padua, Italy
Prof. Dr. **K. Zhou**
Nanyang Technological University, Singapore

Тел.: +7(812)591 65 28 E-mail: mpmjournal@spbstu.ru Web-site: <http://www.mpm.spbstu.ru>

Тематика журнала

Международный научный журнал "Materials Physics and Mechanics" издается Санкт-Петербургским политехническим университетом Петра Великого в сотрудничестве с Институтом проблем машиноведения Российской Академии Наук в печатном виде и электронной форме. Журнал публикует обзорные и оригинальные научные статьи на английском языке по следующим тематикам:

- Механика наноструктурных материалов (таких как нанокристаллические материалы, нанокомпозиты, нанопористые материалы, нанотрубки, наноструктурные пленки и покрытия, материалы с квантовыми точками и проволоками).
- Физика прочности и пластичности наноструктурных материалов, физика дефектов в наноструктурных материалах.
- Механика процессов деформирования и разрушения в традиционных материалах (твердых телах).
- Физика прочности и пластичности традиционных материалов (твердых тел).

Редколлегия принимает статьи, которые нигде ранее не опубликованы и не направлены для опубликования в другие научные издания. Все представляемые в редакцию журнала "Механика и физика материалов" статьи рецензируются. Статьи могут отправляться авторам на доработку. Не принятые к опубликованию статьи авторам не возвращаются.

Журнал "Механика и физика материалов" ("Materials Physics and Mechanics") включен в систему цитирования Web of Science Emerging Sources Citation Index (ESCI), SCOPUS и РИНЦ.

© 2018, Санкт-Петербургский политехнический университет Петра Великого
© 2018, Институт проблем машиноведения Российской Академии Наук

Contents

Design and manufacturing of tailored microstructure with selective laser melting	1-10
A.A. Popovich, V.Sh. Sufiiarov, E.V. Borisov, I.A. Polozov, D.V. Masaylo	
Operational characteristics of the composite aluminum - carbon nanofibers.....	11-15
T.S. Koltsova, A.D. Breki, T.V. Larionova, O.V. Tolochko	
Thermomechanical processing of steels and alloys physical foundations, resource saving technique and modelling.....	16-25
A.I. Rudskoi, G. Kodzhaspirov1, J. Kliber, Ch. Apostolopoulos	
Effect of alumina addition on weld deposits microstructure at the welding of carbon steel	26-32
E.V. Bobrynina, T.V. Larionova, T.S. Koltsova, S.A. Ginzburg, V.G. Michailov	
The influence of different types of mesodeflects on the formation of strain induced broken dislocation boundaries at the faceted grain boundary	33-39
S.V.Kirikov, J.V. Svirina	
Technique of durability estimation for thin beryllium foils during their work in X-ray detectors	40-47
V.V. Mishin, I.A. Shishov, A. Minchena	
Contactless electromagnetic acoustic techniques of diagnostics and assessment of mechanical properties of steel rolled bars	48-53
V.V. Murav'ev, O.V. Murav'eva, K.V. Petrov	
Microstructure evolution of a Ti/TiB metal-matrix composite during high-temperature deformation.....	54-63
M.S. Ozerov, M.V. Klimova, N.D. Stepanov, S.V. Zherebtsov	
Severe plastic deformation influence on engineering plasticity of Copper	64-68
A.I. Rudskoi, A.M. Zolotov, R.A. Parshikov	
On anisotropy of mechanical properties of aluminum alloys under high temperature deformation.....	69-75
G.E. Kodzhaspirov, D.A. Kitaeva, Sh.T. Pazylov, Ya.I. Rudaev	
On the development of the new technology of severe plastic deformation in metal forming	76-81
A.I. Rudskoi, A.A. Bogatov, D.Sh. Nukhov, A.O. Tolkushkin	
Examination of hardening curves definition methods in torsion test	82-89
M.V. Erpalov, E.A. Kungurov	

Competition between the volume solution and the surface segregation of solved elements in α-Fe	90-110
V.P. Filippova, E.N. Blinova, A.M. Glezer, R.V. Sundeev, A.A. Tomchuk, L.F. Muradimova	
Carbide forming special features and fracture mechanisms under the austenitic chromium-nickel 304 steel post-life ageing	111-118
S.N. Petrov, O.Yu. Prokoshev, B.Z. Margolin, A.M. Shumko	
Gas-jet method of metal film deposition: direct simulation monte-carlo of He-Ag mixture flow	119-130
N.Y. Bykov, A.I. Safonov, D.V. Leshchev, S.V. Starinskiy, A.V. Bulgakov	

DESIGN AND MANUFACTURING OF TAILORED MICROSTRUCTURE WITH SELECTIVE LASER MELTING

A.A. Popovich, V.Sh. Sufiiarov*, E.V. Borisov, I.A. Polozov, D.V. Masaylo

National Technology Initiative Center of Excellence in Advanced Manufacturing Technologies at Peter the Great
St. Petersburg Polytechnic University, Russia, 195251, St.Petersburg, Polytechnicheskaya, 29

*e-mail: vadim.spbstu@yandex.ru

Abstract. The current paper presents the results of a complex investigation of effect of Selective Laser Melting process parameters on microstructure and properties of Inconel 718 bulk specimens. The possibility of obtaining bulk specimens with tailored microstructure was studied. The specimens with tailored microstructure were obtained and studied. It was shown that after heat treatment and hot isostatic pressing the differences in microstructure and mechanical properties of fine-grained and coarse-grained areas still remain in place. Finally, the feasibility of applying the developed approach was shown by manufacturing a gas-turbine engine blade with tailored microstructure in specific areas.

Keywords: additive manufacturing; selective laser melting; Inconel 718; EBSD; turbine blade, tailored microstructure.

1. Introduction

Selective Laser Melting (SLM) process is nowadays considered to be as one of the most advanced technologies among metal additive manufacturing processes [1-3]. SLM is already used for manufacturing metal parts, which is due to possibility of producing parts with a shape as close as possible to the final product. The latter is especially important in such areas as aviation and medicine [4-7]. The aviation, where titanium and nickel-based alloys are widely used, imposes specific requirements for the parts. Applying additive manufacturing allows creating parts with a geometry that simultaneously provides light-weight and high mechanical properties [4].

Inconel 718 nickel-based alloy attracts high attention among researchers due to its wide use in gas turbines, aerospace parts, petrochemical and nuclear industries, which resulted from its thermal stability and high-temperature properties [8]. Conventionally Inconel 718 parts are produced by forging, rolling and casting. However, in order to advance the modern manufacturing industry, it is necessary to create a manufacturing of complex metal parts with high precision and mechanical properties, which are sometimes not possible to achieve by conventional methods.

There are some studies in the literature that investigate the SLM process of Inconel 718 alloy, where the effect of process parameters on material's relative density has been studied. However, usually they put a focus on only laser power and scanning speed, while other parameters are kept fixed [9-13]. In order to control the SLM process, it is necessary to understand an influence pattern of a particular parameter on the final results. Nevertheless, not enough information has been published on a possibility of using SLM particularities as a means to create a specific crystallographic structure and grain size. Also, few information can be found about the relation of anisotropy, microstructure and mechanical properties of the

alloy [14-18]. Therefore, the aim of this work is to determine the relation between obtained microstructure from the initial process parameters and to develop a method for production of bulk parts with tailored microstructure and study their properties, as well.

2. Materials and Methods

The bulk specimens were manufactured using a SLM 280HL machine (SLM Solutions GmbH, Germany). Gas atomized Inconel 718 heat-resistant alloy powder was used as the raw material. The measured chemical composition of the Inconel 718 powder is presented in Table 1.

Table 1. The chemical composition of Inconel 718 powder particles measured by energy dispersive X-ray spectroscopy.

Element	Ni	Cr	Fe	Nb	Mo	Ti	Al	Co	Mn
Content, wt%	51.4	19.4	18.5	5.3	3.4	1.0	0.7	0.1	0.1

The particle size distribution was measured using laser diffraction method with Analysette 22 NanoTecPlus device with a full-scale range of 0.01–2000 μm . The flowability of the powder was measured with a calibrated funnel (Hall Flowmeter). The surface morphology, microstructure of powder particles, as well as microstructure of the bulk specimens, texture characterization (EBSD) were investigated using scanning electron microscope (SEM) TESCAN Mira 3 LMU. EBSD analyses was carried out with the accelerating voltage of 20 kV and 5 μm step. The X-ray diffraction analysis was carried out using Bruker D8 Advance diffractometer. The mechanical properties were analyzed in accordance with ISO 6892-1 using Zwick/Roell Z100 testing machine. The relative density of bulk samples was measured by metallographical method and the Archimedes principle. Hot isostatic pressing (HIP) was carried out in an Avure Quintus at temperature of 1180°C and pressure of 150 MPa during 3 hours. Heat treatment was carried out in two steps: 1) solution annealing at 1065°C for 1 hour with air cooling; 2) two step aging: holding at 760°C for 10 hours, then cooling to 650°C for 2 hours and holding at 650°C for 8 hours following air cooling.

3. Results and Discussion

SEM investigation of Inconel 718 powder (Fig. 1) showed that the powder particles have shape close to spherical. Some particles have satellites attached to them (Fig. 1, b). The presence of such particles is typical for gas atomized powder. The surface morphology of the particles features some roughness, which represents the casted microstructure and belongs to cellular-dendritic type of crystallization [19].

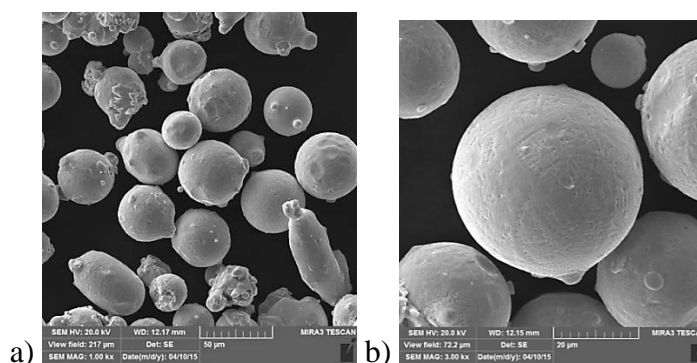


Fig. 1. SEM-images of Inconel 718 alloy powder particles produce by gas atomization: a) general view; b) particle's surface morphology.

In order to determine the correlation between SLM process parameters and bulk samples relative density, some researcher use such characteristic as energy density, but different equations are used. Some use linear energy density [7], others – volume energy density [8]. The authors of this work consider volume energy density to be a value that is more appropriate to estimate specific heat input. The main process parameters responsible for parts density can be grouped in a volume energy density E (J/mm^3) equation:

$$E = P/Vht, \quad (1)$$

where P – laser power (Wt), V – scanning speed (mm/s), h – hatch distance (mm), t – layer thickness (mm).

The summarized results of bulk samples relative density measurements, obtained with a fixed layer thickness of $30 \mu\text{m}$ at different volume energy density, are shown in Fig. 2.

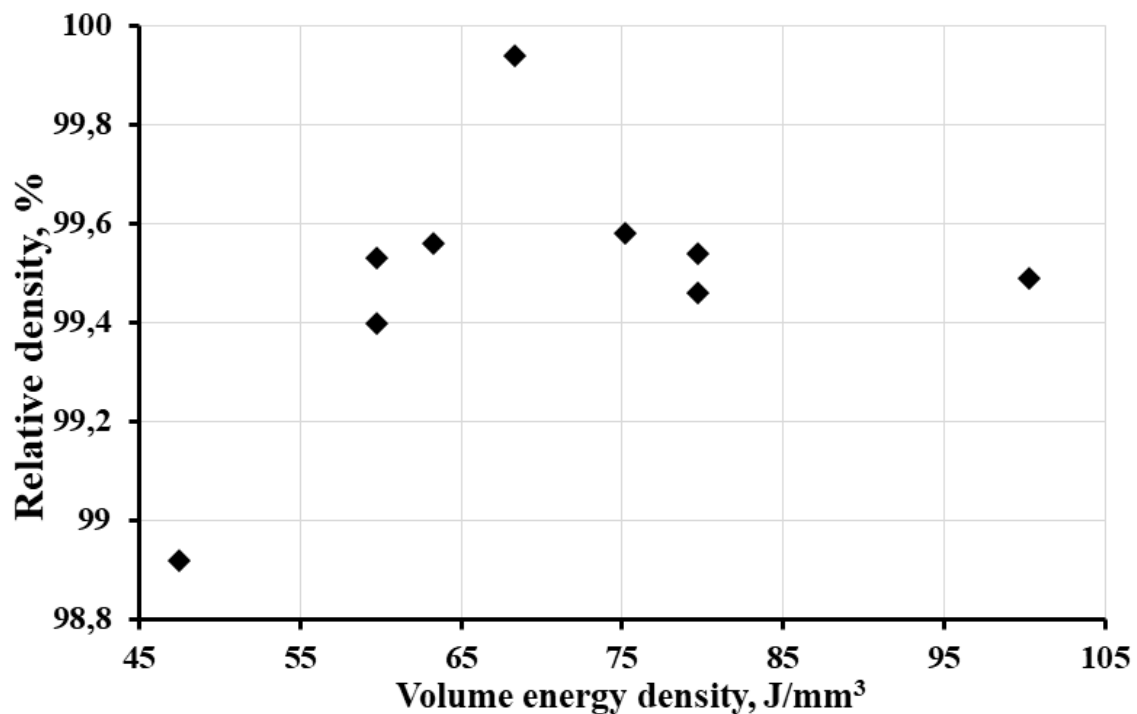


Fig. 2. Bulk samples relative density dependence on volume energy density.

The highest density, measured by the Archimedes principle, was determined for the sample obtained at $63.3 \text{ J}/\text{mm}^3$ energy density. The sample with the lowest density was produced at low energy density ($47.5 \text{ J}/\text{mm}^3$), which resulted in insufficient melting of particles and joining the current layer with the previous one.

The process parameters, which resulted in the highest density of the samples at $30 \mu\text{m}$ layer thickness, and process parameters with identical energy density and layer thickness $50 \mu\text{m}$ and $100 \mu\text{m}$ were used to obtain samples for studying microstructure, phase composition and mechanical properties.

Due to fast cooling rates during SLM process (10^4 – $10^6 \text{ K}/\text{s}$), the as-SLM microstructure features fine cellular dendrites. The crystallization rate and, consequently, the cells size depend on layer thickness used during the SLM process (Fig. 3).

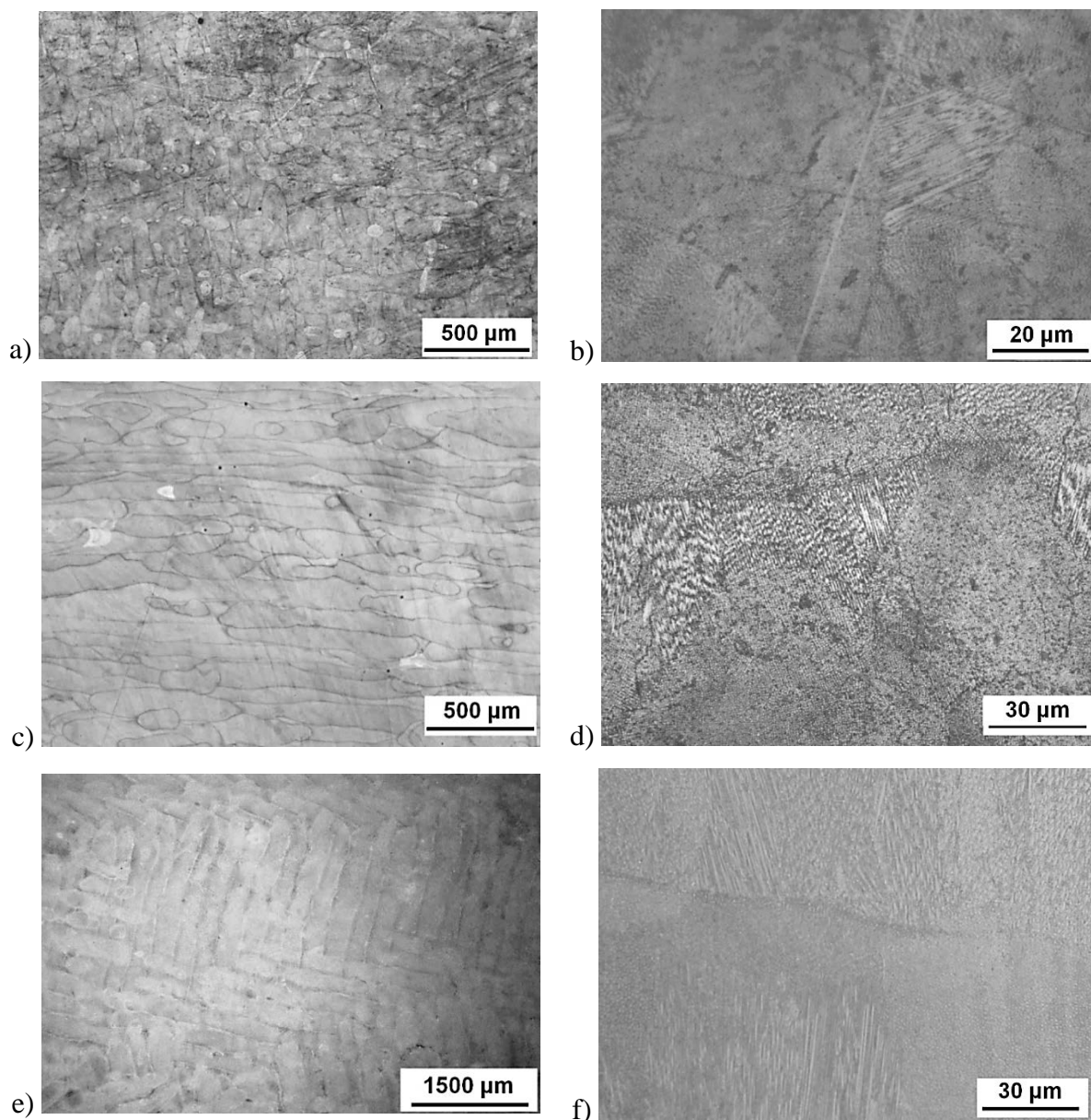


Fig. 3. Microstructures of the samples obtained by SLM at different layer thickness: (a, b) 30 μm , (c, d) 50 μm , and (e, f) 100 μm .

The average cell size at 30 μm layer thickness is 0.7–0.9 μm , at 50 μm layer thickness it is 0.9–1.1 μm , and at 100 μm layer thickness – 1.3–2.0 μm . The other differences at microstructure formation at different layer thicknesses are shown in Fig. 4, where the materials' crystallographic textures, studied with EBSD analysis, are shown.

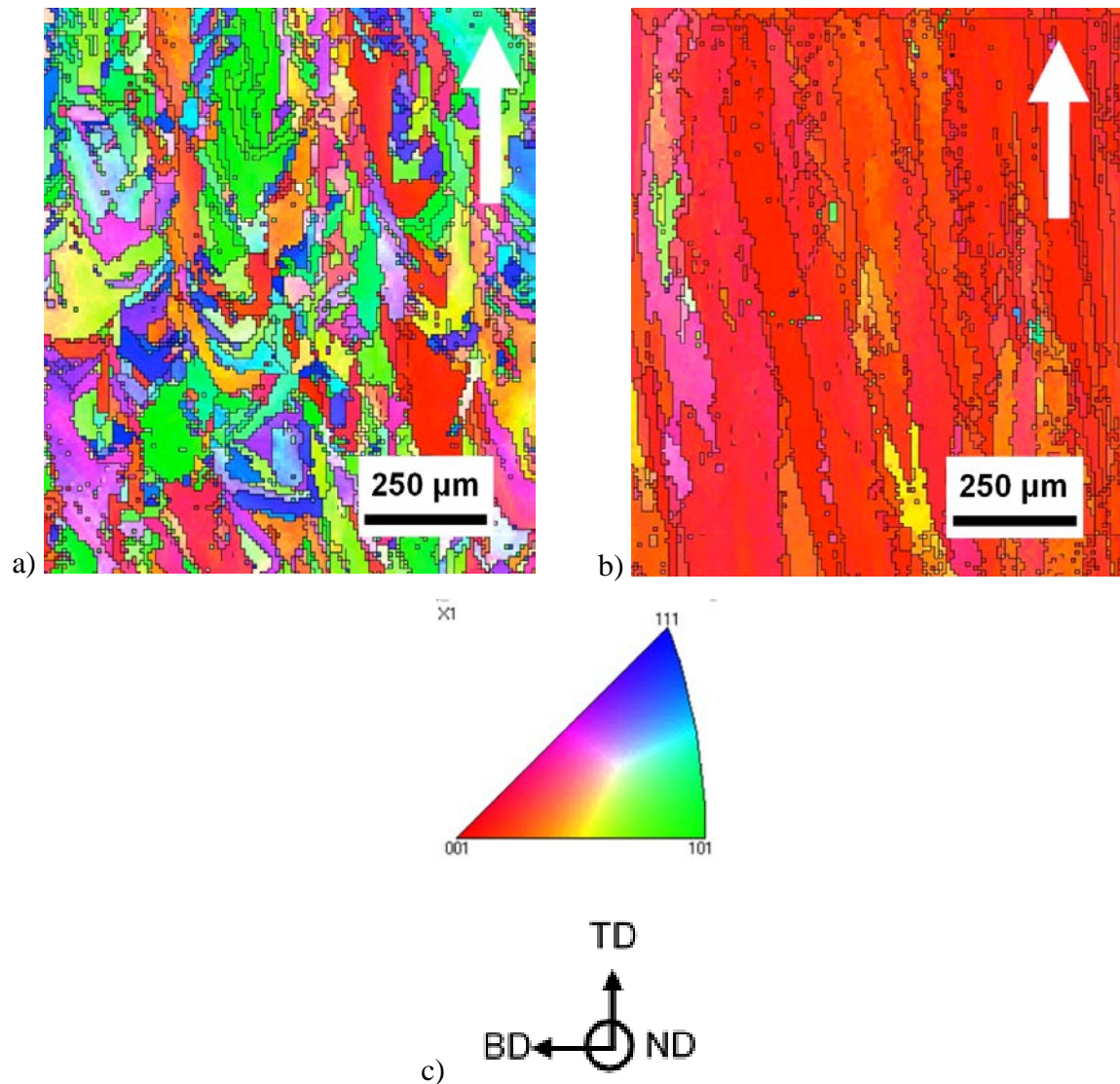


Fig. 4. EBSD analysis of the samples obtained by SLM:
 a) inverse pole figure (IPF) for the samples produced at 50 μm layer thickness; b) IPF for the samples produced at 100 μm layer thickness; c) The index of IPF and the reference coordinate;
 white arrows at figures a) and b) show building direction during SLM process.

The microstructure of the sample produced at 50 μm layer thickness features equiaxed grains with no predominant orientation, while the microstructure of sample obtained at 100 μm layer thickness has columnar grains with $\langle 001 \rangle$ predominant orientation.

The differences in microstructures should have an impact on mechanical characteristics of the material. In order to evaluate the tensile properties of the material, cylindrical specimens were produced to test the properties in accordance with ISO 6892-1. The information about yield strength, tensile strength and elongation at break for the produced specimens are shown in Table 2.

After solution annealing and aging the mechanical properties are much higher than in the non-heat-treated state (see Table 2). This was caused by phase composition change, specifically precipitation of $\gamma''\text{-Ni}_3\text{Nb}$ strengthening phase. After HIP the strength properties decreased due to coarsening of the grains at elevated temperatures, however HIP treatment resulted in higher elongation of the material.

Table 2. The results of tensile tests at room temperature for Inconel 718 specimens obtained by SLM.

Layer thickness, μm	Yield strength, MPa	Tensile strength, MPa	Elongation at break, %
SLM			
50	650 ± 11	845 ± 9	28 ± 4
100	543 ± 2	782 ± 6	31 ± 6
SLM + HIP			
50	645 ± 6	1025 ± 14	38 ± 1
100	481 ± 11	788 ± 12	34 ± 3
SLM + HIP + Solution annealing + Aging			
30	1157 ± 13	1363 ± 12	21 ± 1
50	1145 ± 16	1376 ± 14	19 ± 1
100	1065 ± 20	1272 ± 12	15 ± 4
Casted [20]	488	786	11
Hot rolled, grain size ~40 μm [15]	1245	1415	24
Hot rolled, grain size ~100 μm [15]	1145	1290	24

High-temperature properties are important characteristics for superalloys. Inconel 718 parts are usually not utilized for long times at temperatures higher than 650°C. Table 3 presents the results of tensile tests at 650°C, carried out in accordance with ISO 6892-2, for the specimens with and without heat treatment and HIP.

Table 3. The results of tensile tests at 650°C for Inconel 718 SLM specimens after HIP and heat treatment.

Layer thickness, μm	Yield strength, MPa	Tensile strength, MPa	Elongation at break, %
SLM			
30	716 ± 11	828 ± 9	27 ± 4
50	650 ± 11	845 ± 9	28 ± 4
100	543 ± 2	782 ± 6	31 ± 6
SLM + HIP			
50	626 ± 8	857 ± 14	29 ± 1
100	479 ± 5	665 ± 7	28 ± 2
SLM + HIP + Solution annealing + Aging			
50	942 ± 11	1078 ± 8	20 ± 2
100	872 ± 13	1005 ± 12	17 ± 4

The results of mechanical tests at elevated temperature showed stable results with the elongation at break about 30% for SLM and SLM + HIP specimens. The specimens after HIP and subsequent solution annealing and aging have lower elongation at break compared to other specimens.

Comparing the results of mechanical tests at room and elevated temperatures for the specimens obtained at different layer thicknesses and with different post-treatment, it can be concluded that the lower layer thickness leads to higher strength.

Designing and manufacturing of samples with tailored microstructure. The next step was to develop an approach to manufacture specimens with tailored microstructure in specific areas. In order to produce different areas of the specimens, 50 μm and 100 μm layer thicknesses were used in those areas. Different combinations of these areas in the bulk specimens were used in order to determine a possibility of their spatial variation in the final part. The produced samples are shown in Fig. 5.

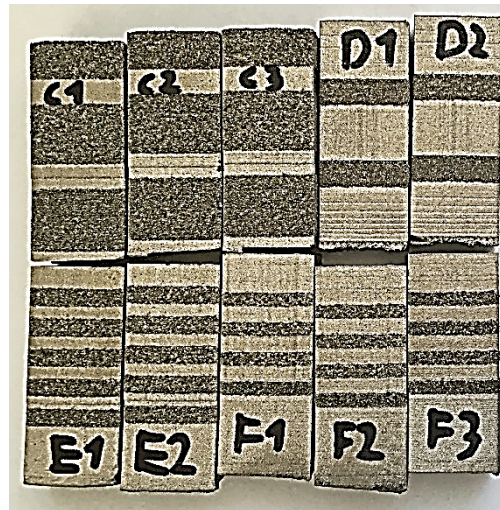


Fig. 5. The specimens with tailored microstructure areas. The dark areas correspond to 100 μm layer thickness, the light areas correspond to 50 μm layer thickness.

EBSD-analysis of the specimens (Fig. 6) shows that on the boundary of different areas a mutual penetration of fine-grained and coarse-grained areas can be seen there, thus a transition area is present in the specimen. Its size is about 500 μm depending on mutual arrangement of fine-grained and coarse-grained areas.

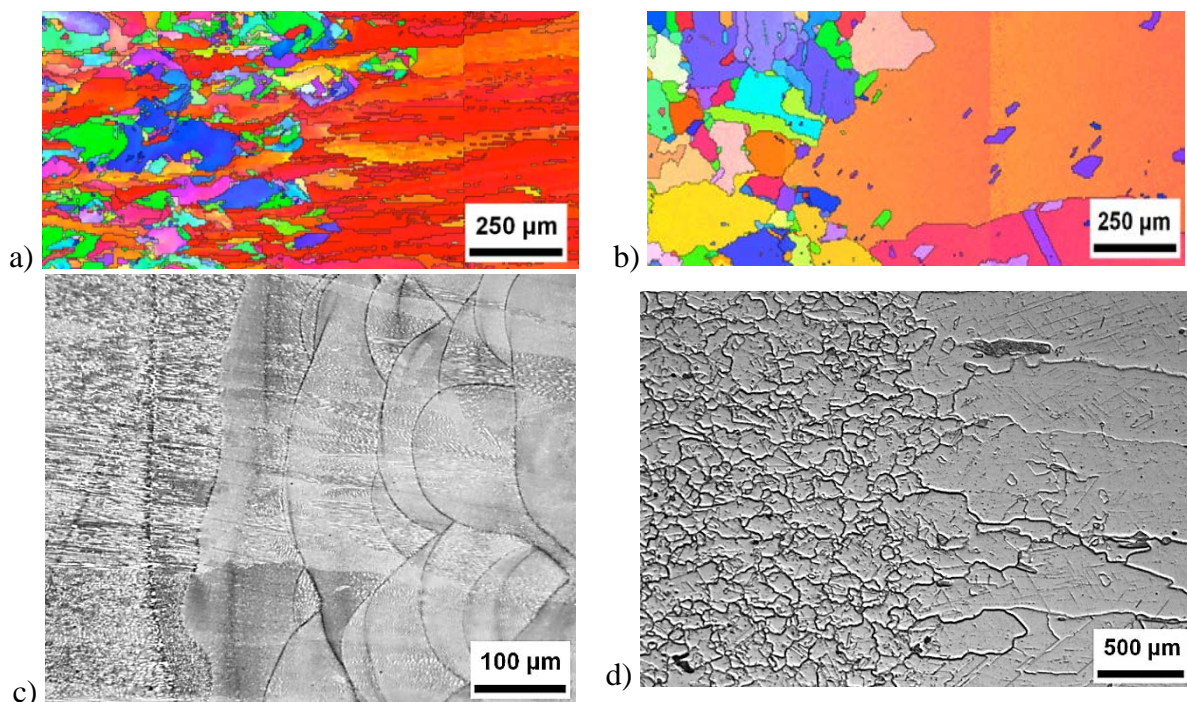


Fig. 6. Microstructure of the transition region between areas produced at 50 μm (left) and 100 μm (right) layer thicknesses after SLM (a, c) and SLM+HIP (b, d).

The effect of HIP on the microstructure can be seen in Fig. 6. Heating above recrystallization temperature point resulted in coarsening of the grains and formation of equiaxed grains in the 50 μm layer thickness area. Thus, formation of two regions occurs after heat treatment – a region of directional columnar grains and a region of fine equiaxed grains. There is NbC carbide network around those grains (Fig. 7).

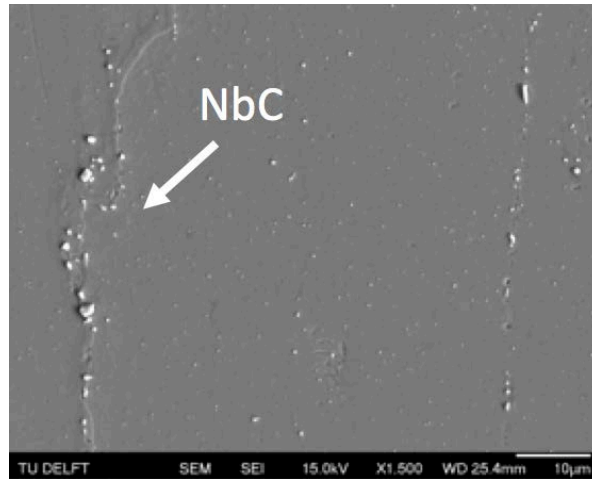


Fig. 7. SEM-image showing the presence of carbides in the bulk material.

The presence of carbides inhibits grain growth during the HIP and heat treatment, and also contributes to strengthening of the material [20].

Figure 8 shows the results of hardness measurements for specimens with tailored microstructure after SLM.

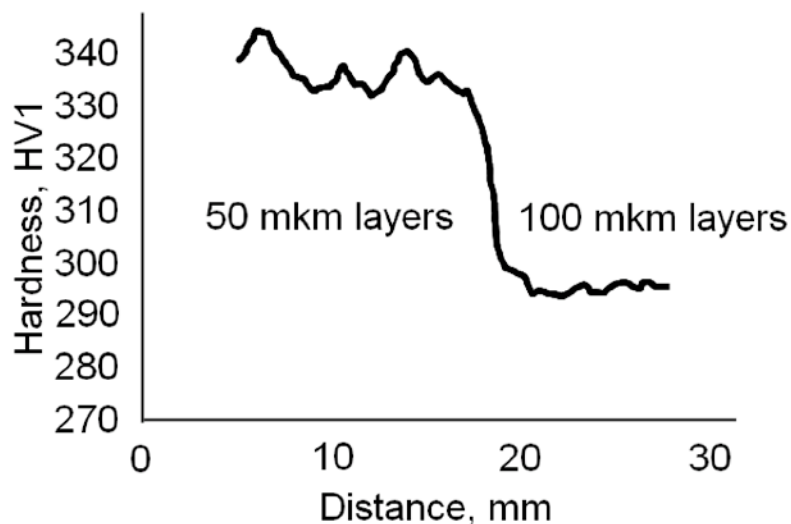


Fig. 8. Hardness of the specimens with tailored microstructure.

It can be seen that there is about 20% difference in hardness values between areas produced at different layer thicknesses. Equiaxed grain region has higher hardness than columnar grain region.

It is known that in order to improve the performance of turbine blades and vanes, dedicated methods of directional solidification can be applied to form a columnar or a monocrystalline structure. According to literature data, this kind of structure improves creep resistance of the materials, but at the same time has lower fatigue strength compared to a finely dispersed equiaxed microstructure.

There are two major elements in a turbine blade: a blade airfoil and a blade root. A blade airfoil works for a long time at high temperature and is under significant stress due to the effect of centrifugal forces. Thus, creep resistance is the most critical property for this part of the blade. At the same time, the blade root works at lower temperatures and is under multidirectional load. For this reason, fatigue resistance is the most critical for the blade root.

From the above reasoning, an approach for producing a prototype of a turbine blade with controlled microstructural areas by selective laser melting has been developed. For manufacturing of the blade root section, we used SLM process parameters that allow to obtain equiaxed fine-grained microstructure (50 μm layer thickness). The blade airfoil portion was produced at 100 μm layer thickness in order to obtain directed columnar grains with $\langle 001 \rangle$ orientation. Fig. 9 shows the photograph of the produced blade and its microstructure along the blade's section.



Fig. 9. The photograph of the produced blade (a) and its microstructure (b).

Thus, it is possible to control the formation of microstructure at specific regions of the part in order to provide the required properties depending on the load conditions.

4. Conclusions

The results of complex investigation of selective laser melting process of Inconel 718 powder is presented in the paper. The effect of process parameters on the relative density of bulk samples was shown. It was shown that higher layer thickness leads to bigger cells size in the microstructure of the bulk Inconel 718 alloy samples. EBSD analysis showed that varying layer thickness leads to changing the grains' morphology. Using higher layer thickness, it is possible to implement a solidification of direct columnar grains during selective laser melting process. The mechanical properties of the specimens depend on the layer thickness: lower layer thickness leads to higher strength. The results of microstructure studies of the samples with alternate areas of fine and coarse grains were presented. Hardness measurements showed the local changes in mechanical properties. Based on the carried out investigation, an approach for manufacturing parts with controlled microstructural areas was proposed. Using a turbine blade as an example, the possibility of manufacturing complex-shaped parts with tailored microstructure and properties by selective laser melting was shown.

Acknowledgments. *The work was carried out with the funding from the Federal Target Program «Research and Development in Priority Areas for the Development of the Russian Science and Technology Complex for 2014-2020». The unique identifier of the project RFMEFI57817X0245.*

References

- [1] T. Wohlers, *Wohlers Report 2017: Additive Manufacturing and 3D Printing State of the Industry - Annual Worldwide Progress Report* (Wohlers Associates, Inc., Colorado, 2017).
- [2] M.J. Holzweissig, A. Taube, F. Brenne, M. Schaper, T. Niendorf // *Metallurgical and Materials Transactions B* **545** (2015) 46.
- [3] A. Popovich, V. Sufiiarov, In: *Metal Powder Additive Manufacturing*, ed. by I. Shishkovsky (InTech, 2016), Vol. 10, p.215.
- [4] A. Popovich, V. Sufiiarov, I. Polozov, E. Borisov, D. Masaylo // *METAL 2016 - 25th Anniversary International Conference on Metallurgy and Materials Conference Proceedings* (2016) 1504.
- [5] D.F. Paulonis, J.J. Schirra // *Superalloys* **718** (2001) 13.
- [6] A.K. Abraham, V.G. Sridhar // *Trends in Biomaterials & Artificial Organs* **29(3)** (2015) 258.
- [7] W.E. Frazier // *Journal of Materials Engineering and Performance* **23** (2014) 1917.
- [8] V.Sh. Sufiiarov, A.A. Popovich, E.V. Borisov, I.A. Polozov // *Tsvetnye Metally* **1** (2017) 77.
- [9] K.N. Amato, S.M. Gaytan, L.E. Murr, E. Martinez, P.W. Shindo, J. Hernandez, S. Collins, F. Medina // *Acta Materialia* **60** (2012) 2229.
- [10] Q. Jia, D. Gu // *Journal of Alloys and Compounds* **585** (2014) 713.
- [11] R. Wauthle, B. Vrancken, B. Beynaerts, K. Jorissen, J. Schrooten, J.P. Kruth, J. Van Humbeeck // *Additive Manufacturing* **5** (2015) 77.
- [12] V.G. Smelov, A.V. Sotov, A.V. Agapovichev // *Chernye Metally* **9** (2016) 61.
- [13] J. Strößner, M. Terock, U. Glatzel // *Advanced Engineering Materials* **17** (2015) 1099.
- [14] H. Meier, C. Haberland // *Materialwissenschaft und Werkstofftechnik* **39** (2008) 665.
- [15] J.P. Pedron, A. Pineau // *Materials science and engineering* **56** (1982) 143.
- [16] S. Bai, L. Yang, J. Liu // *Applied Physics A* **122** (2016) 1.
- [17] T. Niendorf, F. Brenne, M. Schaper, W. Reimche // *Rapid Prototyping Journal* **22** (2016) 630.
- [18] A.V. Agapovichev, V.V. Kokareva, V.G. Smelov, A.V. Sotov // *IOP Conference Series: Materials Science and Engineering* **156** (2016) 012031.
- [19] V.M. Golod, V.Sh. Sufiiarov // *IOP Conference Series: Materials Science and Engineering* **192** (2017) 012009.
- [20] B. Baufeld // *Journal of materials engineering and performance* **21** (2012) 1416.

OPERATIONAL CHARACTERISTICS OF THE COMPOSITE ALUMINUM - CARBON NANOFIBERS

T.S. Koltsova, A.D. Breki, T.V. Larionova, O.V. Tolochko*

Peter the Great St. Petersburg Polytechnic University, Polytekhnicheskaya St., 29, St. Petersburg, 195251 Russia

*e-mail: ol_tol@hotmail.com

Abstract. The operational properties of aluminum-based composites reinforced by carbon nanostructures were considered. It was determined that increasing of carbon content in the sample leads to reduction of the coefficient of friction. The determining factor affecting the wear resistance is the thermal conductivity of the material.

Keywords: metal matrix composite; aluminum; carbon nanofibers; thermal conductivity; wear.

1. Introduction

Carbon nanotubes (CNTs) and nanofibers (CNFs) are introduced into the metal matrix to increase its strength. [1]. Besides, carbon nanotubes hinder dislocation motion in the matrix material during plastic deformation and cause strain hardening [1-3]. The increase in strength is generally accompanied by an increase in wear resistance. Carbon layers of CNTs lubricate the surface of the wear crater and reduce the coefficient of friction. In [4], the tribological properties of Al-CNTs composites were studied depending on the method of preparation, and it was noted by the authors that the key to achieving antifriction and antiwear properties is the good dispersion of carbon nanostructures in the matrix.

Earlier we published articles on preparation of composite powder materials with carbon nanofibres, obtained by CVD synthesis of carbon nanostructures directly on the surface of aluminum particles [5, 6].

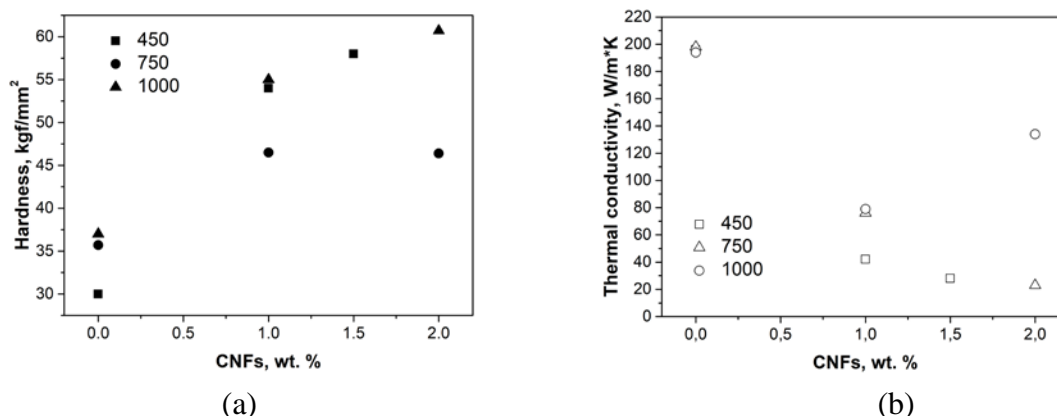


Fig. 1. Change of hardness (a) and thermal conductivity (b) of the material depending on the CNFs content.

In the present article, the composite powder material based on aluminum with 1, 1.5 and 2 wt. % of CNFs is compacted by hot pressing at a pressure of 2 GPa and at temperatures of

450, 750 and 1000°C. According to the Clapeyron-Clausius equation the melting point of aluminum rises by 50°C per 1 GPa [7] with increasing the pressure. As a result, for the presented samples melting took place near the mark of 760°C. Fig. 1 shows the graphs of the hardness and thermal conductivity of the material, depending on the CNFs content.

Figure 1 shows that an increase in the carbon content leads to an increase in hardness. The samples obtained at the melting temperature have a hardness dip, which can be explained by the interaction of CNFs with the aluminum matrix and the destruction of the structure of CNFs, which are graphitized at higher temperatures [5]. The thermal conductivity of the samples with the increase of carbon content decreases due to the formation of a thermal barrier at the aluminum-carbon interface. However, as the pressing temperature increases, the thermal conductivity increases slightly due to the increase in the number of aluminum-aluminum contacts formed upon melting the matrix.

2. Experimental details

Experimental studies of the coefficient of friction and wear rate were carried out in accordance with the document P 50-54-62-88 "Provision of wear resistance of products. Method of accelerated assessment of rubbing surfaces wear resistance ". Accepted for friction testing, the assembly of the friction unit includes a roller fixed to a lifting carriage in a special holder, fixed perpendicularly to a plate and movement direction. In each experiment, one pass of the roller along the plane was realized. The length of the friction path in one pass was 70 mm. The average sliding speed of the roller along the plane was ≈ 5 mm/s. The roller was pressed against the plane with a force of 45H. The material of the counterbody is 12X1 steel. Wear studies were carried out in the friction mode of turning the steel grade IIX15 on a flat surface of the composite material. The investigations were carried out using an end face friction machine. The ball-on-plane (ball diameter is 8 mm) type wear tester was used. The load was 6.5 N, while the rotational speed of the spindle with the ball fixed to it was 620 rpm; the time of one test was 5 minutes.

3. Results and discussion

The graphs of the frictional force against time for the samples of pure aluminum and aluminum with the addition of 1 to 2 wt.% of CNFs obtained in the same conditions are shown in Fig. 2. From the dependences obtained, it can be seen that the force of limit of static friction for friction of pure aluminum are ≈ 14 N under the selected conditions of frictional interaction (load, speed). Further, a decrease in the friction force after force of limit of static friction is observed, but starting from ~ 5 s friction force sharply increases, which is associated with the destruction of the oxide film and the appearance of an adhesive interaction of friction surfaces.

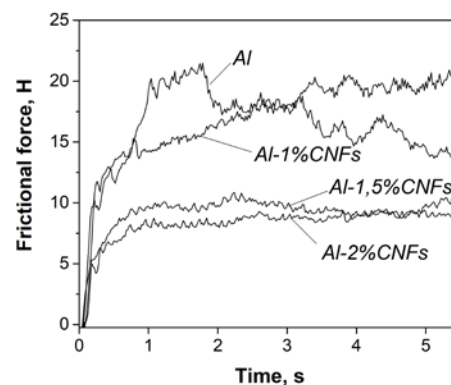


Fig.2. Dependence of sliding frictional force on the time when testing samples Al and Al-CNFs composites.

The graph of friction against time shows that the force of limit of static friction is 35% less for a sample with carbon nanofibers than for the aluminum sample, which is due to the presence of CNFs. Further, after force of limit of static friction the force of friction continues to increase slightly and is set at a value of $\approx 11\text{N}$. The absence of a sharp intermediate increase in the frictional force indicates the stability of the destruction and recovery of the oxide film. The friction force of a sample material containing 1.5% of nanofibers is $\approx 31\%$ less than that of pure aluminum, as well as the anti-friction action of carbon nanofibers. For a sample with 1.5% CNFs, it is seen that its force of limit of static friction is 53.6% (2 times) less than for aluminum samples ($\approx 6\text{N}$), which is due to the presence of CNFs. Samples of Al-1.5% CNFs have higher hardness and 62.5% (2.7 times) less frictional force compared to pure aluminum. This indicates the anti-friction action of carbon nanofibers with increasing their concentration in the matrix. For a sample with 2% CNFs, it can be seen that its force of limit of static friction ($\approx 5\text{H}$) is 64.3% (2.8 times) less than of the aluminum samples, which is due to the presence of CNFs. Further, after overcoming the limit of static friction, the frictional force increases slightly and is set at a value of $\approx 7\text{N}$. Just like in the previous case, the absence of a sharp intermediate increase in the frictional force indicates the stability of the destruction and recovery of the oxide film. Material with 2% CNFs has a hardness higher and a friction force of about 56% (2.3 times) less than that of pure aluminum, which also indicates the anti-friction action of carbon nanofibers. Fig. 3 shows the dependence of the change in friction coefficient on the content of CNF. The coefficient of friction was determined according to the equation:

$$f = F_f / F_n, \quad (1)$$

where f is the coefficient of sliding friction; F_n is the normal load in the contact, F_f is the sliding friction force.

From the summary graph (Fig. 3(a)), it can be seen that an increase in the carbon content in the sample leads to a decrease in the coefficient of friction. The coefficient of sliding friction is minimal at 1.5-2% CNFs, and is 0.14-0.15.

For the quantitative evaluation of wear, the diameter of the wear crater was used as an indicator. Dependences of the diameter of wear crater on the concentration of CNFs are shown in Fig. 3(b) as well as the hardness values for the samples. As it can be seen from the graph, with increasing in carbon content, the hardness of the samples also increases, and the wear dependence has a minimum near 1% CNFs.

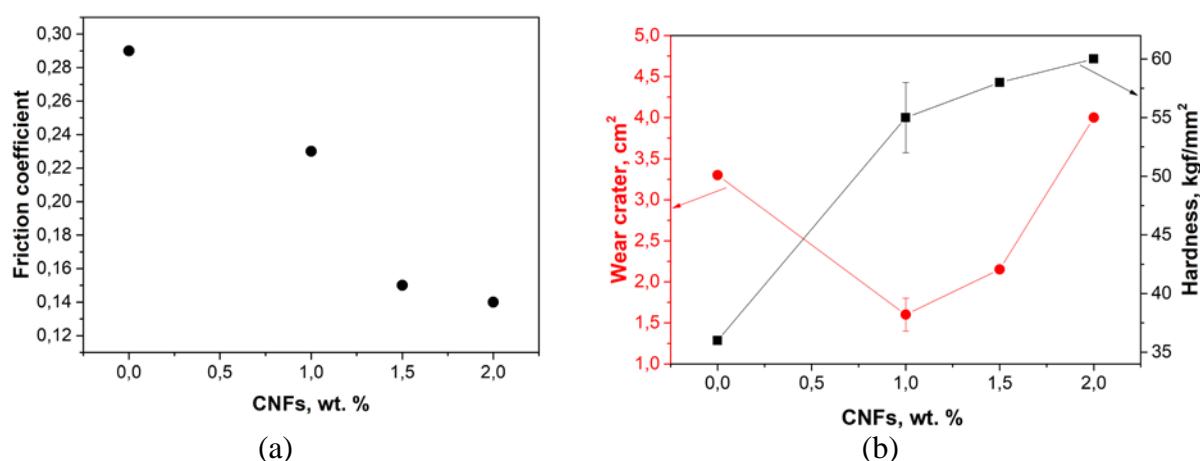


Fig. 3. Dependences of the change in friction coefficient (a), wear crater and hardness (b) on the content of CNFs.

The wear crater in the sample with 1% CNFs decreased by 50% compared to pure

aluminum, and further increase in the carbon content did not lead to a significant increase in wear resistance, despite the higher hardness of the composites. At the same time, the wear of a material containing 2% CNFs is not much higher in comparison with pure aluminum.

One of the problems in carrying out the wear tests was the spreading of the aluminum matrix of the sample onto the counterbody, especially in case of pure aluminum sample. In this connection, additional tests were carried out according to the conical body-plane scheme. In this case, the counterbody was a cone made of high-speed steel (P6M5) with an angle of 114.2 degrees, the plane was an aluminum composite. The load was 36 N, shaft rotational speed was 620 rpm, test time was 2 min.

Carrying out a series of tests according to two schemes showed a direct dependence of the wear of the material on hardness (Fig. 4(a)). A wide spread of values in the region of 45 HB is observed for the samples with low density.

A comparison of wear with the thermal conductivity of the material showed an interesting trend (Fig. 4(b)). Increasing the thermal conductivity leads to a decrease in wear of the material. When carbon nanofibers were introduced into the samples, the thermal conductivity of the material was reduced due to the occurrence of a thermal barrier at the interface, especially with increase in the content of CNF (samples with hardness of in the region of 55 HB, Fig. 1(b)). Also, low thermal conductivity is observed in materials with high porosity (samples with hardness in the region of 45 HB, Fig. 1(b)).

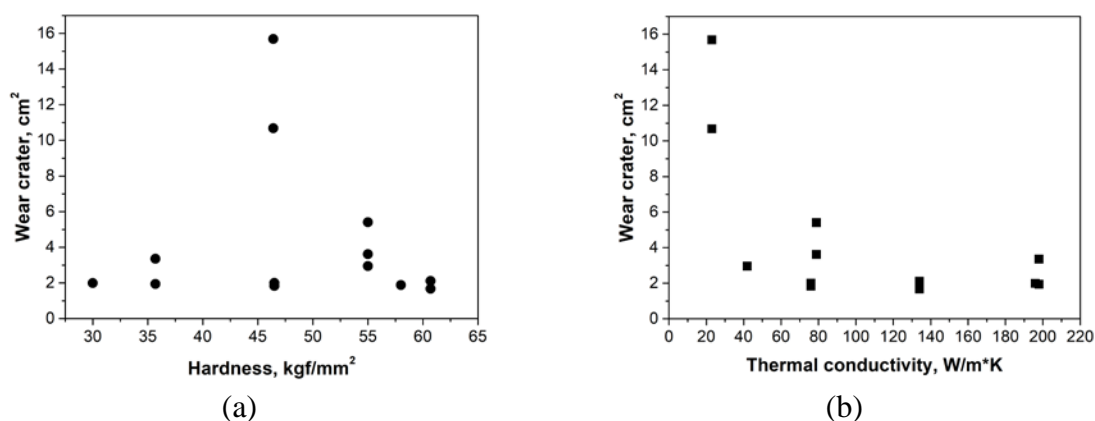


Fig. 4. Dependence of the change in the wear crater of the material on the hardness of the material (a) and of the wear crater on the thermal conductivity (b).

When subjected to friction in the spin friction, the material undergoes local heating in the contact zone, which leads to its more softening in case of its overheating. In this regard, materials reinforced with CNFs, despite the high hardness, show increased wear due to low thermal conductivity.

4. Conclusion

As a result, the paper shows that the introduction of carbon nanofibers into an aluminum matrix leads to an increase in the hardness of the composite. As the carbon content increases, the thermal conductivity of the samples decreases due to the formation of a thermal barrier at the aluminum-carbon interface.

Investigations of tribotechnical properties of composite materials showed the antifriction effect of carbon nanofibers, which manifests itself both at the time of friction and during the movement of friction surfaces relative to each other. An increase in the carbon content to 1.5-2% of CNFs in the sample leads to a decrease in the coefficient of sliding

friction to 0.14-0.15. For anti-wear properties, a sample with 1% CNFs has the best properties. It can be assumed that the thermal conductivity of the material is the determining factor influencing the anti-wear properties, since local heating in the contact zone leads to its softening.

Reference

- [1] X.H. Chen, J.C. Peng, X.Q. Li, F.M. Deng, J.X. Wang, W.Z. Li // *J. Mater. Sci. Lett.* **20** (2001) 2057.
- [2] F.M. Deng, X.H. Chen, W.X. Chen, W.Z. Li // *Trans. Nonferrous Met. Soc. China* **14** (2004) 681.
- [3] T. Larionova, T. Koltsova, Y. Fadin, O. Tolochko // *Wear* **319** (2014) 118.
- [4] I.Y. Kim, J.H. Lee, G.S. Lee, S.H. Baik, Y.Z. Lee // *Wear* **267** (2009) 593.
- [5] A.I. Rudskoy, O.V. Tolochko, T.S. Kol'tsova, A.G. Nasibulin // *Metal Science and Heat Treatment* **55** (2014) 564.
- [6] T.S. Kol'tsova, F.M. Shakhov, A.A. Voznyakovskii, A.I. Lyashkov, O.V. Tolochko, A.G. Nasibulin, A.I. Rudskoi, V.G. Mikhailov // *Technical Physics* **59** (2014) 1626.
- [7] A.P. Babichev, N.A. Babushkina, A.M. Bratkovsky, *Physical quantities* (Energoatomizdat, M., 1991).

THERMOMECHANICAL PROCESSING OF STEELS AND ALLOYS PHYSICAL FOUNDATIONS, RESOURCE SAVING TECHNIQUE AND MODELLING

A.I. Rudskoi¹, G. Kodzhaspirov^{1*}, J. Kliber², Ch. Apostolopoulos³

¹Peter the Great St. Petersburg Polytechnic University, 29, Polytehnicheskaya, 195251 Russia, St. Petersburg

²VŠB – Technical University of Ostrava, Ostrava – Poruba, Czech Republic

³University of Patras, Panepistimioupolis Rion, 26500 Patras-Greece

*e-mail: gkodzhaspirov@gmail.com

Abstract. The physical fundamentals, resource-saving technique and modelling of Thermo-mechanical Processing (TMP) applied to steels and alloys are described. Structural and phase transformations under TMP and their role in formation of final structure and mechanical properties in the different steels and alloys are presented. The basic physical principles of TMP as a base for developing of new resource-saving technologies of metal products manufacturing and examples of industrial application are presented. Different TMP schemes developed for producing of bar and sheet rolling products, annular billets cylindrical billets with variable sections of profile are demonstrated. Modelling, including Physical and Numerical simulation, Experimental Planning and FEM applied to control structure and mechanical properties of TMP treated products are presented.

Keywords: thermomechanical processing (TMP); physical foundations; steels; dynamic recrystallization.

1. Introduction

Steels and alloys, including ferritic-pearlitic, austenitic and duplex, TWIP and other steels and superalloys grades as well have been widely used in industry because of their good combination of mechanical and functional properties. Thermomechanically processed steels and alloys with a high strength, good toughness and weldability, cold and heat resistance, high corrosion resistance etc. have been a great commercial success as a structured materials for many years [1-3]. TMP applied to austenitic stainless steels could produce high-strength plates and stocks with yield strength of higher than 400 MPa, and 600 MPa for high nitrogen steels [4, 5]. It has been reported that TMP can give pearlitic low alloyed steels substructure hardening which rise strength without much reduction in ductility and toughness and functional properties such as cyclic torsion strength [6]. It is possible to obtain this or that combination of properties by controlling the structure evolution.

2. Physical Foundations

In Thermomechanical Processing thermo-deformation action makes the structure evolve. With growth in the strain degree all the structural levels (including atomic, micro- and meso-) involved progressively [7, 8]. The structural transformations occurring at the mesolevel are primarily responsible for formation of the final structure and hence for the properties of metals and alloys subjected to TMP. The efficiency of TMP depends primarily on process parameters

such as temperature, strain, strain rate, divisibility, and time elapsed from the deformation to the start of quenching, in the case of High Temperature Thermomechanical Processing (HTMP). In last case (HTMP), deformation is realized in the hot and hot-warm temperature range. It is known that in this case the rearrangement of the dislocation structure of the high-temperature phase (for steels this is austenite) is a consequence of competing and successively preparing each other process of mechanical hardening, dynamic recovery (or cell and fragment substructure formation), and dynamic recrystallization. In the initial stages of the deformation the prevailing process is the first one. With growth in the strain and strain rate the dislocation density increases. In accordance with the modern theory of high plastic deformation collective forms of motion arise in a dislocation ensemble and cause substantial restructuring, i.e., breakage of the body of grains first into somewhat off-oriented cells and then into fragments [9, 10]. From the standpoint of the modern physics of plastic deformation of crystals the appearance of collective forms of motion means the appearance of rotary modes of plasticity in the crystals. At the specific loading rate the deformed material becomes incapable of dissipating the mechanical energy supplied to it as a result of only plastic displacements. So it breaks into a set of randomly oriented micro-regions (cells, fragments) each of which turns in a plastic manner in the deformation process and thus absorbs additional portions of energy. With increasing of the loading rate (growth in the strain and strain rate) the rotary modes and their structural feature (fragmentation) should intensify continuously. This goes on until the rate of supply of mechanical energy to the billet exceeds the next threshold value at which the fragmented structure becomes unsteady and dynamic recrystallization, which is the most powerful energy dissipation structural mechanism, comes into play. It is the change in the thermomechanical temperature-strain parameters which is responsible for the kinetics of structure evolution, for the attainment of this or that state (often a heterogeneous structure consisting of regions of this or that structural mode in various proportions and distributed with different degrees of uniformity over the volume of the billet, and, correspondingly, for the attainment of a specific combination of properties.

The results of experimental studies applying single phase austenitic stainless steel alloyed by Ti and Nb the described above theory has been successfully confirmed [11]. In steel 18Cr10NiNb with a different deformation schedule fine structure evolved by different mechanisms. In case of fractional deformation, increase in total strain degree leads to increase the dislocation density. The greatest change is takes place after the first pass: from 10^8 to $2,5 \times 10^{10} \text{ cm}^{-2}$. Subsequent increase in total strain degree has practically no effect on the dislocation density. After 5 passes it is remains at the level of 10% strain degree. The spatial distribution of dislocations after the first pass is characterized by the presence of sections with a weakly expressed cellular substructure as well as sections of fragmented substructure. In the similar corrosion-resistant austenitic Ti-bearing steel the sections where fragmentation is observed against the background of a deformational micro-twins are often encountered (Fig. 1a).

With fractional accumulation of the total deformation the fraction of the volume occupied by cellular substructure decreases monotonically, while the fraction of the volume occupied by fragmented substructure increases.. Thus after third pass, the fraction of volume with a fragmented substructure reached $\sim 60\%$ and after 5 passes $\sim 90\%$ for steel with Ti, and 80% - after 3 passes and 95% after 5 passes for Nb-bearing steel correspondingly (Fig. 1 b). No signs of dynamic recrystallization are seen even after 50% strain degree with a fractional accumulation of the strain (5 passes per 10% in each pass). The mentioned above takes place applied to both steels. Structure formation in one-time deformation also has distinctive features. In both steels the proportion of the volume occupied by cellular substructure decreases monotonically with increase of strain degree. The proportion of the volume occupied by fragmented substructure increases steadily. The most significant difference in the

variation in structure in one time deformation in comparison with the fractional case is that sectioned of dynamic recrystallization appear in steel with increase in the strain degree on one time rolling reduction. They are first observed after 30% strain degree. The proportion of the volume covered by recrystallization structure increase in the both steels with increasing of single pass strain degree to 50% (Fig. 1 c,d). Similar structure transformation has been found in duplex austenitic–ferritic corrosion-resistance steel [10]. The mechanical, corrosion, and corrosion-mechanical properties and the high-temperature strength change accordingly primarily as a function of the structural modes, of the sizes of the structural components, and of the off-orientation angles. For example, the highest strength is observed in steel with non-recrystallized structure and decreases with growth of recrystallized volumes.

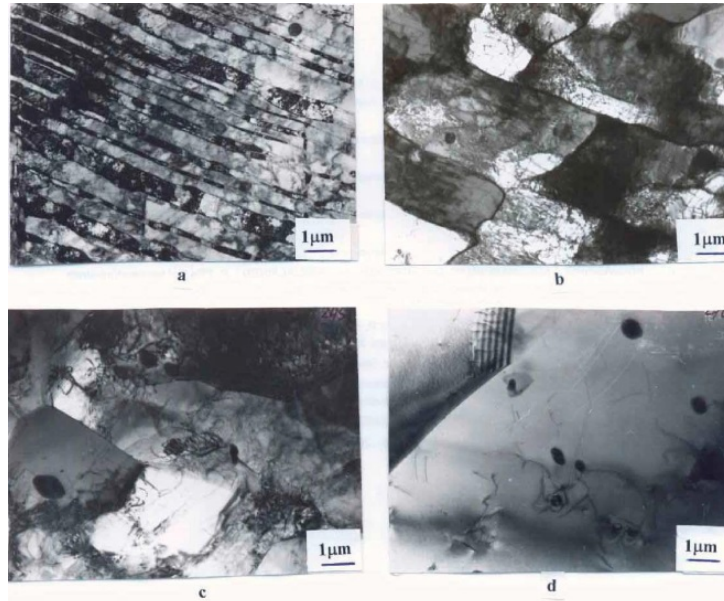


Fig. 1. Fine structure of austenitic stainless steels: Ti bearing steel, subjected to 10% strain for 1 pass (a); Nb bearing austenitic stainless steel subjected 50% strain for 5 passes (b); Nb bearing austenitic stainless steel subjected 50% strain degree for 1 passes (c, d) [7].

In alloys undergoing phase transformations the kinetics of structure formation is more complex but its main feature is inheritance of the dislocation structure of the deformed alloy by the forming phase. For example, in alloys undergoing martensitic transformation the martensite formed as a result of accelerated cooling after HTMP inherits the dislocation substructure including polygonal and fragmented ones of hot-deformed austenite. The latter circumstance promotes suppression of brittleness [2, 10]. In the case of HTMP with deformation in austenite-pearlite temperature range and accelerated cooling at a rate lower than the critical one the formed intermediate structures of pearlitic type have smaller sizes of pearlite grains than those ensured by cooling of non-deformed steel, which produces a positive effect on the mechanical properties [12].

3. Resource-saving technologies

Optimization of the TMP invites investigations of the structural-mechanical behavior and to develop resource-saving technology and proper equipment to manufacture different metal billets and parts. The mentioned above physical fundamentals based on the recent ideas of the physics of plastic deformation had been taken into account for the control of structure formation during thermomechanical processing (TMP) of steels and alloys [10]. By now there are many schemes of resource-saving TMP are developed up to days. The most important of

which: HTMP, Ausforming, Controlled Rolling (CR), and etc. (Fig. 2) [1, 2, 10, 13, 14].

High Temperature Thermomechanical Processing. The High-Temperature Thermomechanical processing (HTMP) of steel, involving the hot deformation of austenite followed by accelerate cooling, is aimed at improving the mechanical properties of an austenite due to the formation of a well-developed substructure (for example in the austenitic heat-resistant and corrosion resistant steels and alloys) and also at improving the mechanical properties of the products of austenite transformation (martensite, bainite, pearlite) due to hereditary influences on their morphological and substructural characteristics [2, 10, 14, 15]. Of considerable interest is information about the features of formation of the austenite structure and of its change under the conditions of hot deformation within the HTMP cycle since the substructure is the primary factor that determines the structure and therefore the whole set of mechanical properties of the products of the austenite transformation.

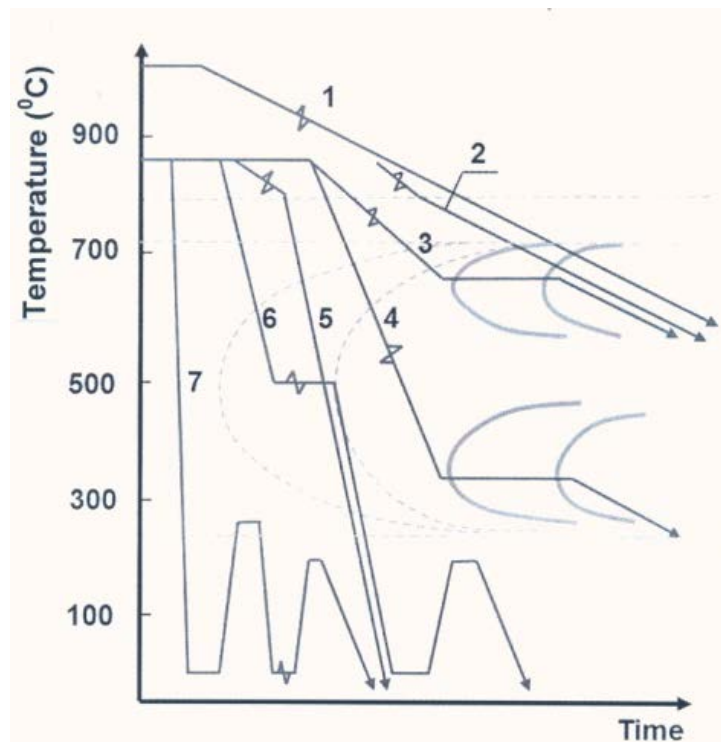


Fig. 2. The scheme of Thermomechanical Processing: 1 – hot rolling; 2 – Controlled Rolling; 3 – TMP with pearlitic transformation; 4 – TMP with bainitic transformation; 5 – HTMP; 6 – Ausforming; 7 – Strain age-hardening of martensite.

Thermomechanical processing of steel plates. Most of the structural steel grades are flat products rolled on plate mills or hot strip mills. The application of microalloying elements since the 1960's mainly in combination with special rolling regimes developed first on plate mills enables a wide range of new economical, weldable, formable, tough and ductile high strength low alloy steel grades to be produced.

Last decades the considerable research efforts were directed toward the development of high strength low alloy (HSLA) steels [16-18]. The plates are used for structural applications such as buildings, bridges, ships, pressure vessels, tube and pipelines, and for automotive applications. In these cases the important mechanical properties are strength, ductility, and toughness at low temperatures, ductile-brittle transition temperature, and weldability. The basic difficulty is that these properties are often incompatible in HSLA steels. Later developed variants of CR with accelerated cooling make it possible to obtain a bainitic structure in some

steels, which also inherits the mesostructure of hot-deformed austenite and, correspondingly, the positive effect due to this. Accelerated controlled cooling after hot rolling alters the microstructure of plate from ferrite-pearlite to fine grained ferrite-bainite and consequently increases the strength without a loss in low temperature toughness [19, 20]. The deleterious effect of precipitation hardening of Nb(C,N) or V(C,N) on impact toughness is counteracted by improved grain refinement.

The aims of recrystallization controlled rolling especially followed by accelerated cooling (RCR+ACC) are to produce hot rolled steel products having high strength, high toughness and good weldability. The concept of RCR+ACC is attractive in that it is a relatively uncomplicated and high productivity process and can be applied on conventional mills. This procedure is intrinsically more economical than controlled rolling at low finish rolling temperatures and also lends itself well to use in many mills which are not sufficiently strong for low temperature controlled rolling practice to produce heavy plates and long products. The key to success with recrystallization rolling is to define rolling schedules combining a maximum degree of microstructural refinement with acceptable low rolling loads, good shape control and high productivity.

Ausforming. Ausforming treatment is applied to the steel while it is in the metastable austenitic condition prior to quenching to martensite (Fig. 2). The principal benefit of this treatment is that it can produce significant improvements in strength without degrading toughness and ductility. In some steels, toughness is actually improved simultaneously with strength. The low temperature nature of this treatment produced very little thermal distortion, thus making it ideally suited for precision finishing operations. The Ausforming process can be directly substituted for groups of conventional finishing processes saving considerable cost while optimizing mechanical performance. The strengthening effect of Ausforming is attribute to the inheritance of the dislocation substructure and carbide distribution, generated in the metastable austenite during deformation, to the final martensite after quenching [13]. A fine dispersion of carbides is formed during the working of austenite, stabilization not only the grain size but the subgrain size as well [14]. Ausforming results in a very high dislocation density in the final martensite. The dislocation network produced is not the normal one where the dislocations are concentrated at the cell walls, rather they are more uniformly dispersed. Larger scale microstructure effects also play an important role in the strengthening process. The low temperature of working (in the range from room temperature to $\sim 600^{\circ}\text{C}$ depending on alloy composition tends to restrict austenite grain growth and hence, ultimately, the martensite plate size.

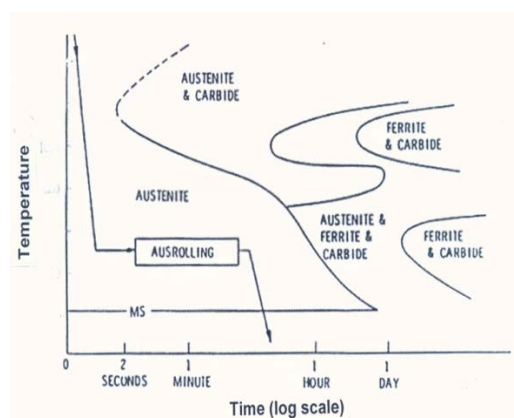


Fig. 3. Schematic illustration depicting ausrolling time-temperature regime quench from austenitizing temperature.

Ausforming steels can eliminate stage tempering which would have occurred during the tempering of conventionally quenched martensite. Thus, autotempering appears to be promoted by ausforming. For surface ausforming, optimum tempering treatments are most likely not those used for conventionally developed martensite. The principal features of the apparatus for precision ausforming of gears are interactive forming utilizing closed-loop control and high accuracy forming die. Low temperature thermomechanical processing has considerable potential for the finishing of precision machine elements to net shape. In this process, the final dimensions and finish quality are achieved by thermomechanically working the carburized case of gear teeth while they are still in the metastable austenitic condition prior to quenching to martensite. The results of such processing methods are (1) the elimination of several manufacturing steps including grinding and hard finishing, (2) the generation and retention of surface compressive residual stresses, and (3) the achievement of strengthening in the surface layers subjected to the high operating stresses. The following benefits are derived from these effects: significantly lower manufacturing costs, greater yield strength, improved fracture resistance, greater pitting and bending fatigue strength, and greater product reliability and as a result resource-saving effect. The encouraging results from previous studies justify additional research and development to refine and implement the technology and to extend it to be other machine elements such as bearings, splines, cams, roller, clutch surfaces and shafts.

Resource-saving technologies for TMP of rings, shafts and axles. One of the most advanced methods of producing precision billets is rolling that ensures the metal utilization coefficient on the level of 0,7-0,8, while the similar coefficient for conventional methods is on the level of 0,25-0,45. At present there are several varieties of this method, among them - radial rolling, face rolling and longitudinal rolling in idle rollers.

The realization of the given methods for plastic deformation under the conditions of the thermomechanical processing (TMP) gives a substantial increase of their application efficiency. In this case the parameter level increase of mechanical and functional properties is possible and it is determined as a result of the inheritance of the dislocation structure elements formed during the deformation process on the products transformation formed to the end of the TMP. The different TMP schemes developed for application to two rolling methods - radial- face rolling for producing annular billets including billets with Z-shaped profile. The rotating treatment taking place during the radial-face rolling provides reduction of the deformation stress due to local loading which in turn allows to apply deformation in rather a wide temperature interval and to receive high-precision billets. The possibility of temperature lowering till the warm temperature deformation creates preconditions for realization of special TMP due to the regulation of structure formation by the control of temperature-strain regime of the hot-warm deformation taking place very often without application the subsequent special cooling. On the basis of studies carried out for the rings, diameter from 150 to 700 mm, made of low alloyed steels with 0,4% C and others it were developed the basic principles of non-isothermal TMP of annular billets and realized as new resource-saving technologies. The regulation of cooling velocity was carried out by means of variation of water consumption or by water-air mixture prepared in special spraying device that provided cooling of rings of different profile sections according to predetermined regime (Fig. 4).

The deformation of middle-carbon steels in the temperature interval 1000-600°C under continuous air cooling with velocity from 10 to 1°C/s causes processes of partial cementite coagulation in the pearlite component, the formation of cellular and fragmented structure in ferrite with dislocation density inside of cells and fragments in the interval 10^9 - 10^{10} cm⁻². The temperature lowering in the end of the deformation causes gradual increase of defects of both structure components with some growth perlite portion component. Due to such type TMP it is possible to adjust mechanical and technological properties in the wide range.

The cold longitudinal rolling is one of the most advanced methods of producing parts of "axle" and "shaft" type. With the help of this method it is possible to produce parts from carbon steels as well as from alloyed steels, and besides quite recently the rolling of parts from heat resistant dispersion-hardened alloys of type 1%Cr, 65%Ni, 1%Mo, 1%Ti, 1%Al, 1%W was also applied. The list of parts includes parts beginning from force studs, whose diameter is 23,5 mm before treatment and length 322 mm to the waggon axles with diameter 200 mm and length - 1800 mm. The realization of producing steel parts according to scheme of Preliminary Thermomechanical Processing (PTMP) makes possible along with shaping to provide an increase of this or that property complex due to structure regulation by means of its level change of parameters with simultaneous reduction of product cost price (Fig. 5).

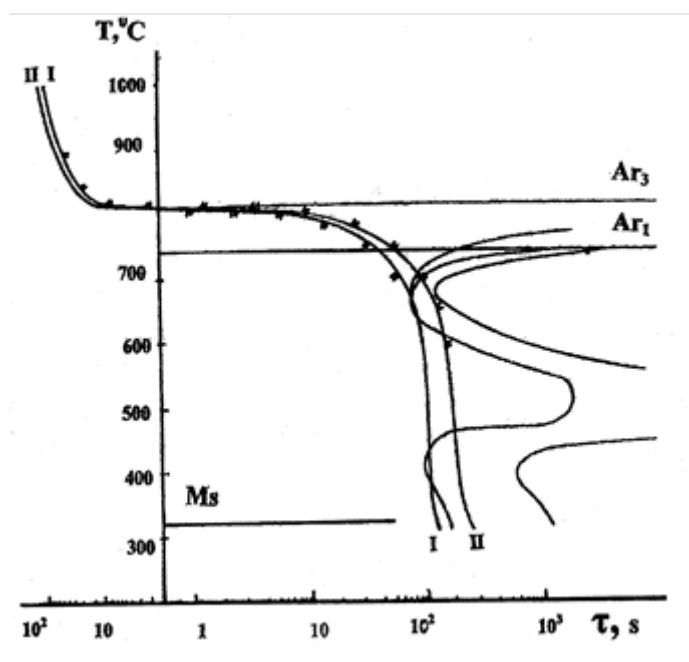


Fig. 4. Cooling and rolling curves of steel (0,38CCrSi) rings under the non-isothermal regimes with deformation in the range 900 - 700°C (I) and 800-600°C [12].

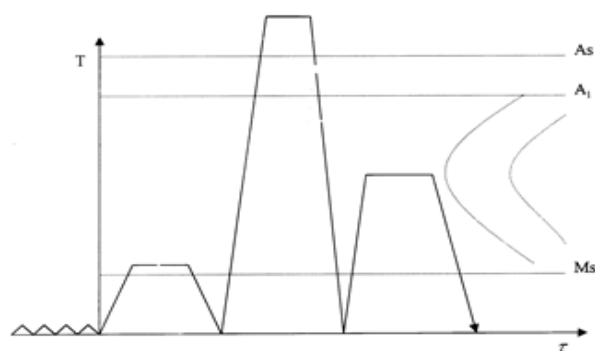


Fig. 5. The scheme of Preliminary Thermomechanical Processing (PTMP).

Substructural strengthening result in PTMP, when applied cold deformation with the combination of post deformation annealing and induction hardening based on the of dislocation structure inheritance effect on the mechanical properties such as torsion static

strength has been studied in [6]. There were carried studies of the value influence of particular and total reductions, of the deformation fractionality and of the post-deformation heating temperature on structure, mechanical properties and cyclic durability of parts from steels 0,6%C, 2%Si, 1%Cr; and 0,45%C, 1%Cr, 2%Ni, 1%Mo, 1%V.

The rolling of initial billets with pretreatment annealing was applied on the mill "PR-100" with capacity 100t. The deformation was carried out for different number of particular reduction ($\varepsilon_i=4-12\%$) under total degree $\varepsilon_\Sigma=50\%$, ensuring the required technological plasticity and a given profile of the finished billet. As a result of studies carried out with the use of optic and electron microscopy it was established that the initial ferrite-perlite structure changes substantially under the influence of the plastic deformation. Ferrite locations prolong along the deformation direction, and electron microscopic studies shows ferrite fragmentation. In this case the cementite plates are broken and bended (sometimes), but the main deformation taken place in the more mild and plastic ferrite matrix. The further studies were carried out on the cold-deformed billets with the following heating in the temperature interval 300-700°C. The temperature increase till 500°C causes the polygonization in the ferrite matrix before induction hardening followed by low temperature tempering and allows to realize the positive effect of TMP. The results of mechanical tests shows an increase of the level of plasticity characteristic and impact strength by 30-40% in comparison with non-deformed condition. Functional characteristics, evaluated by laboratory testing, correspond to 3-4 fold increase of requirements, imposed to similar parts.

4. Modelling of thermomechanical processing of steels and alloys

In the development of TMP mathematical, physical and numerical simulations have important roles to play. By using best current knowledge and modern facilities, these modelling techniques can enable the rapid and economic evaluation and prediction of TMP processes and applications. There are different techniques are used for the creation of the models described effect of the main process parameters to the structure and mechanical and functional properties. The most popular are: physical simulation based on the torsion (or compression), Experiment planning method (EPM); Finite element method (FEM) based model of structure development in metal forming processes. As for physical simulation of TMP there are different testing systems are developed including Setaram and Gleeble systems. As for advanced Gleeble 3800 there are four mobile convert units (MCU) that could be connected to main load unit: universal Pocket Jaw MCU for tension/compression uniaxis tests, torsion MCU for torsion tests; Hydrowedge MCU for high speed compression uniaxis tests; MaxStrain MCU for multiaxis deformation tests. All MCUs mentioned above could be used for multistage plastic deformation physical simulation. The development of the optimum TMP technology, which could provide the required structure including proper substructure and recrystallization ratio as well as dynamic recrystallization grain size, requires preliminary investigations by physical and numerical simulation. The properties of metals and alloys after TMP are determined by the special feature of the structure formed of two processes: strengthening and softening. The kinetics of these processes depends on the temperature-strain parameters of TMP. The kinetics are determines by the combined effect of parameters, i.e. multifactoral process. The conventional methods of the effect of TMP parameters examination, the main of which are deformation temperature (T_d , °C), the degree (ε , %), or the rate ($\dot{\varepsilon}$, s^{-1}) of deformation, and the time elapsed from the end of deformation to the start of quenching (τ , s) are based on the variation of the factor with the remaining process parameters being constant. This greatly complicated the search for the optimum conditions. For this reason, EPM has been used on an increasing scale for the examination of the combined effect of the HTMP parameters on the structure and properties. The main problem in the development of TMP is the construction of the model which could be used to control

the process, moreover to create mathematical model, which may be foundation for computer modelling. In the first stage, this includes the construction of polynomial models for various steels, alloys, and possibility, also of their typical groups. The second stage may consist of optimization in respect of the main optimization parameter. To achieve precise prediction control of product quality, the details of microstructural evolution occurring during to deformation and accelerate cooling and relationship between the TMP parameters, structure and mechanical properties is still somewhat complicated. In its present state it is not an everyday tool for the engineer. With a more user-friendly EPM and FEM will make a great important compared existing design method. Experiment planning method has proved to be a good tool for the definite relationship between TMP parameters and mechanical properties. Simulation of TMP for the definite cross-section of profile by FEM on the base of the data obtained by experiment planning method allowed to predict structure and mechanical properties and to develop computer modelling for the different cross-section of rolling profile [21]. Using the physical simulation of dynamic recrystallization it's possible estimate the microstructure evolution under TMP and to predict final properties as demonstrated in Ni-based super alloy [22]. The results of modelling of dynamic recrystallization in the manufacture of workpieces of complicated profile cross-section based on the physical and numerical simulation allow to optimize the technological process of plastic forming and reduce the development of technology costs. Simulation of HTMT for the definite cross-section of profile by Finite Element Method (FEM) on the base of the data obtained by physical simulation and EPM allowed to predict structure and mechanical properties and to develop computer modelling for the different cross-section of rolling profile.

5. Conclusions

Thermomechanical Processing using a variety of plastic forming methods based on the understanding of physical fundamentals is a progressive resource-saving technique to produce metal billets and parts with the high level of structural strength and functional properties applying to different type steels and alloys. By using best current knowledge and modern facilities, numerical and physical simulation techniques can enable the rapid and economic evaluation prediction and control of TMP processes.

Acknowledgments. *The research was carried out within the state assignment 11.12832.2018/8.9.*

References

- [1] A.J. DeArdo // *Materials Science Forum* **426-432** (2003) 49.
- [2] G. Kodzhaspirov (Kodzhaspirov), I. Kim, *Thermomechanical Processing of steels* (St.Petersburg State Technical University, St.Petersburg, 1998).
- [3] J. Kliber, P. Kawulok, I. Schindler, G. Kodzhaspirov, In: *Proceedings of the 24th International Conference on Metallurgy and Materials (METAL 2015)* (Tanger, Brno, 2016), p.176.
- [4] M. Tendo, Yu. Tadokoro, K. Suetsugu, T. Nakazava // *ISIJ International* **41** (2001) 262.
- [5] G.E. Kodzhaspirov, L.P. Karjalainen, M.O. Speidel // *Materials and Manufacturing Processes* **19** (2004) 87.
- [6] G.E. Kodzhaspirov, A.I. Rudskoy // *Acta Physica Polonica A* **128** (2015) 527.
- [7] G. Kodzhaspirov, A. Rudskoy // *Materials Science Forum* **879** (2016) 2407.
- [8] A. Kelly, G. Groves, *Crystallography and Crystal Defects* (Longman, Bristol, 1970).
- [9] V.V. Rybin, *Large Plastic Deformations and Fracture of Metals* (Metallurgiya, Moscow, 1986). (In Russian)
- [10] G.E. Kodzhaspirov, A.I. Rudskoy, V.V. Rybin, *Physical Fundamentals and Resource-*

- Saving Technologies in the Production of Parts by Plastic Deformation* (Nauka, St.Petersburg 2007). (In Russian)
- [11] G.E. Kodzhaspirov, A.I. Rudskoy, A. Borowikow // *La Metallurgia Italiana (Italian Metallurgy)* **2** (2014) 51.
- [12] G.E. Kodzhaspirov (Kodzhaspirov), V.V. Rybin, P.A. Drakatos, In: *Proceedings of the 2nd Int. Symposium on Physics and Mechanics of Large Plastic Strains (PMLPS 2007)* (St.Petersburg, 2007), p.323.
- [13] J. Skaret, F. Habrovec, J. Kounichy, P. Rys // *J. Iron and Steel Inst.* **205** (1967) 330.
- [14] A.R. Cox, P. Jones // *J. Mater. Science* **4** (1969) 890.
- [15] S.S. Gorelik, S.V. Dobatkin, L.M. Kaputkina, *Recrystallization in metals and alloys* (MISIS, Moscow, 2005). (In Russian)
- [16] K. Hulka, In: *PTD Conference Proceedings* (1988), p.13.
- [17] A.I. Rudskoi, G.E. Kodzhaspirov, S.V. Dobatkin // *Russian Metallurgy* **5** (2012) 72.
- [18] V.V. Orlov, V.A. Malyshevskii, E.I. Khlusova, S.A. Golosienko // *Steel* **44** (2014) 696.
- [19] M. Katakami, N. Mori, T. Haze, K. Ito, In: *Proceedings of the Int. Conf. Microalloyed HSLA steels* (Chicago, 1988).
- [20] K. Amano, T. Hatomura, C. Shiga, T. Enami, In: *Proceedings of the Int. Conf. THERMEC'88* (1988), p.368.
- [21] G.E. Kodzhaspirov, A.I. Rudskoy // *Materials Science Forum* **762** (2013) 289.
- [22] G. Kodzhaspirov, A. Borowikow, M. Terentyev // *Materials Science Forum* **762** (2013) 753.

EFFECT OF ALUMINA ADDITION ON WELD DEPOSITS MICROSTRUCTURE AT THE WELDING OF CARBON STEEL

E.V. Bobrynina^{1*}, T.V. Larionova¹, T.S. Koltsova¹, S.A. Ginzburg², V.G. Michailov²

¹Peter the Great St.Petersburg Polytechnic University, Russia

²Brandenburgische Technische Universität Cottbus-Senftenberg, Germany

*e-mail: bobrynina@inbox.ru

Abstract. The formation of acicular ferrite in the structure of weld deposits when welding carbon steels is often associated with the introduction of nonmetallic additives into the electrode material. Fe–alumina composite powders with alumina particles less than 1 μm were used as a filler for cored welding wire and the influence of aluminum oxide additives up to 2,5 wt.% on the structure of the welded seam was studied. It was shown that the addition of aluminum oxide to the welding wire led to the initiation of the formation of intragranular acicular ferrite in the weld deposit and to a more even distribution of hardness through the zones of weld seam.

Keywords: acicular ferrite; alumina; welding; carbon steel.

1. Introduction

The addition of dispersed oxide particles into ferritic steels significantly improves their mechanical properties at elevated temperatures [1], since the stable at high exploitation temperatures submicron oxide particles inhibit the movement of dislocations and grain growth [1-3]. To date, dispersed-strengthened (DS) steels have been widely discussed in scientific literature as the materials for reactors and gas turbines operating at up to 700°C [1, 4].

On the other hand, the presence of oxide particles in the weld pool often has a beneficial effect on the structure of the weld and on the final properties of the welded products [5-10]. For example, it was shown in [5-7] that the introduction of titanium oxide nanoparticles into electrode coating allowed to modify the structure and to improve the properties of the welded joint. Introduction of 1.2 wt.% of zirconia made it possible to increase the strength of low-carbon steel joints by about 37% [8].

Often, the increase in strength and impact strength at negative temperatures is associated with the presence of acicular ferrite (AF) in the weld structure [8-9]. It is believed that the formation of AF is associated with the presence of nonmetallic inclusions [11-12]. According to literature data [7-12] the formation of AF may be initiated by oxides such as titania, zirconia and others, for example, authors [9], by introducing small additions of titanium oxide, obtained welds with the structure of acicular ferrite.

The possible reasons of the formation of acicular ferrite in the presence of nonmetallic inclusions had been discussed in detail in the works of H. Badeshia, S.S. Babu and R. Honeycombe, and generalized in [11]. The authors show the possible mechanisms for the initiation of acicular ferrite in the presence of oxide particles and conclude that there are many possibilities (nucleation at crystal lattice matching, stimulation of ferrite growth by thermal deformations upon cooling, or the presence of chemical inhomogeneities near the

inclusion / matrix interface) that help make the nonmetallic phase a heterogeneous site for the nucleation of ferrite. In fact, nonmetallic inclusions tend to consist of many crystalline and amorphous phases, so that it becomes difficult to identify the specific component and mechanism responsible for the initiation of acicular ferrite in each case. It was suggested in [13] that under certain conditions all oxide inclusions should initiate the formation of AF.

In general, despite of the fact that various types of nonmetallic inclusions have already been investigated, inconsistent information prevails about aluminum oxide [14]. Aluminum oxide has been used successfully for the dispersive hardening of materials based on copper, nickel and iron, while it is not actively used as a modifier of the structure of welded joints, despite the good correspondence of the crystal lattices of ferrite and gamma alumina [11]. Therefore, the purpose of this work was to carry out additional studies on the effect of alumina particles on the structure and properties of the welded seam. To produce a powder material with a highly distorted crystal lattice, the most common method was used - grinding in a high-energy mill, which is widely used to create composite powder materials [15].

2. Experimental

Iron and alumina (corundum) powders with a particle size of less than 100 μm have been used as starting materials. The grinding of alumina powder was carried out in 80 ml beakers in a Pulverisette 7 planetary mill. As can be seen from Fig. 1, the initial alumina powder has the average particle size of more than 20 μm . Powder was grinded in the planetary mill at a rotation speed of 400 rpm for 4 h with ceramic balls of 10 mm in diameter, the mass of the sample was 8 g, and balls-to-powder mass ratio was 1:10.

Additional grinding of a mixture of Fe and Al_2O_3 , was carried out by milling with balls of hardened steel with a diameter of 10 mm. In order to prevent oxidation, the milling was carried out in an Ar atmosphere. The preparation of the composite powder was carried out in two stages: first was the mixing at 200 rpm for 2 hours, then grinding at 600 rpm also for 2 hours. Alumina content in final powders was varied from 2.5 to 10 wt%.

To create filled welding wires, a steel tube made of Steel 10 was used, the diameter of the tube was 6 mm, the wall thickness was 1 mm, and the initial length was 10-12 cm. A powder was pressed into the steel tube. The wire was rolled by a rolling mill from a starting diameter to 2 mm. After that, the finished flux cored wires were surfacing melted onto the substrate (steel 45) by the argon-arc welding method ($I = 200 \text{ A}$).

The study of powder composite materials was carried out on a scanning electron microscope MIRA 3 TESCAN, X-ray diffraction (XRD) analysis was carried out on a DRON-2 diffractometer in monochromatized $\text{CuK}\alpha$ radiation. The microstructure of the welded seam (WS) and the heat-affected zone (HAZ) was studied using the metallographic method at x100-x500 magnifications using the Leica-DMI5000 optical microscope and using a Phenom ProX scanning electron microscope. The microhardness was measured on a ZWICK ZHU equipment at a load of 100 H.

3. Results and discussions

The micrographs of the initial and pre-grounded alumina are shown in Fig. 1 (a and b respectively). The powder consists mainly of agglomerated particles with the size of about 2 microns; the size of the individual particles in agglomerates is less than 100 nm. After grinding, alumina is X-ray amorphous (insertion in Fig. 1(b)).

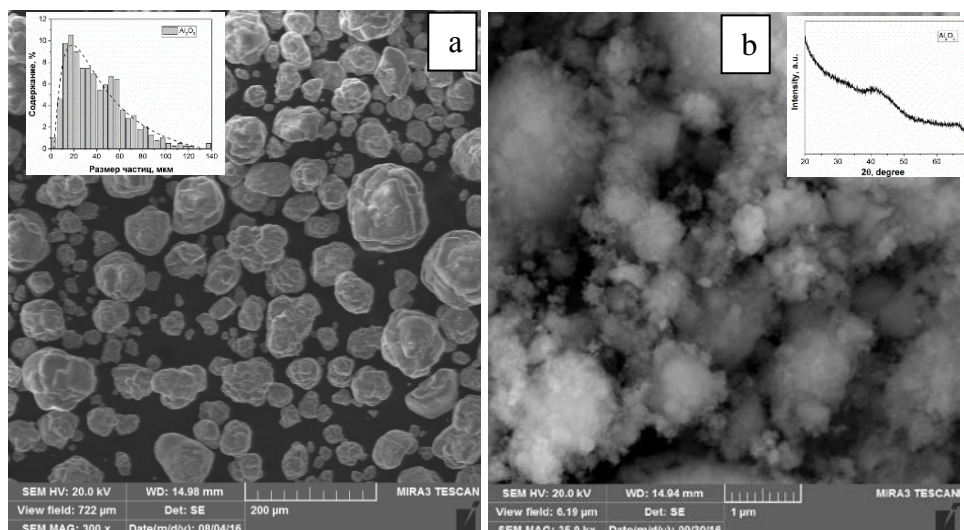


Fig. 1. Micrographs of initial alumina powder (a) and alumina powder after ball milling at 400 rpm for 4h (b). The insertion in Fig (a) shows particle size distribution in the initial powder and in (b) the result of XRD analysis powder after ball milling.

The microphotography and diffractograms of the composite powder $\text{Fe-Al}_2\text{O}_3$ are presented in Fig. 2. The results of X-ray diffraction analysis show the presence of reflexes from pure iron, peaks belonging to alumina are not observed. As can be seen in Fig. 2, the increase in the content of aluminum oxide did not affect the position and shape of the iron peaks.

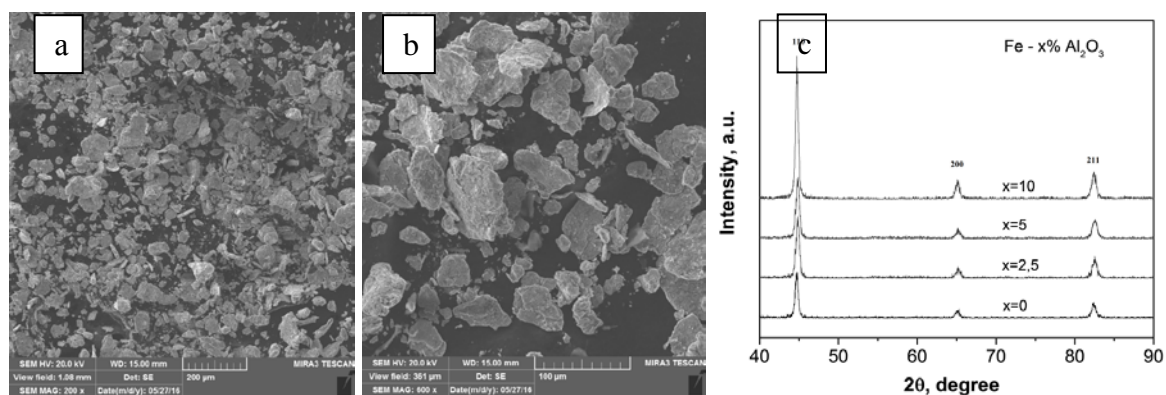


Fig. 2. Micrographs at different magnifications (a, b) и and XDR patterns (c) of composite $\text{Fe-Al}_2\text{O}_3$ powders after milling at 600 rpm for 2 h.

According to the procedure described above, the wires with different alumina contents were manufactured from the resulting powder. The final content of alumina in wire was 2.5 mass%, 1.2 wt.% and 0,6 wt% (made from starting powder Fe-10; 5; 2.5 wt% Al_2O_3 respectively). For comparison, the wire with a pure iron powder is prepared.

Surfacing was obtained by the method of argon-arc welding. Figure 3 shows the microstructures of the central zone of the weld.

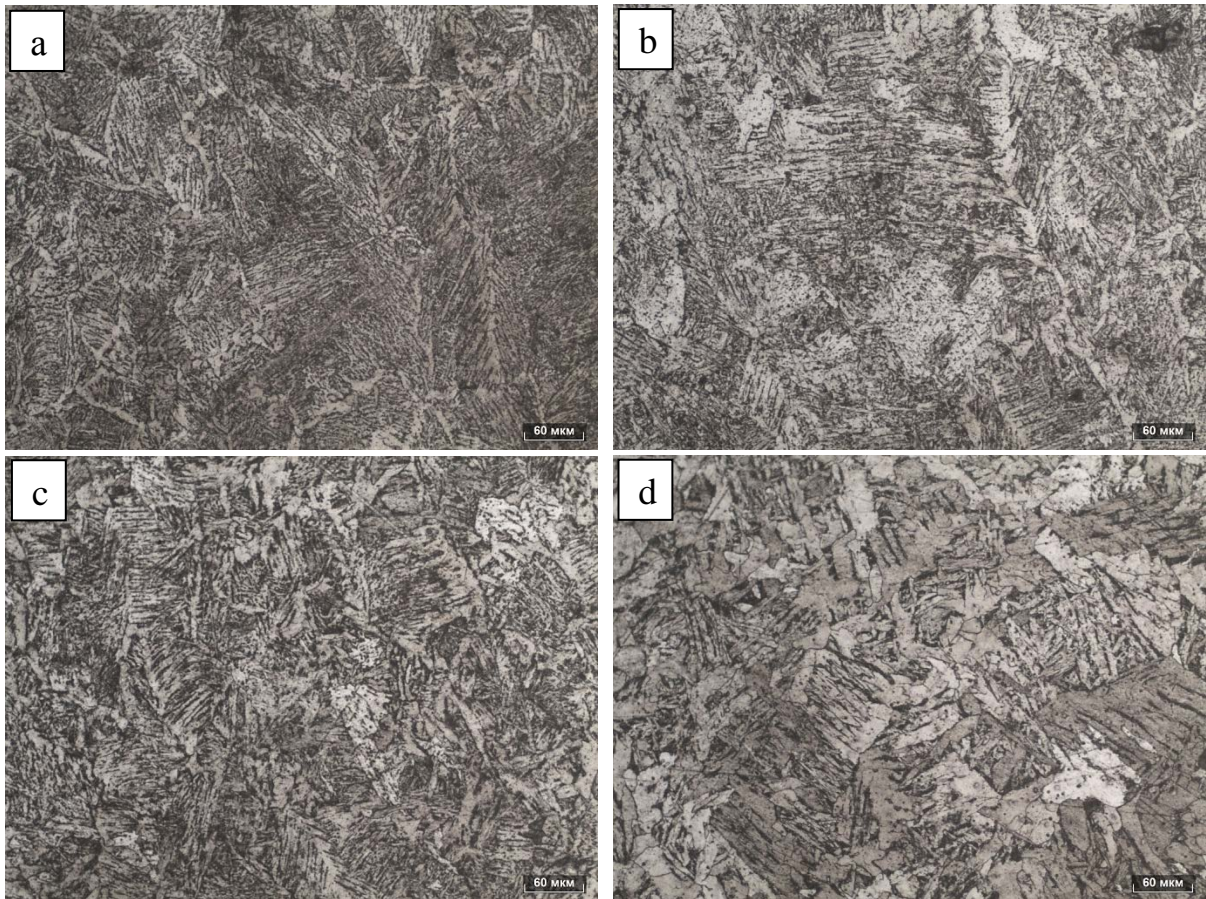


Fig. 3. Microstructure of the central zone of the welded seam. The welds were made by using a welded wire with an aluminum oxide content of 0 (a), 0.6 (b); 1.2 (c) and 2.5 wt% (d).

In structures ferrite along the boundaries of austenite grains, polyhedral ferrite, a bainitic-martensitic structure, and a small amount of acicular ferrite were identified. In the initial seam, when using the wire without the addition of alumina, the main structural constituents are grain-boundary ferrite and a bainitic-martensitic structure. When aluminum oxide is added, polyhedral ferrite appears and its proportion increases with increasing oxide concentration, the proportion of acicular ferrite also increases, with the bainite component practically disappears. An obvious coarsening of the microstructure is also observed.

Figure 4 shows the microstructure of the columnar zone of welded seams. With the addition of aluminum oxide, the columnar structure becomes more pronounced; the size of the structural components significantly increases. The increase of polyhedral ferrite fraction and the decrease in the proportion of the bainitic-martensitic component, together with the general coarsening of the microstructure, can be explained only by a decrease of the cooling rate of the weld pool, which takes place most likely due to a change in the thermophysical characteristics of the electrode and the weld pool when nonmetallic particles are added.

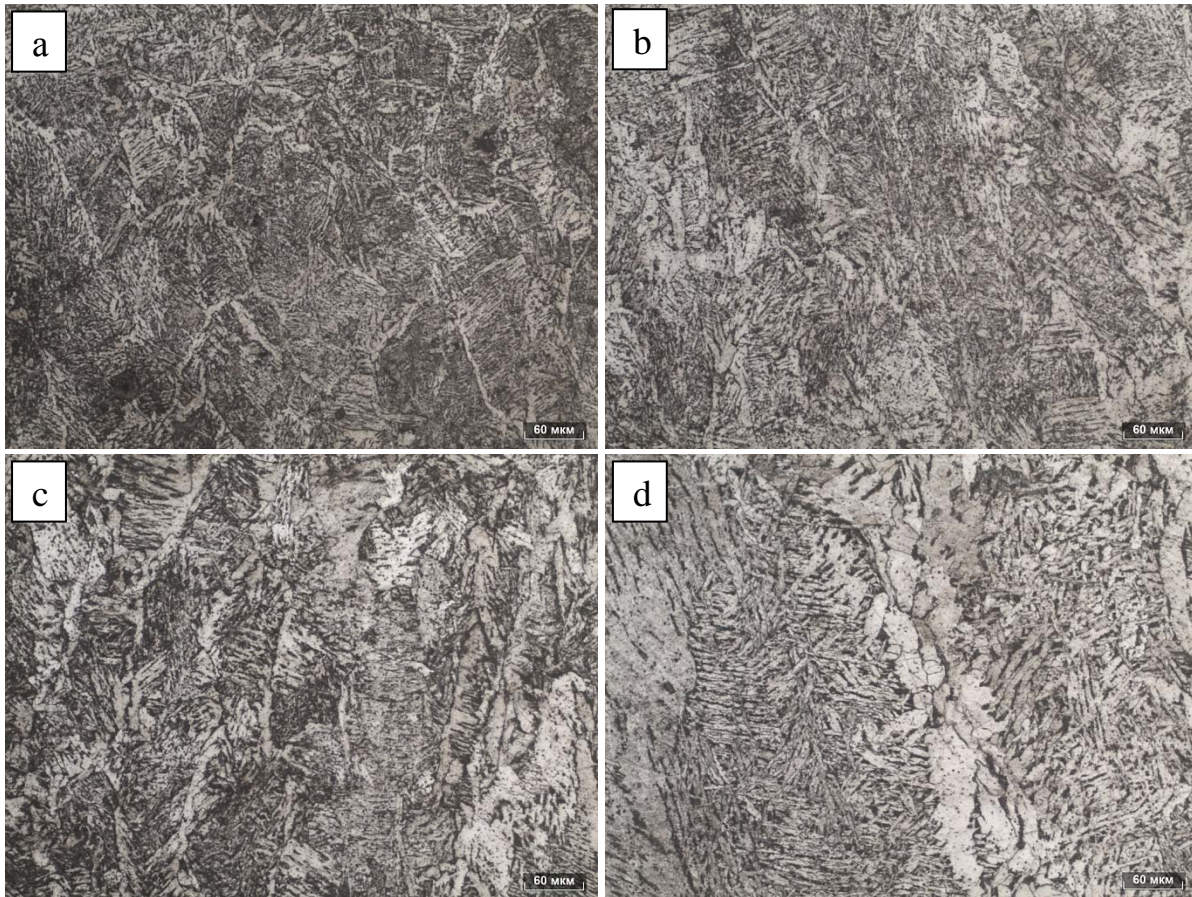


Fig. 4. The microstructure of the weld zone near HAZ made with the use of welded wire containing 0 (a), 0.6 (b); 1.2 (c) and 2.5 wt% (d) of aluminum oxide.

As noted above, alumina is considered not to be a non-metallic inclusion, which is potentially active for the formation of acicular ferrite, however, as can be seen in Fig. 4d, in the structure with the maximum aluminum oxide content (2.5%) there is a significant volume fraction of intragranular acicular ferrite (IF) (Fig. 4, d). Taking into account the wide spectra of polymorphous modifications of alumina, the activity of nonmetallic inclusion for the nucleation of acicular ferrite may be caused not only by its chemical composition, but also by the crystal structure, and this question requires further consideration. In addition, as it is known, the probability of needle-like ferrite nucleation on nonmetallic inclusions increases sharply with the increase in the size of nonmetallic particles up to 1-2 μm . Apparently, at high temperatures the agglomeration and sintering of nanoscale alumina particles occurred to form larger particles that served as nucleation centers for acicular ferrite.

In Fig. 5, microhardness profiles along the welded seam up to the base metal are given. There is an obvious correlation of the values of hardness with the microstructure. The weld with the bainitic-martensitic structure (Fig. 3(a), 4(a)) obtained with the use of welded wire without the addition of oxide has the maximum hardness. The structure with a high volume fraction of polyhedral ferrite has the minimum hardness (Fig. 3(d), 4(d)) obtained with the maximum content of aluminum oxide.

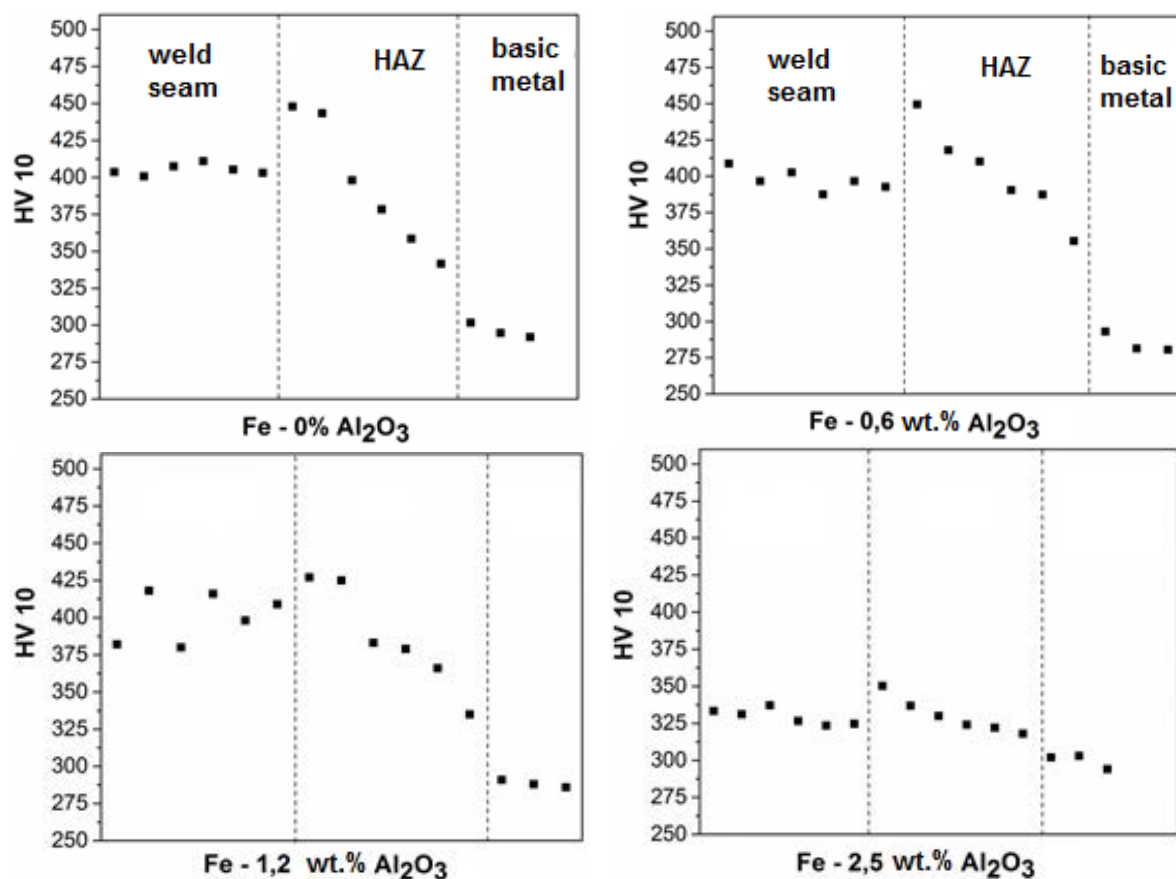


Fig. 5. Microhardness profile through the zones of weld.

Figure 6 shows the values of the microhardness of the welded seam, depending on the content of aluminum oxide in the welded wire. The hardness of the welded samples at alumina content from 0 to 1.2 mass% is almost 1.5 times higher than the hardness of the base material, which is due to the formation of a nonequilibrium bainitic martensitic structure due to the high cooling rate. When the aluminum oxide content is 2.5 mass%, the hardness of the welded material is higher than the hardness of the base material by only 10%.

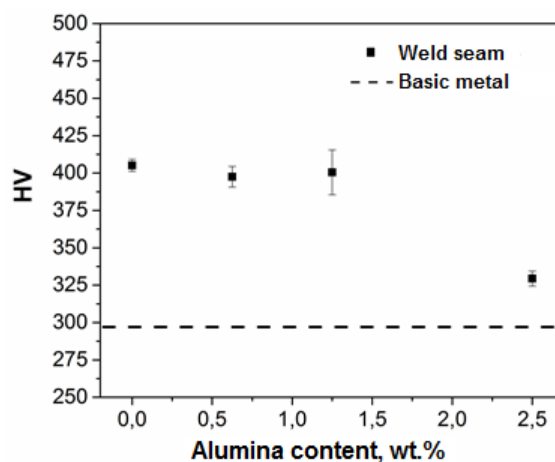


Fig. 6. Dependence of the microhardness of the welded joint on the content of aluminum oxide in the welding wire.

4. Conclusions

The main effect of alumina additions to the welding wire is the coarsening of the weld metal structure, which is apparently connected with a significant change in the thermophysical characteristics of the electrode and the weld pool. It is shown that the addition of alumina to the welding wire led to the initiation of the formation of intragranular acicular ferrite in the welded material, and the effect of dispersed hardening due to the inhibition of grain growth and movement of dislocations is not pronounced, which on the whole resulted in a more even distribution of hardness over the zones of the welded seam.

Acknowledgments. The authors would like to thank the Russian Foundation for Basic Research (RFBR) (Grant no: 16-58-76008\17) for providing financial support in the frames of collaborative project “Nano Wire CWM” of ERA.Net RUS Plus program.

References

- [1] G. Sundararajan, R. Vijay and A.V. Reddy // *Cur. Sci.* **105** (2013) 8.
- [2] D.W. Lee, O. Tolochko, C.J. Choi and B.K. Kim // *Powder Metall.* **45** (2002) 3.
- [3] Y.S. Xu et al. // *Advanced Materials Research* **887-888** (2014) 32.
- [4] K.A. Darling, M. Kapoor, H. Kotan, B.C. Hornbuckle, S.D. Walck, G.B. Thompson, M.A. Tschopp, L.J. Kecskes // *J. Nucl. Mater.* **467** (2015) 205.
- [5] B. Beidokhti, A.H. Koukabi, A. Dolati // *Mater. Charact.* **60** (2009) 225.
- [6] M.V. Abramov, S.B. Maslenkov, V.B. Kireev // *Metallovedenie i termicheskaya obrabotka metallov (Metal Science and Heat Treatment of Metals)* **2** (1981) 59.
- [7] M. Fattahi, N. Nabhani, M.R. Vaezi, E. Rahimi // *Mater. Sci. Eng. A* **528** (2011) 8031.
- [8] B.A. Wang, N. Wang, Y.J. Yang, H. Zhong, M.Z. Ma, X.Y. Zhang, R.P. Liu // *Mater. Sci. Eng. A* **692** (2017) 168.
- [9] M. Fattahi, N. Nabhani, E. Rafiee, M. Nasibi, E. Ahmadi, Y. Fattahi // *Mater. Chem. Phys.* **146** (2014) 105.
- [10] M. Fattahi, N. Nabhani, M. Hosseini, N. Arabian, E. Rahimi // *Micron.* **45** (2013) 107.
- [11] H. Bhadeshia and R. Honeycombe, *Steels: Microstructure and Properties* (Elsevier Ltd, 2017).
- [12] S.S. Babu // *Current Opinion in Solid State and Materials Science* **8** (2004) 267.
- [13] T. Pan, Z.-G. Yang, C. Zhang, B.-Z. Bai, H.-S. Fang // *Mater. Sci. Eng. A* **438-440** (2006) 1128.
- [14] D. Loder, S.K. Michelic, C. Bernhard // *J. of Mater. Sci. Resear.* **6(1)** (2017) 24.
- [15] N. Travitzky, P. Kumar, K.H. Sandhage, R. Janssen, N. Claussen // *Mater. Sci. Eng. A* **344** (2003) 245.

THE INFLUENCE OF DIFFERENT TYPES OF MESODEFFECTS ON THE FORMATION OF STRAIN INDUCED BROKEN DISLOCATION BOUNDARIES AT THE FACETED GRAIN BOUNDARY

S.V.Kirikov*, J.V. Svirina

Mechanical Engineering Research Institute of RAS, 85 Belinsky str., 603024 Nizhny Novgorod, Russia

*e-mail: ksv.kirikov@yandex.ru

Abstract. In this paper we analyze mesodefects accumulating during plastic deformation on the faceted high angle grain boundaries. It is shown that the system of mesodefects can be represented as a set of linear mesodefects of the rotational type (junction disclinations), and planar mesodefects of the shear type (uniformly distributed dislocations with Burgers vector lying in the plane of the facet). The process of formation of broken dislocation boundaries in the elastic fields of various configurations of the abovementioned mesodefects is studied within the framework of computer simulation.

Keywords: fragmentation; broken dislocation boundaries; mesodefects; computer simulation.

1. Introduction

According to the modern concepts [1-2], the formation of misoriented structures at the initial stage of fragmentation of crystalline solids is caused by the accumulation of plastic incompatibilities on the boundaries and in the junctions of grains. Being relatively regular, they form the mesodefects (disclinations, dipoles of disclinations, planar mesodefects) that generate powerful nonuniform elastic stresses in grains of polycrystals [3-9].

These stresses disturb and redistribute the flows of lattice dislocations providing plastic deformation in the volume of grains and it leads to an unequal strain in the grain mesovolumes. As a consequence, spatially localized regions with an increased density of dislocation charge are formed near the mesodefects, which can be considered in the first approximation as broken dislocation boundaries separating mutually misoriented mesovolumes of the grain. Namely the strain induced broken dislocation boundaries are the most typical elements of the structure of materials at the early stages of fragmentation [1-2]. In recent years, a large number of papers have been devoted to the investigation of the formation of strain induced broken dislocation boundaries in the elastic field of isolated mesodefects [10-13]. It has been shown that the appearance of broken dislocation boundaries leads to a decrease in the elastic energy and to a decrease in the gradients of the internal stresses generated by mesodefects.

In fact, the systems of mesodefects appear on the grain boundaries of the plastically deformed polycrystal. Its configuration depends on the morphology of the grain boundary and the geometry of the lattice slip in the body of grains. In this paper, we analyze the influence of different mesodefect configurations on the formation of strain induced broken dislocation boundaries in case of a faceted tilt grain boundary.

2. Analysis of mesodefects formed on the faceted grain boundary during plastic deformation

Different configurations of mesodefects can be formed on the grain boundary during plastic deformation depending on its geometry and orientation of the active slip planes. This is due to the fact that grain boundaries have morphological features in the form of ledges, facets and kinks existing in the initial state or arising during deformation [14-15]. In this paper, we consider mesodefects arising on a faceted tilt grain boundary consisting of identical structural elements, one of which is shown in Fig. 1. The normal components of Burgers vectors of dislocations accumulating during plastic deformation on the j^{th} facet of the grain boundary in the course of its interaction with the lattice dislocations flows (Fig. 1a) cause an additional misorientation $\vec{\theta}_j$.

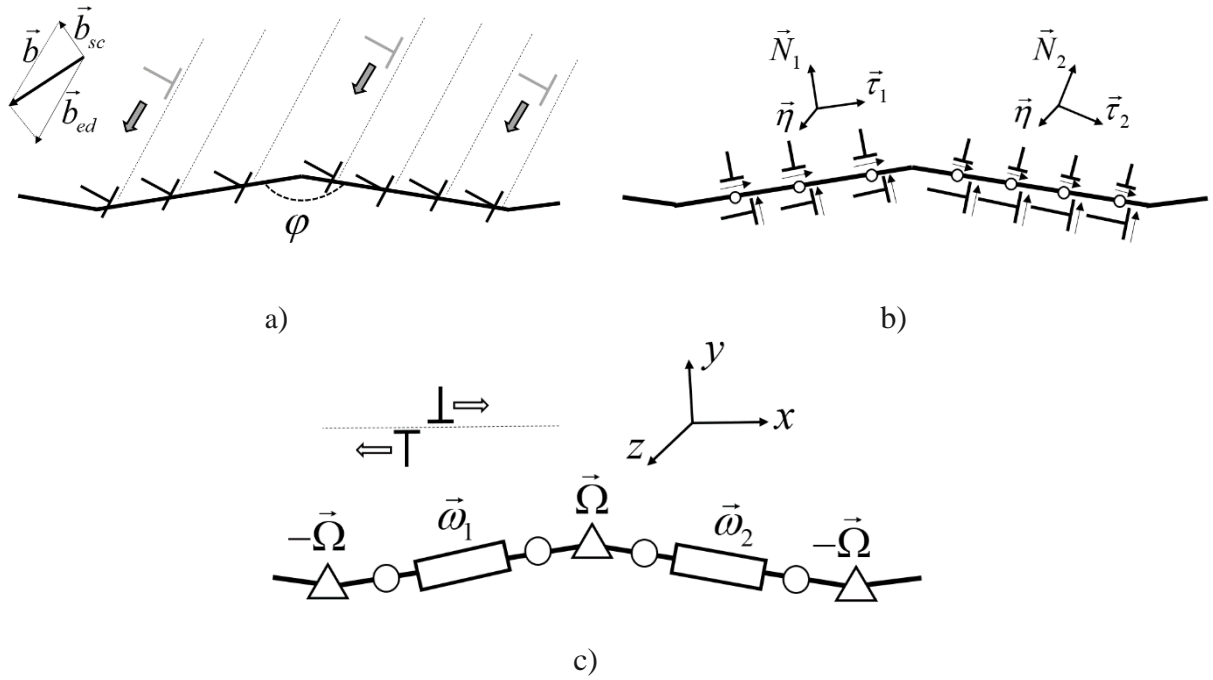


Fig. 1. Schematic plot of the system of mesodefects accumulating on a faceted tilt grain boundary during plastic deformation: (a) dislocations accumulating on the grain boundary due to its interaction with the flow of lattice dislocations; (b) representation of the dislocations in the form of edge and screw dislocations systems with normal and tangential components of the Burgers vector (the \circ symbols denote screw components); (c) the equivalent configuration of mesodefects: Δ - junction disclinations, \circ - planar mesodefects, consisting of screw components, \square - planar mesodefects, consisting of edge components.

The linear mesodefects of the rotational type (i.e. unlike strain induced junction disclinations (Fig. 1c) with the strength $\vec{\Omega}_{j,j-1}$) appear at the tops of the joining facets as a result of a mismatch of additional plastic rotations $\vec{\theta}_j$ and $\vec{\theta}_{j+1}$:

$$\vec{\Omega}_{j,j+1} = \vec{\theta}_j + \vec{\theta}_{j+1}. \quad (1)$$

The tangential components of Burgers vectors form a planar mesodefect with the strength $\vec{\omega}_j = [\omega_\tau \vec{\tau} + \omega_\eta \vec{\eta}]_j$ on the j^{th} facet. Here, $\omega_{\tau,j}$ and $\omega_{\eta,j}$ are the densities of Burgers vector of edge and screw of dislocations correspondingly. Thus, generally, the system of

meso-defects on the faceted boundary is a combination of junction disclinations and planar meso-defects (Fig. 1c). This general conclusion is valid for arbitrary geometry of lattice slip.

To calculate the meso-defects strength at the grain boundary with the normal \vec{N} both in cases of discrete dislocations and its continual distribution with the given plastic distortion jump $\Delta\hat{\beta}$ it is necessary to find the tensor of Burgers vector density:

$$\hat{B} = \sum_k [\rho(\vec{\xi} \otimes \vec{b})]_k = -\vec{N} \times \Delta\hat{\beta}, \quad (2)$$

where $\Delta\hat{\beta}$ is the difference of plastic distortion between joining grains, ρ_k is the linear dislocation density at the grain boundary and $\vec{\xi}_k$ is the unit vector of dislocation line for k^{th} slip system. For the considered case of tilt grain boundary, the strengths of the abovementioned meso-defects are equal to:

$$\vec{\theta}_j = (\vec{\eta} \cdot \hat{B} \cdot \vec{N})\vec{\eta} = [(\Delta\beta_{xx} - \Delta\beta_{yy})N_x N_y + N_y^2 \Delta\beta_{xy} - N_x^2 \Delta\beta_{yx}]_j [\vec{l} \times \vec{N}], \quad (3)$$

$$\omega_{\tau,j} = (\vec{\eta} \cdot \hat{B} \cdot \vec{\tau})_j = [\Delta\beta_{xx} N_y^2 + \Delta\beta_{yy} N_x^2 - (\Delta\beta_{xy} + \Delta\beta_{yx}) N_x N_y]_j, \quad (4)$$

$$\vec{\omega}_{\eta,j} = (\vec{\eta} \cdot \hat{B} \cdot \vec{\eta})_j = [N_y \Delta\beta_{xz} - N_x \Delta\beta_{yz}]_j. \quad (5)$$

Expressions for the fields of elastic stresses of junction disclination and the planar meso-defect consisting of the edge components of the dislocations are given in [9]. Calculation of the tensor of elastic stresses of planar meso-defect consisting of screw components of dislocations in the laboratory coordinate system (Fig. 1c) gives the following expressions:

$$\sigma_{xx} = \sigma_{yy} = \sigma_{zz} = \sigma_{xy} = 0,$$

$$\sigma_{xz} = \frac{G\omega_{\eta}}{2\pi} \left[\arctg\left(\frac{x-a}{y}\right) - \arctg\left(\frac{x+a}{y}\right) \right],$$

$$\sigma_{yz} = \frac{G\omega_{\eta}}{4\pi} \ln \left[\frac{(x+a)^2 + y^2}{(x-a)^2 + y^2} \right],$$

where G is the shear modulus.

3. Description of the model

The simulation was carried out for 2D approximation in the framework of the approach described in [10,16-19]. To analyze the dynamics of a dislocation ensemble, we used the equation of dislocation motion in a quasi-viscous approximation [11, 16]:

$$v_k^i = M \left(\vec{n} \cdot (\hat{\sigma}^{ext} + \hat{\sigma}^{int}) \cdot \vec{b} \right)_k^i, \quad (6)$$

where v_k^i is the velocity of i^{th} dislocation in k^{th} slip system, $\left(\vec{n} \cdot (\hat{\sigma}^{ext} + \hat{\sigma}^{int}) \cdot \vec{b} \right)_k^i$ is the force acting on the dislocation in the slip plane, $\hat{\sigma}^{int}$ is the internal stresses tensor, defined as the total elastic field from the system of meso-defects and from the lattice dislocations ensemble, M is the dislocations mobility. Mobility, generation rate and radius of annihilation of dislocation are chosen to provide sufficiently high strain rate value $(10^{-3} - 10^{-2})\text{s}^{-1}$.

An analysis of the dynamics of the dislocation ensemble and the formation of the strain induced broken dislocation boundaries in the elastic fields of the considered meso-defects was carried out for the case of a faceted grain boundary with periodic arrangement of its structural elements. Let us consider separately the influence of boundary conditions on the results of the simulation. In order to reduce the influence of the size of the model crystal on the results of the calculation, the simulation of this process was carried out in the crystal central region containing only three structural elements of the faceted boundary (i.e. 6 facets), far from the edges of the model grain.

In this case, the total number of facets was chosen so that the difference in the values of the elastic stresses $\sigma(x,y)$ from the mesodefects at neighboring "equivalent" points of the considered area, normalized to the value of averaged over these points stress value, did not exceed a certain value χ (<2%), characterizing the deviation from the periodic conditions. Results of the calculation of the value χ

$$\chi = \frac{1}{n} \sum_{i=1}^n \text{abs}\left(\frac{\sigma(x, y) - \sigma(x + x_p, y)}{\bar{\sigma}}\right), \quad (7)$$

performed for 400 different points from the considered area of the crystal depending on the number of facets n on each side of this region, are shown in Fig. 3. As can be seen from Fig. 4, a good approximation to periodic conditions is achieved even at a value $n \geq 20$.

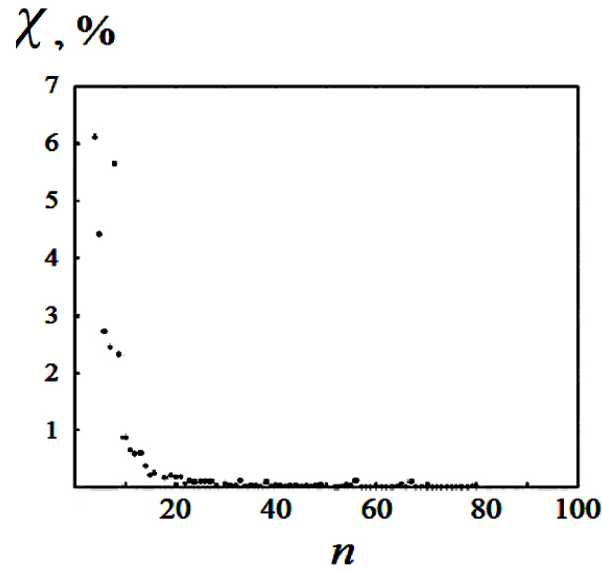


Fig. 2. Dependence of the value χ on the number of grain boundary facets.

Below, the crystal size for the computer simulation was chosen in such a way as to satisfy this condition.

4. Simulation results

The simulation was performed using the following parameters: the size of the considered region is $8 \mu\text{m} \times 4 \mu\text{m}$, the external stress is $\sim 0.008 \text{ G}$, the loading axis is oriented perpendicular to the average orientation of the faceted boundary. The angle between the facets φ varied in the range of $\varphi = 90^\circ - 150^\circ$, the size of the facet $x_p = 2 \mu\text{m}$, the orientation of the accommodation slip plane of the dislocations $\alpha = 0^\circ$ (Fig. 1). Various combinations of mesodefects induced by various plastic distortion jumps on the faceted boundary were considered.

The results of the research show that well-defined strain induced broken dislocation boundaries are formed in two limiting cases. The first one is realized when the influence of the elastic field of planar mesodefects on the motion of lattice dislocations in the accommodation slip plane can be neglected. In this case, broken dislocation boundaries are formed under the junction disclinations stress field and are mainly located perpendicular to accommodation slip plane.

For the selected deformation scheme at $\Delta\beta_{xx} = -\Delta\beta_{yy}$, $\Delta\beta_{xy} = \Delta\beta_{yx} = \Delta\beta_{xz} = \Delta\beta_{yz} = 0$ these conditions are satisfied for $|2N_x N_y| \gg |N_y^2 - N_x^2|$ as follows from eq.(3, 4). As an

example, the results of simulation of broken dislocation boundaries formation are shown in Fig. 3 for $\Delta\beta_{xx} = -\Delta\beta_{yy} = 0.02$, $\Delta\beta_{xy} = \Delta\beta_{yx} = \Delta\beta_{xz} = \Delta\beta_{yz} = 0$.

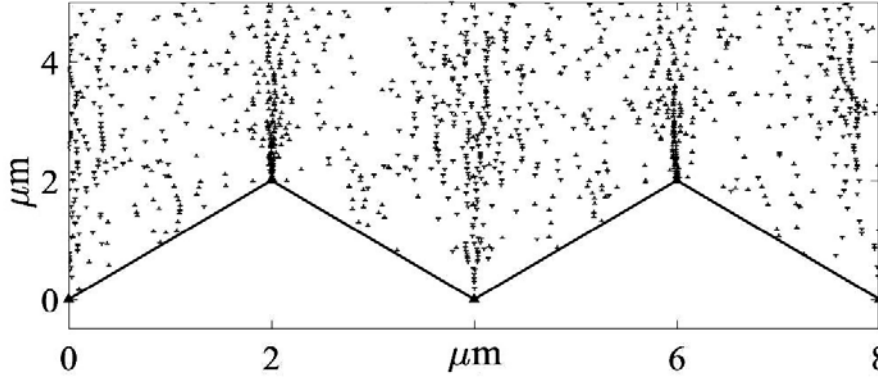


Fig. 3. Strain induced broken dislocation boundaries formed in field of elastic of junction disclination's system.

In the second limiting case, with a small or zero strength of junction disclinations, a well-defined broken dislocation boundary is formed only in the case of a symmetrical arrangement of planar mesodefects, and accommodation slip plane parallel to the medium orientation of the faceted grain boundary. When deviation from the symmetrical arrangement of facets occurs, formation of such broken dislocation boundaries is suppressed.

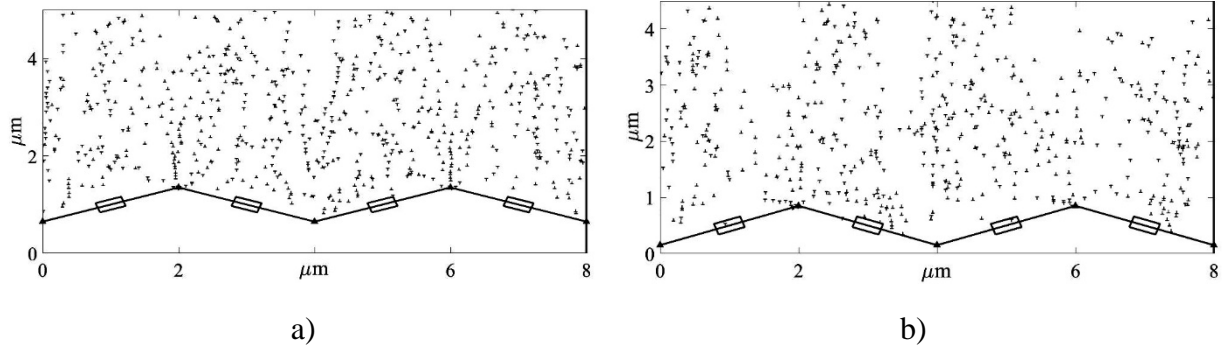


Fig. 4. Dislocation structure formed near grain boundary in the case of a) symmetric distribution of planar mesodefect (the strength of planar mesodefect is comparable to the strength of junction disclination) b) asymmetric distribution of planar mesodefect (the strength of planar mesodefect is comparable to the strength of junction disclination).

In the general case, the simulation shows that the presence of planar mesodefects suppresses the formation of broken dislocation boundaries. As an example, the results of simulation of dislocation structures formation near the facets tops are shown in Fig. 4 for a) $\Delta\beta_{xx} = -\Delta\beta_{yy} = 0.02$ $\Delta\beta_{xy} = \Delta\beta_{yx} = \Delta\beta_{xz} = \Delta\beta_{yz} = 0$ b) $\Delta\beta_{xx} = -\Delta\beta_{yy} = 0.02$ $\Delta\beta_{xy} = \Delta\beta_{yx} = 0.01$ $\Delta\beta_{xz} = \Delta\beta_{yz} = 0$.

5. Discussion

Discrete dislocation dynamics simulations have been used to investigate the formation of strain induced broken dislocation boundaries on the faceted grain boundary with the periodic arrangement of its structural elements. Despite this idealization, the broken dislocation boundaries morphology calculated by computer simulation methods is close to the

experimentally observed boundaries, which appear near grain boundaries containing quasiperiodic facets with different sizes and orientations. It can be seen that broken dislocation boundaries are formed in the vicinity of the faceted high-angle grain boundary, growing from the tops of the joining facets into the body of grain.

As it follows from the simulation results, the field of elastic stresses created by the system of junction disclinations is responsible for their formation. The length of broken dislocation boundaries is comparable with the length of the facet. It can be shown that the broken dislocation boundaries are located along the zero-level stresses lines generated by a system of unlike junction disclinations.

As the simulation shows, well-defined broken dislocation boundaries are formed in the case when the strength of junction disclinations is much greater than the strengths of the planar mesodefects. For the given jump of plastic distortion tensor, this condition is satisfied only for a certain interval of orientations of the facets plane N_j and the interval of angles between the facets φ .

Nevertheless, it can be assumed that the formation of strain induced broken dislocation boundaries is possible in a more general case, when planar mesodefects and junction disclination have comparable strength. In our opinion, the process of broken dislocation boundaries formation may occur stepwise. At first, when a certain critical value of the planar mesodefect strength is reached, its relaxation occurs by plastic shear along the slip planes close to the facets plane.

This process should lead to the emission of lattice dislocations in the body of the grain. As a result, the strength of the planar mesodefect decreases, its elastic field relaxes and the conditions for the initiation of the accommodation process of junction disclination occurring by the formation of broken dislocation boundary are created. Such shear-rotational mechanism of relaxation of the elastic stress fields of mesodefects can explain the prevalence of strain induced broken dislocation boundaries near the facets and ledges of boundaries in plastically deformed polycrystals.

6. Conclusion

1. The computer simulation shows that well-defined strain induced broken dislocation boundaries are formed when the influence of the elastic field of planar mesodefects on the motion of lattice dislocations in the accommodative slip plane can be neglected. In this case, broken dislocation boundaries are formed under the effect of the elastic field of junction disclinations.

2. In the general case of comparable mesodefects' strengths, the formation of strain induced broken dislocation boundaries can be implemented by two sequentially occurring accommodation processes. The first one is associated with the relaxation of the planar mesodefect due to the emission of the plastic shear located on the facet into the body of the grain. The second one starts when the planar mesodefect strength decreases and is related to the broken dislocation boundaries formation.

Acknowledgments. This work was supported by the Russian Foundation for Basic Research, project No. 18-33-00195\18 and was carried out within the Russian state task of the Institute of Applied Physics for conducting fundamental scientific research for 2013-2020 on the topic No. 0035-2014-0401.

References

- [1] V.V. Rybin, *Large plastic deformation and fracture of metals* (Metallurgiya, Moscow, 1986) (in Russian)
- [2] V.V. Rybin // *Problems of materials science* **33** (2003) 9.

- [3] A.E. Romanov, V.I. Vladimirov, In: *Dislocations in Solids*, ed. by F.R.N. Nabarro (North Holland, Amsterdam, 1992), Vol. 9, p.191.
- [4] A.E. Romanov, A.L. Kolesnikova // *Progress in Materials Science* **54** (2009) 740.
- [5] V.V. Rybin, A.A. Zisman, N.Yu. Zolotarevskii // *Sov. Phys.Solid State* **27** (1985) 105.
- [6] M.Yu. Gutkin, K.N. Mikaelyan, A.E. Romanov, P. Klimanek // *Phys. Status Solidi A* **35** (2002) 193.
- [7] P. Klimanek, V. Klemm, M. Motylenko, A. Romanov // *Adv. Eng. Mater.* **6** (2004) 861.
- [8] K.N. Mikaelyan, M. Seefeldt, M.Yu. Gutkin, P. Klimanek, A.E. Romanov // *Phys. Solid State* **45** (2003) 2104.
- [9] V.N. Perevezentsev, G.F. Sarafanov // *Rev. Adv. Mater. Sci.* **30** (2012) 73.
- [10] V.N. Perevezentsev, G.F. Sarafanov, Yu.V. Svirina // *Materials Physics and Mechanics* **21** (2014) 78.
- [11] E.A. Rzhavtsev, M.Yu. Gutkin // *Scripta Materialia* **100** (2015) 102.
- [12] G.F. Sarafanov, V.N. Perevezentsev // *Technical Physics Letters* **33** (2007) 87.
- [13] V.V. Rybin, V.N. Perevezentsev, Yu.V. Svirina // *Technical Physics* **86** (2016) 100.
- [14] O.A. Kaibyshev, R.Z. Valiev, *Grain boundaries and properties of metals* (Metallurgia, Moscow, 1987).
- [15] A.N. Orlov, V.N. Perevezentsev and V.V. Rybin, *Grain boundaries in metals* (Metallurgia, Moscow, 1980). (in Russian)
- [16] E. Van der Giessen, A. Needleman // *Model Simul. Mater. Sci. Eng.* **3** (1995) 689.
- [17] R.J. Amodeo and N.M. Ghoniem // *Phys. Rev. B* **41** (1990) 6958.
- [18] J.Th.M. De Hosson, A. Roos, E.D. Metselaar // *Philos. Mag. A* **81** (2001) 1099.
- [19] A. Roos, J.Th.M. De Hosson, E. Van der Giessen // *Comput. Mater. Sci.* **20** (2001) 1.

TECHNIQUE OF DURABILITY ESTIMATION FOR THIN BERYLLIUM FOILS DURING THEIR WORK IN X-RAY DETECTORS

V.V. Mishin^{1*}, I.A. Shishov¹, A. Minchena²

¹Peter the Great St. Petersburg Polytechnic University (Polytechnicheskaya, 29, St. Petersburg, Russia)

²BECORP LTD (Hatfield, United Kingdom)

*e-mail: m_v_v_m@mail.ru

Abstract The stress-strain state for thin beryllium windows of circular shape under cyclic loading by external pressure was calculated using finite element method. The technique for estimating the beryllium window's fracture probability was proposed. Technique is to compare the accumulated plastic strain in a foil with a certain value of the critical plastic strain, determined experimentally by foil samples bending tests. An experimental study of the durability for beryllium windows with a thickness of 8 μm under cyclic loading with external pressure was performed. Good convergence between the predicted and the fact number of load cycles without fracture was established.

Keywords: thin beryllium foils; beryllium fracture; beryllium cyclic deformation; beryllium X-ray windows.

1. Introduction

Beryllium foils of circular shape (so-called beryllium windows) with a thickness from 5 to 10 μm are widely used in the manufacture of Si-Pin, SDD and other X-ray detectors [1-4]. The characteristics of X-ray detectors directly depend on the thickness of used foil, which pasted or soldered to detector body (Fig. 1).

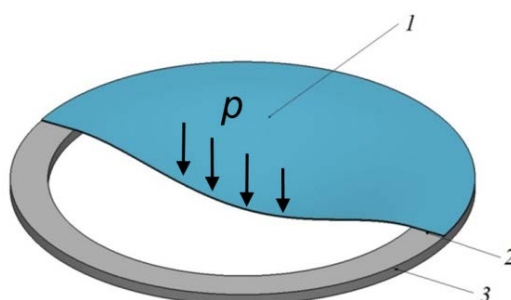


Fig. 1. Scheme of beryllium window fixed on the X-ray detector (1 – beryllium window, 2 – soldering area, 3 – metal frame).

To operate the X-ray detector, it is necessary to provide a high vacuum with a residual pressure of $10^{-5} - 10^{-7}$ Pa inside its chamber. So the beryllium window is exposed to an external pressure of 1 atmosphere (101325 Pa) during the detector operation. In some cases, the pressure can reach a value of 1.2 atmospheres. External pressure provides a significant mechanical load on the detector window, as result of which the foil experiences deformation.

Beryllium is a brittle material with low plasticity, so even a slight plastic deformation can cause fracture of the beryllium window, which will lead to vacuum loss and detector failure.

During X-ray detector operation a significant number of exhaust and inflow cycles of atmosphere is performed in its chamber, i.e. loading is cyclical. External pressure does not affect the whole area of beryllium window, but only the part of it that is not fixed in the frame (Fig. 1) called «window aperture» or «active area». Producers of X-ray detectors tend to increase the active area. However, it is important to ensure the absence of foil fracture during detector operation. Thus, it is necessary to have information about plastic deformation in the beryllium window under loading and its fracture probability at a given strain.

The aim of this work is to develop the technique of durability estimation for thin beryllium foils during their work in X-ray detectors under cyclic loading. It will allow selecting the optimal ratio of aperture and thickness for beryllium X-ray window reliable operation.

2. Numerical simulation of window cyclic loading by external pressure

The problem of plastic deformation for thin foil does not have an exact analytical solution, thus it was solved in ABAQUS using an axisymmetric setting.

Mesh consisted of 50 SAX1 elements, which thickness corresponded to the loaded foil thickness. For points of mesh, belonging to the soldering area, any translational and rotational displacements were excluded. For nodes, which corresponding to the aperture region, pressure p equal to 1 or 1.2atm, given by a cyclic law with a duration of one complete loading cycle of 4s, was applied.

The material properties were determined by the stress-strain curve [5], the elasticity modulus $E = 290$ GPa, and the Poisson's ratio $\nu = 0.02$ [6].

3. Results of modeling and their discussion

As result of the calculations, distribution fields of stresses, displacements, and accumulated strains in beryllium windows were obtained and their change during number of cycles increasing was established.

The maximum values of maximum principal stress σ_I and strain ε_i appear in a narrow window area directly bordering on the embedding (Fig. 2), in this region beryllium deforms plastically. Thus, it is the critical area where the foil fracture is most probable.

As the number of cycles increases, the values of accumulated plastic strain ε_i in the critical window region first increase sharply, and then stabilize, staying unchanged (Fig. 3). Calculations show that the strain ε_i in the critical region cease to increase when 1000 to 1500 loading cycles are reached (Fig. 3).

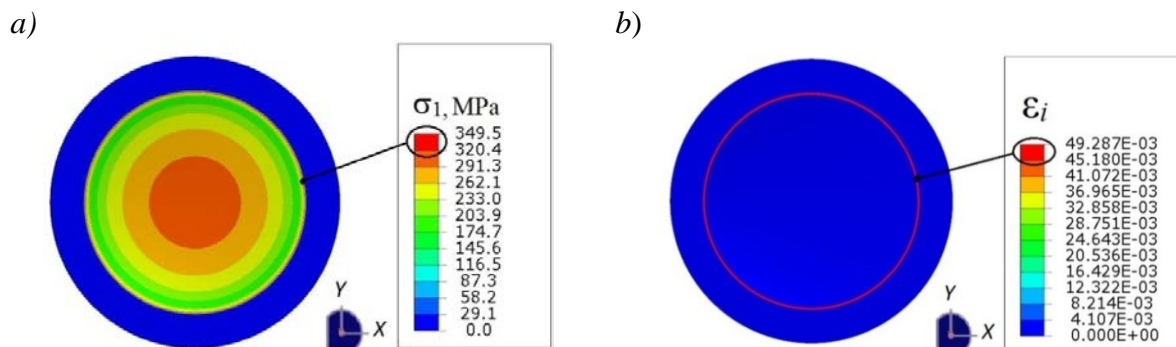


Fig. 2. The distribution field of maximum principal stress σ_i (a) and accumulated plastic strain ε_i (b) for a window with diameter of 9.2 mm, aperture of 7 mm and thickness of 8 μm after 1500 cycles of loading with external pressure at 1 atm.

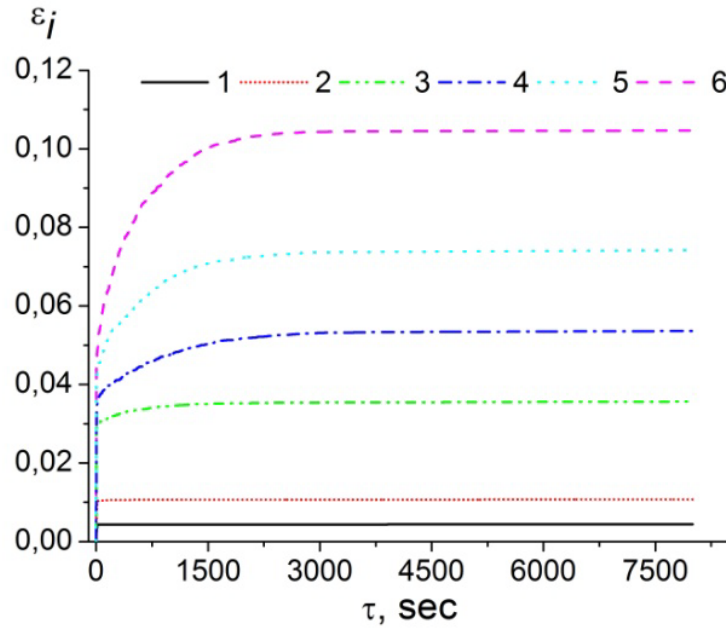


Fig. 3. Dependence of the accumulated plastic strain ε_i values change in the critical region on the loading time for beryllium window with aperture of 10 mm at cyclic load by external pressure $p = 1$ atm for different foil thicknesses: 1 – 30 μm ; 2 – 25 μm ; 3 – 15 μm ; 4 – 12 μm ; 5 – 8 μm ; 6 – 5 μm .

As a result of the calculations, values of maximum deflections at center of beryllium window (U_{max} , Fig. 4, *a*) and maximum accumulated strains in the critical region (ε_i , Fig. 4, *b*) for different foil thicknesses and pressure levels were obtained. Deflections and strains are determined by the aperture and the thickness of used foil and can both substantially increase and practically not differ from zero.

a)

b)

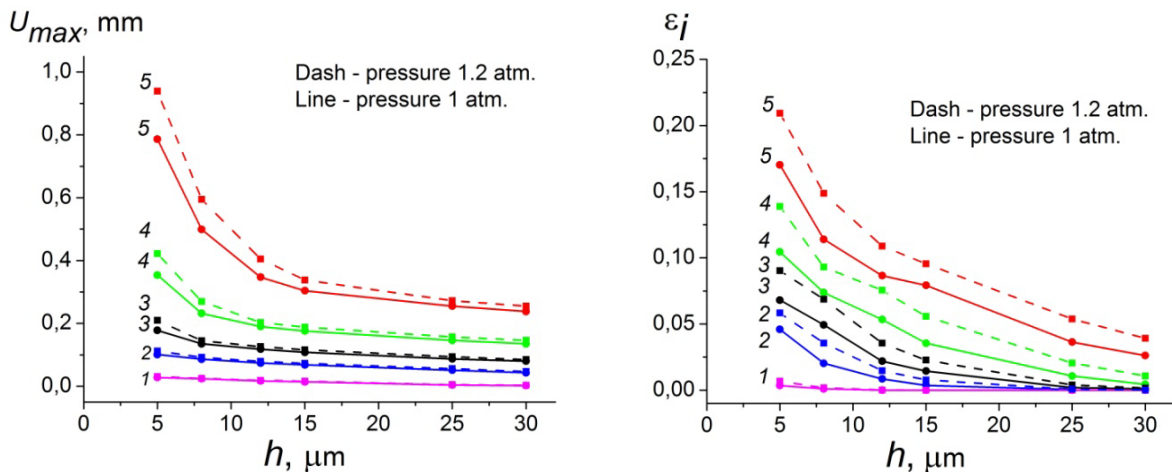


Fig. 4. Dependence of the change in the maximum displacement value U_{max} (*a*) and dependence of the change in the accumulated plastic strain ε_i value in the critical region of the beryllium window (*b*) after 1500 loading cycles on the window thickness at different pressures and apertures (1 – 2 mm, 2 – 5 mm, 3 – 7 mm, 4 – 10 mm, 5 – 15 mm).

4. Method for determining of ultimate plastic strain values

For foils with a thickness of 5 – 30 μm from brittle materials such as beryllium, it is impossible to perform an evaluation of mechanical characteristics using standard techniques as tensile test, compression test, etc. Proceeding from this, to determine the ultimate values of plastic strain, the most informative and available are the tests for foil samples bending up to fracture. When bending, the plastic deformation is localized in the bending region, in this same part the main tensile stresses act (Fig. 5).

Knowing the bending angle at the fracture moment (i.e., the formation of the first cracks) during experimental testing, it is possible to calculate the accumulated plastic strain for a given bending angle, which will be the limiting (C_{ult}).

Calculation of the accumulated plastic strain values at beryllium foil bending can also be performed using the finite element method (Fig. 5). For comparison, Fig.5 also presents the results of bending modeling for foils with a thickness of 200 and 250 μm . In Fig. 6 shows the calculated dependences of the accumulated strains on the bending angle α for different foil thicknesses. It has seen that the value of deformation achieved during bending decreases with decrease in thickness of curved foil at same bending angle.

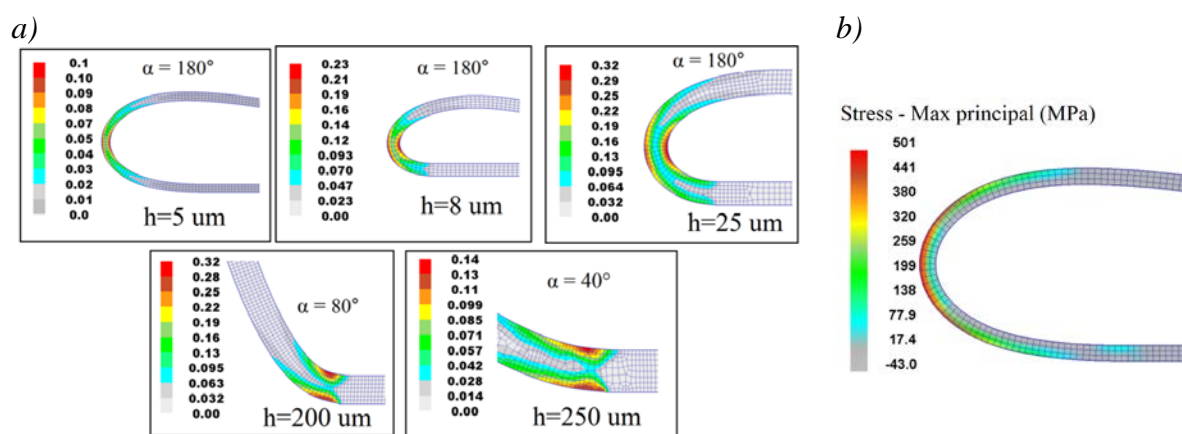


Fig. 5. The distribution of accumulated plastic strain in foils with a thickness of 5-250 μm after bending with angle α (a) and distribution of maximum principal stress σ_1 (b) at bending of 5 μm thickness foil.

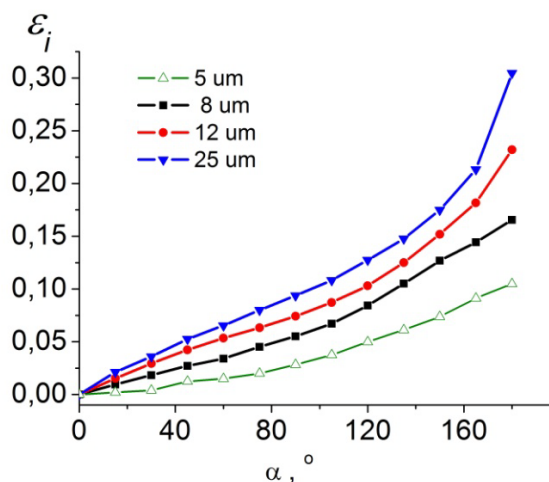


Fig. 6. The calculated dependencies of the accumulated plastic strain values at the bending angle α for different foil thicknesses.

5. Experimental investigation of beryllium windows fracture under cyclic loading by external pressure

To test the adequacy of the developed technique, cyclic tests for beryllium foil samples were performed. Foils with a thickness of 8 μm were chosen to testing, since it is most often used in X-ray detectors, and is also more prone to fracture compared to samples having a large thickness.

The outer diameter of the samples was 15 mm with aperture of 10 mm. The foils were connected to the metal frame using low-melting solder. The tests were carried out either before reaching 2000 loading cycles, or before the beginning of window fracture. Samples with an initial helium leakage rate no more than 10^{-10} mbar l/sec were used for the test. To control the moment of fracture begin the helium leak detector MS-40 from VIC was used.

It should be noted that beryllium X-ray windows have a very high cost, and therefore the scope of experimental investigations was limited. The tested foils were obtained from distilled beryllium grades by hot, warm and cold rolling methods in combination with heat treatments in vacuum. The studies were performed on foil samples with relatively low and high plastic properties. Surface defects (cracks, chains of inclusions, etc.) were on some foils (Fig. 7). The reasons for the various mechanical properties and features of their change during beryllium foils production were not considered in this work. We only note that increase in the beryllium plasticity is possible due to using of severe cold plastic deformation, which contributes to the fine crystalline structure formation in beryllium. It is widely known that this can significantly improve the metal mechanical properties [7-10].

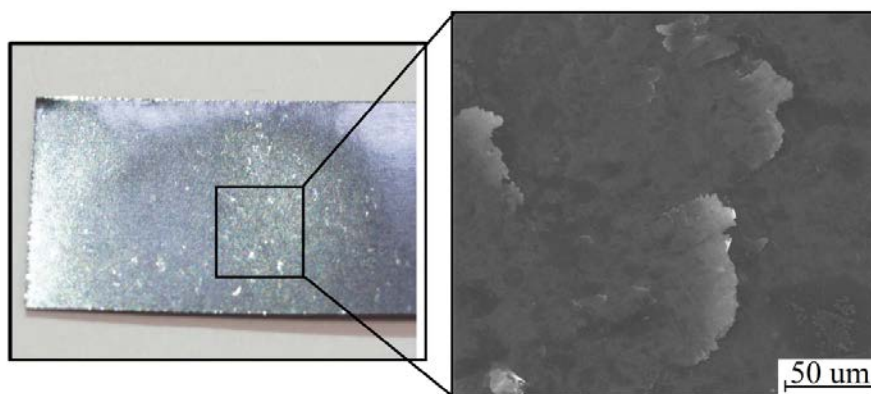


Fig. 7. Photograph and SEM-image of surface defects on beryllium foil.

Before cyclic tests, the ultimate plastic strain values were experimentally established for each group of foils according to the proposed bending test technique.

Results of bending for foil sample with surface defects presents in Fig. 8. It has seen that in the region of tensile stresses fracture and exfoliation of beryllium occur even at small deformations. Bending accompanies by cracks formation and their size can reach 300 – 500 μm . Thus, the presence of defects in the beryllium foil will lead to its instantaneous fracture at first loading. Beryllium windows for X-ray should not have any surface defects.

When bending samples with relatively low plastic properties, but without of surface defects, sample fracture occurred at bending angles 70-80°. Fracture character for this samples type is shown in Fig. 9. When bending samples with relatively high plastic properties at angle 180° no their fracture occurs (Fig. 10, *a*). SEM analyze showed that an insignificant number of microcracks are located along the grain boundaries in this case (Fig. 10, *b*).

Estimated number of loading cycles which beryllium foil is able to sustain without fracture was predicted (Table 1) from the dependence on Fig. 3.

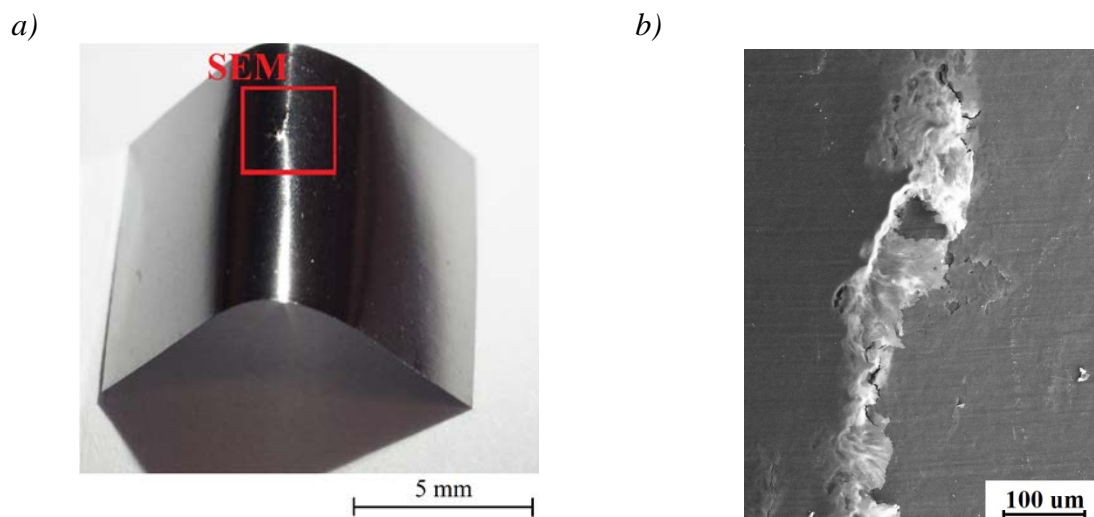


Fig. 8. Photograph (a) and SEM-image (b) of defect opening after bending at angle 30° (b).

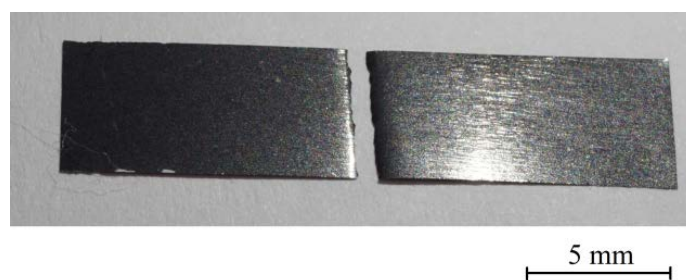


Fig. 9. Photograph of fractured sample with relatively low plastic properties after bending at angle 75° .

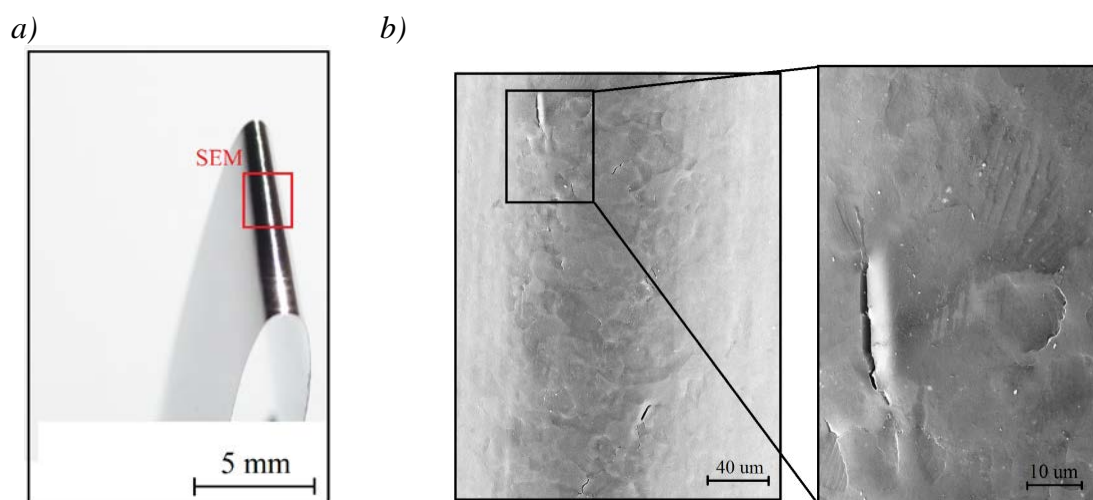


Fig. 10. Photograph of sample with a thickness of $8 \mu\text{m}$ with relatively high plastic properties after bending with angle 180° (a) and SEM- image of bending region (b).

The results of cyclic tests showed (Table 1) that foil samples having ultimate values $C_{\text{ult}} > 0.165$ withstand 2000 cycles of loading without fracture signs, while foil samples with

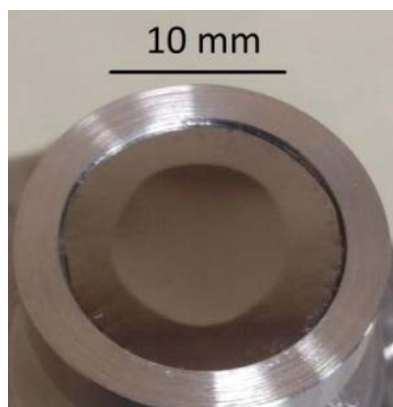
values $C_{ult} = 0.045$ begin to destruct after reaching 44 – 75 cycles. The cracks formation is indicated by an increase of helium leakage rate to $10^{-4} - 10^{-6}$ mbar l/sec.

Table 1. Results of cyclic testing for foil samples thickness of 8 μm an aperture of 10 mm with difference in plastic properties.

Number of sample	Experimental values of ultimate plastic strain (C_{ult})	Number of cycles without fracture, predicted	Number of cycles without fracture, actual	Leak rate, mbar l/sec
1	<0.02 (with surface defects)	0	0	$>10^{-4}$
2	<0.02 (with surface defects)	0	0	$>10^{-4}$
3	<0.02 (with surface defects)	0	0	$>10^{-4}$
4	0,045	60	44	$>10^{-6}$
5	0,045	60	52	$>10^{-6}$
6	0,045	60	75	$>10^{-6}$
4	>0.165	> 2000	2000	$<10^{-10}$
5	>0.165	> 2000	2000	$<10^{-10}$
6	>0.165	> 2000	2000	$<10^{-10}$

In Fig. 11 shows photos of the foil sample at the stages of vacuum buildup and atmosphere inflow respectively. Level of the maximum vertical displacement in the window center during the vacuum buildup measured using the epoxy resin imprint method applied to the window aperture, was 250 – 270 μm which corresponds to the modeling data (see Fig. 4, *a*).

a)



b)

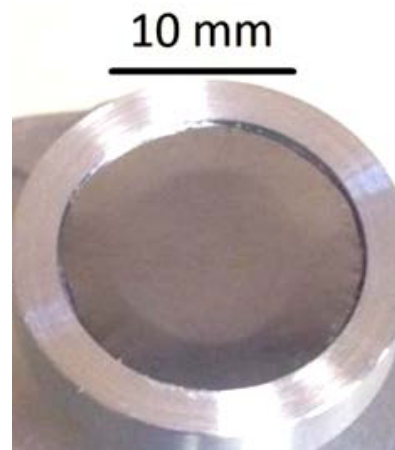


Fig. 11. Deformation of the foil sample at the stages of vacuum buildup (*a*) and atmosphere inflow (*b*).

According to Fig. 11 beryllium window remains concave at the atmosphere inflow stage, which indicates the beryllium plastic deformation in the critical region (Fig. 2).

Since the fracture of beryllium windows without defects under cyclic loading is facilitated by the accumulation of plastic strain combined with low plasticity of the beryllium foil, reduction of fracture probability can be achieved either by increasing the foil thickness (at constant aperture) or by increasing the beryllium foil plastic properties. The second way is more preferable, since increasing the window thickness adversely affects the characteristics of the X-ray detectors.

6. Conclusions

1. It has been established that when a thin beryllium window is operated in an X-ray detector under cyclic loading conditions, emergence and accumulation of plastic deformation in a narrow window area directly bordering on the embedding are possible. The presence or absence of plastic deformation is determined by window aperture and foil thickness.
2. It is shown that the probability of beryllium window fracture can be estimated by comparing the accumulated plastic strain value in a foil with a certain value of the ultimate plastic strain value which determined experimentally by bending test.
3. The low plasticity of the beryllium window has an extremely negative effect on its durability in the X-ray detector. Foils with thickness of 8 μm or less for their reliable use in X-ray detectors should have high plastic properties and not have any surface defects.

Acknowledgement. *This work was financially supported President of the Russian Federation grant (agreement Nr. MK-1402.2017.8).*

References

- [1] M. Imříšek et al. // *Nukleonika* **61** (2016) 403.
- [2] J. Prost, P. Wobrauschek, C. Streltsov // *Powder Diffraction* **30** (2015) 93.
- [3] O. Scharf et al. // *Analytical Chemistry* **83** (2011) 2532.
- [4] M. Röllig et al. // *Fusion Engineering and Design* **100** (2015) 177.
- [5] N. Kolbasnikov et al. // *Russian Metallurgy (Metally)* **2014** (2014) 785.
- [6] K. Walsh, *Beryllium Chemistry and Processing* (ASM International, 2009).
- [7] A.I. Rudskoy // *Tsvetnye Metally* **4** (2014) 22.
- [8] G.E. Kodzhaspirov, A.I. Rudskoy // *Acta Physica Polonica A* **128** (2015) 527.
- [9] A.I. Rudskoy et al. // *Tsvetnye Metally* **4** (2014) 36.
- [10] A.A. Naumov et al. // *Materials Science Forum* **762** (2013) 62.

CONTACTLESS ELECTROMAGNETIC ACOUSTIC TECHNIQUES OF DIAGNOSTICS AND ASSESSMENT OF MECHANICAL PROPERTIES OF STEEL ROLLED BARS

V.V. Murav'ev^{1,2*}, O.V. Murav'eva^{1,2}, K.V. Petrov¹

¹Kalashnikov Izhevsk State Technical University, 7 Studencheskaya Str., Izhevsk, 426069, Russia

²Udmurt Scientific Center of Ural Branch of Russian Academy of Sciences, 34 T. Baramzinoy Str., Izhevsk, Russia 426067

*e-mail: vmuraviev@mail.ru

Abstract. The acoustic technologies of the mechanical properties assessment and diagnostics of steel rolled bars based on using contactless electromagnetic acoustic (EMA) transducers of longitudinal, shear and Rayleigh waves and a mirror-shadow technique on multiple reflections are presented. Dependencies of the structural sensitive acoustic factors (absolute values of longitudinal, shear and Rayleigh wave velocities, their changes during the mechanical loading, acoustoelastic coefficients, efficiency of EMA transformation) on elastic and mechanical properties, the quality of heat treatment, the structural and stress-strain state of steel bar samples from springing, low-alloyed perlite and chrome-nickel steels are investigated.

Keywords: electromagnetic-acoustic technique; velocities of elastic waves; structure; mechanical properties; stress-strain state; acoustoelasticity; defects.

1. Introduction

A wide arsenal of nondestructive physical magnetic and acoustic techniques and instruments are used to solve the problems of determining the structure, the anisotropy, the elastic and strength properties of constructional materials [1–8]. Electromagnetic acoustic (EMA) techniques of non-destructive testing are the progressive ones among modern trends of methods and means of predicting of the structure [9–14]. Contactless EMA method of excitation-receipt does not require application of the contact liquid, thus giving the possibility to perform control procedures for rough and contaminated surfaces of objects, at high and low temperatures and for objects moving at high speeds. It is important that EMA transducers allow for generating different types of waves with various polarization which in turn increases the number of informative parameters sensitive to the structure and discontinuity flaws of the metal [10].

To perform the structural analysis and flaw detection of steel rolled bars, the authors developed the technique of the mirror-shadow method on multiple reflections [15] with application of specialized transmission-type EMA transducers for radiation-receipt of shear and longitudinal radial waves [14] and surface EMA transducers for radiation-receipt of Rayleigh waves along the bar perimeter [13].

The paper presents the results of applying the developed technique for flaw detection and assessment of mechanical properties of steel rolled bars made of springing and structural steels.

2. Applied approaches and methods

In order to assess the influence of the structure, mechanical properties and discontinuity flaws on the measured characteristics of acoustic waves, we used rolled bar samples made of structural springing steels UNS G95620 and UNS G10600 (such rolled bars are applied when producing the railway springs) and rolled bar samples made of structural low-alloy perlite steels UNS G51400, UNS G41180 and UNS G41400, and chrome-nickel steels UNS S20910 applied when producing the responsible parts of oil mining equipment: bar blanks of pump rods and shafts of centrifugal pumps. In order to assess the influence of the structural state and mechanical characteristics, the samples have been investigated on delivery and during operations of the manufacturing cycle at the stage of heat treatment for martensite, sorbite and perlite structures. To assess the sensitivity of the developed method to flaws, the following samples have been subjected to production tests at "SPC "Pruzhina", Ltd: bars made of steel UNS G95620 having diameters from 10 to 30 mm with different types of flaws – both surface and internal.

Figure 1a shows the photo of the experimental stand used at investigations [16]. In order to investigate the influence of the stress-strain state on acoustic properties, the samples have been subjected to tension at the machine Instron 300DX in the direction of the longitudinal axis (Fig. 1b). Schemes of acoustic wave propagation and specific oscillograms for a series of multiple reflections of the shear wave along the bar diameter are shown in Fig. 2.

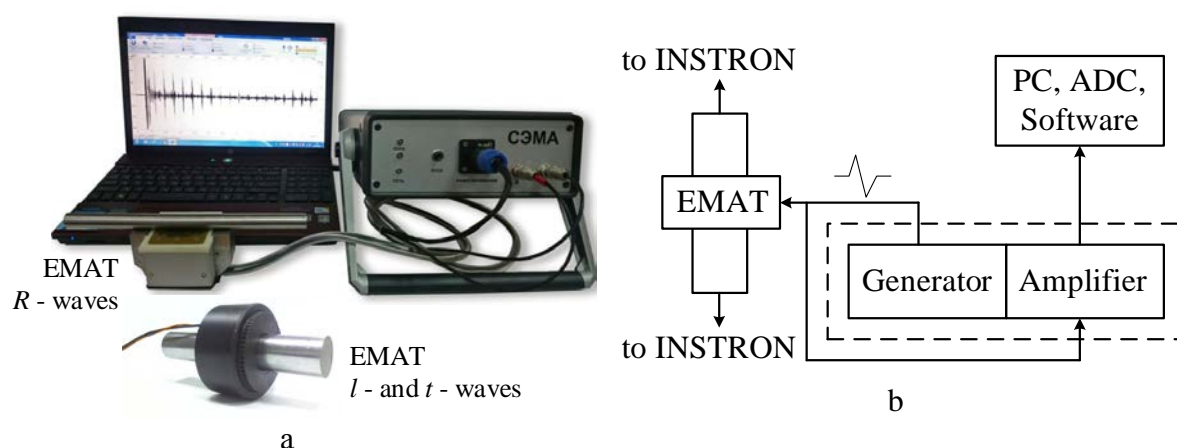


Fig. 1. Experimental stand for structural analysis and flaw detection of bars with transmission-type and surface EMA-transducers (a), and the scheme of mechanical loading of samples (b).

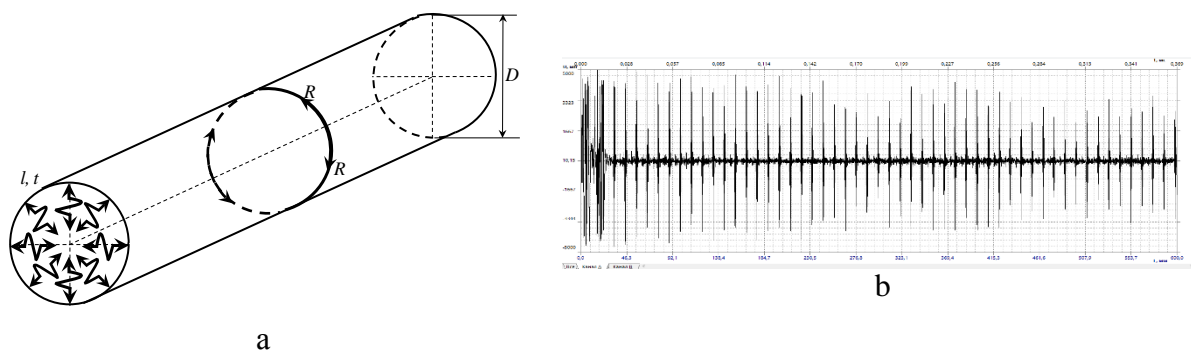


Fig. 2. Scheme of propagation of longitudinal l and shear t radial waves along the section and Rayleigh R waves along the bar enveloping line (a), specific oscillograms for a series of multiple reflections of the shear wave along the bar diameter (b).

Velocities of propagation of longitudinal C_l , shear C_t and Rayleigh C_R waves are calculated in accordance with formulas:

$$C_{t,l} = \frac{D \cdot n}{t_n}, \quad C_R = \frac{\pi D \cdot n}{t_n}, \quad (1)$$

where D is the bar diameter, t_n is the time of the n -th reflection of the pulse in the oscillogram.

High frequency of discretization of analog-digital conversion, possibility of obtaining a series of multiple reflections and the consequent interpolation provide high accuracy of determining the velocity (0.5 m/s or 0.01%). When assessing the elastic modules of bars (Young modulus E , shear modulus G , Poisson's factor ν), their functional relation with velocities of propagation of volume (longitudinal and shear) and Rayleigh waves in the object at the known density ρ is used.

Equations of acoustic elasticity for the considered loading scheme and polarization of the applied acoustic waves are described by formulas:

$$\Delta C_l / C_{l0} = \beta_{zz}^c \sigma_{zz}, \quad \Delta C_t / C_{t0} = \beta_{zz}^c \sigma_{zz}, \quad \Delta C_R / C_{R0} = \beta_{z\varphi}^c \sigma_{zz}, \quad (2)$$

where β_{ij} are acoustic elastic coefficients of velocity determined by Lamé elasticity constants of the second order λ , μ and Murnaghan elasticity constants of the third order l , m , n .

3. Discussion of investigation results

Histograms of relative velocities of elastic waves for samples of steel UNS G51400 ranges in ascended order are shown in Fig. 3. The propagation velocity for longitudinal, shear and Rayleigh waves has low value in the structure of martensite obtained by hardening with the maximum degree of distortions of the crystal lattice. The consequent tempering, martempering and especially softening treatment like normalization, lead to increasing the velocity of ultrasound waves. Note, that for the most balanced hypoppearlitic structures the velocities of volume and Rayleigh waves take the maximum value. At the same time, in structures of fine grain sorbite the velocity of volume and Rayleigh waves take the intermediate value between structures of martensite and the hypoppearlitic mixture.

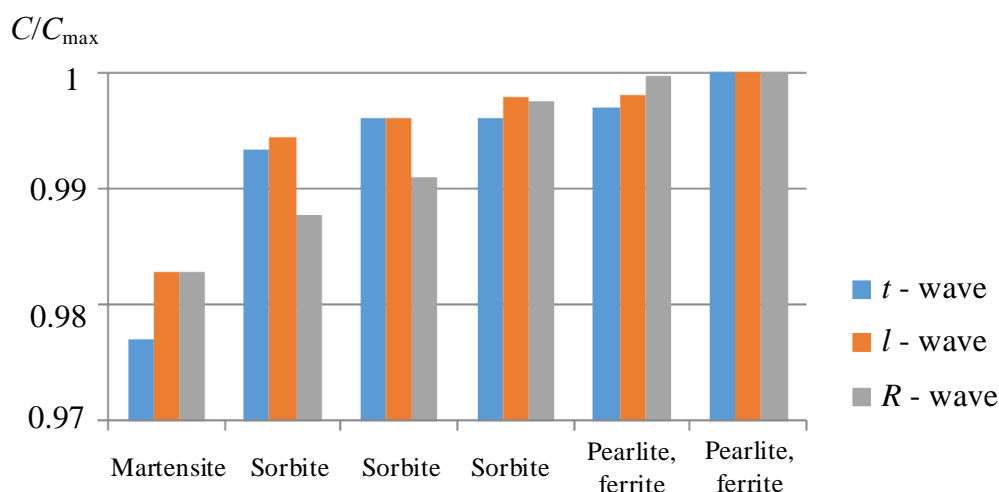


Fig. 3. Relative velocities of shear, longitudinal and Rayleigh waves vs. the structure of steel UNS G51400 samples.

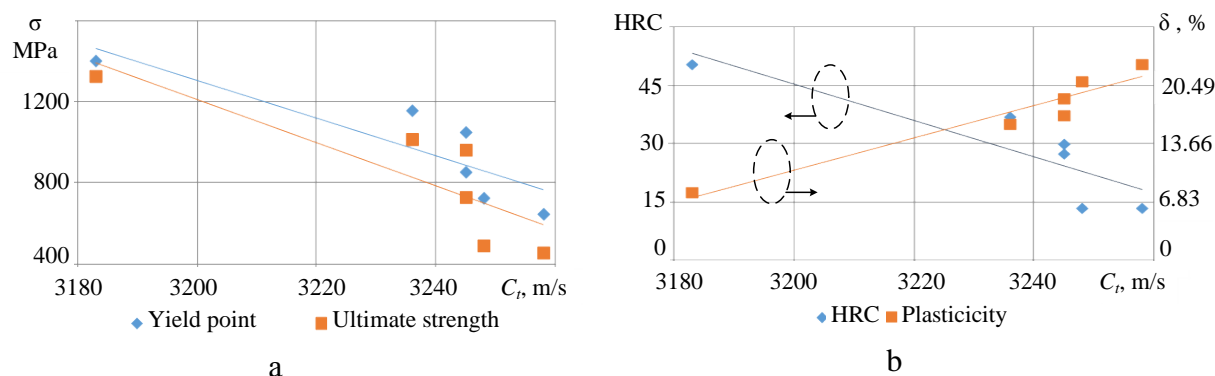


Fig. 4. Correlation of the velocity of shear waves with mechanical properties of steel UNS G51400 samples.

Here, mechanical properties (hardness, Yield point and ultimate strength, relative elongation) correspond to the structural state of samples and correlate properly with velocities of propagation of shear, longitudinal and Rayleigh waves (Fig. 4). The velocity of waves decreases with the growth of the Yield point and ultimate strength; and it increases with the growth of plasticity and relative elongation.

When the tensile load is increased, one can observe the linear decrease of the velocity of propagation of shear, longitudinal and Rayleigh waves in the elastic area for the considered grades of steel (Fig. 5a). The sensitivity of shear waves to mechanical stresses is maximum due to coincidence of their axial polarization with the direction of the applied load. As for longitudinal and Rayleigh waves with elliptical polarization, the sensitivity to mechanical stresses is considerably lower.

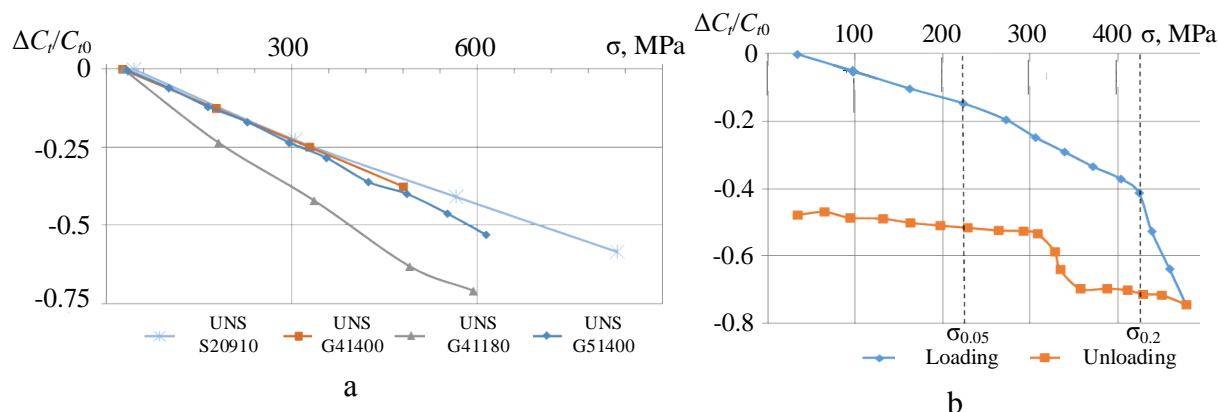


Fig. 5. Velocity of shear waves vs. the applied tensile load for steel UNS G51400 in the elastic area (a), for steel UNS G10600 in the elastic and plastic area at loading and unloading modes (b).

In order to investigate the effect of acoustoelasticity in areas of proportionality and plasticity, steel UNS G10600 samples were subjected to high temperature annealing (820°C, 30 minutes, cooling down in the furnace) to decrease the Yield point. Fig. 5b shows the results of variation of velocities of elastic waves in steel UNS G10600 in the elastic and plastic areas at loading and unloading of the sample. Non-linearity in the character of the curve line is observed when transiting to the elasticity area (up to 220 MPa) and farther to the Yield area (420 MPa), the coefficients of acoustoelasticity being increased here. The values of acoustoelastic coefficients of the investigated steel grades are given in Table 1.

Table 1. Acoustic elastic coefficients for velocity β_{xx}^C , 1/TPa.

UNS S20910	UNS G41400	UNS G41180	UNS G51400	UNS G10600		
				in elastic area	in proportionality area	in plastic area
-4.7	-5.5	-8.8	-8.2	-6.5	-14.5	-55.3

Materials and structures of the investigated samples are of essential influence on the efficiency of EMA transformation which is the additional informative parameter at structural analysis.

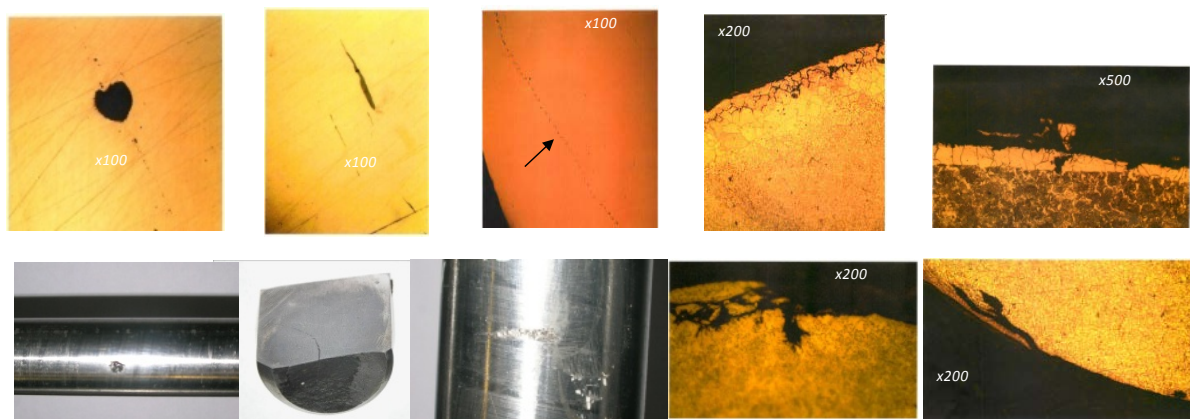


Fig. 6. Revealed defects of the rolled bars: non-metallic inclusions, folds, decarburized layer, rolled blisters, hollows.

The developed EMA techniques are applied for flaw detection of bar stocks having diameters from 10 to 30 mm with various quality of surface treatment, made by different manufacturers, used for production of extra heavy pump rods, springs, parts of special-purpose machinery at mechanical engineering enterprises. Fig. 6 presents the photos of micro slices for certain types of the revealed defects.

It should be noted that the depth and opening of cracks, dimensions of inclusions comprise tenths of the length of the acoustic wave, whereas the traditional echo-method of ultrasound control allows for revealing the defects comparable with the wave length.

4. Conclusions

Therefore, the developed contactless EMA technique is the fine tool for assessing the elastic properties, quality of heat treatment, structural and stress strain state of rolled bars. The performed investigations revealed the possibility of its applying for the structural analysis and assessment of the stress strain state of steel bars for the following structure-sensitive factors: absolute values of velocities of longitudinal, shear and Rayleigh waves, their variation in the process of the mechanical loading, corresponding acoustic elastic coefficients vs. the velocity; and the relative variation of the amplitude under the loading process that characterizes the efficiency of EMA transformation.

Due to tuning out the acoustic contact quality and the possibility of obtaining a series of multiple reflections, the high accuracy, repeatability and validity of methods for acoustic structural analysis and flaw detection are provided.

Acknowledgements. *The reported study was funded by Ministry of Education and Science of the Russian Federation according to the project no. 3.5705.2017/6.7 of the state order for Kalashnikov Izhevsk State Technical University for a period of 2017—2019, section "Management of scientific research".*

References

- [1] E.S. Gorkunov, E.I. Yakushenko, S.M. Zadvorkin, A.N. Mushnikov // *The Physics of Metals and Metallography* **116** (2015) 147.
- [2] V.N. Kostin, O.N. Vasilenko, D.Y. Filatenkov, Yu.A. Chekasina, E.D. Serbin // *Russian Journal of Nondestructive Testing* **51** (2015) 624.
- [3] M.B. Rigmant, M.K. Korkh, D.I. Davydov, D.A. Shishkin, Yu.V. Korkh, A.P. Nichipuruk, N.V. Kazantseva // *Russian Journal of Nondestructive Testing* **51** (2015) 680.
- [4] Y. Ivanova, T. Partalin, D. Pashkuleva // *Russian Journal of Nondestructive Testing* **53** (2017) 39.
- [5] B. Wang, X. Wang, L. Hua, J. Li, Q. Xiang // *Ultrasonics* **76** (2017) 208.
- [6] A.N. Smirnov, N.V. Ababkov, E.V. Kozlov, N.A. Koneva, N.V. Bykova // *Steel in Translation* **44** (2014) 742.
- [7] S.A. Barannikova, A.V. Bochkareva, A.G. Lunev, G.V. Shlyakhova, L.B. Zuev // *Steel in Translation* **46** (2016) 552.
- [8] A.N. Smirnov, N.V. Ababkov, V.V. Murav'ev, S.V. Fol'mer // *Russian Journal of Nondestructive Testing* **51** (2015) 94.
- [9] B. Hutchinson, P. Lundin, E. Lindh-Ulmgren, D. Lévesque // *Ultrasonics* **69** (2016) 268.
- [10] M. Hirao, H.Ogi, *EMATS for science and industry: noncontacting ultrasonic measurements* (Kluwer Academic Publishers, Boston, 2003).
- [11] O.V. Murav'eva, M.Yu. Sokov // *Bulletin of Kalashnikov ISTU* **19(3)** (2016) 46.
- [12] V.V. Murav'ev, O.V. Murav'eva, V.A. Strizhak, A.V. Pryakhin, E.N. Fokeeva // *Russian Journal of Nondestructive Testing* **50** (2014) 435.
- [13] O.V. Murav'eva, V.A. Zorin // *Russian Journal of Nondestructive Testing* **53** (2017) 337.
- [14] V.V. Murav'ev, O.V. Murav'eva, K.V. Petrov // *Russian Journal of Nondestructive Testing* **53** (2017) 560.
- [15] O.V. Murav'eva, V.V. Murav'ev, M.A. Gabbasova, I.V. Buldakova, M.Y. Sokov // *Optoelectronics, Instrumentation and Data Processing* **52** (2016) 367.
- [16] V.A.Strizhak, A.V. Pryakhin, S.A. Obukhov, A.B. Efremov // *Intellekt. Sist. Proizv.* **1** (2011) 243.

MICROSTRUCTURE EVOLUTION OF A Ti/TiB METAL-MATRIX COMPOSITE DURING HIGH-TEMPERATURE DEFORMATION

M.S. Ozerov, M.V. Klimova, N.D. Stepanov, S.V. Zhrebtsov*

Laboratory of Bulk Nanostructured Materials, Belgorod State University, Belgorod, Russia

*e-mail: zhrebtsov@bsu.edu.ru

Abstract. A Ti/TiB metal-matrix composite (MMC) was produced by spark plasma sintering using a Ti-10wt.%TiB₂ powder mixture at 850°C under a load of 40 MPa for 15 min. The microstructure evolution and mechanical behavior of the Ti/TiB composite during uniaxial compression at the temperature range 500 - 1050°C was studied. The evolution of microstructure of the titanium matrix was associated with the formation of dislocation cells at 500°C, continuous dynamic recrystallization at 700°C and discontinuous dynamic recrystallization at temperatures $\geq 850^\circ\text{C}$. The apparent activation energy of the deformation and processing map were analyzed. The contributions of different strengthening mechanisms of the composite were evaluated.

Keywords: metal-matrix composite; spark plasma sintering; uniaxial compression; dynamic recrystallization; activation energy; precipitation hardening.

1. Introduction

Titanium and its alloys are attractive for applications in various industries due to its encouraging properties (high specific strength, corrosion resistance). However, practical usage of titanium alloys is often limited by their insufficient strength, hardness, and wear resistance. One of the solutions to this problem is creating composites based on titanium, using a reinforcing high-strength component. In this case, the high strength of the reinforcing component is combined with the high toughness of the titanium matrix.

Among the various reinforcements, TiB is the most attractive because it has a density close to that of titanium, a high Young modulus, creates minimal residual stresses due to a close coefficient of thermal expansion, and also has good crystallographic interphases with a titanium matrix [1-3].

During synthesis of the Ti/TiB composite by spark plasma sintering (SPS) process, the TiB phase is formed as a result of the chemical reaction $\text{Ti} + \text{TiB}_2 \rightarrow \text{Ti} + 2\text{TiB}$ [1, 3]. This method has certain advantages: high synthesis speed helps to preserve the high dispersity of the original powders; besides, it is possible to achieve almost 100% density of the specimens [4, 5].

Meanwhile, the presence of the TiB hardening phase not only increases the strength but also significantly reduces the plasticity of the composite. The possibility of increasing ductility of a titanium alloy reinforced with TiB fibers due to high-temperature 2D deformation was shown in [7]. Unfortunately, this is a limited number of thorough investigations of the microstructure evolution during thermomechanical processing [8]. Therefore, additional studies of different temperature-rate conditions of thermomechanical processing on the structure and mechanical properties of the Ti/TiB composite are required.

2. Materials and methods

To synthesize the Ti/TiB composite, titanium powder (99.1% purity) with an average particle size of $25\pm 10\ \mu\text{m}$ and titanium diboride TiB_2 powder (99.9% purity) with a mean particle size of $4.0\pm 1.5\ \mu\text{m}$ were used. The weight fraction of TiB_2 in the initial mixture was 10%, which corresponded to 17 vol. % TiB after synthesis [10]. The selected amount of reinforcing component provides practically the maximum strengthening effect, further increase of TiB_2 in the initial mixture does not give an appreciable increase in strength, but leads to a sharp drop in ductility [1]. A mixture of Ti powder with 10 wt. % of TiB_2 was prepared using a Retsch RS200 vibrating cup mill for 1 h in ethanol at the milling rotation speed of 700 rpm. The grinding set was cooled with liquid nitrogen ($T=-196^\circ\text{C}$) to prevent heating of the mixture during mixing. The spark plasma sintering process was carried out using the Thermal Technology SPS10-3 unit at a temperature of 850°C at a pressure of 40 MPa and a holding time of 5 minutes. Specimens $\varnothing 19\times 15\ \text{mm}$ were obtained. The temperature of the polymorphic transformation of the titanium matrix of the composite was $\sim 915^\circ\text{C}$.

Samples $\varnothing 7\times 10\ \text{mm}$ were cut from composite blanks using the electro-erosion machine Sodick AQ300L. Specimens were compressed isothermally in air at 500, 700 or 850°C (α phase field) and 950, 1000 or 1050°C (β phase field) with an Instron mechanical testing machine at a nominal strain rate of $10^{-3}\ \text{s}^{-1}$ to a true strain $\varepsilon \approx 1.2$ (corresponding to a 70% reduction). The holding time of the specimen at the desired temperature before the start of deformation was 15 minutes. Immediately after stopping the deformation, the sample was removed from the furnace and cooled on air.

Strain-rate jump compressive tests were conducted at temperatures of 800, 850, 950, 1000 and 1050°C and at strain rates of 10^{-2} , 5×10^{-3} , 10^{-3} and $5\times 10^{-4}\ \text{s}^{-1}$. The obtained data were used to determine the activation energy of the plastic deformation of the Ti/TiB composite in accordance with [11-13].

The tensile testing was conducted at temperatures of 20°C , 400°C , 500°C , 600°C , 700°C and an constant strain rate of $10^{-3}\ \text{s}^{-1}$. The tensile samples had the gauge length of 4mm and a rectangular gauge cross-section of $3\text{mm}\times 1.5\text{mm}$. The specimens were carefully mechanically polished. Elongation to fracture was determined by measurements of spacing between marks designating the gauge length before and after the test.

X-ray diffraction (XRD) analysis was done for the shear plane of specimens using an ARL-Xtra diffractometer with $\text{CuK}\alpha$ radiation. Quantitative phase analysis was performed using the Rietveld method [14] with PowderCell software. The microstructure in the axial section was studied using scanning electron microscope (SEM) FEI Quanta 600 FEG microscope and a transmission electron microscope (TEM) JEOL JEM 2100. Etching was carried out with Kroll's reagent (95% H_2O , 3% HNO_3 , 2% HF) for SEM observations.

3. Results and discussion

The initial microstructure. The microstructure of the Ti/TiB composite after sintering at 850°C consisted of three structural components: Ti matrix, TiB whiskers that formed during in situ $\text{Ti} + \text{TiB}_2 \rightarrow \text{Ti} + 2\text{TiB}$ reaction, and retained TiB_2 particles (Figure 1a). The volume fraction of pores in the structure was 0.5%. The average diameter of TiB whiskers was $36\pm 15\ \text{nm}$. The TEM analysis showed the heterogeneous distribution of TiB whiskers in the titanium matrix (Fig. 1b). The TiB whiskers had an irregular hexagonal shape with the sides the parallel to the (100), $(10\bar{1})$ and (101) planes [8] (the insert in Fig. 1b). Many stacking faults were observed in the (100) plane of the TiB whisker. The fractions of the phases determined by the quantitative X-ray analysis were 74.0% Ti, 15.6% TiB and 10.4% TiB_2 .

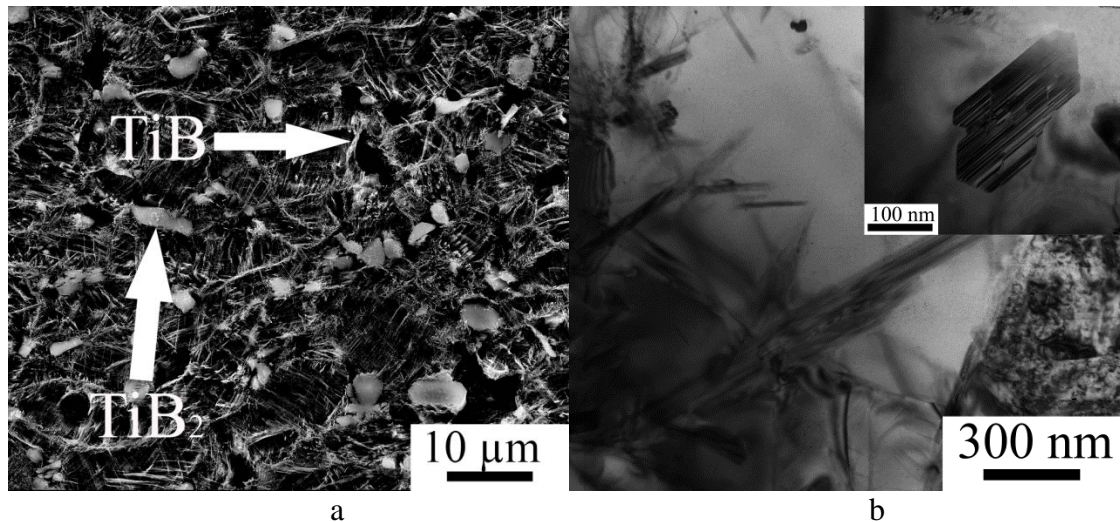


Fig. 1. SEM (a) and TEM (b) images of the Ti/TiB microstructure after SPS at 850°C.

Mechanical properties. The tensile testing of the composite at the temperature range of 400-700°C (Fig. 2) demonstrated appreciable ductility only at temperatures $\geq 500^\circ\text{C}$. At 400°C the sample was ruptured in the elastic region (corresponding stress-strain curve not presented). It worth noting that the shape of the stress-strain curves obtained at 500-700°C indicated early localization of the plastic flow and a short stage of the uniform deformation. Such deformation behavior is typical of heavily deformed or ultrafine grained metallic materials because of the lack of an effective hardening mechanism [15]. Thus, the obtained results have been showing the possibility of mechanical processing of the Ti/TiB composite at temperatures above 500°C.

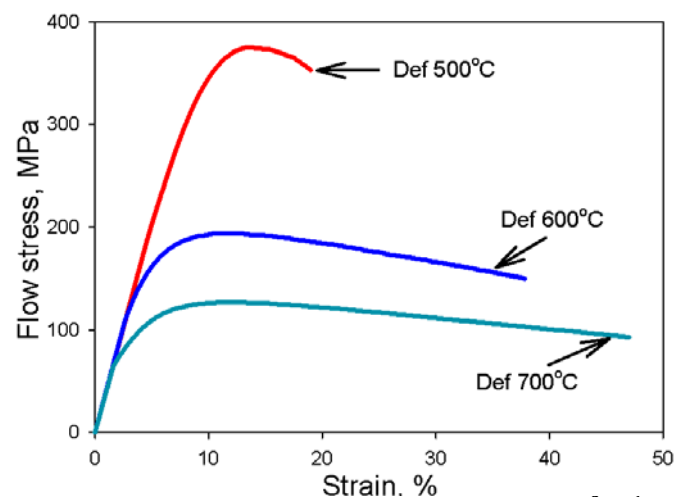


Fig. 2. Tensile stress-strain curves obtained at a strain rate of 10^{-3} s^{-1} at temperatures of 500, 600 and 700°C.

To study the mechanical behavior of the Ti/TiB composite compression tests at temperatures 500-1050°C were carried out. The appearance of the samples after destruction showed the presence of surface cracks up to a temperature of 1050°C (Fig. 3a). The sample compressed at 500°C demonstrated the continuous hardening after the beginning of plastic flow. The stress-strain curves obtained at temperatures of 700-1050°C of the Ti/TiB composite showed the presence of an initial hardening transient, the achievement of a peak flow stress, and then flow softening (Fig. 3h). This behavior can be associated with the processes of dynamic recrystallization or recovery.

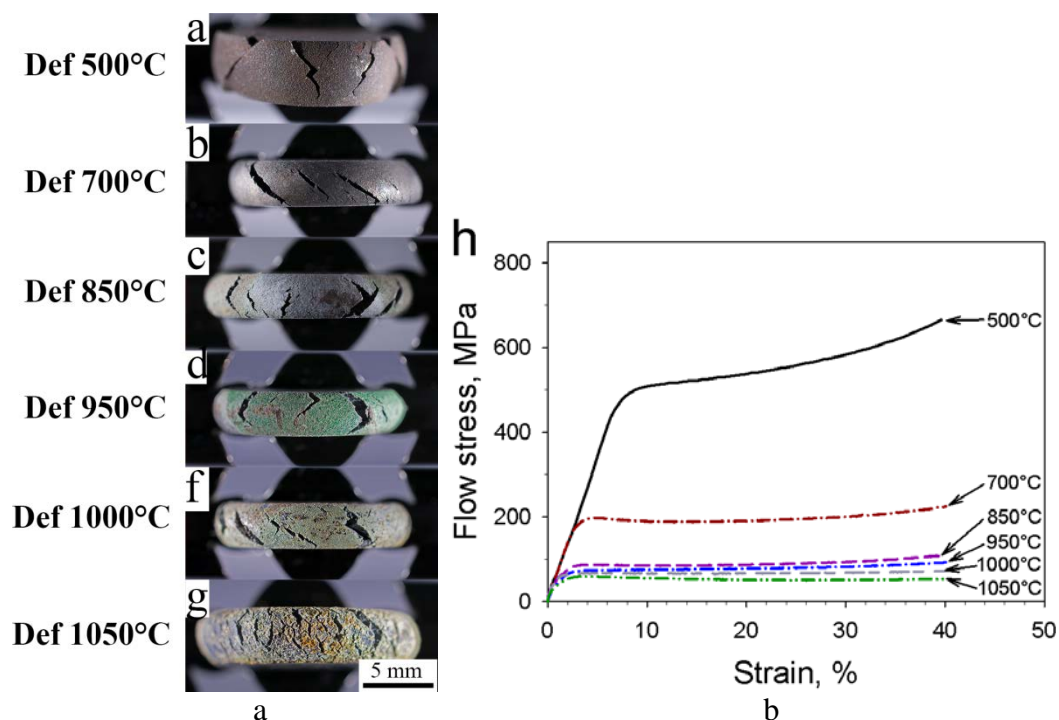


Fig. 3. Specimens of the Ti/TiB composite after isothermal compression at 500 (a), 700 (b), 850 (c), 950 (d), 1000 (e), 1050°C (f) and flow curves obtained during compression at 500-1050 °C and a nominal strain rate of 10^{-3}s^{-1} (h).

The microstructure evolution of the Ti/TiB composite during compression tests. The microstructural changes observed in SEM were associated with the rotation of the TiB whiskers in the direction of the plastic flow; the intensity of this process decreases with an increase in the deformation temperature (Fig. 4). Redistribution of the TiB whiskers with the formation of clusters was observed at the deformation temperatures 500-950°C. At higher compression temperatures of 1000-1050°C the TiB whiskers remained rather inhomogeneously distributed in the titanium matrix. A decrease in the fraction of residual TiB_2 is observed with an increase in the deformation temperature.

The TEM investigation showed a more pronounced dependence of the structural changes on the deformation temperature (Fig. 5). The titanium matrix had a typical cellular structure with a high dislocation density after deformation at 500°C (Fig. 5a). The boundaries of the cells were rather wide and loose. The size of the cells varied from a hundred to several hundred nanometers. The interphase Ti/TiB boundaries were blurred due to high internal stresses caused by the high dislocation density. Regions with a size of 1.0-1.5 μm with a low dislocation density, surrounded by rather loose and wide boundaries were observed in the deformed structure after compression at 700°C (Fig. 5b). After deformation at 850°C, grains with a size of $\sim 1 \mu\text{m}$ with boundaries having a fairly perfect structure with a characteristic banded contrast were found (Fig. 5c). The formation of new grains occurred mainly in regions with a low density of the TiB whiskers. The high density of the TiB particles hindered grain boundary movement thereby preserving deformed microstructure. A completely recrystallized structure with an average grain size of $\sim 2.5 \mu\text{m}$ is observed (Fig. 5d) after compression at 1000°C, corresponding to the β phase field of the titanium matrix.

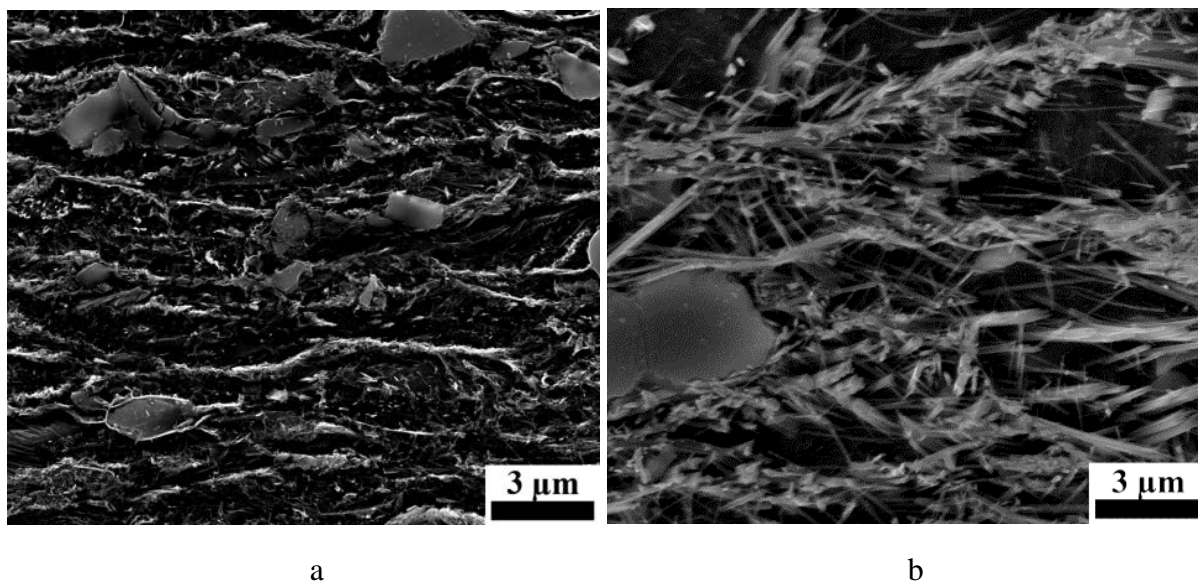


Fig. 4. Microstructure (SEM) of the Ti/TiB composite after compression to 70% at 500 (a) and 1050°C (b).

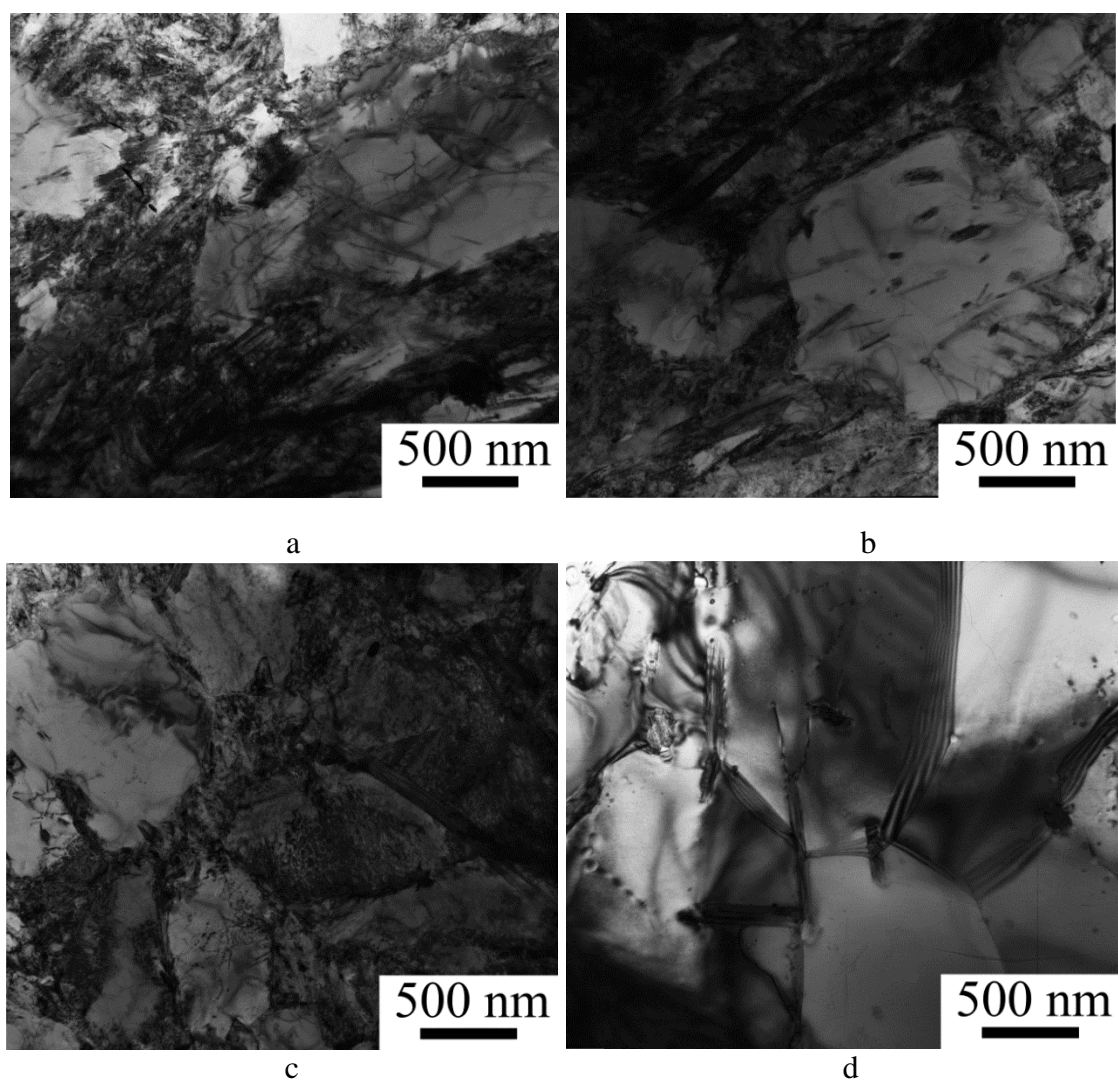


Fig. 5. Microstructure (TEM) of the Ti/TiB composite after compression to 70% at 500 (a), 700 (b), 850 (c) and 1000°C (d).

Quantitative analysis of the TiB whiskers size (Fig. 6) showed a slight change in the transverse dimension (diameter) depending on the deformation temperature in the α field. Some increase in the transverse size of the TiB whiskers (Fig. 6a) was noted after deformation in the β field ($T > 900^\circ\text{C}$) in comparison to the initial state. Probably, it can be associated with a high diffusion rate in the β field. The length of the TiB whiskers sharply (~ 4 times) decreased as a result of deformation in the α field, and, to a lesser extent (~ 2.5 times), in the β field. According to [9], the aspect ratio (length to the size of the cross-section) of the TiB whiskers (rather than the diameter) is the main factor which affects the mechanical properties of the titanium-matrix composites. The ratio of length to transverse dimension in the investigated Ti-TiB composite remained constant ~ 10 (in the initial state ~ 55) during the deformation.

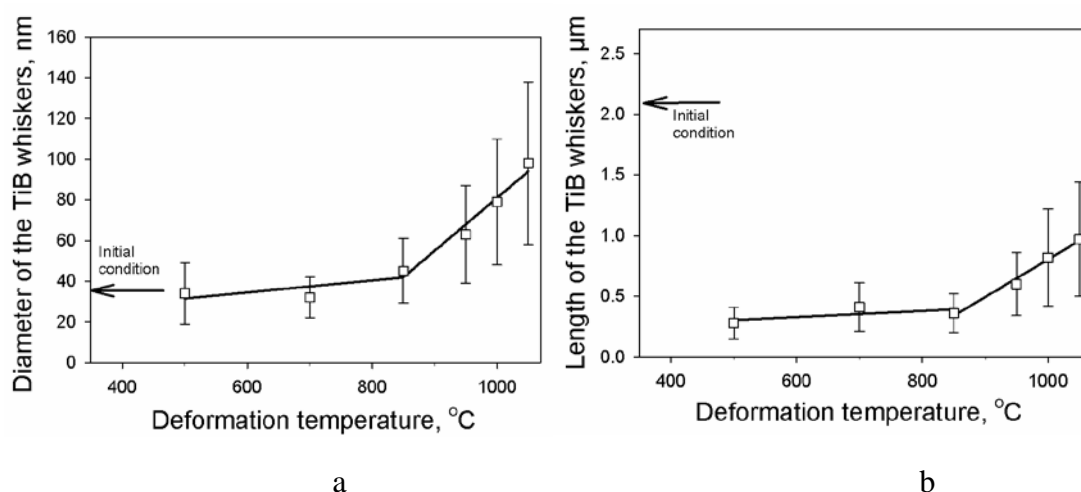


Fig. 6. Change in the transverse dimension (diameter) (a) and length (b) of the TiB whiskers as a result of the Ti/TiB composite's compression tests at temperatures of 500-1050°C.

Thermoactivation analysis. The results of the analysis of the apparent activation energy of the plastic deformation indicated the presence of three stages (Fig. 7). The value of the activation energy obtained at low deformation temperatures (500-800°C) at a strain rate of 10^{-3}s^{-1} and a factor of $n=7$ was $Q=309$ kJ/mol. In this temperature range the appearance of partially recrystallized regions and the development of continuous dynamic recrystallization (cDRX) was observed. It is also worth noting that the results obtained are consistent with those given in [16], when the controlling mechanism of deformation is the thermally activated overcoming of the interstitial solute atom obstacles by dislocations. At a deformation temperature of 850°C, the value of the activation energy dropped by ≈ 3 times. This is apparently due to the development of discontinuous dynamic recrystallization (dDRX) and the formation of recrystallized grains. A further increase in the deformation temperature (above 900°C) leads to the activation of new, more energy-intensive processes, providing an increase in the value of the activation energy, which is associated with the $\alpha \rightarrow \beta$ phase transition of titanium ($\sim 910^\circ\text{C}$). Some increase in Q values in comparison with the literature data can be due to the development of DRX during deformation [17].

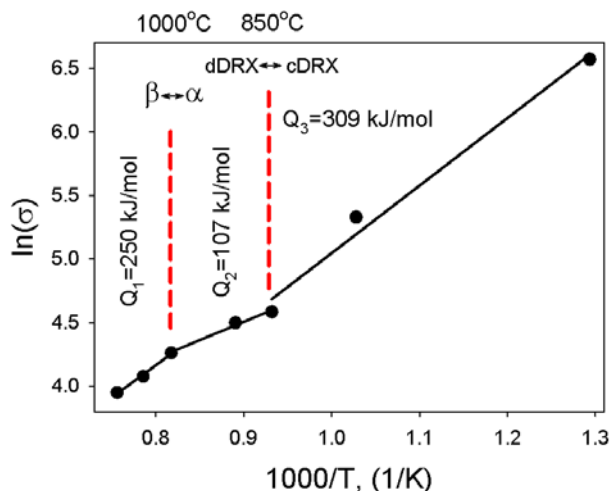


Fig. 7. Arrhenius plot of the logarithmic steady-state flow stress vs the inverse of temperature.

Processing map analysis. The mechanical behavior of metals during hot deformation is often studied to determine optimal temperature-rate parameters for hot working. Processing map analysis reveals areas where the deformation capacity of the material is maximal (for example, the regions of dynamic recrystallization or superplasticity), as well as regions with the unstable plastic flow (for example, the formation of localized shear bands) or with the formation of cracks [18]. For the purpose of such an analysis, a processing map with the strain rate sensitivity of flow stress m (for Ti/TiB $m=0.12$) was constructed based on the results of mechanical tests. The calculations were made using the following equations:

$$m = \frac{\Delta \log \sigma}{\Delta \log \dot{\epsilon}}, \quad (1)$$

where σ is the flow stress and $\dot{\epsilon}$ is the strain rate.

The efficiency of power dissipation (η) of a work piece can be estimated by comparing its power dissipation through microstructural changes with that occurring in an ideal linear dissipator ($m = 1$) [19]:

$$\eta = \frac{m/(m+1)}{1/2} = \frac{2m}{m+1}. \quad (2)$$

The power dissipation map represents the projection of a three-dimensional surface describing the variation of η with temperature and strain rate on the $T-\dot{\epsilon}$ plane.

Figure 8 shows a map for the true strain $\varphi=1.2$. The map presented a peak with a value of 0.36 in the temperature range of 850°C and low rates of deformation. According to the results of the microstructural analysis, this region corresponded to the development of dDRX (Fig. 5). This result is confirmed by the literature data [18]. The deformation temperature of 850°C is optimal: at lower temperatures extensive formation of cracks occurred (Fig. 3); while at higher deformation temperatures (especially in the β field) the formation of a coarse-grained structure is expected.

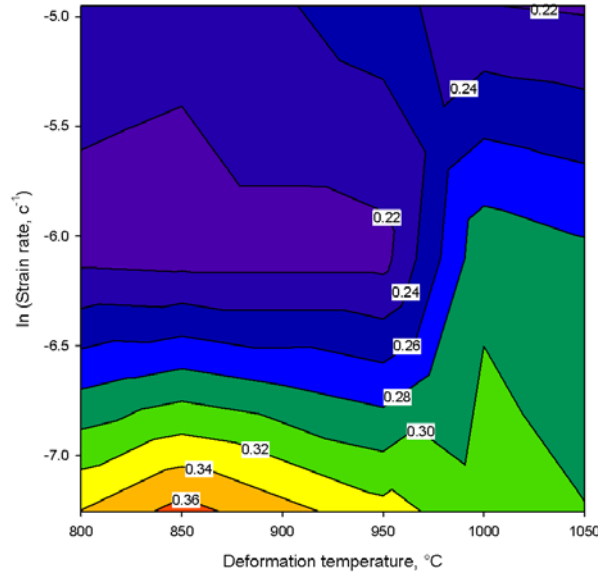


Fig. 8. Processing map of the Ti/TiB composite at a true strain $\phi=1.2$.

Hardening mechanisms. The introduction of the reinforcing TiB component into the ductile titanium matrix, as expected, should change the contribution of the hardening mechanisms during deformation to the resulting value of the composite strength. The contributions of the most relevant hardening mechanisms in hardness of the composite can be expressed as [20, 21]:

$$\sigma_{\Sigma} = \sigma_0 + \sigma_{\rho} + \sigma_{H-P} + \sigma_{L-T} + \sigma_{TiB(OR)}, \quad (3)$$

where σ_0 is the frictional stress including solid-hardening by C, O, N (300 MPa) atoms, σ_{ρ} is the substructure hardening, σ_{H-P} is Hall-Petch hardening, σ_{L-T} is the hardening of the load transfer strengthening effect, $\sigma_{TiB(OR)}$ - the precipitation hardening by the debris of the TiB whiskers (Orowan mechanism).

The substructure hardening can be expressed as [20]:

$$\sigma_{\rho} = M\alpha Gb\sqrt{\rho}, \quad (4)$$

where M is the average Taylor factor, α is the constant, G is the shear modulus, b is the Burgers vector, ρ is the dislocation density. For the calculation, the values of M equal to 3 and α equal to 0.5 were taken.

The Hall-Petch contribution to the strength is typically of the form [20]:

$$HV_{H-P} = K_y d^{-1/2}, \quad (5)$$

where K_y is the Hall-Petch coefficient and d is the grain size.

The hardening of the load transfer strengthening effect can be calculated using the formula [21]:

$$\sigma_{L-T} = \left[\left\{ V_{TiB} \left(\frac{S+2}{2} \right) + V_{Ti} \right\} - 1 \right], \quad (6)$$

where V_{TiB} and V_{Ti} - the value of the volume fraction of the phase TiB and titanium, S - the parameter of the aspect ratio of the TiB whiskers.

The precipitation hardening by the debris of the TiB whiskers can be expressed as [22]:

$$\sigma_{TiB(OR)} = \frac{Mgb}{2.36\pi} \ln\left(\frac{0.57DS^{\frac{1}{3}}}{b}\right) \frac{1}{(0.92V^{-\frac{1}{3}} - 1.14)DS^{\frac{1}{3}}}, \quad (7)$$

where D is the diameter of TiB whiskers, V is the volume fraction of TiB, and S is the aspect ratio of TiB whiskers.

Some input parameters for the titanium matrix were taken from [23]: $K_y=0.3 \text{ MPa}\cdot\text{m}^{1/2}$, $\sigma_0=320 \text{ MPa}$ and $b=2.9\times 10^{-10} \text{ m}$. The value of the shear stress $G=130 \text{ GPa}$ for the Ti/TiB composite was taken from [1].

The ultimate compression strength of the Ti/TiB composite after compression testing at room temperature is 2400 MPa. The theoretical strength calculated by summing the contribution of all the above hardening mechanisms showed a close value of 2200 MPa. The precipitation hardening by the debris of the TiB whiskers makes the most appreciable contribution - 1430 MPa (~ 65%), in [24] a close value was obtained. The hardening due to the load transfer strengthening effect was 220 MPa, the values of the substructure hardening and the Hall–Petch contribution were 140 and 110 MPa, respectively.

4. Conclusions

- 1) The initial microstructure of the Ti/TiB composite consisted of the TiB whiskers heterogeneously distributed within the Ti matrix. The average diameter of the TiB whiskers was $36 \pm 15 \text{ nm}$. The brittle-to-ductile transition temperature of the Ti/TiB composite was 500°C .
- 2) During the deformation in the temperature range of $500\text{--}1050^\circ\text{C}$ the length of the whiskers TiB decreased considerably while the diameter of the whiskers was weakly affected. Thus the aspect ratio of the TiB whiskers decreased from ~ 55 to ~ 10 and remains constant up to a deformation temperature of 1050°C . Growth in the diameter and length of the TiB whiskers was observed with an increase in the deformation temperature (above 900°C).
- 3) The microstructure evolution during the deformation and the apparent activation energy analysis revealed 3 stages: i) 700°C : the controlling mechanism of deformation - continuous dynamic recrystallization - $Q=309 \text{ kJ/mol}$; ii) $850\text{--}950^\circ\text{C}$: decrease in Q up to 107 kJ/mol , development of discontinuous dynamic recrystallization; (iii) $1000\text{--}1050^\circ\text{C}$: an increase in the activation energy up to 250 kJ/mol , which is due to the $\alpha \rightarrow \beta$ phase transition of titanium ($\sim 910^\circ\text{C}$). An analysis of the deformation map confirmed the development of discontinuous dynamic recrystallization at a deformation temperature of 850°C .
- 4) Calculations had revealed that the precipitation hardening by the debris of the TiB whiskers provided the biggest contribution to the hardening of the Ti/TiB composite $\sim 65\%$.

Acknowledgements. *The authors gratefully acknowledge the financial support from the Russian Science Foundation (Grant Number 15-19-00165). The authors are grateful to the personnel of the Joint Research Centre, Belgorod State University for their assistance with the instrumental analysis.*

References

- [1] K. Morsi, V.V. Patel // *J. Mater. Sci.* **42** (2007) 2037.
- [2] K.S. Ravi Chandran, K.B. Panda, S.S. Sahay // *JOM* **56** (2004) 42.
- [3] H. Feng, Y. Zhou, D. Jia, Q. Meng and J. Rao // *Crystal Growth & Design* **7** (2006) 1626.
- [4] M. Selva Kumar, P. Chandrasekar, P. Chandramohan, M. Mohanraj // *Mater. Charact.* **73** (2012) 43.
- [5] A.V. Ragulya, In: *Encyclopedia of Materials: Science and Technology*, ed. by K.H. Jürgen Buschow et al. (UK, Oxford, 2010), p.1.
- [6] M. Ozerov, N. Stepanov, A. Kolesnikov, V. Sokolovsky, S. Zherebtsov // *Materials Letters* **187** (2017) 28.
- [7] R.A. Gaisin, V.M. Imayev, R.M. Imayev and E.R. Gaisina // *Russian Physics Journal* **58** (2015) 848.
- [8] M. Ozerov, M. Klimova, A. Kolesnikov, N. Stepanov, S. Zherebtsov // *Materials and Design* **112** (2016) 17.

- [9] M.Y. Koo, J.S. Park, M.K. Park, K.T. Kim and S.H. Hong // *Scripta Materialia* **66** (2012) 487.
- [10] L.J. Huang, L. Geng, B. Wang, L.Z. Wu // *Mater. Design* **45** (2013) 532.
- [11] C.M. Sellars // *Phil. Trans. R. Soc. London A* **288** (1978) 147.
- [12] T. Sakai, J.J. Jonas // *Acta Metall.* **32** (1984) 189.
- [13] T. Sakai, A. Belyakov, R. Kaibyshev, H. Miura, J.J. Jonas // *Prog. Mater. Sci.* **60** (2014) 130.
- [14] G. Will, *Powder Diffraction: The Rietveld Method and the two-Stage Method to Determine and Refine Crystal Structures from Powder Diffraction* (Springer, G., 2006).
- [15] S. Zherebtsov, E. Kudryavtsev, S. Kostjuchenko, S. Malysheva, G. Salishchev // *Mater. Sci. Eng. A* **536** (2012) 190.
- [16] H. Conrad // *Prog. Mater. Sci.* **26** (1981) 123.
- [17] S.V. Raj, T.G. Langdon // *Acta Metall.* **37** (1989) 843.
- [18] K.P. Rao, Y.V.R.K. Prasad // *Comprehensive Materials Processing* **3** (2014) 327.
- [19] *Hot Working Guide: a Compendium of Processing Maps*, ed. by Y.V.R.K. Prasad, S. Sasidhara (ASM International, Materials Park, OH, 1997).
- [20] M.A. Meyers, A. Mishra, D.J. Benson // *Prog. in Mat. Sc.* **51** (2006) 427.
- [21] K.S. Munir, Y. Zheng, D. Zhang, J. Lin, Y. Li, C. Wen // *Mater. Sci. Eng. A* **696** (2017) 10.
- [22] B. Chen, J. Shen, X. Ye, L. Jia, S. Li, J. Umeda, M. Takahashi, K. Kondoh // *Acta Mater.* **140** (2017) 317.
- [23] H.J. Frost, M.F. Ashby, *Deformation-Mechanism Maps* (Pergamon Press, UK, 1982).
- [24] S. Zherebtsov, M. Ozerov, N. Stepanov, M. Klimova and Yu. Ivanisenko // *Metals* **7** (2017) 507.

SEVERE PLASTIC DEFORMATION INFLUENCE ON ENGINEERING PLASTICITY OF COPPER

A.I. Rudskoi, A.M. Zolotov, R.A. Parshikov*

Peter The Great Saint-Petersburg Polytechnic University, 195251, St.Petersburg, Polytechnicheskaya 29, Russia

*e-mail: plast-ftim@mail.ru

Abstract. In present paper experimental research results of extra-pure Copper mechanical properties after severe plastic deformation are presented. Equal channel angular pressing was used for processing. Engineering plasticity of ultrafine grain Copper during cold rolling was estimated.

Keywords: equal channel angular pressing; extra-pure Copper; mechanical properties; cold rolling.

1. Introduction

One of the crucial tasks of material science is developing of new materials as well as improving the ones already known that have high physical-and-mechanical properties. Solving of such problems is in the field of highly effective technology creation and is possible with use of modern and advanced technologies.

During recent years there were many researches aiming to improve strengthening characteristics of metals and alloys due to structure refinement up to submicrocrystalline level [1-2]. As it is known, combination of high strength at the current proper plasticity is necessary condition for developing of advanced materials of high quality. Use of new methods of physical-and-mechanical strengthening and plastic deformation allows improving the level of mechanical and working properties of materials that have different functional area. Similar works with alloys on basis of Aluminum [3], Titanium [4], Copper [5] etc.

Structure size reduction is performed by methods basing on severe plastic deformation. In particular, one of them is equal channel angular pressing (ECAP) with its advantage of possibility to obtain bulk billets. This allows researching not only of the structure forming during treatment but also mechanical properties of materials.

2. Experimental research

In present paper samples of Copper alloys: HCP (99,95% Cu) and OFE (99,99% Cu) were used as test materials.

HCP Copper is alloyed with small amount (0,002-0,007%) of phosphorous. This small quantity of phosphorous will not reduce significantly the electrical and thermal conductivity of the alloy but help to obtain homogenous grain size in the product. This copper may be heat treated, welded and brazed without need for special precautions to avoid hydrogen embrittlement. Oxygen Free Electronic Copper (10 mg/dm³) as well as HCP Copper do not need special conditions during heat treatment, welding and brazing.

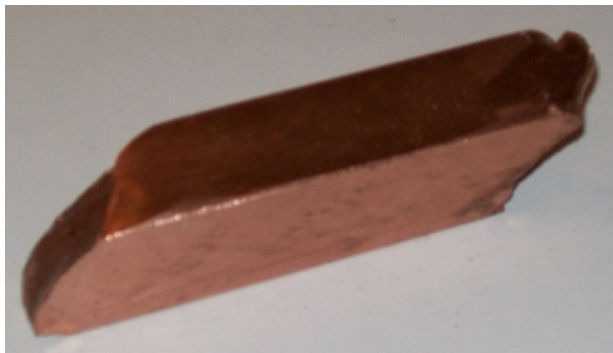
This copper of high purity is used in microelectronics, radio- and instrument making (thin-film technologies and cables in audio-systems, jewelry and building industry (pipes and wires for working in strong electromagnetic fields, electrochemistry anodes etc).

Samples of square cross-section 20x20x120 mm were processed by ECAP with help of special instrument presented on Fig. 1. The die has two channels of 20mm width with intersection angle of 105° [6]. Samples were deformed by the scheme relating to route B_c. Total deformation after treatment was $\epsilon \sim 6,3$ (number of passes $n=9$).



Fig. 1. Experimental equipment for ECAP.

In total more than 40 copper billets with sizes 20x20x110mm were deformed. After each pass four samples were selected: three for mechanical properties investigation of the billet material and one for structure research. Fig. 2a shows photo of the sample of copper alloy after sequential ECAP pass.



a)



b)

Fig. 2. Appearance of copper billet after sequential ECAP pass (a) and samples for tensile testing (b).

Mechanical characteristics were estimated on Zwick/Roell Z100 tensile testing machine. Fig. 2b shows samples for tensile testing. Due to deformation process features specimens used in the present work were short and cylindrical.

As an example, mechanical characteristics test results of one of the materials (OFE copper) are presented in table 1 and on Fig. 3. The behavior of the second material is similar therefore HCP copper data is not performed.

Table 1. Mechanical characteristics of OFE copper after ECAP.

Pass number, n	Yield stress $\sigma_{0.2}$, MPa	Tensile strength σ_b , MPa	Vickers microhardness	Percent elongation δ , %	Contraction Ψ , %
0	98.4	299.4	54.4	47.4	96.3
1	321.7	349.9	93.1	17.4	50.9
2	379.3	390.4	101.6	14.1	45.7
3	398.2	413.8	106.8	12.9	44.4
4	399.5	415.4	108.3	12.9	44.4
5	405	418,3	107.2	12.8	45.1
6	408	419.1	111	12.8	44.6
7	410	420.2	111.5	12.7	43.4
8	409	419.9	107.6	12.6	42.8
9	410	420.4	108.6	12.6	41.7

The analysis of the table data shows that significant changes of both strength and plasticity characteristics of the material are observed after first four passes. To make the picture perception easier the flow curves of OFE copper are presented only after these passes.

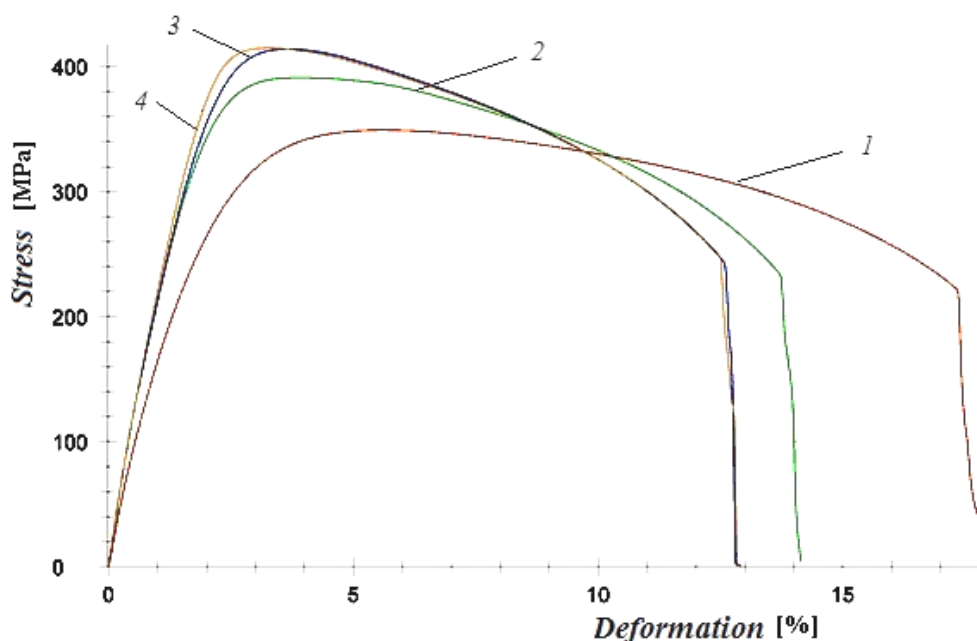


Fig. 3. Flow curves of OFE copper during tensile test for 1-4 passes correspondingly.

Figure 4 shows microstructure of OFE copper samples in the initial state (a) and after the 9th pass (b) obtained by the optical microscope Zeiss and the raster electron microscope Supra 55VP accordingly.

The initial structure of copper samples is characterized by the grain size of 47 μm . After severe plastic deformation the ultrafine grain copper with the average size of structure elements of 330 nm (cross direction) was received.

The material was exposed to cold deformation in order to study its engineering plasticity. Rolling process by the smooth rolls was carried out the following way. For width $h=2$ mm the draught was 0,5mm for the pass. Further the sample was deformed with

$\Delta h=0,2$ mm for each pass until the final width of $h=2$ mm. No half-way heat treating operations during rolling process were required.

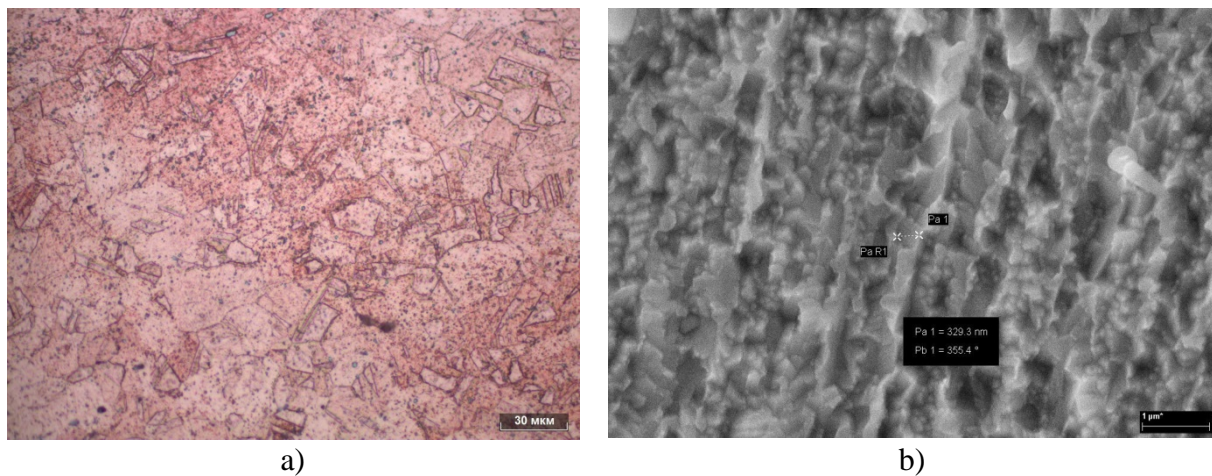


Fig. 4. Photos of OFE copper samples. Initial microstructure (a) and after nine ECAP passes (b).

Figure 5 shows a photo of ultrafine grain copper sample before and after cold rolling. It can be seen that cold deformation of ultrafine grain copper sample goes on without any difficulties. And, in spite of not high plasticity values shown during standard tensile tests, in case of stress condition scheme change there is also a significant change in material behavior.

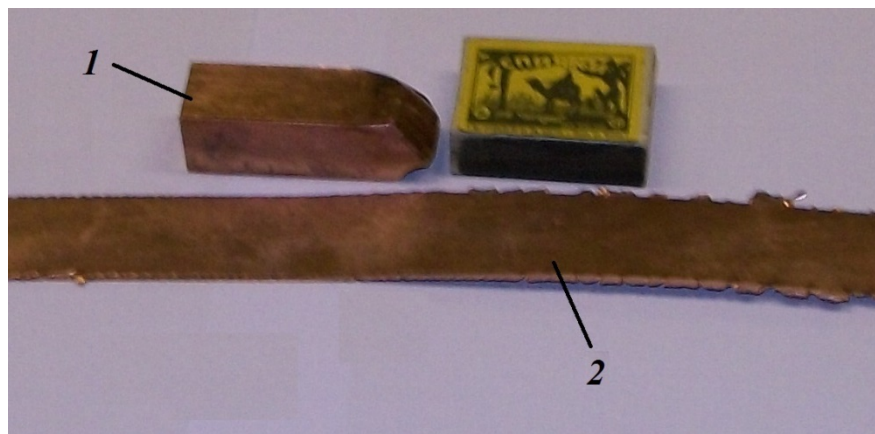


Fig. 5. Copper sample after ECAP, $n=9$ before (1) and after (2) cold rolling.

Along the edges of deformed stripe there are transverse cracks, though they are located in overflows and their sizes are not big. The occurring of similar defects is explained by specific features of the deformation zone.

3. Conclusions

Thus the researched material after ECAP along with strength increase and expected plasticity decrease at uniaxial tension shows high level of engineering plasticity. This quality will allow using it in the next forming operations and reduce accompanying labour costs.

Reference

- [1] R.Z. Valiev, *Bulk nanostructured materials: fundamentals and applications*, ed. by Ruslan Z. Valiev, Alexander P. Zhilyaev, Terence G. Langdon (Wiley-TMS, 2013), p. 456.

- [2] F.Z. Utyashev, G.I. Raab, *Deformation methods for receipt and treatment of ultrafine grain and nanostructured materials*, In: Bashkirskaya entsiklopediya (Ufa, Gilem, 2013), p. 376.
- [3] M.Yu. Gryaznov // *Vestnik of Lobachevsky university of Nizhni Novgorod* **6(1)** (2011) 49.
- [4] V.V. Stolyarov // *Vestnik nauchno-technicheskogo razvitiya* **4(68)** (2013) 29.
- [5] S.N. Lezhnev // *Processing of solid and laminate materials* **2(43)** (2015) 5.
- [6] R.A. Parshikov, O.V. Tolochko, A.M. Zolotov, A.I. Rudskoy // *Rev. Adv. Mater. Sci.* **34** (2013) 26.

ON ANISOTROPY OF MECHANICAL PROPERTIES OF ALUMINUM ALLOYS UNDER HIGH TEMPERATURE DEFORMATION

G.E. Kodzhaspirov¹, D.A. Kitaeva^{1*}, Sh.T. Pazylov², Ya.I. Rudaev²

¹Peter the Great St.Petersburg Polytechnic University, Polytechnicheskaya st. 29, 195251, St.Petersburg, Russia

²Kyrgyz-Russian Slavic University, Kiev st. 44, 720000, Bishkek, Kyrgyz Republic

*e-mail: dkitaeva@mail.ru

Abstract. The anisotropy factor assessment under various parameters of thermomechanical loading is estimated by the example of experimental studying deformation and structural parameters of anisotropic Al alloy 1561. It is found that the smallest value of the anisotropy factor corresponds to the formation of equiaxed fine-grained structure formed in the temperature-rate conditions of superplasticity.

Keywords: anisotropy factor; dynamic superplasticity; aluminum alloys; phase transformations.

1. Introduction

The anisotropy of mechanical properties is inherent to the majority of structural materials. It is known [1] that anisotropy assessment based on the ratio of cross- and longitudinal specimens properties of sheets is insufficient. However, as experimental creation of spatial charts of deformation is labor-consuming, the attempt to find theoretical calculation methods with the limited number of experimental data is seems to be reasonable.

The effect of technological and structural factors on the anisotropy of mechanical properties of metals is discussed in [2]. Accounting and targeted using of anisotropy promotes the effective utilization of structural metals. It is quite justified to consider the desire in different ways to reduce anisotropy, including thermomechanical and other processing methods. The last ones include methods based on the possibility of implementing superplasticity of the dynamic type [3, 4].

In experimental and theoretical studies related to the problem associated with superplasticity, it should be noted the interdependence of mechanical behavior and the current structural state of the material. Superplasticity will be defined [3] as a special state of polycrystalline material which is plastically deformed at low stress with preservation of the fine-grained structure (structural plasticity) obtained at the preliminary stage or formed during heating and deformation (dynamic superplasticity).

It should be noted that for both types of superplasticity, the prevalence of the mechanism of grain boundary slipping over other forms of mass transfer is supposed to be considered common [5]. Therefore, to realize the superplasticity of dynamic type, the initial structural state of the material must be replaced with another one ready for superplasticity. Such changes are due to coherent superposition of the strain rate and structural (phase) transitions of the evolutionary type in open nonequilibrium systems [6, 7]. The nature of these transformations, of course, depends on the characteristics of the boundary structural states.

2. The peculiarities of temperature-rate deformation of aluminum alloys

We will focus on the results of an experimental study of high-temperature deformation regularities in the wide strain rate ranges, including thermomechanical regimes of superplasticity of industrial aluminum alloys.

The state of deformed alloys is studied taking into account changes in temperatures and strain rates in the form of

$$\sigma = \sigma(\dot{\varepsilon}, \bar{\varepsilon}, \theta), \quad (1)$$

where σ – true stress; θ – temperature; $\bar{\varepsilon}$ – strain; $\dot{\varepsilon}$ – a strain rate.

The experimental procedure, recording and measuring equipment, the results of experiments and the method of statistical processing of experimental data are described in [3]. Testing of tensile experiments it were limited by the deformation of “Gagarin-type” specimens.

In Fig. 1 presented the dependence of the dimensionless flow stress σ/σ_0 versus the dimensionless strain rate $\dot{\varepsilon}/\dot{\varepsilon}_0$ for the deformed AMg5 and D18T alloys at a constant of strain degree $\bar{\varepsilon} = \ln(1 + \varepsilon) = 0.427$ ($\sigma_0 = 10$ MPa; $\dot{\varepsilon}_0 = 1$ s⁻¹; ε – relative strain at the tensile).

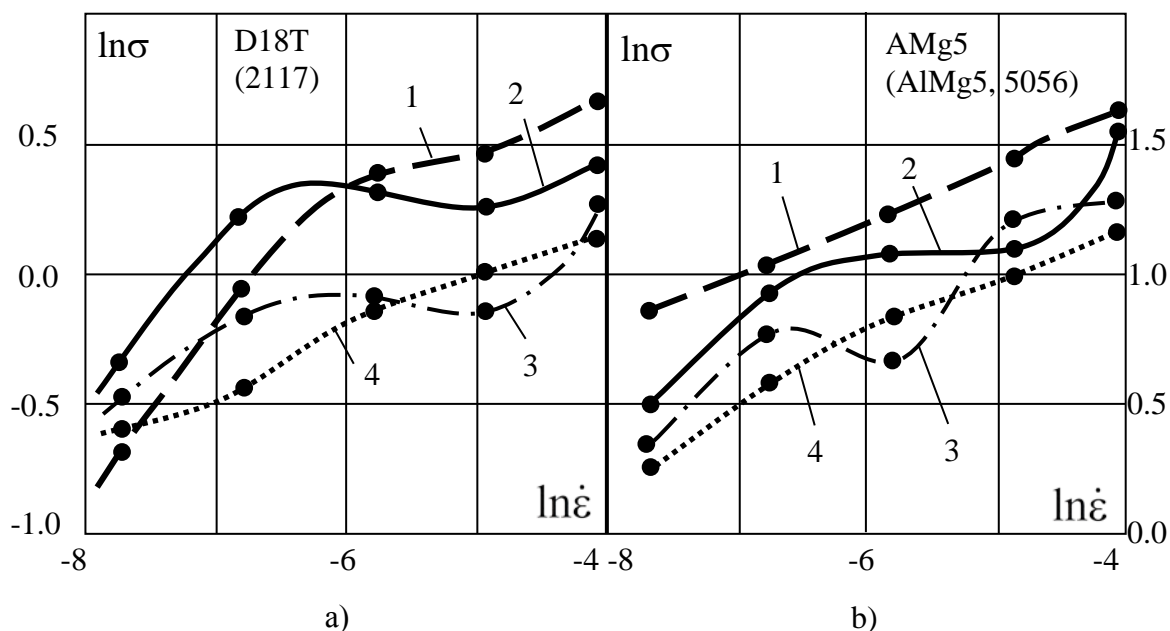


Fig. 1. Stress versus strain rate for $\bar{\varepsilon} = 0.427$ and various temperatures:

a – D18T (2117) alloy (1 – $\theta = 793$ K; 2 – $\theta = 813$ K; 3 – $\theta = 833$ K; 4 – $\theta = 853$ K);

b – AMg5 (AlMg5, 5056) alloy (1 – $\theta = 713$ K; 2 – $\theta = 733$ K; 3 – $\theta = 773$ K;

4 – $\theta = 753$ K).

For aluminum alloys it can sets off the class of isotherms, where the ambiguous dependence stress-strain rate takes place (Fig. 1). The falling branches of the obtained dependences correspond to the manifestation of superplastic properties [3]. The obtained experimental data allow to determine the interval of superplasticity temperatures for alloy AMg5 $\theta = 743...773$ K, for D18T $\theta = 783...823$ K [3]. The characteristic features of superplasticity are observed in the mentioned above ranges: low stress level, high strain capacity (up to 250%) under tensile. It is known that in aluminum alloys during heating and deformation there is only one type of structural transformation – dynamic recrystallization,

first revealed in compression experiments [8], and then tensile [9,10]. The structural changes occurring during dynamic recrystallization consist in the appearance of an equiaxial microstructure with very small grains in transient regimes, the sizes of which (1...10 microns) are approximately equal to the sizes of sub-grains. The effects on grain boundaries described in [11] and the formation of fine-grained structure make it possible to predict the appearance of a structure that contributes to the manifestation of superplasticity. In this case, sliding between grains is observed [5]. This mechanism is not determined by the initial structural state (cast or deformed), but it is partly due to the proper stress-strain state scheme. For example, in 1561 cast aluminum alloy [12], superplastic properties are manifested only under compression conditions because fracture of the specimen at the tensile test occurs before dynamic recrystallization. Consequently, the transition of aluminum alloys to the superplastic state depend not only the chemical composition and the thermomechanical history of the process, but also on the conditions of formation of the initial structure [5].

3. Experimental results and discussion

We will consider the results of the deformed alloy 1561 sheet samples study with thickness of 10^{-2} m produced by multi-stage longitudinal rolling according to the conventional technology [13]. The circular section samples for tensile test were cut in longitudinal direction. The chemical composition of the alloy was the following: 5.88%Mg; 1.03%Mn; 0,16%Zr; 0,12%Si; 0,08% Fe; 92,73%. Al. The tensile tests were carried out at $\theta = 533...773$ K and speed: $V_3 = 0.36 \cdot 10^{-3}$ m/s; $V_4 = 0.15 \cdot 10^{-3}$ m/s; $V_5 = 0.056 \cdot 10^{-3}$ m/s; $V_6 = 0.023 \cdot 10^{-3}$ m/s; $V_7 = 0.008 \cdot 10^{-3}$ m/s.

The tests of 1561 alloy [3] at high strain rates (to 240%) revealed no signs of strain-rate softening (Fig. 1). It is supposed that this is due to the formation at the initial stage of a with an elongated grain oriented in the rolling direction. The peculiarities of the initial structure caused the manifestation of plastic deformation anisotropy in mutually perpendicular transverse directions of the tensile specimen, causing a loss of stability of the cross-section shape. To evaluate the plastic deformation anisotropy it was proposed an anisotropy coefficient [14-17] or its analogue – the coefficient of normal plastic anisotropy [18], which is the ratio of deformations measured by small (ε'') and large (ε') axes of an ellipse cross-section:

$$\psi = \varepsilon'' / \varepsilon', \quad \psi \geq 1. \quad (2)$$

Figure 2 presents the experimental dependence $\psi \sim \varepsilon'$ at the temperature 693 K at the various speeds of movement of the grips V_n of the testing machine (n is the speed at the transmission). It can be seen from the graphs that the ψ decreases with increasing strain ε' . In this case, it is possible to note the tendency to approach curves $\psi \sim \varepsilon'$ with increasing strain, and the minimum values ψ correspond to low strain rates.

In Fig. 3 the data of the effect of the strain rate on the value of the parameter in the form of isotherms at strain degrees 0.083 (Fig. 3a) and 0.4166 (Fig. 3b) are presented. From the presented graphic dependences we will pay attention to the temperature range 743...783 K, in which the effect of superplasticity of the alloy 1561 is realized [3]. Isotherms 4 and 5 correspond to the specified range. Note that curve 4 on Fig. 3a and curve 5 on Fig. 3b is close to horizontal at all strain rates [14-17]. Of particular interest are the experimental dependences of the anisotropy coefficient on temperature at different values of strain rate and strain (Fig. 4). The analysis of the experimental data (Fig. 2-Fig. 4) shows that the coefficient of anisotropy depends significantly on the thermo-mechanical process conditions. Thus, in the vicinity of temperature at all values of the deformation speed there is a local increase in the coefficient (Fig. 4). As this takes place the decrease in the maximum values corresponds to an

increase in the strain speed. Note that as the strain degree increases, the influence of strain speed on the anisotropy coefficient (Fig. 4) is decreases. The established in [3] effect is observed at temperatures preceding the values corresponding to the metastable state.

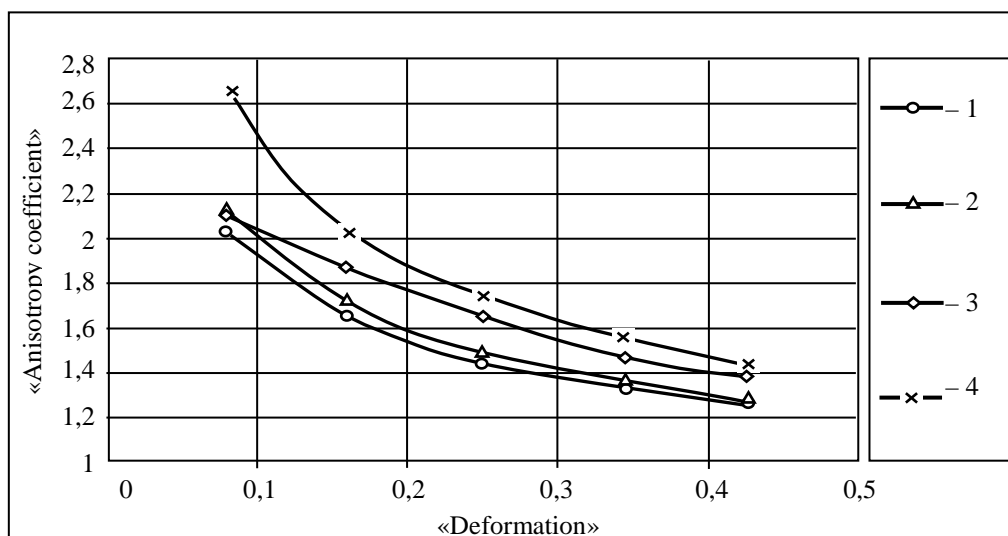


Fig. 2. Anisotropy coefficient ψ versus deformation ε' for temperature 693 K and strain rates: 1 – $V_3 = 0.36 \cdot 10^{-3}$ m/s; 2 – $V_4 = 0.15 \cdot 10^{-3}$ m/s; 3 – $V_5 = 0.056 \cdot 10^{-3}$ m/s; 4 – $V_6 = 0.023 \cdot 10^{-3}$ m/s.

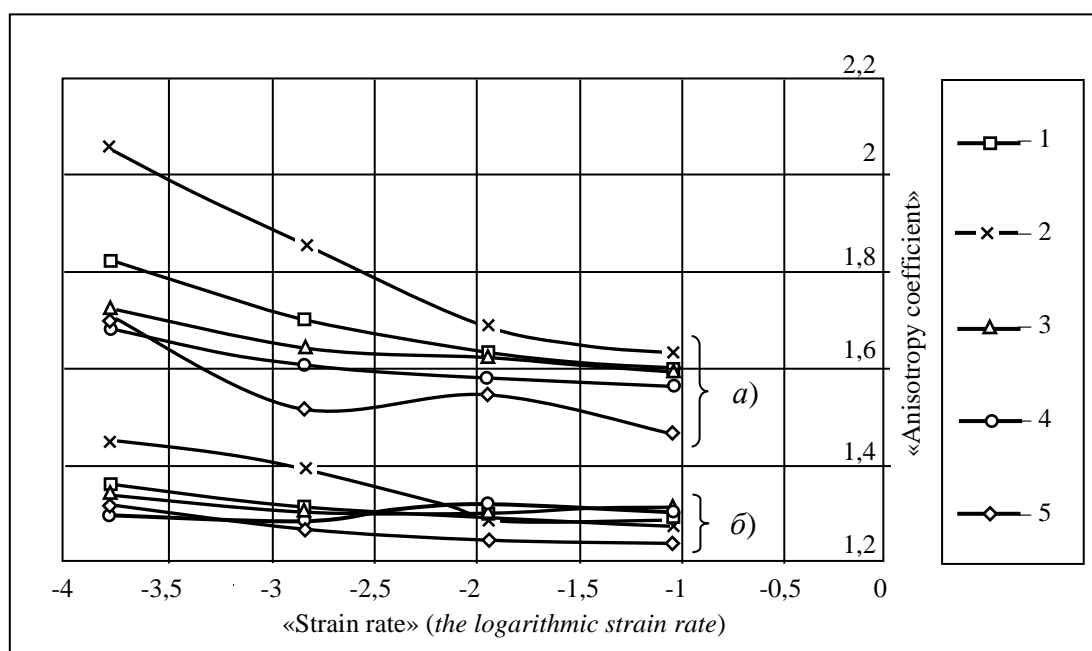


Fig. 3. Anisotropy factor ψ versus strain rate ($\psi \sim \ln V$) for deformation: a) $\varepsilon' = 0.083$ и b) $\varepsilon' = 0.4166$.

Curves 1...5 correspond temperatures: 1 – 653 K; 2 – 693 K; 3 – 733 K; 4 – 753 K; 5 – 773 K.

At high temperatures ($\theta > 723$ K) it is possible to allocate an interval 753...773 K in which superplasticity is realized. In this range the anisotropy is minimal, their importance in various strain rates are close, and at high strain degrees (Fig. 4) almost identical. This

suggests that minimal values of the anisotropy coefficient ψ in the superplasticity regimes are taken place.

A similar result was obtained in [5], with the reduction of the coefficient due to superplastic deformation.

In [19, 20] it was found the correspondence between the results of mechanical experiments and the results of structural state study of the alloy 1561. It should be reminded that the experiments were carried out on samples made of 10^{-2} m thick sheet produced by multistage longitudinal rolling at the above values of temperature, speed and strain degree, including the values corresponding to the initial non-deformed state.

As was mentioned in [5], the formation of fine-grained structure is a prerequisite for the implementation of the slipping mechanism along grain boundaries, typical for superplasticity effect. The formation of fine-grained equiaxial structure during superplastic deformation of alloy 1561 contributed to practically isotropic deformation in mutually perpendicular directions in cross-sections of samples (anisotropy coefficient $\psi \approx 1.25$).

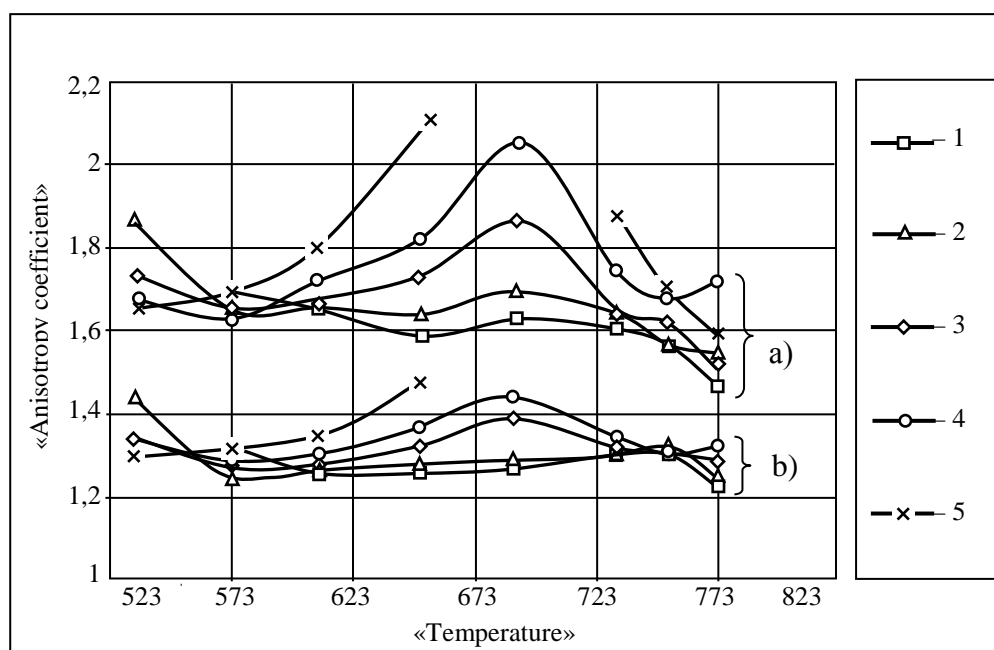


Fig. 4. Anisotropy coefficient ψ versus temperature ($\psi \sim \theta$) for deformation:

- a) $\varepsilon' = 0.083$ и b) $\varepsilon' = 0.4166$; and strain rates: 1 – $V_3 = 0.36 \cdot 10^{-3}$ m/s;
 2 – $V_4 = 0.143 \cdot 10^{-3}$ m/s; 3 – $V_5 = 0.057 \cdot 10^{-3}$ m/s; 4 – $V_6 = 0.023 \cdot 10^{-3}$ m/s;
 5 – $V_7 = 0.009 \cdot 10^{-3}$ m/s.

In [4, 13] an attempt was made to optimize the temperature-strain rate at rolling parameters of hot-rolled sheets of initially cast aluminum alloy 1561 based on the experiment data on superplasticity in axial compression [12]. The necessity of possible approximation of strain rate to the ones corresponding to the real rolling process was taken into account.

It was supposed that the optimal combination of power and kinematic parameters should arise the formation of the most favorable structure in the metal produced, approaching the structure of fine-grained, and as a result-to the most rational combination of strength and deformation characteristics, and, consequently, to a minimum anisotropy of mechanical properties. As a result of rolling in conditions of superplasticity the data confirming formation of structure close to fine-grained (7-12 microns) has been received. This is also evidenced by

the data of mechanical tests of “Gagarin’s” samples cut from the sheet in the longitudinal and transverse directions given in Table 1 [16].

Table 1. The average values of mechanical characteristics of alloy 1561 produced by rolling in the superplasticity regimes.

Direction	YS, MPa	TS, MPa	A, %
Longitudinal	164	350	21,6
Transverse	168	330	15,3

Note: YS – yield strength; TS – tensile strength; A – the maximum elongation

The data obtained result in the rolling of cast alloy 1561 are indirectly confirmed by the data of analytical solution of two-dimensional isothermal boundary (including the regimes of superplasticity) of the sheet rolling task at a small angle of tip with the assessment of the effect of high homological temperatures on the roll force [21-23]. The power and kinematic parameters of the process were established using the dynamic model [3, 7], which adequately reflects the experimental data obtained on the industrial aluminum alloys (Fig. 1). The founded solution allows to select and mathematically limit the area of superplasticity in the zone of deformation. Thus, it is possible to control the grain size in the process of heating and deformation and predict the production of parts and semi-finished products with a high-quality structure close to fine-grained. Naturally, the formation in temperature-strain rate conditions of superplasticity condition meet the minimum values of rolling force.

6. Conclusions

It is found that the anisotropy coefficient depends on the alloy structure. Deformation under conditions of superplasticity is one of the thermo-mechanical ways to reduce structural and deformation anisotropy of material. The anisotropy coefficient can be considered as one of the macroparameters of the material that characterizes the ongoing structural transformations and allows to estimate the degree and completeness of structural changes relative to the initial state in the changing field of temperatures and strain rates.

Thus, the study of the effect of thermo-mechanical conditions of deformation on the behavior of the anisotropy coefficient and the change in the structure of the alloy allows, for example, to select the proper rolling regimes apply to the sheets subjected to pneumatic and gas forming.

Acknowledgements. *The research was carried out within the state assignment 11.12832.2018/8.9.*

References

- [1] P.G. Miklyaev, Ya.B. Fridman, *Anisotropy of mechanical properties of metals* (Metallurgiya, Moscow, 1986).
- [2] R.A. Adamesku, P.V. Geld, E.A. Mityushov, *Anisotropy of physical properties of metals* (Metallurgiya, Moscow, 1986).
- [3] A.I. Rudskoy, Ya.I. Rudaev, *Mechanics of dynamic superplasticity of aluminum alloys* (Nauka, St.Petersburg, 2009).
- [4] V.I. Kuneev, Sh.T. Pazylov, Ya.I. Rudaev, D.I. Chashnikov // *Journal of Machinery Manufacture and Reliability* **6** (2002) 55.
- [5] O.A. Kaibyshev, *Superplasticity of commercial alloys* (Metallurgiya, Moscow, 1984).
- [6] A.I. Olemskoy, A.A. Katcnelson, *Synergetics of condensed media* (KomKniga (URRS), Moscow, 2003).

- [7] D.A. Kitaeva, Ya.I. Rudaev // *St.Petersburg State Polytechnical University Journal* **4–1(183)** (2013) 274.
- [8] Yu.M. Vainblat, N.A. Sharshagin // *Non-ferrous metals* **2** (1984) 67.
- [9] Sh.T. Pazylov, V.A. Panyaev, In: *Strength of materials and constructions* (Frunze Polytechnical Institut, Frunze, 1987), p.87.
- [10] Yu.S. Zolotorevskii, V.A. Panyaev, Ya.I. Rudaev et al. // *Ship-building industry. Series materials science* **16** (1990) 21.
- [11] O.A. Kaibyshev, R.Z. Valiev, *Grain Boundaries and Properties of Metals* (Metallurgiya, Moscow, 1987).
- [12] N.V. Zhdanov, V.A. Panyaev, Ya.I. Rudaev, D.I. Chashnikov // *Ship-building industry. Series materials science* **15** (1990) 45.
- [13] N.H. Barakhtina, Yu.S. Zolotorevskii, Ya.I. Rudaev et al. // *The Problems of Materials Science* **19/20** (1992) 72.
- [14] Sh.T. Pazylov, N.A. Omorov, Ya.I. Rudaev // *Tambov University Reports. Series Natural and Technical Sciences* **15(3)** (2010) 974.
- [15] Sh.T. Pazylov, N.A. Omorov, A.K. Arzimatov // *Vestnik Kyrgyz-Russian Slavic University* **10** (2010) 144.
- [16] D.A. Kitaeva, Sh.T. Pazylov, Ya.I. Rudaev // *Journal of Applied Mechanics and Technical Physics* **57(2)** (2016) 352.
- [17] D.A. Kitaeva, Ya.I. Rudaev, Sh.T. Pazylov, G.E. Kodzhaspirov, In: *Proceedings of the 14th International Conference on Creep and Fracture of Engineering Materials and Structures (Creep2017)* (Publishing House of Polytechnical University, St.Petersburg, 2017), p.74.
- [18] R.A. Adamesku, E.A. Mityushov, L.L. Mityushova, M.V. Frolova // *Metally* **1** (1990) 173.
- [19] Sh.T. Pazylov // *Vestnik Kyrgyz-Russian Slavic University* **5** (2015) 116.
- [20] D. Kitaeva, G. Kodzhaspirov, Y. Rudaev, In: *Proceedings of the 25th Anniversary International Conference on Metallurgy and Materials (METAL 2016)* (Tanger, Brno, 2016), p.1426.
- [21] G.E. Kodzhaspirov, D.A. Kitaeva, Ya.I. Rudaev, E.A. Subbotina // *Materials Physics and Mechanics* **25(1)** (2016) 49.
- [22] E. Sorochan, V. Artiukh, B. Melnikov, T. Raimberdiyev // *MATEC Web of Conferences* **73** (2016) 04009.
- [23] A. Hirkovskis, D. Serdjuks, V. Goremikins, L. Pakrastins, N.I. Vatin // *Magazine of Civil Engineering* **57(5)** (2015) 86.

ON THE DEVELOPMENT OF THE NEW TECHNOLOGY OF SEVERE PLASTIC DEFORMATION IN METAL FORMING

A.I. Rudskoi¹, A.A. Bogatov², D.Sh. Nukhov^{2*}, A.O. Tolkushkin²

¹Peter the Great St. Petersburg state Polytechnic University, Russia, Saint Petersburg

²Ural Federal University named after the first President of Russia B.N. Yeltsin, Russia, Ekaterinburg

*e-mail: d.s.nukhov@urfu.ru

Abstract. The information about the effect of the plastic deformation mechanism on the formation of the sub-microcrystalline structure of steels is reported. It is shown that the development of the new technological schemes for metal forming with severe alternating deformation is promising. A rolling method by two passes, which provides severe alternating deformation with minor changes of the billet dimensions is proposed. The results of computer simulation showed that with the use of new rolling method the uniformity of deformation along the height and the value of the deformation degree in the plane of symmetry of the billet are increased.

Keywords: severe plastic deformation; alternating deformation; forging; rolling; structure.

1. Introduction

According to the experts in many countries of the world, development and research of the new severe plastic deformation (SPD) methods is still an attractive and urgent task. The interest to the problem caused by the fact that due to severe, and in some cases severe and alternating deformation it is possible to obtain metals with ultrafine-grained (UFG) and nanocrystalline (NC) structure, with a high level of mechanical and functional properties [1-5].

2. The influence of deformation mechanism on the formation of the submicrocrystalline structure in steels and alloys

The founder of the SPD method is P.W. Bridgman. In the work [1] the apparatus, which implements severe alternating deformation in the volume of the billet was presented (Fig. 1). Two disc shaped billets are placed in between dies and anvil, then they are compressed under the pressure of hydraulic press with the load force P . The shearing strain was applied manually by alternating rotation of the anvil by the angle $\alpha=35-60^\circ$ with the necessary number of stages n .

The alternating strain amplitude determined by $\varepsilon_{ii} = (1/\sqrt{3}) \cdot \alpha \cdot r/h$, and the accumulated strain – $\varepsilon_u = \sum_{i=1}^n \varepsilon_{ii}$, where the value of the radius r changes from zero to $d/2$ on the edge. The aim of the research was to gather information on the grain structure evolution for steels and alloys in dependence of the amplitude ε_{ii} , the number of alternating plastic

deformation stages n and the stress state value $\frac{\sigma}{T} = \frac{4\sqrt{3}P}{\pi d^2 \sigma_s}$.

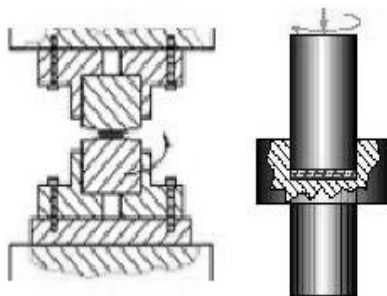


Fig. 1. Scheme of the SPD method on the Bridgman anvil.

The advantage of the SPD method on the Bridgman anvil is the possibility of establishing the dependence of the structure and properties of the metal on the characteristics

of the stress state: $\frac{\sigma}{\sigma_s}$ relative mean normal stress, where $\sigma = \frac{1}{3}\sigma_i$, $\sigma_s = \left(\frac{\sqrt{3}}{2}s_{ij}s_{ij}\right)^{1/2}$,

$s_{ij} = \sigma_{ij} - \sigma\delta_{ij}$ – components of the stress deviator; $\mu_\sigma = 2\frac{\sigma_2 - \sigma_3}{\sigma_1 - \sigma_3} - 1$ – Lode index.

A feature of this method is insignificant shape change of the billet, since the shape of the finished product is close to the shape of the billet, but the structure and properties of metal change drastically.

In the Belarusian Academy of Sciences and later at the Ufa academic center was designed and developed method of equal channel angular pressing (ECAP) [3, 4]. The results of fundamental research of the process are as follows: during the process of ECAP, the billet passing through the matrix channel undergo shear deformation without changing its cross-section dimensions. Based on this principle, it can be concluded, that the deformation applied to the billet in a single pass, mainly depends on the angle φ between the matrix channels. Since the passage of the billet through the ECAP matrix channel does not affect the cross-sectional dimensions, high deformation degree can be achieved by multiple pressing of the billet. The disadvantages of ECAP are the limited cross-sectional dimensions and the length of the billet, as well as the difficulty during pressing high-strength and low-plastic materials.

In the work [6], the authors showed that one of the traditional methods of severe alternating deformation, providing the fine-grained structure is helical rolling of the billet (Fig. 2).

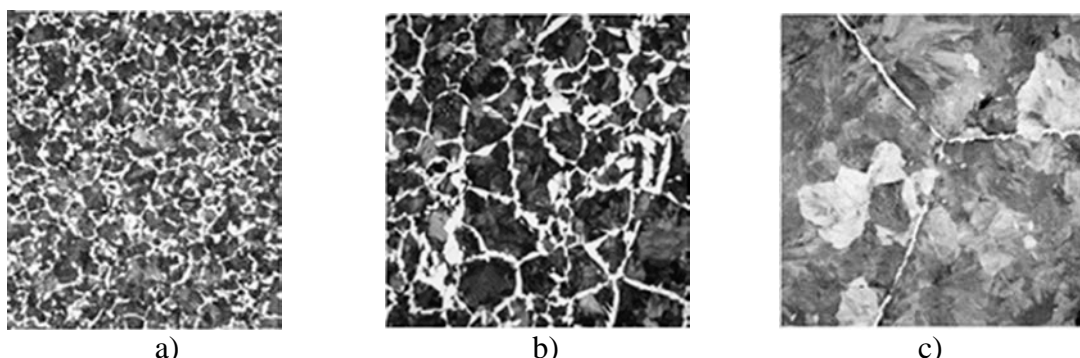


Fig. 2. Microstructure of 32HG steel for continuous cast and rolled billets (resolution 100 μm):

- a – rolled billet after the reduction by the helical rolling method with the elongation ratio $\lambda = 1,56$;
- b – billet after the longitudinal rolling with the elongation ratio $\lambda = 5,94$;
- c – initial continuous casting billet.

The rolling of the continuous casting billet (Fig. 2c) from a diameter of 150 mm to 120 mm on a three-roll mill is characterized by a high deformation degree (on the surface $\varepsilon_u = 4,73$, in the axial zone $\varepsilon_u = 0,51$) with a relatively small reduction (elongation ratio $\lambda = 1,56$). Due to the severe alternating deformation, a fine-grained structure is formed (Fig. 2a). A rolled billet with the diameter 120 mm, obtained by longitudinal rolling on the mill «650» with the elongation ratio $\lambda = 5,94$, has a size of austenitic grain 5-6 times larger (Fig. 2b) than during helical rolling.

3. Development of the forging and the longitudinal rolling methods of billets under severe alternating deformation conditions

Forging in special dies allows processing long billets under the severe alternating deformation conditions. Ingot 1 upsetted in two stages, first in the section-shaped dies 2, then in the flat dies 3. In the section-shaped dies 2 bulges and recesses on the billet are formed. In the flat dies 3 the billet is smoothed and takes former sizes (Fig. 3).

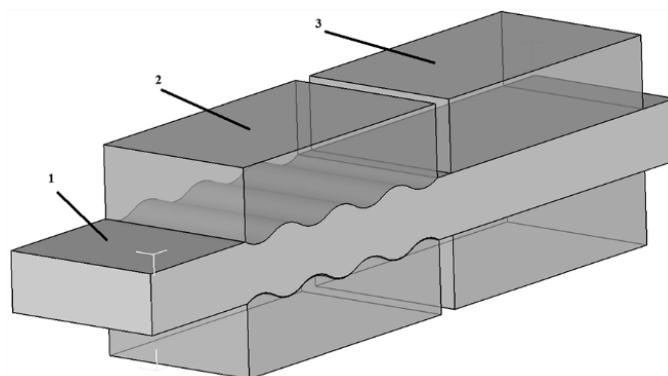


Fig. 3. The design of dual SPD press.

On the section-shaped dies cylindrical form bulges displace metal particles into recesses on the dies. In the flat dies metal particles are displaced from the billet bulges into recesses. Fig. 4 shows vector velocity fields during billet upsetting in section-shaped (Fig. 4a) and flat (Fig. 4b) dies, which indicate the alternating nature of the metal flow. Thus, the severe alternating deformation is implemented. Calculation of the die impression and the upsetting value $\Delta h/h_0$ is carried out from the condition of uniform deformation distribution along the cross section of the billet with taking into account die impression filling on the first stage and smoothing the billet surface on the second stage in such way, that height has reached its initial value.

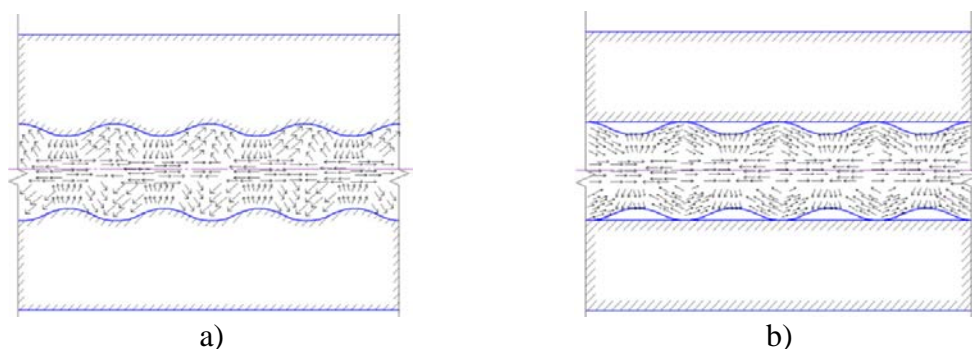


Fig. 4. The vector field of the metal particles velocities during reduction by section-shaped (a) and smooth dies (b).

A similar severe alternating deformation method is proposed to implement during rolling of thick slabs in the double SPD stand (Fig. 5) [7]. Rolling occurs without the billet widening due to the presence of non-driven edging rolls. The surface shape of rolls in the first stand made in the form of alternating annular blockers and collars with the same radius. The rolls are setup in such way, that the gap between collars apexes equals to the value $a=h-\Delta h$, and between blockers apexes to the value $b=h+\Delta h$, where h – height of the rolled billet, Δh – absolute reduction in the plane of the collars.

As in the case of the billet upsetting in dual press, during rolling in a double SPD stand the billet undergoes alternating deformation, and the distribution pattern of the vector velocities field of the metal particles will be the same as shown in Fig. 4.

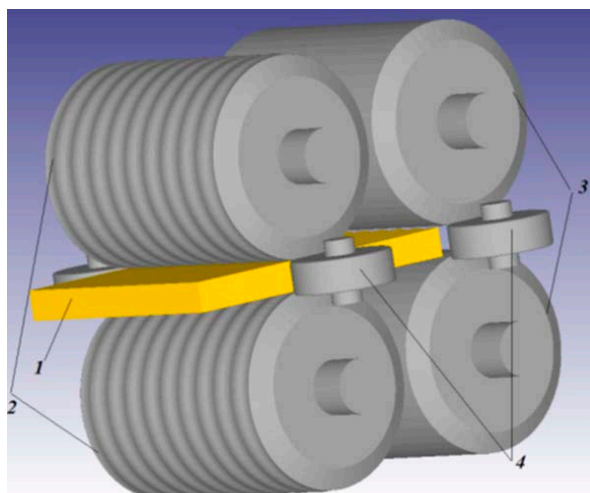


Fig. 5. The solid model of the double SPD stand:

1 – billet; driven horizontal rolls with section-shaped 2 and smooth 3 barrels, 4 – non-driven edging rolls.

Computer simulation of the proposed rolling method was carried out with the aim of determination of optimal blocker and collar sizes of rolls with section-shaped barrel, as well as the reduction value of the billet on the collars Δh in such way, that during rolling in the first stand the blocker was filled with metal, and during rolling in second stand with smooth rolls the surface of the billet was smoothed at the minimal elongation ratio and the fulfillment of the condition of uniform strain in billet sections on blockers and collars. As a result, the calculation methodology of the radius r and the distance e between the lines of the circle centers of collars and blockers, the rational value of the relative reduction of the billet $\frac{\Delta h}{h} \cdot 100\%$ in the first and second stands, which accordingly equal 15% and 20%, was developed.

To assess the efficiency of the new rolling method a comparative analysis of rolling of the thick sheet with height $h=65$ mm made of slab with height $H_0=300$ mm in the rolls with smooth barrel by the existing technology for eleven passes and by the proposed rolling technology with the reduced size billet with height $H_0=160$ mm for sever passes was performed. The criterion of efficiency was the accumulated deformation degree in the plane of symmetry, homogeneity of deformation along the height and the value of energy consumption for the production of rolled thick sheet with height $h=65$ mm. In Fig. 6 curve 1 shows the accumulated deformation degree of the billet with a height $H_0=300$ mm during rolling by the existing technology for eleven passes. Curves 2 and 3 show the accumulated deformation degree of the billet with a height $H_0=160$ mm during rolling by the proposed technology for seven passes, calculated for two sections – under the blocker and the collar of

roll accordingly. As can be seen from curves 2 and 3 in Fig. 6, the total deformation degree for seven passes in the plane of symmetry is 1.15-1.2 times higher than by the existing rolling technology of high billets for eleven passes. Rolling by the new technology allows to reduce strain heterogeneity by 6 times in comparison with the existing technology. This effect was achieved due to the use of severe alternating deformation during rolling by the new method.

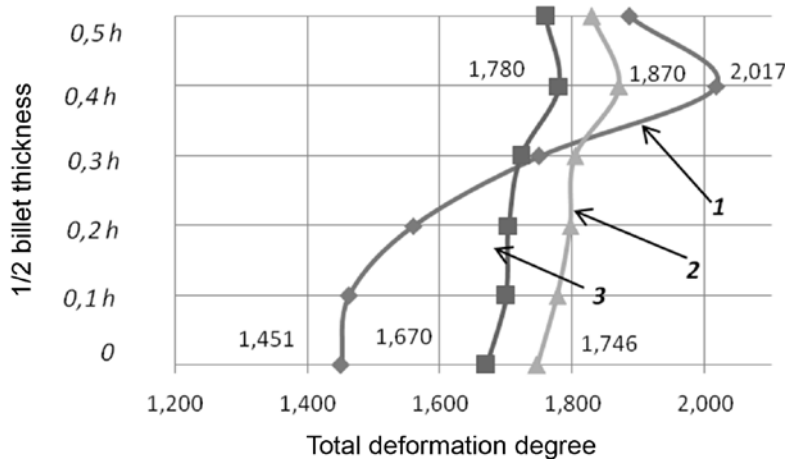


Fig. 6. The distribution of the total deformation degree $\sum \varepsilon_u$ along the billet height by the existing technology for eleven passes and by the proposed technology for seven passes.

According to the results of the comparative analysis of computer simulation it was concluded that the rolling of the billet using new technology can reduce the number of passes from nine to seven. In addition, the new rolling technology of thick plates made of continuous casting billet with height 160 mm instead of 300 mm allows to reduce energy consumption by 1.8 times.

4. Conclusion

The existing SPD methods solve only scientific problems and most of these methods allow processing billets with limited sizes due to specific tool design. In this regard, development of the new SPD methods, which allow processing long billets is relevant. In this work was proposed to use method of slabs rolling in a double SPD stand with high degree and uniformity of strain in fewer passes with simultaneous reduction in energy consumption compared to the existing flat rolling technology.

Acknowledgements. The study was made within the base part of state job in the field of scientific activity № 11.9538.2017/8.9, supported by Act 211 of the Government of the Russian Federation (agreement No. 02.A03.21.0006).

This research is supported by the President of the Russian Federation grant number MK-3011.2017.8

References

- [1] P.W. Bridgman // *Physical review* **48** (1935) 825.
- [2] H. Gleiter, In: *Proc. 2nd Riso Int. Symp. Metallurgy and Materials Science*, ed. by N. Hansen, A. Horswell, T. Leffers, H. Lidholt (Roskilde, Denmark: Riso National Laboratory, 1981), p.15.
- [3] V.M. Segal, V.I. Reznikov, A.E. Dobryshevshiy, V.I. Kopylov // *Russian metallurgy (Metally)* **1** (1981) 99.
- [4] R.Z. Valiev, G.I. Raab // *Tsvetnye Metally (Non-ferrous metals)* **5** (2000) 50. (In Russian)

- [5] A.I. Rudskoy, G.E. Kodzhaspirov, *Technological bases of obtaining of ultrafine-grained metals* (Polytechnic University Publ., St. Petersburg, 2011).
- [6] D.V. Ovchinnikov, A.A. Bogatov, M.V. Erpalov // *Chernye Metally (Ferrous metals)* **3** (2012) 18. (In Russian)
- [7] A.A. Bogatov, D.Sh. Nukhov // *Russian Patent 156711*.

EXAMINATION OF HARDENING CURVES DEFINITION METHODS IN TORSION TEST

M.V. Erpalov*, E.A. Kungurov

Ural Federal University named after the first President of Russia B.N. Yeltsin,

19 Mira Str., Yekaterinburg, Russia

*e-mail: m.v.erpalov@urfu.ru

Abstract. Torsion tests allow studying the rheological properties of materials over a wide range of strain and strain rate values as well as temperature. A key moment in construction of hardening curves is the interpretation of experimental data, which are usually the torque – angle of twist curves. However, there are a number of independent methods to obtain interpretation of experimental data. In addition, there is no single approach to determining the degree of equivalent strain in torsion test. The aim of this paper is to review existing hardening curves definition methods in torsion test and to examine them with the use of finite element modelling.

Keywords: material testing; torsion; rheological properties; strain resistance; equivalent strain.

1. Introduction

Strain resistance σ_s is a key characteristic of the material that is necessary for the successful solution of problems associated with the improvement of existing and the development of new metal forming processes. In general, the material's strain resistance depends on the ongoing processes of speed and strain hardening, as well as the relaxation processes observed simultaneously with this and determined by material's temperature. According to [1] strain resistance at some instant of time can be represented by the following expression:

$$\sigma_s = \sigma_s(\varepsilon, \dot{\varepsilon}, \theta, \varepsilon(t)), \quad (1)$$

where ε and $\dot{\varepsilon}$ are the degree of strain and strain rate respectively, θ is the temperature of material, and $\varepsilon(t)$ is the function that determines the loading history. In the processes of cold deformation, it is assumed that the strain resistance is determined only by the strain hardening process, i.e.

$$\sigma_s = \sigma_s(\varepsilon). \quad (2)$$

The material hardening curves are determined during the tensile, compression or torsion tests of the specimens. The method of torsion testing is characterized by the possibility of achieving large values of the degree of strain without neck formation, as well as the absence of the negative effect of friction forces on the test results that are typical for the tensile and compression tests respectively. The characteristic of the material properties in the torsion test is the shear strain resistance:

$$\tau_s = \sigma_s / \sqrt{3}. \quad (3)$$

According to [2, 3], the data on the strain resistance of materials obtained in tensile, compression and torsion tests differ from each other. In this case, the difference between the values of σ_s reaches 30-40%, which contradicts the single curve hypothesis. This indicates a

lack of knowledge of the process of test specimens in torsion and indicates no reliable experimental data processing algorithm which allows to convert the data obtained in the form of a curve of torque - angle of twist of the sample to the form (1) or (2).

The purpose of the paper is to review and verify with the use of computer modeling of the existing methods for processing experimental data obtained during the torsion test and to determine the rheological properties of the material.

2. Methods for determining the hardening curves by the torsion

In one of the first works on determining shear stresses in the torsion the Nadai technique was proposed [4, 5]. The result of the experiment obtained relationship between the torque M and the angle of twist of the sample φ . Experimental data processing performed by the formula:

$$\tau_s = \frac{1}{2\pi r^3} \left[3M + \gamma \frac{dM}{d\gamma} \right] = \frac{1}{2\pi r^3} \left[3M + \varepsilon \frac{dM}{d\varepsilon} \right], \quad (4)$$

where γ is the magnitude of shear strain, and r is the radius of the working part of the sample. Not contradicting the Nadai technique, in the formula, instead of the shear strain γ , the value of the equivalent strain ε was used in this paper. According to [6], this technique is actively used at present to determine the rheological properties of materials that are insensitive to high-speed hardening. For materials whose strain resistance is determined by the strain rate and the temperature conditions of the process, there is a technique [7, 8]. According to this technique, the shear strain resistance of material is found by the formula:

$$\tau_s = \frac{M}{2\pi r^3} [3 + n + m], \quad (5)$$

where n and m are the coefficients that determine the logarithmic dependence of the torque M on the twisting angle of the active gripper φ and the rate of change of the twisting angle $d\varphi/dt$, respectively:

$$n = \left(\frac{d \ln M}{d \ln \varphi} \right) \Big|_{\frac{d\varphi}{dt} = \text{const}}, \quad (6)$$

$$m = \left(\frac{d \ln M}{d \ln (d\varphi/dt)} \right) \Big|_{\varphi = \text{const}}. \quad (7)$$

In [9], a technique was proposed for processing experimental data obtained in the torsion test, according to which the shear strain resistance is determined by the expression:

$$\tau_s = \frac{3M}{2\pi r^3}. \quad (8)$$

There are other methods for processing experimental data for formation hardening curves [10–12]. However, they are not widely used.

Important in deciphering the experimental data is the precise determination of the equivalent degree of strain accumulated in the sample at each instant of time. However, at present there is a situation that there is no single approach to calculating this quantity. The most widespread expression was [13], known as the equivalent shear strain of von Mises:

$$\varepsilon = \frac{\gamma}{\sqrt{3}}. \quad (9)$$

In [1] the equivalent degree of strain in the torsion test is given by:

$$\varepsilon = \frac{\text{tg}\gamma}{\sqrt{3}}. \quad (10)$$

The work [14] presents an approach to determining the degree of strain based on the Hencky's theory:

$$\varepsilon = \frac{2}{\sqrt{3}} \ln \left[\sqrt{1 + \frac{\gamma^2}{4}} + \frac{\gamma}{2} \right]. \quad (11)$$

In formulas (9-11), the shear strain γ corresponds to the angle of rotation of the lines deposited on the surface of the specimen before testing along the axis:

$$\gamma = \text{arctg} \left(r \frac{\varphi}{l} \right), \quad (12)$$

where φ – angle of twist of the sample, equal to the angle of rotation of the grippers of the testing machine, l – length of the working cylindrical part of the sample.

Known works in which a working part of the specimen is formed as a recess along the radius [15]. It is asserted that when using such samples, the drift phenomenon of the section with maximum deformation is absent and during deformation up to the moment of sample destruction the maximum deformation is localized in the cross section of the neck with the smallest diameter. The value of the angle of rotation of the lines deposited on the surface of the sample with a recess along the radius are determined by the formula:

$$\gamma = \text{arctg} \left(r \frac{d\varphi}{dz} \right), \quad (13)$$

where z is the direction of the coordinate axis, which coincides with the axis of the sample.

Determination of the strain rate during decipherment of the experimental data is carried out according to the known expression:

$$\xi = \frac{d\varepsilon}{dt}. \quad (14)$$

3. Research methods

To study the torsion test, the finite element method implemented in the software product Deform-3D was used. Samples with a cylindrical recess and a radial recess was used. The dimensions of the samples are shown in Fig. 1.

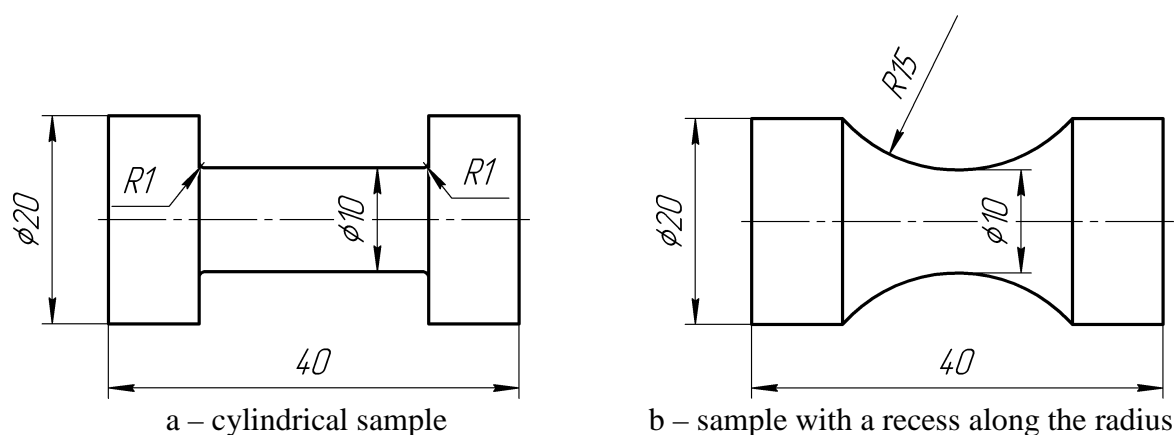


Fig. 1. Models of samples for setting research objectives.

The workpiece material DIN-C45 is selected from the Deform-3D materials database. The use of this material is due to the description of its rheological properties in a sufficient range of the degree of the strain from 0 to 1, the strain rate from 1.6 to 40 s⁻¹, and also the temperature from 20 to 1370°C. The study implements the isothermal formulation of finite

element modeling problems, which corresponds to the basic idea of studying rheological properties at fixed temperatures. The torsion of samples in the Deform-3D program is defined by the motion of the grippers with equal and constant angular velocity π rad/s in opposite directions. The description of the conditions of contact of the workpiece with the tool is given without taking friction forces into account, because the slip of the metal particles of the sample along the surface of the captures is absent. In total, 4 problems were solved for modeling the process of testing samples with different geometry of the working part for torsion at temperatures of 20 and 900°C.

Based on the simulation results, the value of τ_s was calculated using formulas (4, 5 and 8). In this case, the value of the equivalent degree of deformation ε was determined in accordance with (9-11). In this way it was not only the problem of evaluating the methods for determining the hardening curves of materials by the torsion method, but also the adequacy of various approaches to the calculation of the equivalent degree of deformation. The calculated values of τ_s were compared with the value of the shear deformation resistance, which was specified in the material properties during the simulation. For a more accurate comparison of the calculated and given values of τ_s , the tabulated data on the deformation resistance were subjected to bilinear interpolation at the corresponding values of the strain and strain rate at a given temperature. The shear strain γ for cylindrical samples was determined by the formula (12), and the samples with a recess along the radius were determined by the formula (13).

4. Results of the study and discussion

The results of the simulation are given in Table 1 as values of the coefficients of pair correlation of the values of τ_s calculated by known methods and specified in the properties of the material.

The data in Table 1 indicate the failure of the method for calculating the degree of deformation on the basis of the Hencky theory with the aim of establishing the hardening curves of the material. None of the formulas for calculating shear stresses in this case makes it possible to reproduce the hardening curve at the corresponding values of the strain and strain rate. The difference in the values of the shear strain resistance is observed up to 3 times as shown in Fig. 2.

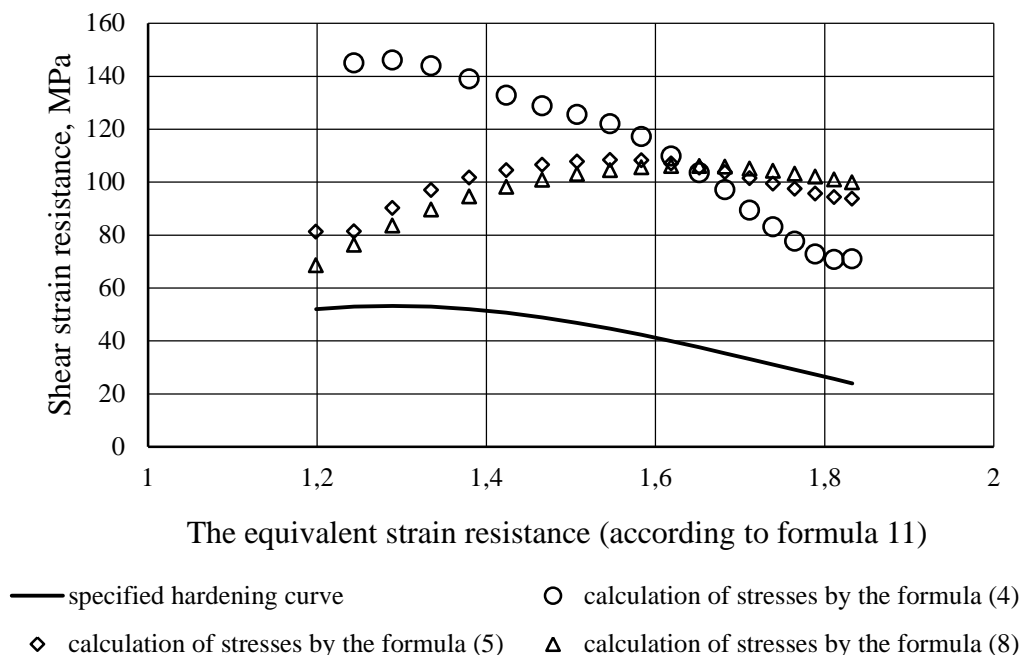


Fig. 2. Shear stresses for a cylindrical sample, 900°C.

Table 1. Values of the coefficients of pair correlation.

A sample form	Temperature	Model for calculating the degree of deformation	Technique for processing experimental data		
			$\tau_s = \frac{1}{2\pi r^3} \left[3M + \varepsilon \frac{dM}{d\varepsilon} \right]$	$\tau_s = \frac{M}{2\pi r^3} [3+n+m]$	$\tau_s = \frac{3M}{2\pi r^3}$
cylindrical sample	20°C	$\varepsilon = \frac{\gamma}{\sqrt{3}}$	0,95	0,96	0,99
		$\varepsilon = \frac{tg\gamma}{\sqrt{3}}$	0,96	0,96	0,99
		$\varepsilon = \frac{2}{\sqrt{3}} \ln \left[\sqrt{1 + \frac{\gamma^2}{4}} + \frac{\gamma}{2} \right]$	0,48	-0,94	-0,95
	900°C	$\varepsilon = \frac{\gamma}{\sqrt{3}}$	0,33	0,08	-0,43
		$\varepsilon = \frac{tg\gamma}{\sqrt{3}}$	0,98	0,98	0,84
		$\varepsilon = \frac{2}{\sqrt{3}} \ln \left[\sqrt{1 + \frac{\gamma^2}{4}} + \frac{\gamma}{2} \right]$	0,58	-0,10	-0,60
sample with a radial recess	20°C	$\varepsilon = \frac{\gamma}{\sqrt{3}}$	-0,04	0,002	0,96
		$\varepsilon = \frac{tg\gamma}{\sqrt{3}}$	0,22	0,01	0,93
		$\varepsilon = \frac{2}{\sqrt{3}} \ln \left[\sqrt{1 + \frac{\gamma^2}{4}} + \frac{\gamma}{2} \right]$	0,30	0,04	-0,88
	900°C	$\varepsilon = \frac{\gamma}{\sqrt{3}}$	0,22	0,46	0,06
		$\varepsilon = \frac{tg\gamma}{\sqrt{3}}$	0,17	0,16	0,56
		$\varepsilon = \frac{2}{\sqrt{3}} \ln \left[\sqrt{1 + \frac{\gamma^2}{4}} + \frac{\gamma}{2} \right]$	0,33	0,44	0,07

The best result of reproducing the hardening curve from the data on the dependence of the torque on the twisting angle is observed on cylindrical samples at a temperature of 20°C. In this case, the models for calculating the equivalent degree of strain (9) and (10) give an identical result. The relative difference between the calculated and given values of the shear strain resistance does not exceed 6% (see Fig. 3).

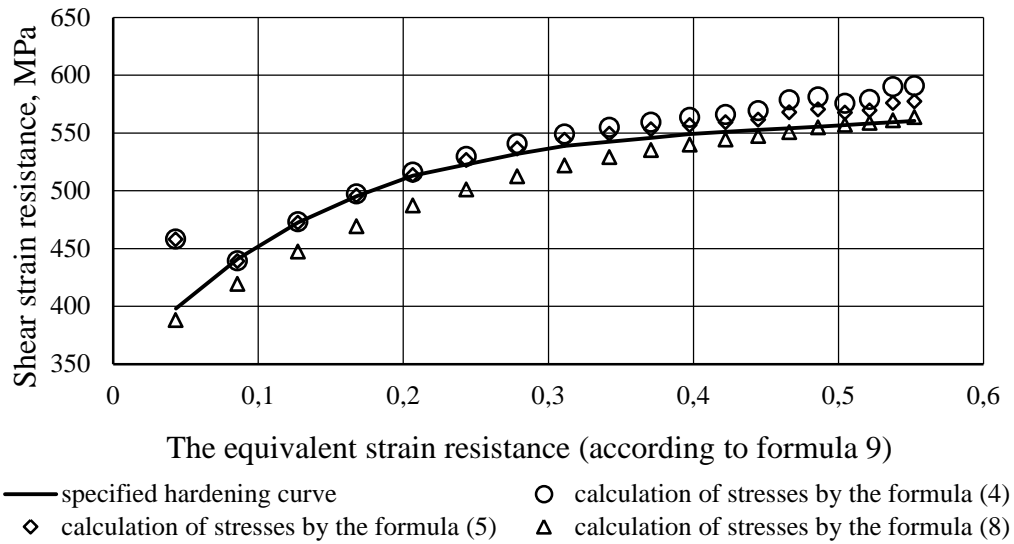


Fig. 3. Shear stresses for a cylindrical sample, 20°C.

When the test temperature of the cylindrical sample is increased to 900°C, despite the sufficiently high values of the pair correlation coefficients, the hardening curve can not be reproduced for any of the considered methods (see Fig. 4). The relative difference between the calculated and given values of the shear strain resistance reaches 85–427%, depending on the model for calculating the equivalent strain and the technique for processing the experimental data. The large deviation of the calculated values of the strain resistance is explained by the increase in the effect on it of the strain rate at elevated temperatures.

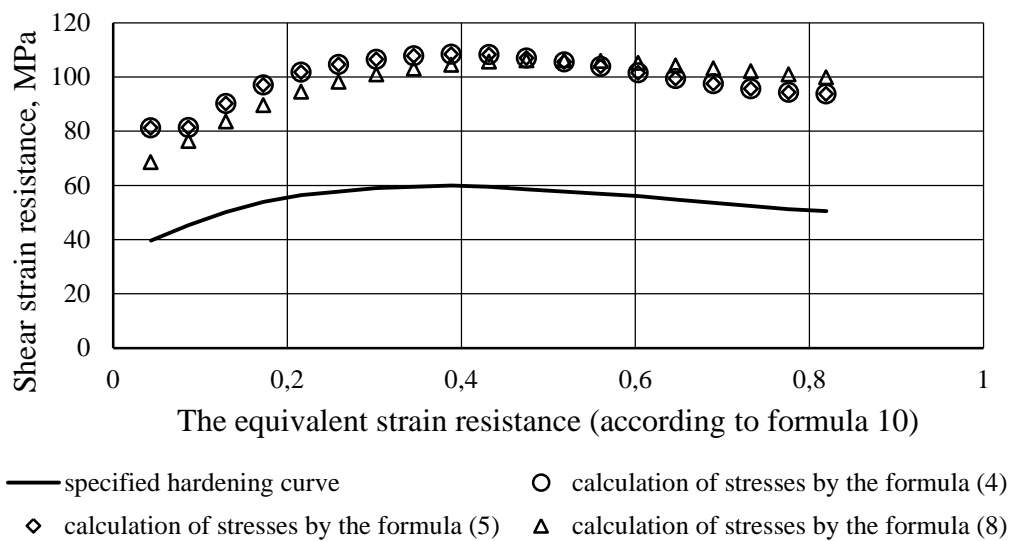


Fig. 4. Shear stresses for a cylindrical sample, 900°C.

In the case of using sample with a recess along the radius, it is possible to calculate the value of shear strain γ with greater accuracy. However, as shown by the simulation results, the hardening curve of the material can be reproduced only with the use of the technique [10] regardless of the strain degree model (9) or (10) (see Fig. 5). The relative difference between the calculated and given values of the shear strain resistance does not exceed 6%. With an increase in the temperature of the sample to 900°C, none of the methods for processing experimental data makes it possible to determine the properties of the material from experimental data.

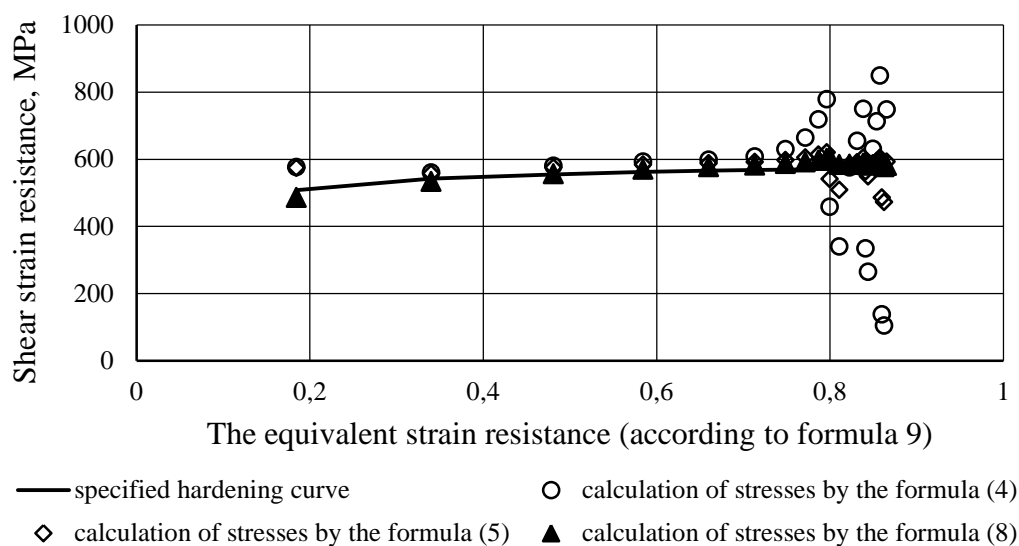


Fig. 5. Shear stresses for a sample with a recess along the radius, 20°C.

5. Conclusions

1. Calculation of the equivalent strain degree based on Hencky's theory for the purpose of establishing hardening curves is untenable.
2. In the case of cold deformation, the experimental data processing technique (8) provides the possibility of calculating the strain resistance for both cylindrical specimens and samples with a recess along the radius.
3. The techniques (4) and (5) do not ensure the convergence of the results of calculating the strain resistance in the cold state with the specified properties of the material when using specimens with a recess along the radius.
4. None of the considered methods for processing experimental data makes it possible to study the properties of materials in the hot state.
5. In order to study the rheological properties of materials in the hot state, it is necessary to develop a reliable algorithm for processing experimental data obtained from the results of torsion test.

Acknowledgements. The study was made within the base part of state job in the field of scientific activity № 11.9538.2017/8.9, supported by Act 211 of the Government of the Russian Federation (agreement No. 02.A03.21.0006).

References

- [1] V.L. Kolmogorov, *Mechanics of metal forming* (Publishing house of the Ural State Technical University – UPI, Yekaterinburg, 2001).
- [2] I.A. Birger, R.R. Mavljutov, *Resistance of materials* ("Nauka", Moscow, 1986).

- [3] V.V. Moskvitin, *Plasticity under variable loading* (Publishing house of MGU, Moscow, 1965).
- [4] A. Nadai, *Theory of flow and fracture of solids, Volume II* (McGraw-Hill Book Company, Inc., New York, 1963).
- [5] Yu.N. Rabotnov, *Resistance of materials* ("Fizmatgiz", Moscow, 1962).
- [6] J.J. Jonas, F. Montheillet, L.S. Toth, C. Ghoh // *Materials Science & Engineering* **591** (2014) 9.
- [7] D.F. Fields, W.A. Backofen // *ASTM Proceeding* **57** (1957) 1259.
- [8] S. Khoddam, P.D. Hodgson // *Materials & design* **31** (2010) 2578.
- [9] I. Schindler, E. Hadasik, In: *Challenges to Civil and Mechanical Engineering in 2000 and Beyond* (Wrocław, 1997), Vol. 3, p.395.
- [10] T. Sheppard, D.S. Wright // *Metals Technology* **6** (1979) 215.
- [11] E. Lach, K. Pöhlandt // *Journal of Mechanical Working Technology* **9** (1984) 67.
- [12] M. Knorr, A. Graber, K. Pohlandt // *Trans NAMRI/SME* (1990) 52.
- [13] J.J. Jonas, C. Ghosh, L.S. Toth // *Materials Science & Engineering* **607** (2014) 530.
- [14] S. Onaka // *Philosophical Magazine* **92** (2012) 2264.
- [15] K. Laber, A. Kawalek, S. Sawicki, H. Dyja // *Key Engineering Materials* **682** (2016) 356.

COMPETITION BETWEEN THE VOLUME SOLUTION AND THE SURFACE SEGREGATION OF SOLVED ELEMENTS IN α -Fe

V.P. Filippova^{1*}, E.N. Blinova¹, A.M. Glezer^{1,2}, R.V. Sundeev^{1,3}, A.A. Tomchuk^{1,4},
L.F. Muradimova²

¹I.P. Bardin Central Research Institute for Ferrous Metallurgy; 23/9-2, Radio str., 105005 Moscow, Russia

²National University of Science and Technology "MISiS"; 4, Leninskiy av., 119049 Moscow, Russia

³Moscow Technological University "MIREA"; 78, Vernadskogo av., 119454 Moscow, Russia

⁴Bauman Moscow State Technical University; 5-1, 2-nd Baumanskaya str., 105005, Moscow, Russia

*e-mail: varia.filippova@yandex.ru

Abstract. It was experimentally shown, using Auger-spectroscopy method, that there is a certain temperature interval of forming surface segregations of an element (C, N, B, P, Mo, Ti, Al, S, Sn, Cu) solved in α -Fe of low-carbon steels and ferrous-based alloys. Proposed mathematical approach based on traditional relationships of the equilibrium thermodynamics and diffusion kinetics models has determined the temperature scale positions of the intervals of forming segregations of the solved elements in α -Fe.

Keywords: solid solution; surface; segregation; ferrous alloys; kinetics; computer modeling.

1. Introduction

Traditionally, relationships between the values of solved elements concentration in the volume and in the surface (or interface) segregations considered from the equilibrium thermodynamics positions realize the enriched field of an alloy as a separate two-dimensional phase [1], describing the segregation phenomenon as internal adsorption in terms of analogues of gas adsorption on the free surface [2]. From the point of equilibrium thermodynamics, there is no difference between the interface (inter-crystalline or grain boundary) and the surface segregation, because the stimulus of the internal adsorption phenomenon for the both cases is the decrease of the total free energy of the system consisting of the volume plus the surface or the volume plus the interface [1, 2]. Difference between the surface and intercrystalline segregations for solved elements in the same solid solution can be proposed to be of a quantitative kind (in the levels and the rates of achievement of equilibrium concentrations) but not of a qualitative one.

The element concentration as a function of the tempering time after exposing and quenching from higher temperature, $X_b(t)$, is described with the Langmuir curve by analogy with gas adsorption on a free surface, or with the Fowler theory accounting inter-atomic interaction in the segregation field [2, 3, 4]. It looks like a curve with saturation as that one in Fig. 1 (a) presented by M.P. Seah in [4] as the equation (1):

$$\frac{X_b(t) - X_b(0)}{X_b(\infty) - X_b(0)} = 1 - \exp\left(-\frac{FDt}{\beta^2 f^2}\right) \cdot \operatorname{erfc}\left(\frac{FDt}{\beta^2 f^2}\right)^{1/2}. \quad (1)$$

The above equation (1) includes the following characteristics: $X_b(t)$ is the segregation level depending on the exposing time (t); $X_b(0)$ is the initial surface concentration equaling to

the volume one (X_v) of a solved element; $X_b(\infty)$ is the saturation level tied with the limited volume solubility by the value β being the ratio between the volume concentration to the volume solubility; f is the coefficient depending on the difference between the solved and the solute atoms; D is the volume diffusion coefficient, $D = D_0 \exp(-Q/RT)$; R is the universal gas constant, $R = 8.314 \text{ J}/(\text{mol} \cdot \text{degree})$; T is the exposing temperature by Kelvin scale; D_0 and Q are the characteristics of the volume diffusivity of a solved element; $F=4$ for interfaces and $F=1$ for surfaces [4].

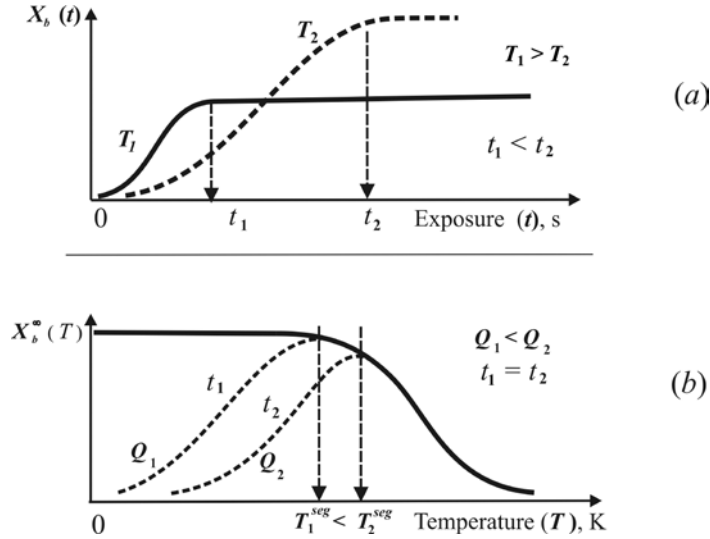


Fig. 1. Relationships of the internal adsorption phenomenon in a solid solution:
a) surface concentration of a solved element ($X_b(t)$) as a function on the tempering time (t);
b) equilibrium surface concentration of a solved element ($X_b^\infty(T)$) as a function on the temperature of isothermal exposing (T).

In general, in spite of some peculiarities of various thermodynamics approaches [1-14], description of the dependence of the equilibrium segregation concentration values, $X_b^\infty(T)$, on those of the volume concentrations (X_v), and the isothermal exposing temperature (T) results in the functions of the following form:

$$\frac{X_b^\infty(T)}{X_v} \sim \frac{X_v}{X_{v0}} \cdot \exp\left(\frac{-\Delta G_{seg}}{RT}\right), \quad (2)$$

where X_v is the volume concentration and X_{v0} is the limited volume solubility; R is the universal gas constant; ΔG_{seg} is a thermodynamics characteristics of the stimulus of segregations forming. The value ΔG_{seg} further will be named as the "segregation energy" (SE). It should be noted, that segregation of a solved element will take place when SE is positive ($\Delta G_{seg} > 0$). It follows from (2) that the level of equilibrium segregation ($X_b^\infty(T)$) is decreasing with the temperature growth. The value of $X_b^\infty(T)$ is directly tied with ΔG_{seg} (according 2). The ratio X_v/X_{v0} in (2) for low soluble impurities, such as S and P in low carbon steels and alloys based on α -Fe, usually being assumed to equal to 1 (one). So, the main factor determining segregations forming to be usually considered is ΔG_{seg} . That one in some works represents the free energy change of the equilibrium segregation forming in the volume-surface (volume-interface) system [5, 6]. Particularly, MacLean evaluated the value ΔG_{seg} in [1] by the elastic energy released at forming the solved atoms segregation. Both surface and interface researching methods are involved for experimental investigation of

segregations [1-15]. Nevertheless, direct experimental measurements of intercrystalline segregations are less available than those ones of free surfaces.

Hondros and Seah [4] proposed a more detailed analogues (3) of the above equation (2) where the limited volume solubility of a low soluble elements in a solid solution to be considered as a function of the temperature $X_{vo}(T)$. So, the relationship (3) including the equilibrium surface concentration (X_b^∞), the volume concentration (X_v), and the volume solubility ($X_{vo}(T)$) is the following:

$$\frac{X_b^\infty(T)}{X_{bo} - X_b^\infty(T)} = \frac{X_v}{X_{vo}(T)} \exp\left[\frac{-\Delta G_{seg}}{RT}\right]. \quad (3)$$

Here, X_{bo} is defined in [4] as the fraction of the enriched surface covered with an atomic layer of a segregating element, that one is a certain reference value ($X_{bo} = 2.5 \div 4.3$) characterizing the equilibrium saturated surface thickness having minimum at mono-atomic layer; the values $X_b^\infty(T)$, X_v , $X_{vo}(T)$ are represented as the molar concentrations). The limited volume solubility is another important characteristics influencing on formation of surface and interface segregations. As it is shown in (2) and (3), the higher is $X_{vo}(T)$ value of a solved element the less is its susceptibility to surface segregation enrichment. And opposite, the less is the limited volume solubility of an element, the higher is its susceptibility to surface enrichment due to internal adsorption. An example of the latter is the brittleness caused by interface segregation of low soluble impurities of P, S, As, etc. in steels [5, 8, 13, 14]. As rule, the limited volume solubility $X_{vo}(T)$ of solved element in α -Fe is increasing with the temperature growth [16, 17], and solving in the volume being the process opposite to segregating in surface or interface [4]. Concluding from the above, the equilibrium segregation value $X_b^\infty(T)$ as the function on the temperature (2, 3) looks like the monotonic curve (the solid line) represented in Fig.1b, where the value $X_b^\infty(T)$ is decreasing with the temperature increase.

Summarizing the known kinetics (1) and thermodynamics models (2, 3) of surface (or interface) segregations forming, it is possible to conclude that the higher temperature of isothermal tempering takes place, the smaller value of the saturation level (X_b^∞) and the lower time of its achievement (t) to be observed (Fig.1, a, b). According to the schemes presented in Fig.1 (a, b), the equilibrium segregation level is more rapidly reached under higher exposing temperatures (Fig.1a), but the value of the equilibrium saturation concentration is much less than that could be under lower temperatures (Fig.1b). So, under a limited time of isothermal exposing, one can propose a certain temperature (T_{seg}) of the maximum level of a solved element segregation to exist, as it is shown with dotted curves in Fig.1b. The temperature T_{seg} further being named as “the segregation stability temperature” (SST) is the temperature-scale position of the temperature interval of preferential surface enrichment by the solved element. Certainly, positions of the intervals in the temperature scale for different solved elements can mismatch with each other, depending on relationships between the thermodynamics and kinetics characteristics of the solvent and the solved ones. Again, the process of segregation under real heat treatment conditions in metallurgy involving rather low temperatures and limited time intervals of isothermal expose is controlled by the diffusion rate, then the equilibrium surface concentration values of some solved elements of low diffusion activity to be not reached (dotted curve in Fig.1a). It follows from the latter that surface segregations of more mobile solved elements will form at lower temperatures than those of slower diffusion activity components.

Literature experimental data on temperature intervals of internal adsorption of solved elements in solids are rather poor. Particularly, reversible temper brittleness observed in low- and medium-carbon steels under exposing at (or slow cooling threw) the temperature

750-800 K can be attributed to phosphorous interface segregations forming in α -Fe just in that temperature interval [5-8]. Also, the temperature interval existence for sulfur segregating in the surface of α -Fe near 950 K was experimentally confirmed with Auger-spectroscopy method in work [9].

To study the competition between the elements `solving in the volume and the segregations forming in the surface under isothermal heating and to find the certain temperature intervals of forming the solved elements segregations, the surface of α -Fe alloys under isothermal exposing in vacuum was experimentally investigated in the present work, using Auger-spectroscopy method. For the purpose, there was also used a mathematical analysis of the kinetics and thermodynamics characteristics tied with the obtained time-temperature segregation relationships.

2. Materials and Original Data

For this work realization, there were the original data on thermodynamics and kinetics characteristics influencing volume solubility of impurities and internal surface segregations formation in α -Fe alloys taken from the literature [5, 10-14].

There are the segregation energy values (ΔG_{seg}) of some elements solved in α -Fe presented in Table 1 without differentiation between “internal” and “external” surfaces. The data [5, 10-14] result from either direct measurements of the system energy parameters tied with the equilibrium segregations forming or inverse calculations from relationships similar to (2) using the determined X_b^∞ / X_v values.

Table 1. Segregation energy values (ΔG_{seg} , kJ/mol) of solved elements in α -Fe based alloys and low-carbon steels, by various scientific References.

[Reference]	[5]	[11]	[12]	[13]	[14]	[10]
Solved element						
C	92	-	-	88	-	16
P	48	16	83	78	11	25
Mo	0,1	-	0	-	-	5
Cr	0	-	0	-	-	2
Ni	3	-	16	-	3	4
B	-	-	-	-	-	-
S	-	27	-	195	19	38
Sn	-	-	-	-	-	23
Al	-	12	-	-	-	-
Cu	-	-	-	-	-	-
N	-	-	-	112	-	-
Ti	-	-	22	-	-	8

As shown in Table 1, both experimentally determined and simulated ones are just only agree by the order, and thus are only valid for qualitative characterization of the elements segregation possibility. Observed variations of the values of ΔG_{seg} is due to the quantitative evaluations dependence on an accepted physical model and an experimental method of measuring the crystallographic and concentration characteristics of the segregation field (surface or interface). Particularly, the concentration value depends on such segregation characteristics as the inter-crystalline boundary width varying from 1 nm (i.e. about one-two inter-atomic distances measured by transmission electron microscopy method) till 1000 nm (when chemical etching grooves measuring with optical microscopic method takes place).

Again, chemical methods of determination of the average concentrations of the elements in an alloy volume are not able of quantitative characterization of a local segregation composition. From the other side, modern local methods of surface analysis, such as Auger- and X-ray photoelectron spectroscopy, etc. providing registration of elements ratio in a surface layer of several atoms thickness, are not reliable for quantitative estimation of real concentration values but only for qualitative ones [4].

There are the volume solubility of some elements in α -Fe against the temperature, $X_{vo}(T)$, presented in Table 2 from the list square method approximation of the literature data [15, 16]. The high accuracy of the approximation coefficients in Table 2 is due to the computer calculations requirements of attachment of the functions branches. According to the obtained data (Table 2), the volume solubility of the most of the elements solved in α -Fe (S, P, B, Sn, Al, Mo, Cu) is increasing with the temperature growth, being in accordance with the proposition in [4]. Exception of the latter is Mn and Ni, which never were segregating in α -Fe.

Table 2. The limited volume solubility, $X_{vo}(T)$, of some elements in α -Fe as a function on the temperature (T).

Solved Element	The limited volume solubility, $X_{vo}(T)$, 10^{-2} at. %	Temperature interval, T , K
P	$61 \cdot 10^{-5}$ $-0.00232 + T \cdot 10^{-5}$ $0.00015 \cdot \exp(0.00455 \cdot T)$	$T < 293$ $293 \leq T \leq 773$ $T > 773$
S	$47.943 \cdot \exp(0.001 \cdot T) \cdot 10^{-6}$	$T < 1183$
C	$0.121 \cdot \exp(0.00823 \cdot T) \cdot 10^{-5}$	$T < 1183$
N	$10^{-5} \cdot \exp(0.007 \cdot T)$	$T < 1183$
B	$3.4353 \cdot 10^{-13} \cdot \exp(0.018 \cdot T)$	$T < 1183$
Mo	$0.005 \cdot (1/0.51316 - 0.00028 \cdot T) + (T/(-0.2037 \cdot T + 432.306))$	$T < 1183$
Cr	$0.0019203 \cdot \exp(0.00557 \cdot T)$ $0.01/(0.23766 - 0.00019 \cdot T)$ 1	$T \leq 700$ $700 < T \leq 1100$ $T > 1100$
Mn	0.035 $0.07365 - 0.00005 \cdot T$ $0.04746 - 0.00002 \cdot T$ $0.1255 - 0.0001 \cdot T$ $0.1935818 - 0.0001636 \cdot T$	$T < 773$ $773 \leq T < 873$ $873 \leq T < 973$ $973 \leq T < 1073$ $1073 \leq T < 1183$
Ni	$0.1482935 - 0.0001265 \cdot T$ 0	$T \leq 1171.9$ $T > 1171.9$
Sn	$0.0021618 \cdot \exp(0.00317 \cdot T)$	$T < 1183$
Al	$0.086035 \cdot \exp(0.00104 \cdot T)$	$T < 1183$
Cu	$26 \cdot 10^{-8} \cdot \exp(0.008 \cdot T)$ $0.01 \cdot (0.839/\exp(0.044 \cdot T))$	$T \leq 1130$ $T > 1130$
Ti	$0.00018 \cdot \exp(0.003 \cdot T)$	$T < 1183$

Table 3. Compositions and parameters of the previous heat treatments (quenching temperature and exposing time) of the investigated alloys based on α -Fe.

Alloy composition (atomic %)	Elements concentration, % (at.)					Quenching temperature (K), Exposing (s)
	P	S	N	C	Other elements, % (at.)	
Fe-0.13P-0.007S-0.025N-0.03C	0.1278	0.007	0.0247	0.0279	0.0579 Al 0.0536 Si	1153 K, 36000 s
Fe-0.6Al-0.07P-0.005S-0.02N-0.03C	0.0665	0.0052	0.0158	0.0324	0.6185 Al	1473 K, 3600 s
Fe-1.2Al-0.05P-0.005S-0.01N-0.04C	0.0501	0.0052	0.0103	0.0369	1.232 Al	1473 K, 3600 s
Fe-5.6Al-0.06P-0.007S-0.01N-0.04C	0.0595	0.0068	0.0166	0.0406	5.6228 Al 0.01 Sn	1473 K, 3600 s
Fe-0.03S-0.14P-0.06N-0.02C-0.005Ti-0.006Cu	0.1441	0.0348	0.0581	0.0186	0.0352 Ni 0.0116 Mo 0.0047 Ti 0.0061 Cu	1373 K, 600 s
Fe-0.02S-0.14P-0.3N-0.04C	0.1441	0.0209	0.0251	0.0372	0.0494 Ni 0.064 Mo	1373 K, 600 s
Fe-0.1Sn-0.1P-0.004S-0.006N-0.1C	0.092	0.0044	0.006	0.014	0.0054 Cr 0.0619 Ni 0.1083 Sn	1153 K, 36000 s
Fe-0.6Cr-0.13P-0.004S-0.001N-0.01C	0.1297	0.0035	0.0011	0.0093	0.5901 Cr	1139 K, 600 s
Fe-1Cr-0.13P-0.004S-0.002N-0.01C	0.1314	0.0035	0.0032	0.0093	1.3725 Cr	1139 K, 600 s
Fe-1Mo-0.16P-0.004S-0.014N-0.02C	0.1596	0.0035	0.014	0.0234	0.9954 Mo 0.05 Si	1139 K, 600 s
Fe-3Mo-0.26P-0.004S-0.06N-0.03C	0.2648	0.0036	0.0626	0.0285	3.1172 Mo 0.0974 Si	1139 K, 600 s
Fe-3Mo-0.15P-0.004S-0.1N-0.01C	0.1545	0.0044	0.1053	0.0142	3.0816 Mo 0.1014 Si	1139 K, 600 s
Fe-0.02B-0.07P-0.005S-0.03N-0.02C	0.072	0.0052	0.0263	0.0186	0.19 Ni 0.0155 B 0.133 Si	923 K, 5400 s
Fe-0.03B-0.02P-0.007S-0.04N-0.02C-2.7Ni	0.0197	0.0069	0.0369	0.0231	2.7458 Ni 0.0257 B 1.049 Si	923 K, 5400 s
Fe-0.002B-0.13P-0.005S-0.003N-0.03C	0.1259	0.0052	0.0032	0.278	0.1234 Ni 0.0021 B 0.0456 Si	923 K, 5400 s
Fe-1Ni-0.14P-0.005S-0.06N-0.01C	0.1405	0.0052	0.0562	0.0093	0.9126 Ni	1153 K, 36000 s
Fe-3Ni-0.03P-0.005S-0.003N-0.014C	0.0343	0.0052	0.0028	0.014	3.0955 Ni	1153 K, 36000 s
Fe-3Ni-0.17P-0.007S-0.05N-0.014C	0.1731	0.007	0.0514	0.014	2.9495 Ni	1153 K, 36000 s

In the present work, the investigated alloys compositions and the previous heat treatment conditions were resulted from analysis of the above data presented in Tables 2. The binary and ternary Fe-based alloys involving P and S (as main impurities inducing brittleness of steels) and one of the alloying element (Mo, Cr, Ni, B, or Al) considered as a potential tool of neutralization of P and S segregations were prepared for the investigation. The original specimens were thin square (10x10 mm) plates of 0.5 mm thickness previously quenched in

water. There were quenching temperatures chosen to provide maximal solution of the involved components in α -Fe. There are the compositions of the investigated alloys, the exposing duration and the temperatures of previous quenching presented in Table 3.

The volume diffusivity characteristics (D_0 , Q) of some elements solved in α -Fe there are presented in Table 4 involving the data from [17-27]. As shown in Table 4, the diffusion activation energy values (Q) of C, N, and B solved in α -Fe are approximately by 3-4 times lower than of P, Mo, Ti, Al, S, Sn, and Cu. According to (1), Fig.1b, we can propose a high segregation level of C, N, and B to develop at lower temperatures than of P, Mo, Ti, Al, S, Sn, Cu.

Table 4. Parameters of the volume diffusion coefficient, D , for solved elements in α -Fe based alloys and low-carbon steels: $D = D_0 \exp(-Q/RT)$.

Solved Element	D_0 , $10^{-4} \text{ m}^2/\text{s}$	Q ,		Ref.
		kcal/mol	kJ/mol (*)	
C	0.0251 ± 0.01	18.3 ± 0.8	76.7 ± 3.4	[17]
N	0.00144	17.7 ± 0.1	74.3 ± 0.4	[18]
B	0.0023	19 ± 2	79.6 ± 8.4	[19]
P	376	65.6 ± 0.5	275.0 ± 2.1	[20]
Mo	0.44	57.0 ± 0.5	238.8 ± 2.1	[21]
Cr	2.53	57.5 ± 0.5	240.9 ± 2.1	[22]
Ni	0.6	62.6 ± 0.6	262.3 ± 2.5	[21, 23]
S	1700	61.2 ± 0.5	256.4 ± 2.1	[24]
Sn	8	61.2 ± 0.5	256.3 ± 2.1	[25]
Al	5.9	57.7 ± 1.0	241.8 ± 4.2	[23]
Cu	6	59 ± 1	247.2 ± 4.2	[26]
Ti	20	58 ± 1	243.0 ± 4.2	[27]

* The literature data related to common conditions (1 kJ/mol = 4.19 kcal/mol).

3. Experimental methods

To study kinetics of internal adsorption of solved elements in α -Fe under isothermal exposing, there was using the Auger-spectroscopy method of surface concentration determination with a combine-spectrometer ESCALAB MK-2 of VG firm (UK). Every investigated specimen was previously cleaned by scraping inside the spectrometer preparation chamber, providing vacuum about 10^{-8} Pa, and then situated in the working chamber, where was heated from the room temperature and exposed at a certain constant temperature (from 300 K to 950K) during several hours (1, 2 or 3 h), vacuum being not worse than 10^{-7} Pa.

The Auger spectra were recorded in the time intervals with duration from 10 minutes to 2 hours, depending on exposing temperature influencing the segregating rate. The recording regimes were chosen from the principles described in [4] to provide high expressivity combined with a satisfactory resolution for analysis of thin electron spectrum structure at the required conditions of the heat treatment in vacuum. So, the recording mode was CRR = 4 with rate of $0.2 \text{ eV}\cdot\text{s}^{-1}$ order; primary electron energy $E = 3000 \text{ eV}$; $\Delta E/E = \text{const}$; the baseband voltage being of 5.0 V. Thickness of the analyzed layer under considered conditions is about 5 atomic sizes, that is comparable with the escape depth of ferrous atoms Auger-electrons having binding energy of 703 eV. For quantitative analysis of elements concentrations in segregation (X_b^i) we used the computational procedure developed in [6]. Here, surface-volume ratio of atomic concentrations (X_b^i/X_v^i) of an element i was equated with the ratio of the intensities of relevant Auger-peaks of the element before and after isothermal exposing, considering that as the ratio of the volume and the surface concentrations. The

volume concentrations values (X_v^i) determined previously by the standard chemical analysis (Table 4) of the alloys under investigation were considered as the etalons for computing the surface compositions from Auger-spectroscopy data. The details of the Auger spectroscopy investigation were the same as those published in [28].

4. Experimental Results

The isotherms of nitrogen, carbon, sulfur, and phosphorus adsorbing on the surface of one of the investigated alloys (Fe-0.13P-0.007S-0.025N-0.03C) under isothermal exposing in vacuum of the Auger-spectrometer working chamber are presented (atomic %) in Fig. 2. The following peculiarities of the elements surface segregation under isothermal exposing of the considered alloy in vacuum can be observed: surface enrichment by carbon runs at relatively low temperatures (till 600 K); nitrogen segregation develops in the temperature interval 500-600 K; phosphorus appreciably enriches the surface at temperatures 550-650 K; sulfur begins creating segregations from 600 K and upper.

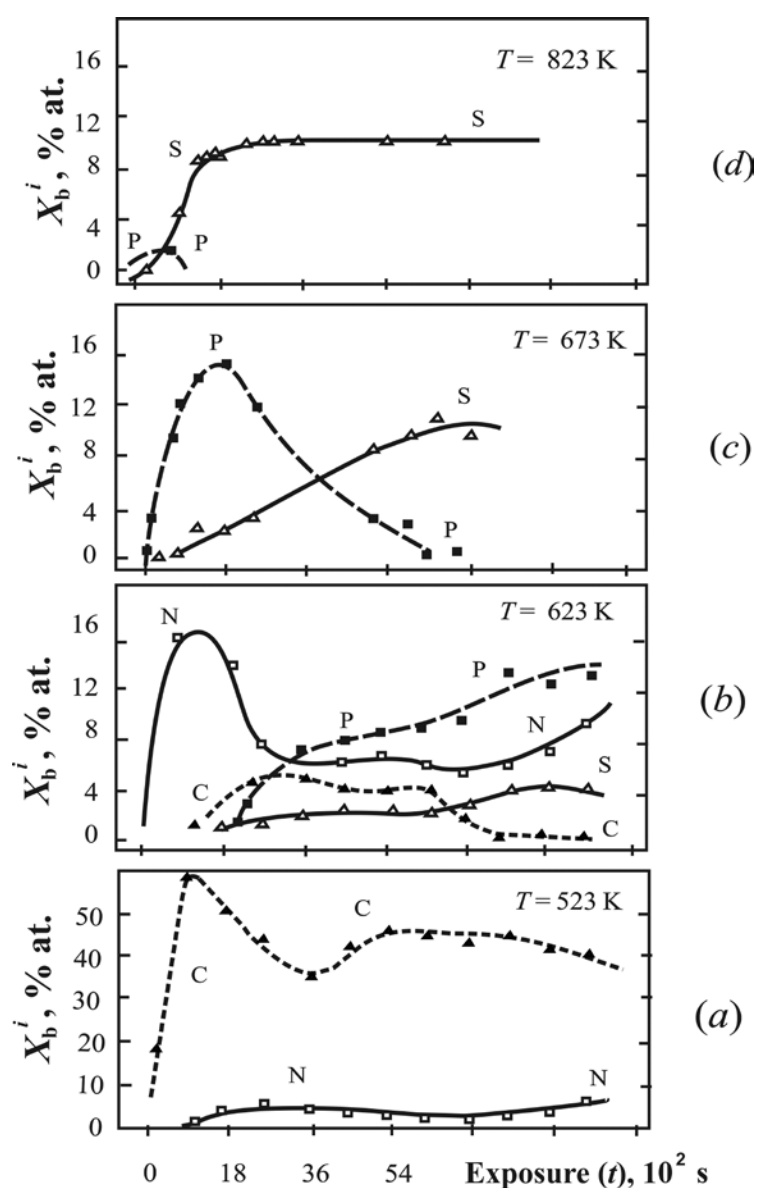


Fig. 2. Isotherms of forming surface segregations of nitrogen (N), carbon (C), sulfur (S), and phosphorus (P) in alloy Fe-0.13P-0.007S-0.025N-0.03C (% at.) under isothermal exposing in vacuum at various temperatures: a) 523 K; b) 623 K; c) 673 K; d) 873 K.

The experimental results on internal adsorption of N, C, S, and P in the surface of Fe-0.13P-0.007S-0.025N-0.03C (% , at.) alloy described above (Fig. 2) are also shown in Fig. 3 as the time-temperature concentration diagrams (TTC-diagrams), where C-curves represent the time of about 50%-75% level of equilibrium segregation attainment. Analogous diagrams for the solved elements forming segregations in Fe-based alloys are shown in Figs. 4-10. The lower branches of the C-curves represent reduction of the time of segregation forming against the exposition temperature growth, the relationship observed being tied with atomic diffusivity increasing. After the exposing temperature has grown till some value, the equilibrium level of segregation goes down (Fig. 1 a), and the time of forming segregation of a considered enrichment level extremely increases (the upper branches of the C-curves in Figs. 3-10).

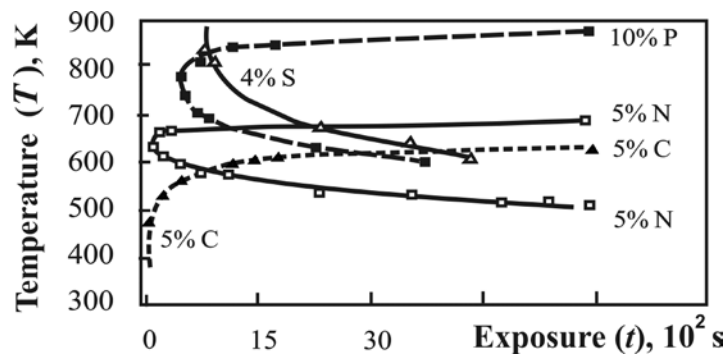


Fig. 3. Time-temperature concentration diagrams of forming 50% level of equilibrium segregations of P, S, N, and C in the free surface under isothermal exposing in vacuum of the alloy: Fe-0.13P-0.007S-0.025N-0.03C (% , at.).

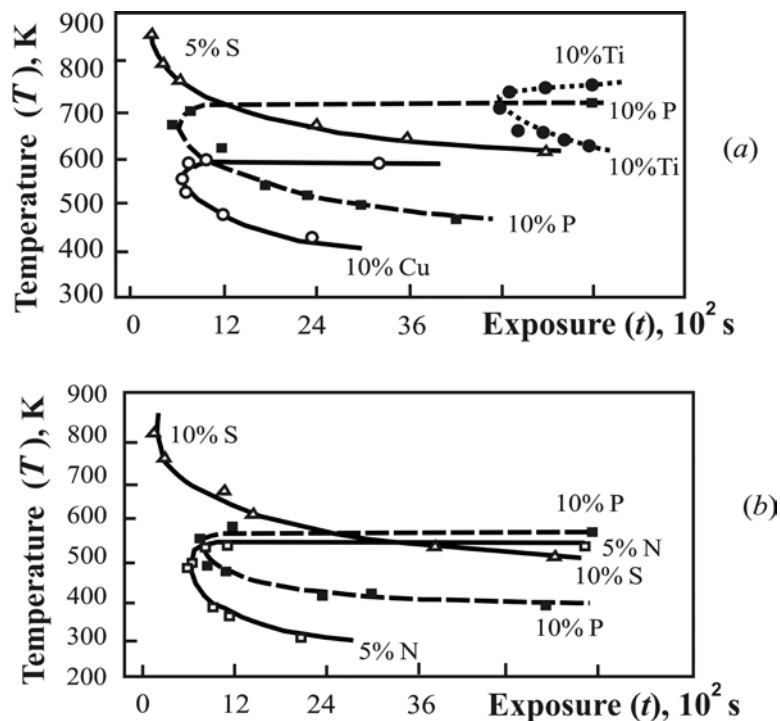


Fig. 4. Time-temperature concentration diagrams of forming 50% level of equilibrium segregations of P, S, N, C, Ti and Cu in the free surface under isothermal exposing in vacuum of the Fe-S-P alloys: a) Fe-0.03S-0.14P-0.06N-0.02C-0.005Ti-0.006Cu; b) Fe-0.02S-0.14P-0.3N-0.04C (% , at.).

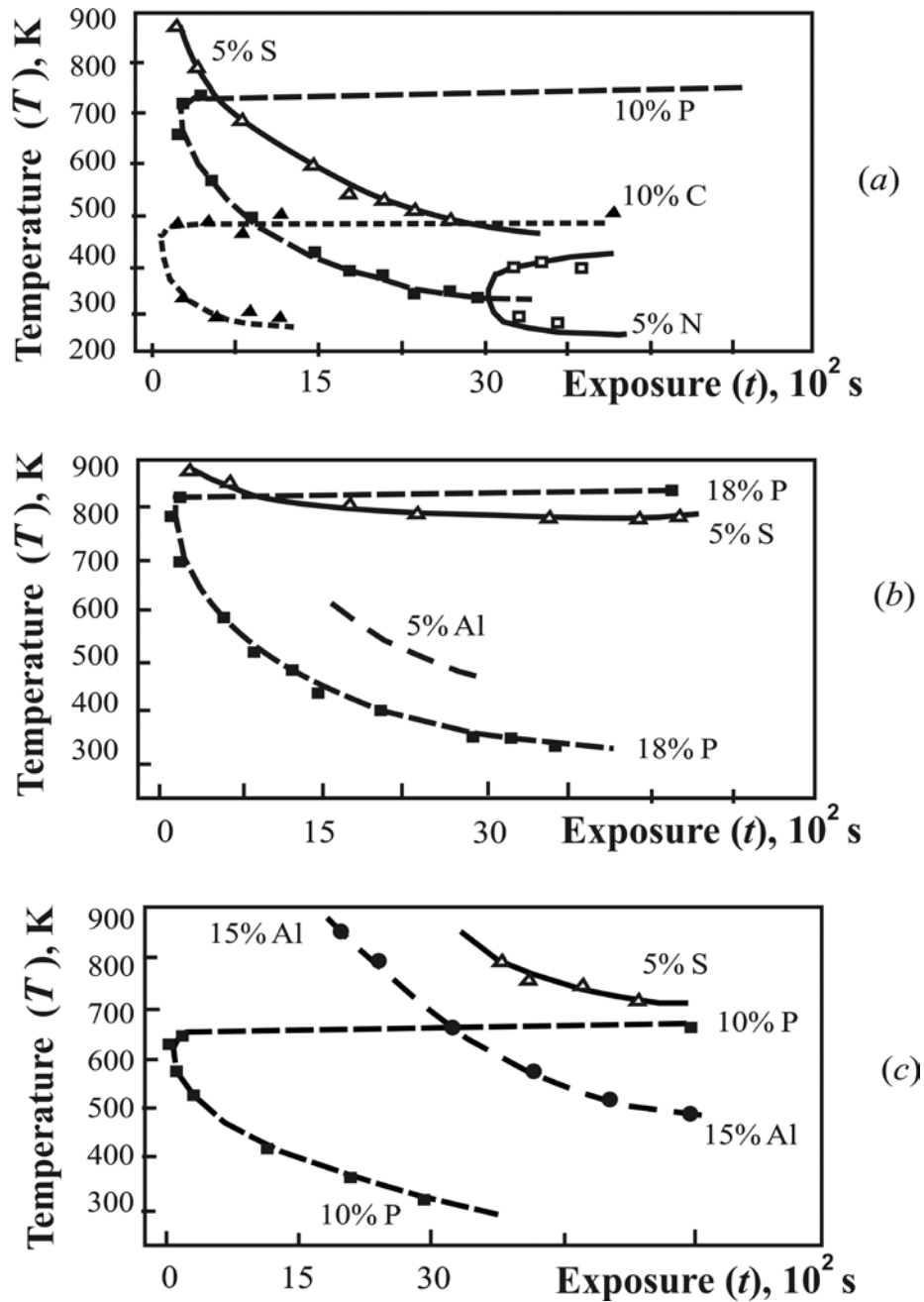


Fig. 5. Time-temperature concentration diagrams of forming 50% level of equilibrium segregations of P, S, N, C, and Al in the free surface under isothermal exposing in vacuum of the Fe-Al-P alloys: a) Fe-0.01Al-0.07P-0.005S-0.02N-0.03C; b) Fe-1.2Al-0.05P-0.005S-0.01N-0.04C; c) Fe-5.6Al-0.06P-0.007S-0.01N-0.04C (% , at.).

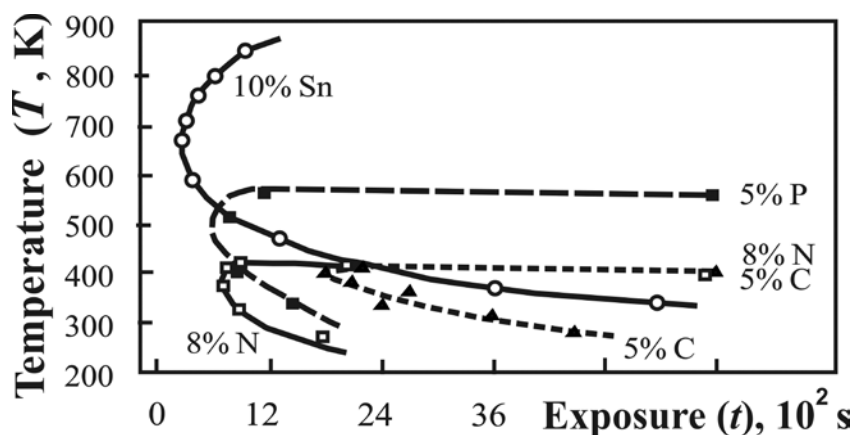


Fig. 6. Time-temperature concentration diagrams of forming 50% level of equilibrium segregations of P, N, C, and Sn in the free surface under isothermal exposing in vacuum of the Fe-Sn-P alloy: Fe-0.1Sn-0.1P-0.004S-0.006N-0.1C (% , at.).

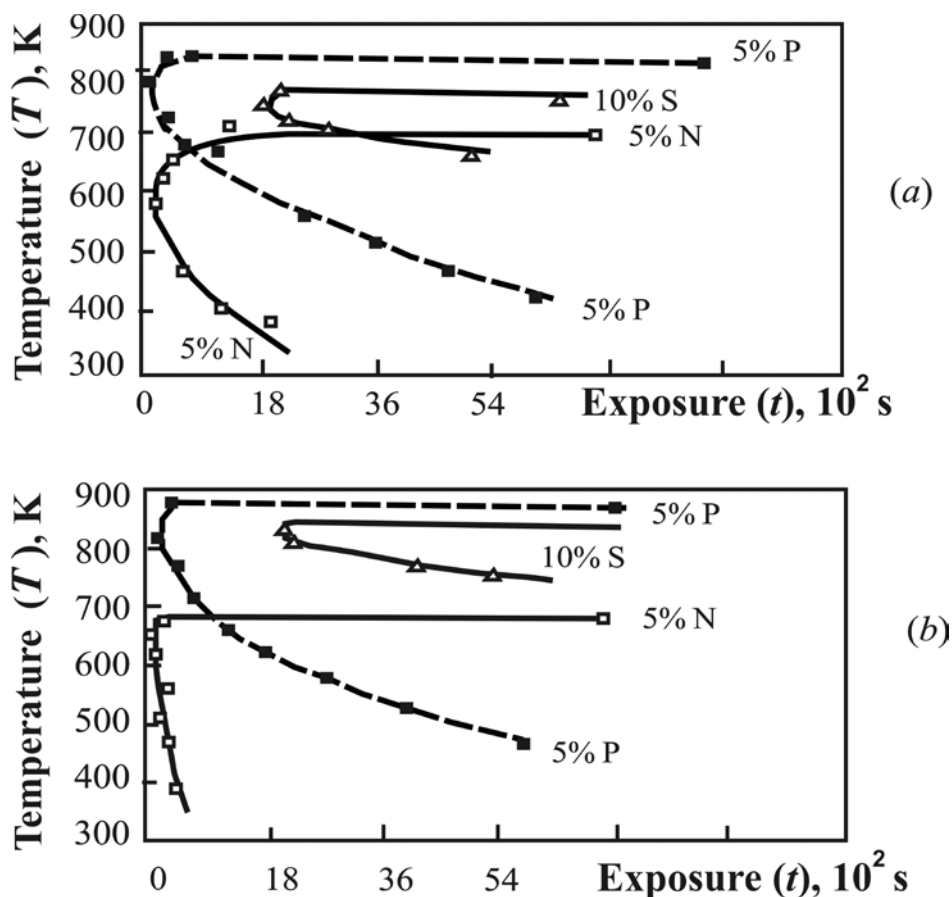


Fig. 7. Time-temperature concentration diagrams of forming 50% level of equilibrium segregations of P, S, and N in the free surface of the Fe-Cr-P alloys under isothermal exposing in vacuum:
 a) Fe-0.6Cr-0.13P-0.004S-0.001N-0.01C; b) Fe-1Cr-0.13P-0.004S-0.002N-0.01C (% , at.).

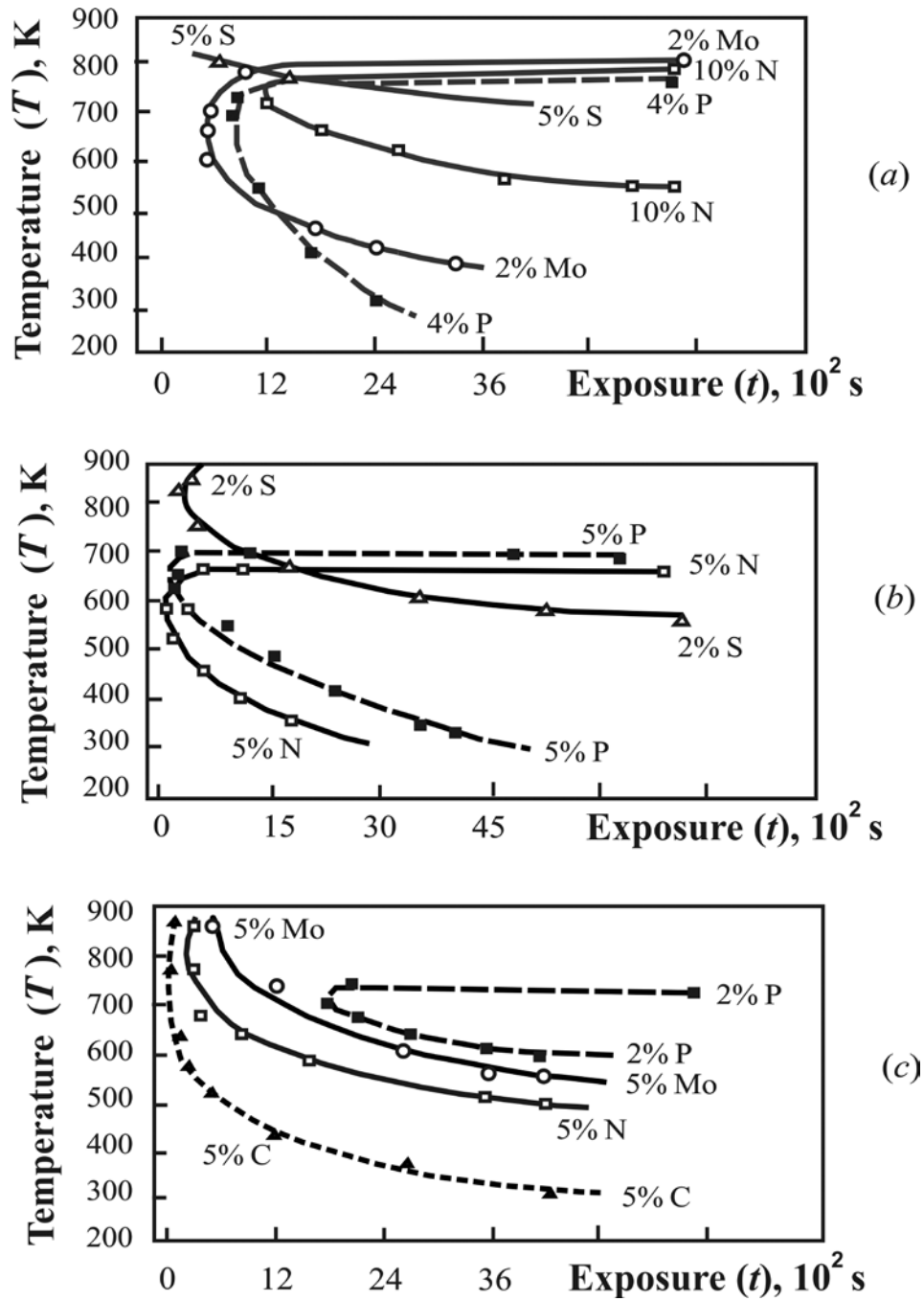


Fig. 8. Time-temperature concentration diagrams of forming 50% level of equilibrium segregations of P, S, N, C, and Mo in the free surface under isothermal exposing in vacuum of the Fe-Mo-P alloys:

- a) Fe-1Mo-0.16P-0.004S-0.014N-0.02C; b) Fe-3Mo-0.26P-0.004S-0.06N-0.03C;
 c) Fe-3Mo-0.15P-0.004S-0.1N-0.01C (% , at.).

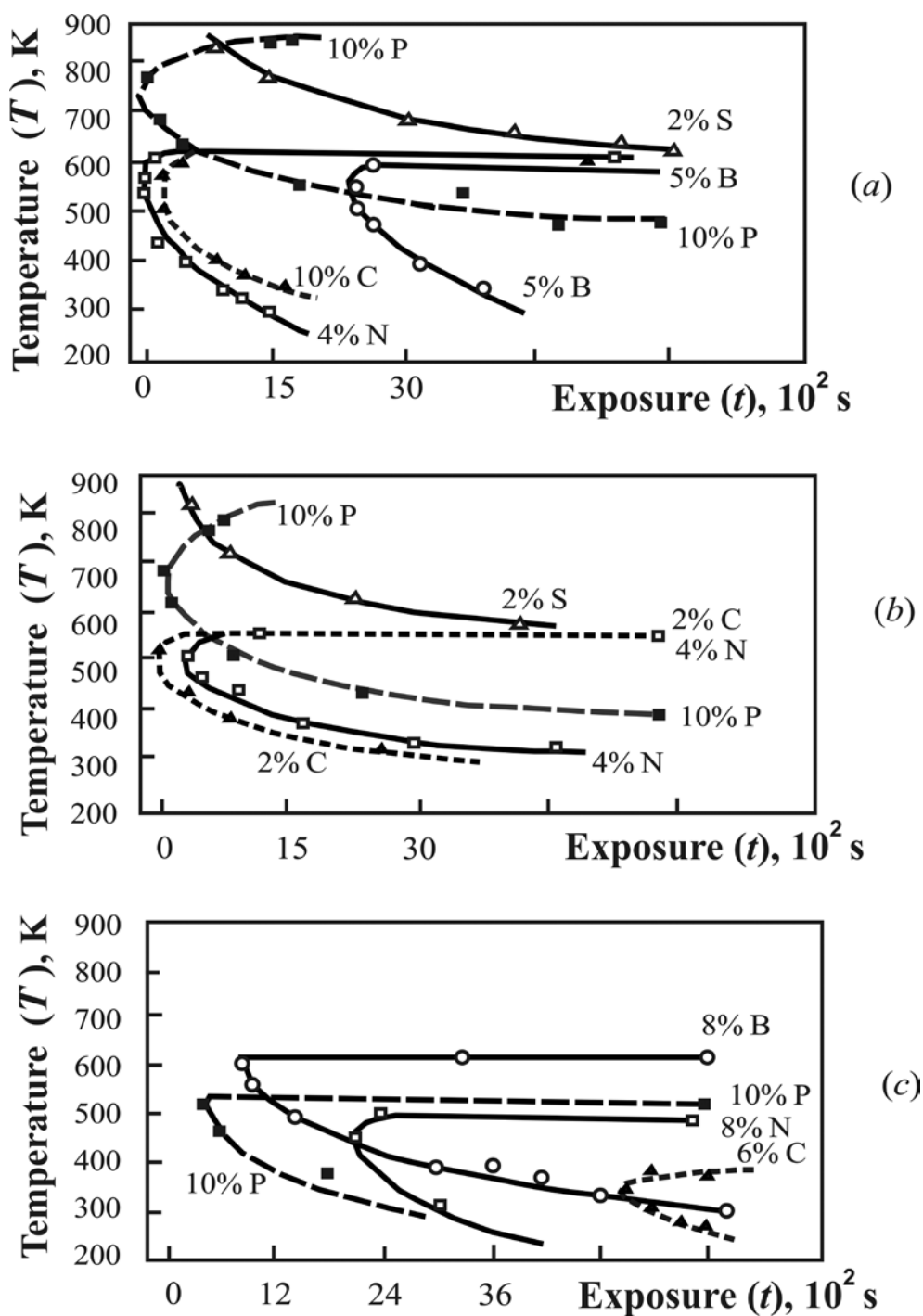


Fig. 9. Time-temperature concentration diagrams of forming 50% level of equilibrium segregations of P, S, N, C, and B in the free surface under isothermal exposing in vacuum of the Fe-B-P alloys:

- a) Fe-0.02B-0.07P-0.005S-0.03N-0.02C; b) Fe-0.03B-0.02P-0.007S-0.04N-0.02C-2.7Ni;
 c) Fe-0.002B-0.13P-0.005S-0.003N-0.03C (% , at.)

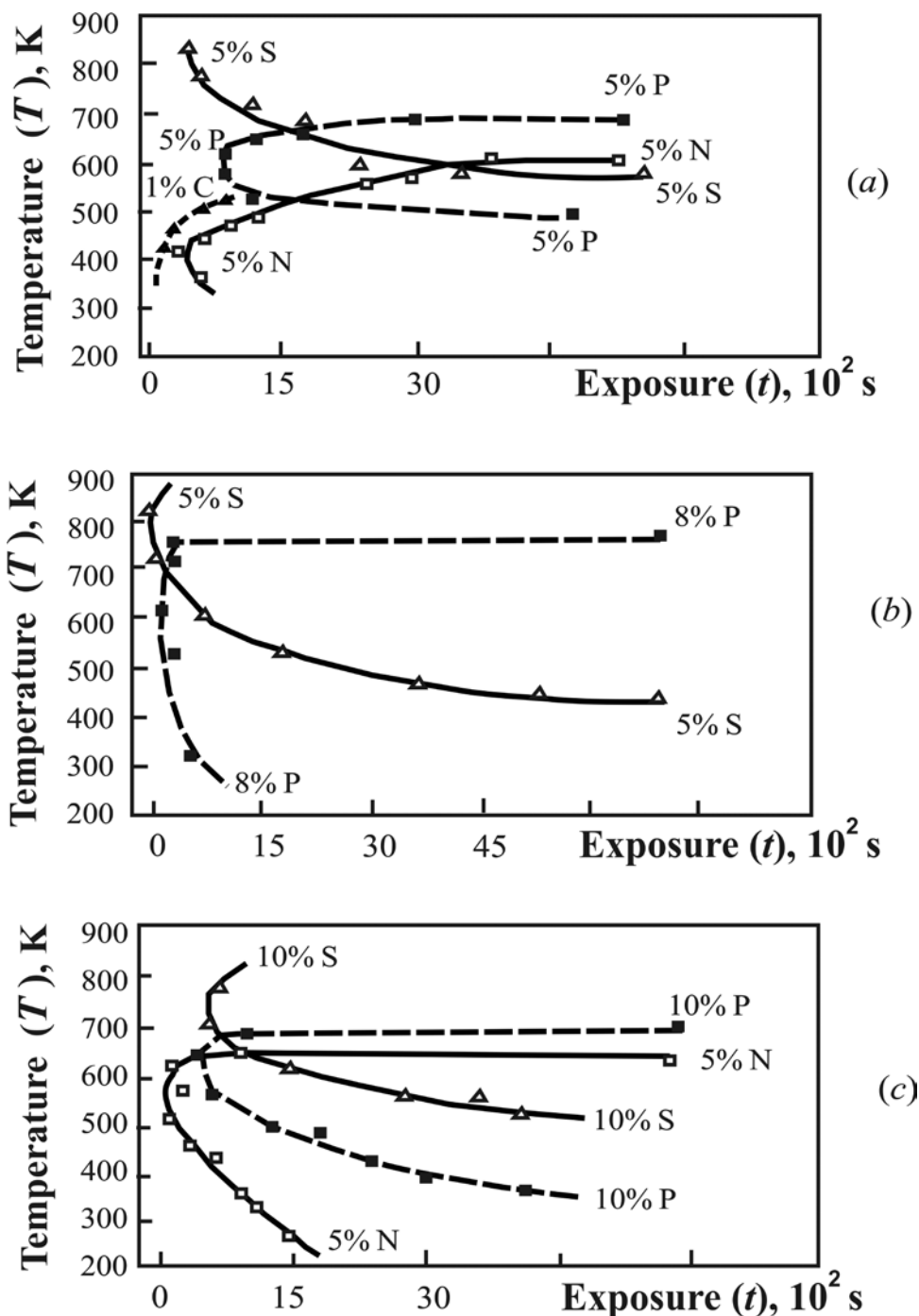


Fig. 10. Time-temperature concentration diagrams of forming 50% level of equilibrium segregations of P, S, N, and C in the free surface under isothermal exposing in vacuum of the Fe-Ni-P alloys:

- a) Fe-1Ni-0,14P-0,005S-0,06N-0,01C;
- b) Fe-3Ni-0.03P-0.005S-0.003N-0.014C;
- c) Fe-3Ni-0.17P-0.007S-0.05N-0.014C (% , at.).

From the experimental data presented in Fig.3-10, one can observe the following temperature peculiarities of soled elements segregations forming in the surface of α -Fe alloys under isothermal exposing in vacuum.

- Surface enrichment with carbon (C) presents in investigated alloys at low temperatures (lower than 600 K).

- Nitrogen (N) segregates in the temperature intervals close to 500 K -650 K.
- Segregations of a maximal concentration of P are observed near one the same temperature (closed to 800 K) coinciding with that of the known reversible temper brittleness interval of low-carbon steels (770-830 K), that was discussed in [7, 8].
- Segregations of S, Al, and Sn develop in the same temperature interval (800-950 K) having position upper than that of P (Fig. 4, 5, 6). Again, Al is segregating together with S (Fig. 5 c); while Sn displacing S, and surface segregation of the latter not forming in spite of that one presenting in the alloy volume (Fig. 6).
- With increase of the volume concentration of Cr, the temperature of P segregation formation grows (Fig. 7), while Al reducing the latter (Fig. 5).
- Influence of Al on segregation development in α -Fe based solid solutions has a complicated mechanism: low concentrations of Al sharply eliminate surface segregations of N and C (Fig. 5 a, b), the latter promoting surface activation of P by that way; with Al volume concentration increasing, the formation temperature and maximum concentration of P segregation are decreasing (Fig. 5 c).
- Segregations of Mo, Ti, and P are forming approximately in the same temperature interval (Figs. 4, 8). But, with increasing the volume concentrations of N and Mo, the temperatures of forming N, C, and Mo segregations grow up to 900K (Fig. 8 c).
- Segregations of B and Cu arise at the same temperature interval as N and C (Fig. 4 a , and Fig. 9 a, b, c)
- Nickel (Ni) eliminates segregation of boron (B) (Fig. 9 b).
- Segregations of Ni in the α -Fe alloys are absent (Figs. 3-10 a, b, c).

There are the segregation forming temperatures (SFT) from the “nose” positions of the equal-concentration curves (Figs. 3-10) for the elements solved in the investigated α -Fe alloys presented in Fig. 11 as gray rectangles having the length corresponding to the results scattering. The segregating elements are disposed along horizontal direction in the order of increase of the arithmetical average means of T_{seg} values (black points). The length of the gray rectangles for Cu, Ti, and Sn corresponds to the experimental accuracy of the Auger-spectroscopy method used: $\Delta T_{seg} = \pm 25K$.

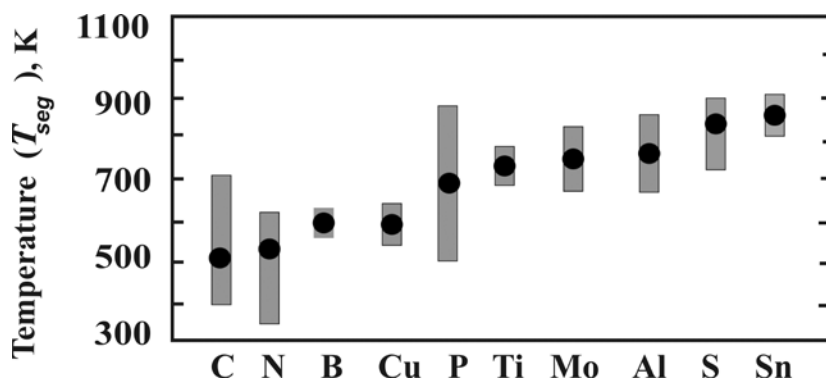


Fig. 11. The segregation forming temperatures (T_{seg}) of the elements solved in the investigated α -Fe alloys, from Auger-spectroscopy data: the gray rectangles have got the length corresponding to the results scattering; the black points are the arithmetical average means of the experimental T_{seg} values.

One can observe a certain relationship between experimental values of T_{seg} (Fig. 11) and the diffusion activation energy of the solved elements in α -Fe (Table 4): C, N, and B, having lower volume diffusion activation energies (Q), form interface segregations at lower

temperatures T_{seg} than those having Q values approximately 3-4 times higher (P, Mo, Ti, Al, S, Sn). The only exclusion is Cu.

5. Discursion of the results and the simulation model

Table 5. The values of the surface segregation temperature corresponding to C-curves “nose” positions (T_{seg} , K) with the accuracy of ± 25 K in the time-temperature concentration diagrams (Fig.3-10) for the investigated α -Fe based alloys during isothermal exposing in vacuum (bold type, an upper line); the values of $-\Delta G_{seg}$ (kJ/mol) computed from the Auger-spectroscopy data (a lower line).

Fig	Alloy volume composition (at.%)	C	N	B	P	S	Mo	Al	Ti	Cu	Sn
2, 3	Fe-0.13P-0.007S-0.025N-0.03C	470 16	630 25	X	750 22	800 5	X	X	X	X	X
4 (a)	Fe-0.03S-0.14P-0.06N-0.02C-0.005Ti-0.006Cu	-	-	X	680 19	900 7.5	X	X	710 13	590 24	X
4 (b)	Fe-0.02S-0.14P-0.3N-0.04C	-	500 15	X	550 7	820 5.8	X	X	X	X	X
5 (a)	Fe-0.6Al-0.07P-0.005S-0.02N-0.03C	420 14	350 7	X	700 20	900 7.5	X	-	X	X	X
5 (b)	Fe-1.2Al-0.05P-0.005S-0.01N-0.04C	-	-	X	820 27	900 7.5	X	650 3	X	X	X
5 (c)	Fe-5.6Al-0.06P-0.007S-0.01N-0.04C	-	-	X	620 16	800 5.5	X	850 6	X	X	X
6	Fe-0.1Sn-0.1P-0.004S-0.006N-0.1C	400 11	400 10	X	550 7	-	X	X	X	X	850 20
7 (a)	Fe-0.6Cr-0.13P-0.004S-0.001N-0.01C	-	600 22	X	780 24	750 4.5	X	X	X	X	X
7 (b)	Fe-1Cr-0,13P-0,004S-0,002N-0,01C	-	610 23	X	870 30	840 6	X	X	X	X	X
8 (a)	Fe-1Mo-0.16P-0.004S-0.014N-0.02C	-	710 30	X	700 22	850 6	650 8	X	X	X	X
8 (b)	Fe-3Mo-0.26P-0.004S-0.06N-0.03C	-	600 22	X	650 17	800 5.5	-	X	X	X	X
8 (c)	Fe-3Mo-0.15P-0.004S-0.1N-0.01C	690 26	750 35	X	700 20	-	800 10	X	X	X	X
9 (a)	Fe-0.02B-0.07P-0.005S-0.03N-0.02C	590 25	590 21	550 50	750 22	820 5.8	X	X	X	X	X
9 (b)	Fe-0.03B-0.02P-0.007S-0.04N-0.02C-2.7Ni	520 20	520 15	-	750 22	-	X	X	X	X	X

9 (c)	Fe-0.002B- 0.13P-0.005S- 0.003N-0.03C	<u>380</u> 10	<u>480</u> 14	<u>610</u> 60	<u>510</u> 6	-	X	X	X	X	X
10 (a)	Fe-1Ni-0.14P- 0.005S-0.06N- 0.01C	<u>460</u> 15	<u>460</u> 15	X	<u>600</u> 10	<u>850</u> 6	X	X	X	X	X
10 (b)	Fe-3Ni-0.03P- 0.005S- 0.003N- 0.014C	-	-	X	<u>750</u> 22	<u>900</u> 7.5	X	X	X	X	X
10 (c)	Fe-3Ni-0.17P- 0.007S-0.05N- 0.014C	-	<u>590</u> 21	X	<u>650</u> 17	<u>780</u> 5	X	X	X	X	X

(X) – the element is absent in the alloy volume composition;

(-) – segregation of the element was not observed in the considered temperature interval: 300 ÷ 1000K.

From the Hondros and Seah equation (3), using the additive approach proposed by Guttman for multi-component systems [12], we can represent the equilibrium concentration of the i -th component as the temperature function, $X_b^{\infty i}(T)$:

$$\frac{X_b^{\infty i}(T)}{X_{bo} - \sum_{i=1}^N X_b^{\infty i}(T)} = \frac{X_v^i}{X_{vo}^i(T)} \exp\left[\frac{-\Delta G_{seg}^i}{RT}\right]. \quad (4)$$

From the latter, we can appreciate the segregation energy values (ΔG_{seg}^i) for the solved components of the investigated alloys from the experimental data of this work (Figs. 3-10). To find the ΔG_{seg}^i value for every i -the element of a multi-component alloy in the present work, the concentration observed at maximal expositions (about 7200 s) with the constant temperature $T=T_{seg}^i$ (Figs. 3-10) being considered as the saturated level ($X_b^{\infty i}(T)$) localized in the layer of two-atomic thickness ($X_{bo}=2$). The limiting volume solubility values (X_{vo}^i) were the temperature functions presented in Table 2. There are the resultant values of ΔG_{seg}^i and T_{seg} from Auger-spectroscopy presented in the above Table 5. For the latter, one can observe an order-of-magnitude agreement of the obtained ΔG_{seg}^i values with the literature data in Table 1 both for surface and interface segregations.

Considering SFT (Table 5) as analogous of SST (Fig. 1b), the value T_{seg} can be mathematically determined from the maximum condition of the concentration-temperature function described with the equation (3) accounting temperature dependence of the volume solubility, as shown further.

As known, the maximum (extreme) condition of a function is equality to null of its derivative. The latter for relationship (4) looks as the following:

$$\partial X_b^{\infty i}(T)/\partial T = 0. \quad (5)$$

Obviously, the precise solution of equation (5) for the function $X_b^{\infty i}(T)$ in form of (3) does not exist, because the latter is a monotonic one similar to the solid line shown in Fig. 1, b. However, it is possible to find an approximate solution of (5) for the latter if consider conditions of the concentration $X_b^i(T)$ being close to saturation (at rather low temperatures and enough long time period of the isothermal exposing). Thus, we believe the following to be true:

$$X_b^i(T) \cong X_b^{\infty i}(T) = const \text{ and } \partial X_b^i(T)/\partial T \cong 0.$$

The segregation concentration ($X_b^{\infty i}(T)$) and the limiting volume solubility ($X_{vo}^i(T)$) are functions on the temperature. Another parameters in (4) are assumed to be independent on the

temperature: the number of segregating components of the solid solution (N); the structure and the total number of the atomic places in the segregation ($X_{bo} = const$); the thermodynamics stimulus for segregating ($\Delta G_{seg}^i/R = const$); volume concentrations of the components ($X_v^i = const$). Also, from the relationship ($\sum_{i=1}^N X_b^{\infty i}(T) = 1$) proposed above in (4), it

follows that: $X_{bo} - \sum_{i=1}^N X_b^{\infty i}(T) = const$.

Differentiating the left and the right part of the equation (4) with respect to the temperature T on the above assumptions and condition (5), we receive the following equation (6) to find $T = T_{seg}^i$:

$$\frac{\partial X_b^{\infty i}(T)}{\partial T} = \left(X_{bo} - \sum_{i=1}^N X_b^{\infty i}(T) \right) \cdot X_v^i \cdot \frac{\partial}{\partial T} \left(\frac{1}{X_{vo}^i(T)} \exp \left(\frac{-\Delta G_{seg}^i}{RT} \right) \right) = 0. \quad (6)$$

Obviously, the equation (6) will have solutions only under condition of equality to zero of the third multiplier being the derivative of a composite function; using transformation rules of the latter, we obtain the following (7):

$$-\frac{1}{(X_{vo}^i(T))^2} \cdot \frac{\partial X_{vo}^i(T)}{\partial T} \cdot \left(\exp \left(\frac{-\Delta G_{seg}^i}{RT} \right) \right) + \frac{1}{X_{vo}^i(T)} \cdot \left(\exp \left(\frac{-\Delta G_{seg}^i}{RT} \right) \right) \cdot \left(\frac{\Delta G_{seg}^i}{RT^2} \right) = 0. \quad (7)$$

Accounting that $\frac{1}{X_{vo}^i(T)} \cdot \left(\exp \left(\frac{-\Delta G_{seg}^i}{RT} \right) \right) \neq 0$, we transform (7) to the following shape

(index i further will be omitted):

$$-\frac{1}{X_{vo}} \frac{\partial X_{vo}(T)}{\partial T} + \frac{\Delta G_{seg}}{RT^2} = 0. \quad (8)$$

The equation for estimation of SST ($T = T_{seg}$) results from (8) as (9):

$$T_{seg}^2 = \frac{\Delta G_{seg}}{R} \left[X_{vo}(T) / \left(\frac{\partial X_{vo}(T)}{\partial T} \right) \right]. \quad (9)$$

Analysis of the equation (9) for the possibility of existing of its solution for T results in the following conclusions. Firstly, solution of (9) for $T = T_{seg}$ being positive by physical interpretation, as the absolute temperature ($T_{seg} > 0$), can exist only if the two conditions simultaneously hold: 1) $\Delta G_{seg} > 0$, that is thermodynamics condition of the element equilibrium segregation forming; 2) the volume solubility of the element is increasing with the temperature, that is $\partial X_{vo}(T)/\partial T > 0$. The latter condition, according to the literature data (Table 2), is valid for the most of elements solved in α -Fe (S, P, B, Sn, Al, Mo, Cu) but Mn and Ni. The volume solubility of the last ones decreases with the temperature growth. In that case, obviously, equation (9) does not have solutions in the field of $T_{seg} > 0$. Secondly, it follows from (9) that SST ($T = T_{seg}$) grows when the value of ΔG_{seg} increases. The latter circumstance can be weighty for development of heat treatment conditions preventing harmful impurities segregation in low-carbon steels and Fe-based alloys, proposing that external and internal surfaces to be identical in case of the internal adsorption phenomenon under consideration. Thirdly, absolute accuracy of the volume solubility temperature data ($X_{vo}(T)$) presented by the list square method approximation in Table 3 [15, 16] is not of so great importance for the fulfilled simulations, as the term inside the square brackets of (9) is nothing less than the relative change of the volume solubility $X_{vo}(T)$ in respect of the temperature.

Solution of the equation (9) for T_{seg} can be found by the step-by-step approaching method. For this, (9) transforms into (10) by the following manner:

$$(T_{seg})_{j+1} = \sqrt{\frac{\Delta G_{seg} X_{vo}(T_j)}{R} / \frac{X_{vo}(T_j + \Delta T) - X_{vo}(T_j)}{\Delta T}}, \quad j = 1, 2, 3, 4, \quad (10)$$

The calculations realized in this work have shown that the equation (10) has a satisfactory convergence for α -Fe based binary systems at the following initial conditions: $300\text{K} \leq T_o \leq 900\text{K}$, $\Delta T = 1 \div 10 \text{ K}$.

So, for a number of the elements forming the surface segregations in α -Fe under isothermal exposing in vacuum (due to internal adsorption), the experimental values of SFT from Table 5 and the simulated SST ones (T_{seg}) resultant from (10) are presented as functions on ΔG_{seg} in Fig. 12, where the solid lines are simulated, and the points being the experimental ones.

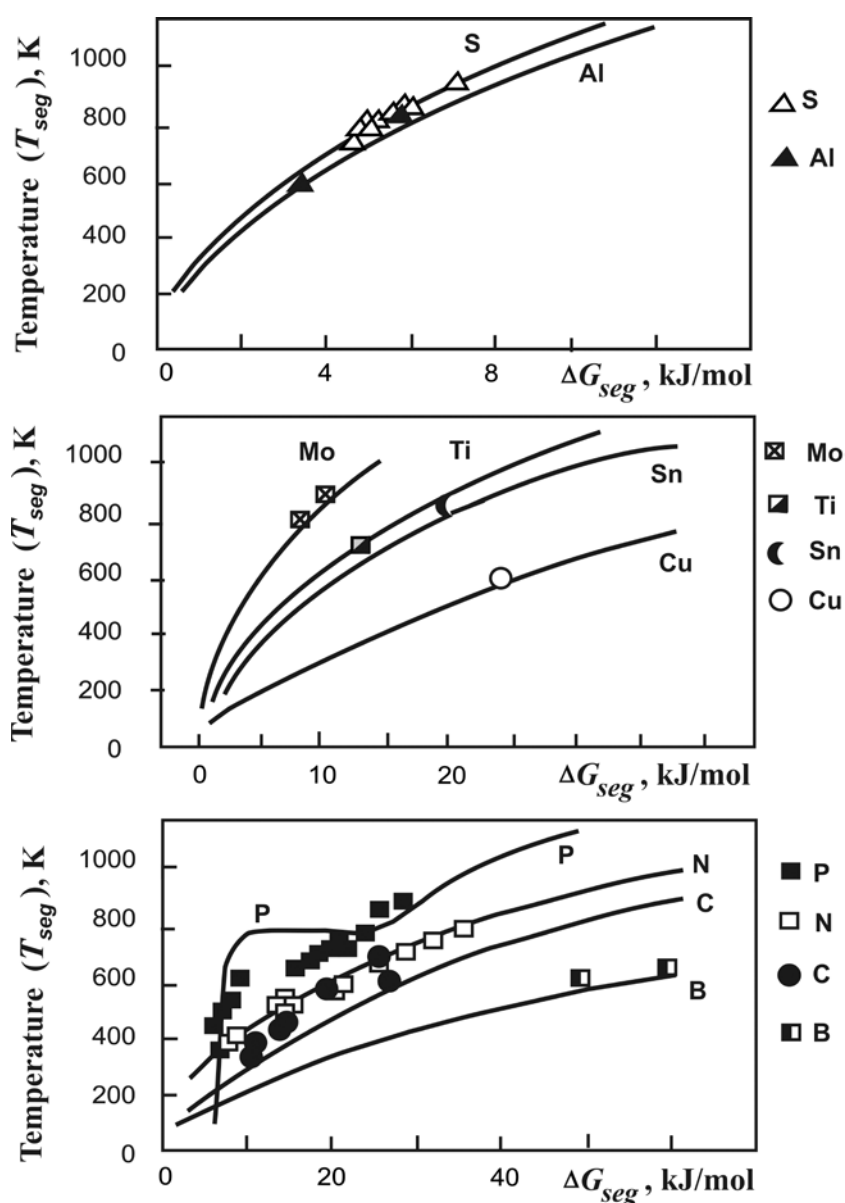


Fig. 12. Experimental (points) and computed (curves) data of the values of T_{seg} against ΔG_{seg} for a number of the elements segregating in the free surface of the investigated α -Fe alloys under isothermal exposing in vacuum.

There is correlation between the experimental points and the simulated curves shown in Fig. 12. Particularly, in the both cases the segregations of C, N, and B are forming in lower temperatures than those of P, Mo, Ti, Al, S, Sn, Cu; segregations of S and Al appear at higher temperatures than P and Mo segregating in the same interval. Again, the last figure (Fig. 12) illustrates the experimentally observed SFT values to be in relation with the thermodynamics parameter ΔG_{seg} , the latter in turn being dependent on the alloy composition. For notice: a relatively low level of SFT for Cu (Fig. 11) is probably due to a low value of the corresponding ΔG_{seg} , according to (9).

6. Conclusions

The obtained experimental data from Auger-spectroscopy method confirm that surface segregations of a solved element (C, N, B, P, Mo, Ti, Al, S, Sn, Cu) in α -Fe alloys under isothermal exposing in vacuum due to internal adsorption are formed in a certain temperature interval that can differ from those ones of the other solved elements. Particularly, it is shown that segregations of the elements such as C, N, B having the low values of activation energy of diffusion in α -Fe are forming in lower temperatures of exposing than those of the slower elements (P, Mo, Ti, Al, S, Sn, Cu) having the higher diffusion activation energies.

There was proposed a theoretical relationship between the temperature interval of forming the surface segregation of an element solved in α -Fe, the thermodynamics stimulus of its segregation (ΔG_{seg}), and its volume solubility change in respect of the temperature ($\partial X_{vo}(T)/\partial T$).

The obtained results can be important for metallurgical technologies using heat treatment to prevent intergranular failure of low carbon structural steels and maraging steels.

Acknowledgements. *This work financially supported by Russian Foundation for Basic Researches (Projects #16-08-00599 and #17-08-01193) and by State Task #2017/113 of Ministry of Education and Science of Russian Federation.*

References

- [1] D. McLean, *Grain Boundaries in Metals* (Oxford University Press, London, 1957).
- [2] E.D. Hondros, M.P. Seah // *Met. Trans.* **8A** (1977) 1363.
- [3] P. Lejcek, *Grain Boundary Segregation in Metals* (Springer, Heidelberg, Germany, 2010).
- [4] M.P. Seah, In: *Practical Surface Analysis by Auger and X-ray Photoelectron Spectroscopy*, ed. by D. Briggs and M.P. Seah (John Wiley & Sons, Chichester, 1983), Chapter 13.
- [5] M. Guttman, Ph. Dumoulin, M. Wayman // *Metallurgical Transactions* **13A(10)** (1982) 1693.
- [6] M.P. Seah, C. Lea // *Scripta Metallurgica* **18(10)** (1984) 1057.
- [7] A.I. Kovalev, V.P. Mishina, G.V. Scherbedinsky // *FMM* **62(1)** (1986) 126. (in Russian)
- [8] A.I. Kovalev, V.P. Mishina // *Metallophysica* **9(4)** (1987) 45. (in Russian)
- [9] Yu.G. Abashkin, A.P. Dementyev, T.M. Jibuty, O.P. Ivanova // *Poverhnost'. Rentgenovskie, Sinkhrotronnye I Neitronnye Issledovaniya (The Journal of Surface Investigation. X-ray, Synchrotron and Neutron Technique)* **11** (1989) 48. (in Russian)
- [10] A.I. Kovalev, V.P. Mishina, G.V. Scherbedinsky // *Metallophysica* **9(3)** (1987) 112. (in Russian)
- [11] K. Masuda-Tindo // *Phys. Stat. Sol. (B)* **134** (1986) 545.
- [12] Ph. Dumoulin, M. Guttman // *Materials Science and Engineering* **42(11-13)** (1979) 249.
- [13] H.J. Grabke // *Materials Technology Steel Research* **57(4)** (1986) 178.

- [14] B.L. Eyre, B.C. Edwards, J.M. Titchmarsh, In: *Adv. Phys. Met. and Appl. Steels Int. Conf.* (Chameleon press, London, 1982), p.246.
- [15] O.A. Bannykh, P.B. Budberg, S.P. Alisova et al., *Phase Diagrams of Binary and Multicomponent Systems based on Ferrous* (Metallurgy, Moscow, 1966). (in Russian)
- [16] O. Kubaschewski, *Iron-Binary Phase Diagrams* (Springer Verlag, Berlin, Heidelberg, Germany, 1982)
- [17] C.B. Zemsky, D.A. Litvinenko // *FMM* **32(3)** (1971) 591. (in Russian)
- [18] J. Wroblewski, J. Rasek, J.W. Morom // *Acta Phys. Pol. A* **A46(6)** (1974) 737. (Poland)
- [19] S.A. Golovin, M.A. Krishtall, A.N. Svobodin // *Fizika i himia obrabotky materialov (Physics and Chemistry of Materials)* **1** (1968) 119. (in Russian)
- [20] T. Matsuyama, H. Hosokawa, H. Suto // *Transactions of Japan Institute of Metals* **24(8)** (1983) 589.
- [21] M.A. Krishtall, A.R. Mokrov // *Zash'ita Metalov (Protection of Metals)* **1** (1967) 18. (in Russian)
- [22] A.M. Huntz, M. Aucouturier, P. Lacombe // *C.R. Acad. Sci.* **265(10)** (1967) 554.
- [23] A. Vignes, J. Philibert, M. Badia, J. Levasseur, In: *Trans. 2nd Natl. Conf.: Electron Microprobe Analysis* (Boston University Press, Boston, 1967), Paper N20.
- [24] P.L. Gruzin, V.V. Mural', A.P. Fokin // *FMM* **32(1)** (1971) 208. (in Russian)
- [25] Y. Adda, J. Philibert, *La Diffusion Dans les Solides* (Par Saclay, Paris, 1966).
- [26] V.A. Lazarev, V.M. Golikov // *FMM* **29(3)** (1970) 598. (in Russian).
- [27] V.P. Shapovalov, A.N. Kurasov // *Metallovedenie i termicheskaya obrabotka metallov (Metal Science and Heat Treatment)* **9** (1975) 71. (in Russian)
- [28] A.I. Kovalev, D.L. Wainstein, In: *Handbook of metallurgical Design*, ed. by G. Totten, Lin Xie and Kiyoshi Funatani (Marcel Dekker Inc., N.Y., U.S.A., 2004), p.57.

CARBIDE FORMING SPECIAL FEATURES AND FRACTURE MECHANISMS UNDER THE AUSTENITIC CHROMIUM-NICKEL 304 STEEL POST-LIFE AGEING

S.N. Petrov^{*}, O.Yu. Prokoshev, B.Z. Margolin, A.M. Shumko

National research centre “Kurchatov Institute” - Central Research Institute of Structural Materials
“PROMETEI”, Saint-Petersburg, 191015, Russia

*e-mail: npk3@crism.ru

Abstract. Post-life ageing of austenitic chromium-nickel 304 steel elements of the fast neutrons reactor equipment was carried out at a temperature above the operating conditions. The change in the short-term mechanical properties of the material was investigated. The relationship between the change in impact strength, fracture mechanisms and the morphology of carbide precipitates was revealed.

Keywords: post-life ageing; austenitic steel; mechanical properties; fracture mechanisms; microstructure; carbides precipitation.

1. Introduction

An operating temperature of the fast neutrons reactor equipment structural elements can be up to 550°C for a long time. Austenitic chromium-nickel 304 steel is one of the main structural materials for these elements. It is known that under these operating conditions, steel exhibits a tendency to thermal ageing, leading to degradation of the material properties [1].

There are a number of publications where changes in the mechanical properties and structure of 304 steel under the thermal ageing effect are considered [1-4]. The investigations were carried out both on metal aged under laboratory conditions [1, 2] and on metal after post-life ageing during 200,000 hours [3]. As shown in work [4], the 304 steel was studied in two states after operation in the intermediate heat exchanger (reboiler) of the fast neutrons reactor at 515-550°C for 170 thousand hours and after laboratory ageing at 700°C. It was confirmed that thermal ageing practically does not affect both to the yield strength and ultimate strength of the material. Thermal ageing most strongly affects to the ductility and impact resistance. These changes in the mechanical properties were associated with microstructural changes, in particular, with the Cr₂₃C₆ carbides precipitation on the grain boundaries, weakening the cohesive strength of the grain boundaries. The plasticity, toughness and crack resistance decreases, the temperature dependence of these properties changes and the tendency to cold-brittle appears under the ageing process.

The fast neutrons reactor design service life may be up to 480 thousand hours. Obviously, in a time-limited period of research and/or constructional design, experimental results which justify such a long service life of materials can only be obtained through accelerated ageing at elevated temperatures. It is desirable to provide such a temperature and holding time combination, so that a mechanism for changing the microstructure and properties at the accelerated ageing was the same for ageing under operating conditions. For the equipment life prediction, it seemed expedient to carry out the service equipment elements

ageing at an elevated temperature, i.e. in fact, it is the ageing of material previously worked at operating temperatures, with the aim of longer service life modeling. In this case, the studies duration due to the operating exposure is reduced, and also, what is important, the full-scale metal of the equipment elements is investigated. The present work is devoted to the problem of the short-term mechanical properties changing and their correlation with fracture mechanisms of austenitic chromium-nickel 304 steel during the post-life ageing process.

2. Materials and methods

The investigations were carried out on a 304 steel samples cutting from the upper tube plate conical transition of the fast neutrons reactor reboiler after exploitation at a 515-550°C range temperature with a duration up to 170,000 hours. In the reboiler manufacturing formulae, the upper tube plate metal before the installation was heat-treated at a 1050°C. To simulate the initial state, some of the metal samples to be studied were heat-treated at the same temperature for 30 minutes in order to restore the properties. The chemical composition of the metal is shown in Table 1.

In laboratory furnaces at a temperature of 700°C, the ageing of metal after exploitation up to 15,000 hours was carried out.

Impact-bending tests were carried out on the Charpy V-notch specimens at the temperature of 20°C, which most sensitive to thermal ageing. The fracture patterns, local elemental and phase composition of precipitates investigations were carried out using a scanning electron microscope Vega II (Tescan).

Table 1. Chemical composition of the investigated steel.

Elements content, mass. %							
C	Cr	Ni	Mn	Si	S	P	Ti
0,09	17,8	8,9	1,36	0,63	0,008	0,010	0,05

3. Mechanical tests results

The impact resistance effects ($T_{\text{test}} = 20^\circ\text{C}$) on the thermal ageing time at a $T = 700^\circ\text{C}$ are shown in Fig. 1. The initial point of this correlation corresponds to the impact strength value after exploitation. The impact resistance value in the simulated initial state is also presented for comparison.

The time dependence of the metal impact resistance under ageing process is nonmonotonic with a maximum in the range from 4000 to 6000 h. When thermal ageing time is more than 6000 h, the impact strength gradually decreases, asymptotically approaching to the metal impact strength values in the state after exploitation.

4. Fractographic investigations results

Fracture surface specimen images under impact loading after exploitation are shown in Fig. 2. The flat facets (Fig. 2-b), formed by the quasi-brittle fracture mechanism, are observed among viscous intergranular fracture points (Fig. 2-a).

The size of these facets without signs of plastic deformation is comparable with the size of the metal grain. At the same time a large number of facets located in a plane that is parallel to the macrocrack propagation. The flat facets are observed at the specimen fracture even visually when the light is reflected. In areas of viscous intergranular cup fracture, particles of a globular shape are observed. The X-ray spectral microanalysis of these particles allows to identify them as a chromium carbides.

The simulated initial state sample fractions are formed entirely by the viscous intercrystalline fracture mechanism.



Fig. 1. "The 304 steel impact strength - the ageing time at a 700 °C" curve. $T_{\text{test}} = 20^{\circ}\text{C}$.
 ◇ - simulated initial state after austenitization, ◆ - state after exploitation,
 ■ - post-life ageing.

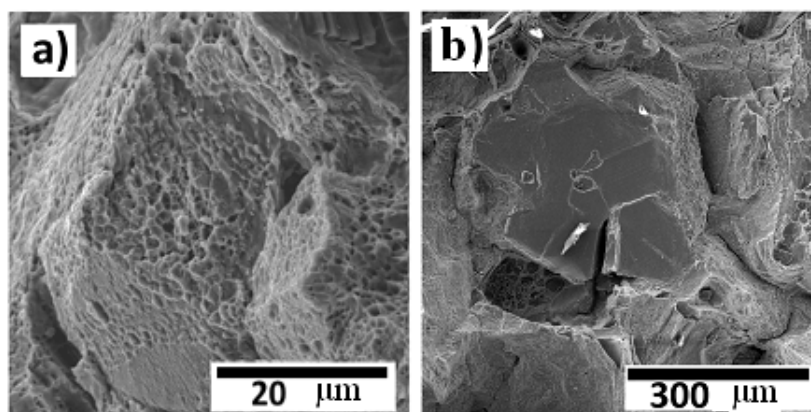


Fig. 2. The sample fracture surface under impact loading after exploitation: a) viscous intergranular fracture area; b) quasi-brittle intergranular fracture facets.

The sample surface fracture in the first stage of post-life ageing ($\tau = 4000$ h) corresponding to the impact strength maximum ($\text{KCV} = 207 \text{ J / cm}^2$) visually looks brushed. The fracture after impact loading is formed mainly by viscous intergranular fracture areas (Fig. 3-a). When the surface was studying in a scanning electron microscope, only individual quasi-flat areas with a traces of plastic deformation (Fig. 3-b) were detected. The depth of the plastic zone in such areas is somewhat smaller in comparison with the surrounding areas.

When ageing time increasing ($\tau = 15,000$ h) and it is correspond to the "plateau" on the "impact resistance – post-life ageing time" curve, facets similar to those found for samples after exploitation (Fig. 2-b) were found on fractures.

Facets images on fractures after exploitation, as well as a quasi-flat areas on the sample fracture after 4000 hours of ageing, obtained at high magnification, are shown in Fig. 4. It was possible to reveal a continuous layer of lamellar particles covering the surface at the flat facets surfaces observed for low magnifications after the exploitation (Fig. 4a). On a quasi-flat area

of the sample's fracture after ageing ($\tau = 4000$), such particles do not form a continuous layer and it have smaller dimensions in the observation plane (Fig. 4b). For the facets after 15,000 hours of ageing, a continuous layer of lamellar particles, as for facets after exploitation, was again found.

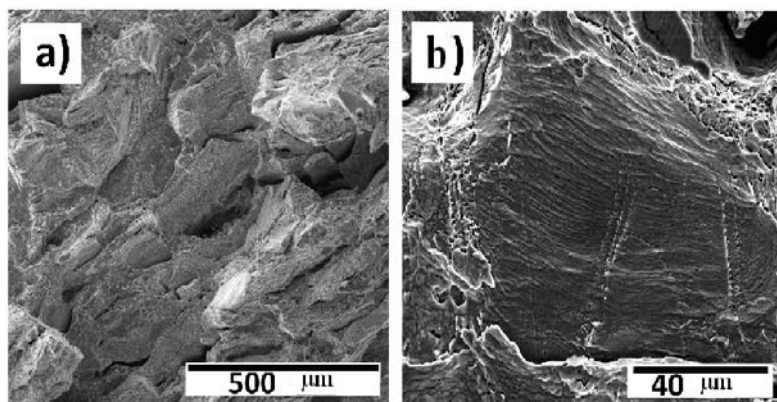


Fig. 3. Samples fracture surfaces under impact loading after post-life ageing process during $\tau = 4000$ h: a) general form, b) quasiplane areas with a traces of plastic deformation.

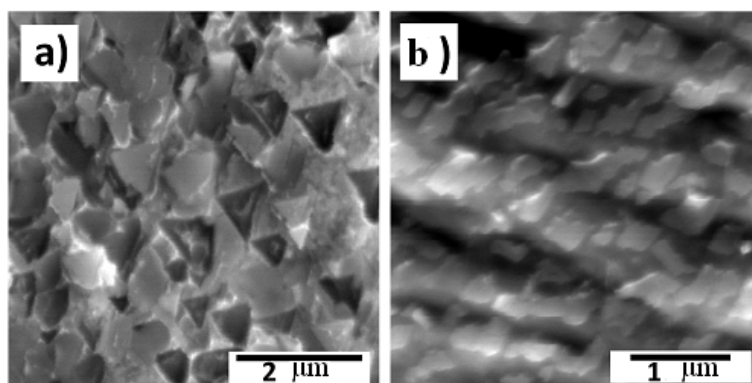


Fig. 4. The flat surfaces fractures images at high magnification: a) after exploitation, b) after post-life ageing ($\tau = 4000$ hours).

X-ray spectral microanalysis (EDX) of the facets surfaces covered with a continuous layer of precipitates, carried out with a variation of the probe electron energy from 10 to 20 keV by the method of [5] made it possible to establish the presence of a chromium carbide layer with a thickness of 0.02 μm .

Identical areas separated by the crack development were identified by comparing the fractions of the two response halves of the sample from the material after exploitation. Images of such facets are shown in Fig. 5. With a low magnification, an imperceptible relief on the facets surface, formed when facets intersect with glide planes, is observed. It should be noted that the surface filled density by the lamellar particles within the frame of facet plane changes. The transition zone is shown in Fig. 5-c, there are few particles in the upper part of the figure, their dimensions are far less than the distance between the glide planes traces, and the lower part of the surface figure is filled with a continuous layer of lamellar particles. A similar picture is observed on the material formed during fracture, and the mutual arrangement of the areas densely filled with particles on both halves of the destroyed sample allows us to conclude that the crack developed in a thin layer of the lamellar particles of chromium

carbide, and not along the carbide-metal interface (Fig. 5-a and 5-b). Identical thickness of the chromium carbide layer from both halves of the specimen fracture, equal to $0.02\ \mu\text{m}$, was detected using the EDX method. This indicates that the tear occurred approximately in the middle of the carbide layer, and its resulting thickness is $0.04\ \mu\text{m}$. When the facets surface observed with a large magnification, it is established that in the observation projection a significant number of the detected particles have the shape of an equilateral triangle (Figs. 4-a, 5-c), moreover, their sides orientation corresponding to the glide planes direction (Fig. 5-c).

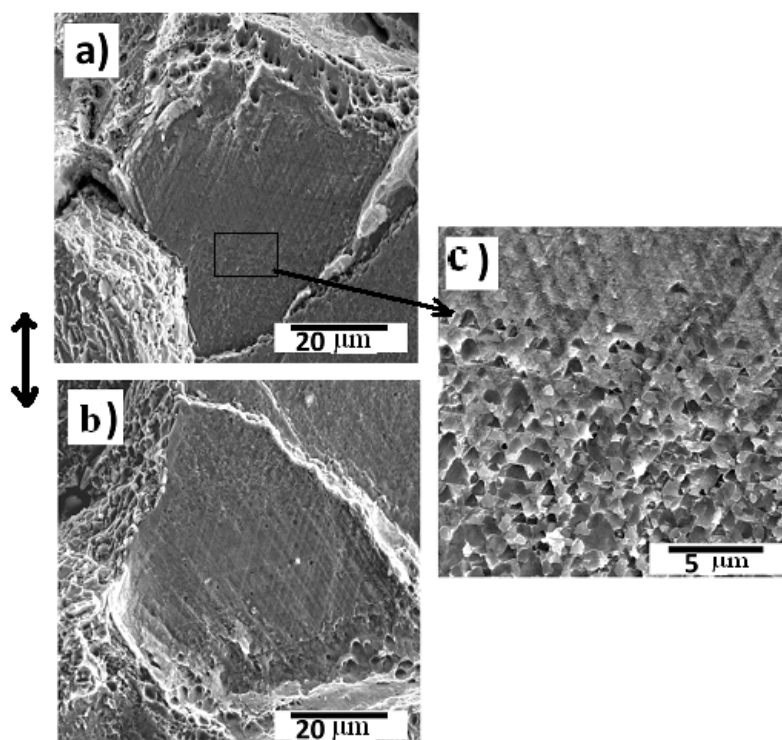


Fig. 5. The facets image of the two response halves (a, b) of the fractured sample after exploitation, and (c) – the transition zone between the areas with different carbide densities.

5. Discussion

The obtained results indicate that degradation of material properties under the thermal ageing of 304 steel occurs due to the formation of grain-boundary chromium carbides, which reduce the cohesive strength of the material. This corresponds to the results of previous studies on thermal ageing [1-4].

It is established that in the formation of globular carbides at the grain boundaries, the mechanism of viscous intergranular destruction due to the nucleation, growth, and association of pores is realized. The formation of a continuous layer of lamellar carbides leads to quasi-brittle fracture by the mechanism of interlayer separation, the crack developing within a thin layer of plate-like carbides. Fractographic studies have shown that changes in mechanical properties during the ageing are directly related to the fracture mechanisms that are being realized. Reduction of toughness and plasticity after a long exploitation is due to a change in the fracture mechanism from the viscous intragranular characteristic of austenitic steels to a viscous intergranular and, in part, quasi-brittle intergranular mechanism. An increase in the toughness at the initial stage of post-life ageing is accompanied by the absence of sections of quasi-brittle fracture (flat facets) observed on metal fractions in a state after exploitation. The

decrease in the toughness at long post-life ageing times is associated with the appearance of newly facets of quasi- brittle fracture. In this regard, the question of the formation of plate-like carbides should be discussed in more detail.

Metals with FCC lattice, as a rule, retain the viscous transcrystalline nature of failure in a wide temperature range, only when the cohesive strength of the grain boundaries of such materials is weakened by various precipitates at low test temperatures; a transition to intergranular destruction, including quasi-brittle, can occur [4, 6]. Intergranular destruction is realized due to the specific interaction of the deformation bands with the grain boundaries, with sufficient plasticity of the FCC materials, the accumulation of the plastic deformation traces in the form of steps of inconsistency on the boundary surface occurs, and when the critical concentration of these steps is reached, destruction will occurs [6]. The presence of steps of discrepancy is clearly observed in the images of the facets of quasi-brittle fracture both for high and low magnifications (Fig. 5). On the other hand, of brittle behavior mechanisms of FCC steels with a high nitrogen content associated with the interaction of active and inactive glide planes have been described [7]. In the case of inhibition of active glide planes by interstitial impurities, in particular, by dissolved nitrogen atoms, when the active planes intersect the inactive tearing voltage in the direction perpendicular to the inactive plane, leading to quasi-brittle failure, can be formed.

On the obtained facet images at high magnification (Fig. 4-a), it is seen that the intersection of the layer of plate-like carbides on the facet surface by glide planes was accompanied by the cracks formation, so that the particles on the facet surface predominantly have the shape of an equilateral triangle. In the area of the facet covered with a less dense layer of carbides, the inconsistency steps (Fig. 5-c) are clearly observed. It can be concluded that the braking of glide planes when they intersect a layer of plate-shaped carbides, the formation of a separation surface along a weak spot, between layers of lamellar carbides led to a quasi-brittle development of the intergranular crack. Later, the crack spread along the boundary along the sections with less dense filling with carbides, but with the accumulated steps of inconsistency.

The specific shape of the plate-like carbide particles in the form of an equilateral triangle, seen on the facets, is evidently formed upon fracture as a result of the intersection of the carbide layer by the glide planes of the $\{111\}\gamma$ family. Plates of carbides in the form of an equilateral triangle, observed on the facet surface, are parallel to one of the faces of the tetrahedron formed by the planes of the $\{111\}\gamma$ family. The triangle would not be equilateral with another orientation of the facet plane relative to the active glide planes. It should be noted that, since in FCC materials the formation of twins occurs along the $\{111\}$ family planes, an extended flat facet of quasi-brittle fracture is the double boundary. This leads to the fact that carbides of a specific plate form are formed on the twin boundary surface. The specific plate form of carbides was studied in detail by Beckith and Clark [8], who proved that in the presence of the orientation relation of the cube-cube:

$$\begin{aligned} & \{100\}_{\gamma} \parallel \{100\}_{M_{23}C_6} \\ & \langle 010 \rangle_{\gamma} \parallel \langle 100 \rangle_{M_{23}C_6}, \end{aligned} \quad (1)$$

in the case of the conjugation of crystallite $Cr_{23}C_6$ with austenite substrate along the (111) plane, the maximum correspondence of the crystal lattice sites of the growing particle and substrate is reached, and the matching parameter of crystal lattices in this case approaches 0.99.

In this connection, when a germ is formed on the twin boundary, the orientation ratio is satisfied on both sides of the growing carbide. This is the reason for the specific platelet shape of the particle and this creates the conditions for the formation of a continuous layer of particles along the entire surface of the twin. At the intergranular boundaries, chromium

carbides with globular shape predominate. Both types of particles reduce the cohesive strength, but the destruction of grain boundaries is accompanied by plastic deformation, since the globular particles do not cover the sections of the boundary with a continuous layer. On the fracture, they are usually located as a "cups" form on the surface (Fig. 2-a). Plastic deformation during fracture along these boundaries is absent when twin boundaries are densely filling with plate-shaped carbides (Fig. 2-a). The absence of quasi-brittle fracture on fractures after post-life ageing during 4000 hours, as well as a significant decrease in the filling density of quasi-plane surfaces with carbides, indicates about a partial dissolution of plate-like carbides (Fig. 4b). Apparently, in the transition from operating conditions to a post-life ageing at elevated temperatures, conditions for the dissolution of carbides are created, and this leads to a partial restoration of the steel properties. It can reasonably be assumed that the specific shape of the plate-like carbides leads to their faster dissolution as compared with a globular carbides, due to a much larger specific surface area. After a longer post-life ageing, the formation of lamellar carbides on the twin boundaries begins again, it leads to the appearance of facets of quasi-brittle fracture and, as a consequence, to the material degradation. Thus, the change in the process direction, the partial dissolution of the carbides in the first stage of post-life ageing, and the return to their growth with an increasing of ageing time, cause the formation of a maximum on the "impact resistance – post-life ageing time" curve.

It can be assumed that the presence of a significant chromium concentration gradient in the border regions after thermal ageing under operating conditions is a probable cause of partial dissolution of carbides in the first stage of post-life ageing. A prolonged holding at a relatively low temperature, from the point of view of the substitution element diffusion rate, as well as the reaction of carbide formation on the grain boundary, controlled by the slow diffusion of chromium, but with a very high equilibrium constant, provides the border zone formation depleted of chromium. A similar phenomenon is observed in tests for intergranular corrosion under conditions of provocation of carbide formation [9]. The dissolution will continue until the chromium concentration is equalized at the boundary of the carbide with the metal at equilibrium under these conditions; after this, due to the diffusion of chromium from the volume, the carbide growth process will begin again and will proceed at a higher rate because of the higher diffusion mobility of chromium. A rigorous justification of the hypothesis proposed requires detailed thermodynamic and kinetic calculations, which is beyond the scope of this article.

6. Conclusions

1. The nonmonotonic dependence of the toughness after post-life ageing at an elevated temperature at 700 °C of 304 steel, previously operated in heat exchanging equipment of fast neutron reactor at a range temperature up 518 to 550°C for 1700000 hours, was detected. Partial restoration of impact strength with a maximum in the range of 4000-6000 hours of attrition occurs at the initial stage of ageing, then the values decrease, asymptotically approaching the level for the metal after exploitation. Such post-life ageing of steel does not conservatively model its further operational ageing.
2. It has been shown that the partial reduction of impact strength at the initial stage of ageing is mainly due to the dissolution of lamellar chromium carbides on the twin boundaries and, as a result, by the removal of facets of quasi- brittle fracture on fractures.
3. It is shown that the specific plate form of carbides is due to the orientation relationship with the growth of carbides at the twin boundaries.

Acknowledgements. *Experimental research was carried out on the equipment of the Center of the common facilities "Composition, structure and properties of structural and functional materials" SRC "Kurchatov Institute" - CRISM "Prometey" with the financial support of the state represented by the Ministry of Education and Science under the agreement No. 14.595.21.0004, unique No. RFMEFI59517X0004.*

References

- [1] J.A. Horak, V.K. Sikka, D.T. Raske, In: *International conference on nuclear power plant aging, variability factor and reliability analysis (San-Diego, Ca (USA), 7-12 July, 1983)*, p.301.
- [2] Y. Minami, H. Kimura and Y. Ihara // *Mater. Sci. and Tech.* **2** (1986) 795.
- [3] R.N. Grishmanovskaya, A.S. Kudryavtsev, V.G. Markov, In: *"Material issues in design, manufacturing and operation of nuclear power plants equipment"* (Pushkin-Saint-Petersburg, 2006), Vol. 2, p.290.
- [4] I.P. Kursevich, B.Z. Margolin, O.Yu. Prokoshev et al. // *Inorg. Mater.: Appl. Res.* **6** (2013) 562.
- [5] J.D. Brown, R.H. Packwood // *X-Ray Spectr.* **11** (1982) 187.
- [6] V.V. Rybin, V.N. Perevesentsev // *Soviet Physics, Solid State* **17** (1975) 2103.
- [7] Y. Tomota, Y. Xia, K. Inoue // *Acta Mater.* **46** (1998) 1577.
- [8] F.R. Beckitt, B.R. Clark // *Acta Metallurg.* **15** (1967) 113.
- [9] S.C. Bali, V. Kain, V.S. Raja // *Corrosion* **65** (2009) 726.

GAS-JET METHOD OF METAL FILM DEPOSITION: DIRECT SIMULATION MONTE-CARLO OF He-Ag MIXTURE FLOW

N.Y. Bykov^{1*}, A.I. Safonov², D.V. Leshchev¹, S.V. Starinskiy², A.V. Bulgakov²

¹Peter the Great St. Petersburg Polytechnic University, Polytechnicheskaya str., 29, St.Petersburg, 195251, Russia

²Kutateladze Institute of Thermophysics SB RAS, Lavrentyev Ave., 1, Novosibirsk, 630090, Russia

*e-mail: bykov_nyu@spbstu.ru

Abstract. Nanostructured silver films were produced by the gas-jet deposition method for the temperatures of the Ag vapor source (a crucible) in the range 1200-1400K. The direct simulation Monte Carlo method was applied for modeling the silver–helium mixture flow inside the crucible with subsequent jet expansion into vacuum and detailed information on jet gasdynamics was obtained. The helium carrier gas is shown to play an important role in the deposition process by increasing both the metal atom velocity and flux onto the substrate. An optimal helium flux resulting in the maximal silver deposition rate is found. The onset of cluster formation in the Ag-He jet is determined. It is shown that for the experimental conditions silver clusters are not generated in the jet and thus the observed nanostructures are formed on the substrate surface due to diffusion and nucleation of the deposited atoms.

Keywords: silver films; gas-jet deposition method; direct simulation Monte Carlo; silver-helium vacuum expansion; cluster formation process.

1. Introduction

Thin nanostructured films of noble metals play an important role in medicine, electronics and optics due to their unique properties [1-4]. There are some different techniques of such film production including very promising gas-jet method of the metal deposition from a supersonic jet [5-8]. This method provides the evaporation of a metal inside a crucible, the mixing of a metal vapor with a carrier inert gas, the outflow of the mixture through (usually) a sound nozzle into vacuum or a low-pressure environment, the deposition of metal particles on a substrate and finally the particle assembling into a nanostructured film on the substrate surface [9-11]. The mixture expansion can be accompanied by the metal cluster formation in a flow region. Clusters that have reached the substrate can promote the formation of nanostructures on the substrate surface. Estimation of jet parameters (fluxes, velocities, temperatures of monomers and clusters) is necessary to control and optimize the gas-jet deposition technique.

The previous analysis of the flow of a metal vapor - inert gas mixture was carried out analytically and experimentally [12, 13]. Analytical estimations were based on the inviscid supersonic jet model [14] and made it possible to predict gas parameters in the far field of the jet. The gas outflow regime of interest can be near free-molecular or transient for which the characteristic Knudsen number $Kn = \lambda_0/R > 0.01$ (λ_0 is the mean free path determined by gas stagnation parameters inside the crucible, R is the nozzle exit radius). The use of the inviscid continuum model is questionable for mentioned above flow regimes. Within the experimental work an empirical expression for estimating the cluster formation rate inside the jet was

obtained. This expression allowed estimating the technological parameters which correspond to three possible flow patterns: (i) without clusters, (ii) with a low rate of the cluster formation and (iii) with large clusters (whose sizes exceed 100 atoms). The proposed approach did not provide detailed information on clusters size distributions, velocities and internal energies.

The modern state of computation technologies makes it possible to carry out the modeling of a motion of a metal vapor - inert gas mixture in whole flowfield including the crucible and the substrate region and obtained all necessary information of flow parameters. The most adequate method for numerical investigations of flows from free-molecular to near-continuum regimes is the direct simulation Monte Carlo (DSMC) [15]. The DSMC code may be supplemented with models of chemical reactions [16-18] including cluster formation processes [19].

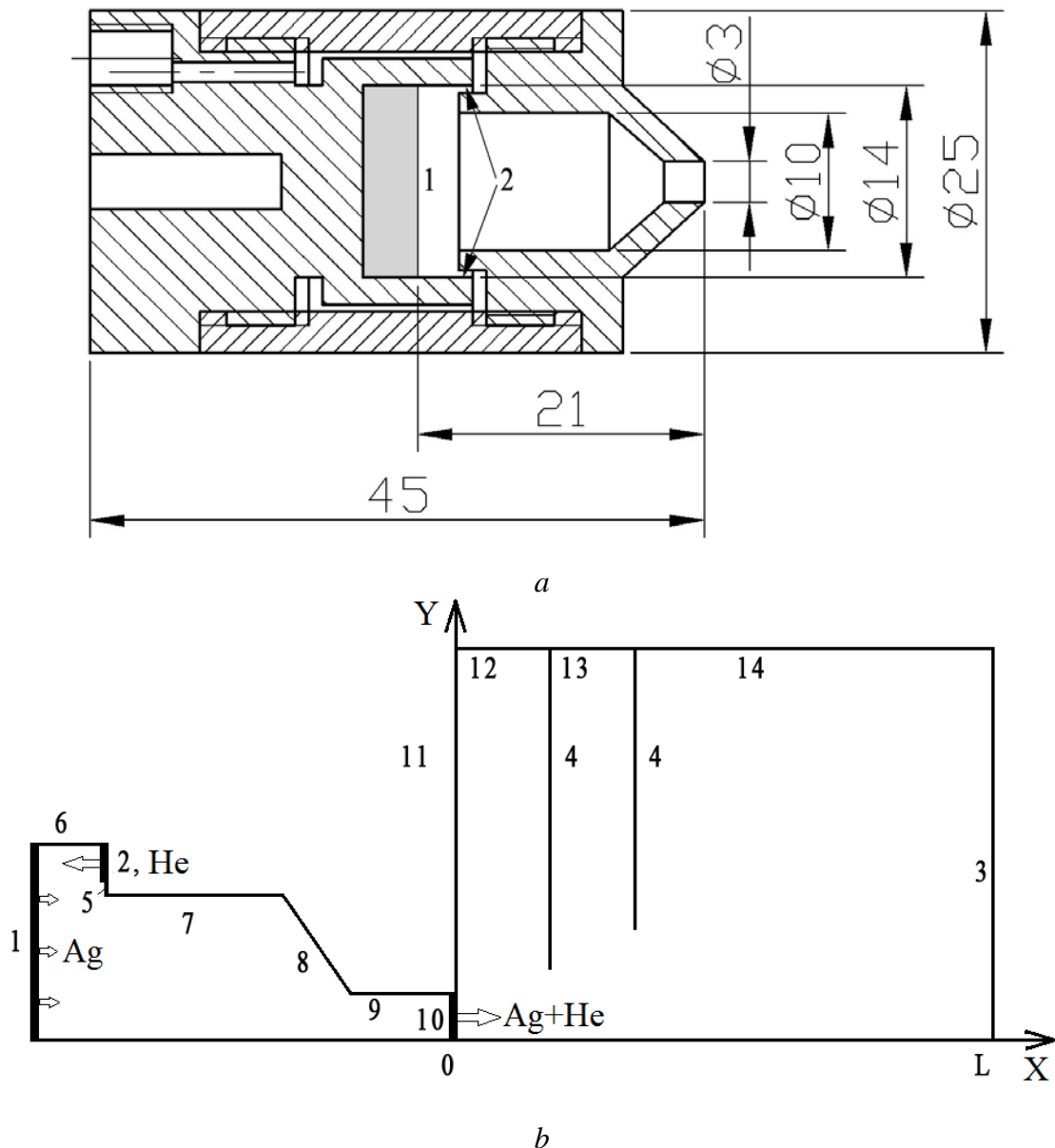


Fig. 1. (a) The scheme of the high-temperature source (crucible), all sizes in mm; (b) the scheme of the simulation area. 1 - the surface of the silver melt; 2 - the section of the annular helium load channel; 3 - the plane of the substrate; 4 - the shields; 5,6,7 the inner surfaces of the crucible; 8,9 - the inner surfaces of the confuser and cylindrical parts of the nozzle unit; 10 - the section of the nozzle unit; 11-14 external boundaries of the expansion zone.

The main purposes of the work are (i) to present obtained experimental data on nanostructured silver films, (ii) to investigate numerically by the DSMC method the Ag-He flow under experimental conditions, (iii) to analyze rates of the cluster formation and the possible impact of the condensation process inside the jet on the nanostructured film growth.

2. The nanostructured silver film deposition by the gas-jet method

The schemes of the crucible and the gas flow region for the metal film deposition technique are presented in Fig. 1. The molybdenum crucible is heated to a temperature T_0 . Silver atoms are evaporated from the melt surface 1. The inert gas is loaded into the crucible with the rate Q through the annular orifice 2. The mixture of gases outflows from the nozzle exit orifice of radius $R=1.5\text{mm}$ into the deposition chamber. The plane of the substrate 3 is located at a distance L from the nozzle exit. In order to reduce the thermal radiation heating the substrate, shields 4 are installed between the nozzle exit and substrate surface.

Thin silver films were deposited on monocrystalline silicon substrates (100). The temperature range of the crucible was $T_0=1200\text{-}1400\text{ K}$ at a fixed flow rate of helium $Q_{\text{He}}=36\text{ sccm}$. The nozzle-substrate distance was varied in the range $L=70\text{-}100\text{ mm}$. An analysis of the morphology of films obtained under different deposition regimes was carried out by the method of Scanning Electron Microscopy (SEM, JEOL JSM-6700F microscope).

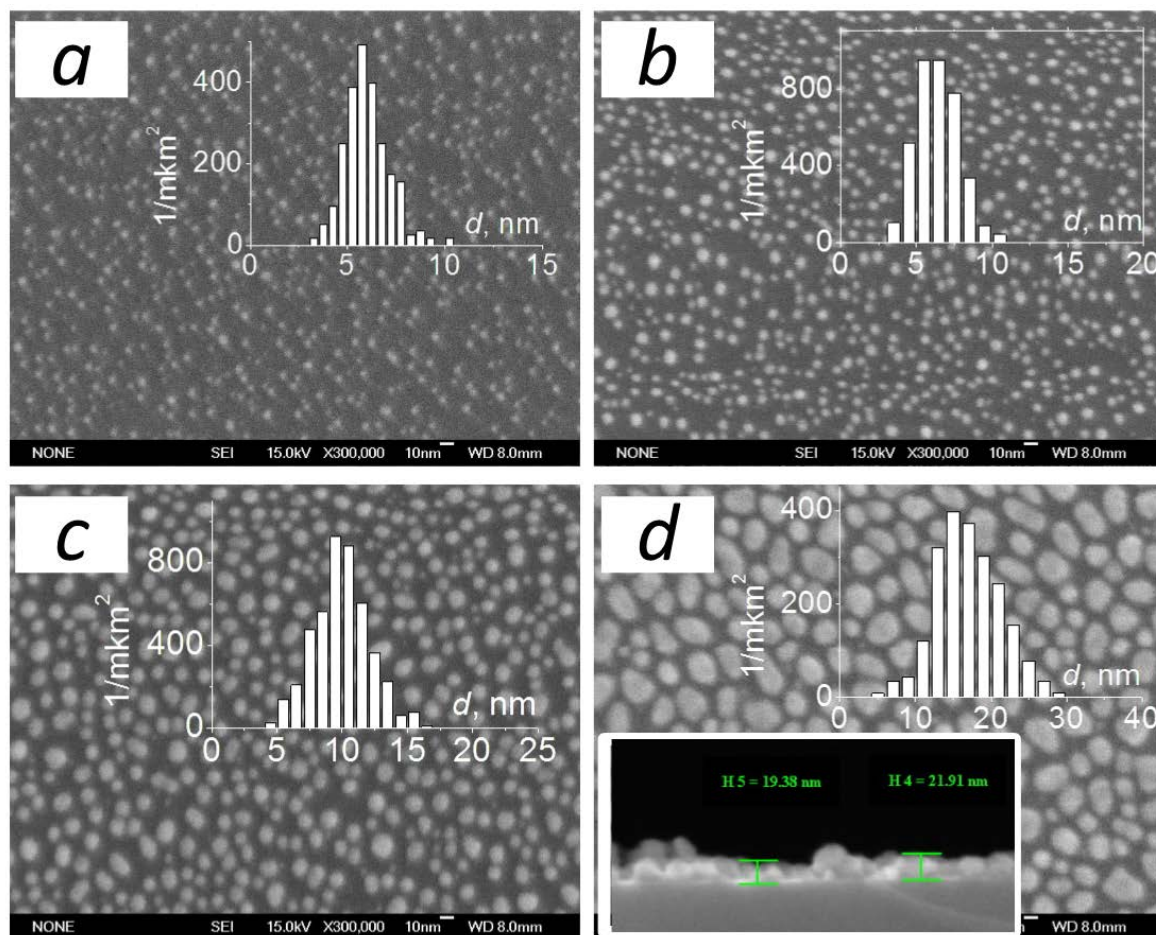


Fig. 2. SEM images of films deposited on the substrate, heated to 473 K. The distance to the crucible is 100 mm, the deposition time is 30 min. The source temperatures: (a) 1233 K, (b) 1276 K, (c) 1314 K, (d) 1377 K. The inserts show the histograms of the particle size distribution, and also the SEM image of the cross-section of the sample.

SEM images of silver films are shown in Fig. 2. The images were made at a fixed deposition time, but for different temperatures of the crucible. In all cases, the films are nanostructured, consisting of individual nanoparticles. The average size of nanoparticles rises with increasing of the crucible temperature from ~ 6 nm at 1233 K to ~17 nm at 1377 K. The particle size distribution is rather narrow (see histograms shown in Fig. 2). The image of the film cross-section (Fig 2, d) indicates that the nanoparticles have a shape close to spherical.

Estimations of the volume of nanostructures deposited on the surface were made and the average thickness of coatings was reconstructed. Based on these data, the fluxes of silver atoms $F_{Ag,L}$ on the jet axis for the distance $L=100$ mm was estimated: for $T_0=1233$ K — $F_{Ag,L}=4.17 \cdot 10^{16}$ m⁻²s⁻¹, for $T_0=1276$ K — $F_{Ag,L}=5.09 \cdot 10^{16}$ m⁻²s⁻¹, for $T_0=1314$ K — $F_{Ag,L}=1.36 \cdot 10^{17}$ m⁻²s⁻¹, for $T_0=1377$ K — $F_{Ag,L}=2.69 \cdot 10^{17}$ m⁻²s⁻¹.

The questions arise on (i) the influence of the carrier gas on the deposition process and (ii) the possibility of the cluster formation process directly in the jet volume. The deposited clusters which formed in the jet can play a role of precursors for surface nanostructures growth process. The answers can be obtained with the help of modeling by the direct simulation Monte Carlo method.

3. The direct simulation Monte-Carlo of He-Ag mixture flow for the temperature range $T_0=1230-1380$ K

Simulations were carried out by the DSMC method for the axisymmetrical domain (Fig. 1b). The flux of silver evaporated atoms through the surface l corresponds to the Hertz-Knudsen equation

$$F_{Ag}^+ = n_{0,Ag} \left(8kT_0 / (\pi m_{Ag}) \right)^{1/2} / 4, \quad (1)$$

where $n_{0,Ag}(T_0)=p_{0,Ag}(T_0)/(kT_0)$ is the equilibrium concentration of the silver vapor at a temperature T_0 , m_{Ag} is the mass of a silver atom. The saturation pressure $p_{0,Ag}(T_0)$ is defined according data of [20].

The flux of helium inside the crucible can be defined from the known load Q_{He} with the additional assumption about the value of speed relation at the inlet section $s = V_{He}/(2kT_0/m_{He})^{1/2}$ (V_{He} — the velocity of helium gas, m_{He} — the helium atom mass). For considering case $s \ll 1$ and the value $s=0.1$ was used in simulations.

Silver atoms returning back to the evaporating surface are condensed on it (are removed from simulation). Collisions of silver and helium atoms with other internal surfaces of the crucible (5, 6, 7, 8, 9) are supposed to be diffusive with full energy accommodation and temperature T_0 . Helium atoms are reflected diffusively with full energy accommodation from the evaporating surface l . Atoms of helium returning back to the inlet surface 2 are reflected specularly from it. All atoms leaving computation domain through surfaces 3, 11, 12, 13, 14 are excluded from simulation processes. The surfaces of shields condense all Ag atoms and reflect (with full accommodation energy and temperature T_0) He atoms. At the beginning of calculations ($t = 0$, t is the time) there are no particles in simulation region.

The variable hard sphere (VHS) model with parameters [15] $d_{ref,He} = 2.33$ Å, $T_{ref,He}=273$ K, $\omega_{He}=0.66$ ($d_{ref,He}$, $T_{ref,He}$ — reference values of collision diameter and temperature, ω_{He} — parameter defined by viscosity dependence on temperature) was employed. The diameter of Ag atoms is supposed to be constant (the hard-sphere model (HS)) and equal to the van der Waals diameter 3.44 Å [21].

The parallel algorithm based on decomposition of the domain was employed for computer simulations.

The main parameters that determine the flow pattern under considering problem setting are the crucible (and shields) temperature T_0 , the helium load rate Q_{He} , the geometric sizes and relative locations of the crucible and shields. The Knudsen numbers $Kn_{0,Ag}=\lambda_{0,Ag}/R$ and $Kn_{0,He}=\lambda_{0,He}/R$ ($\lambda_{0,Ag}$ — the mean free path of Ag atoms estimated by equilibrium

concentration $n_{0,Ag}(T_0)$, $\lambda_{0,He}$ — the mean free path of He atoms estimated by average helium density inside the crucible) may be introduced for the definition of the flow rarefaction degree.

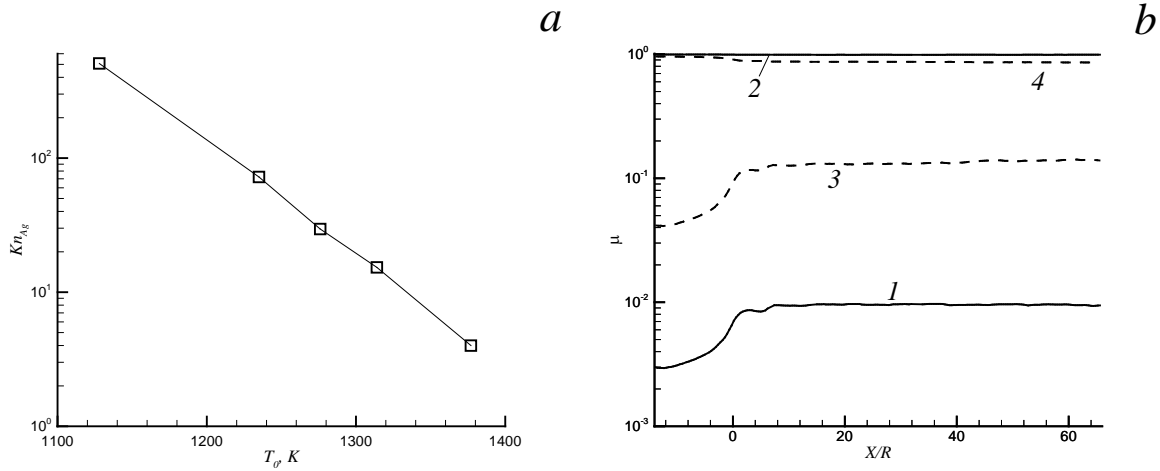


Fig. 3. (a) The dependence of the Knudsen number Kn_{Ag} for silver atoms on the temperature of the crucible T_0 ; (b) mole fractions of silver (1, 3) and helium (2, 4) at the flow axis for the case $Q_{He}=36$ sccm, $T_0=1233$ K (1,2) and $T_0=1377$ K (3,4).

The temperature dependence of Knudsen number for the Ag vapor is presented in Fig. 3a. $Kn_{0,Ag} \gg 1$ for all considered crucible temperatures, silver atoms move without mutual collisions. The He load of 36 sccm leads to helium densities inside crucible of near $5.6 \cdot 10^{21} \text{ m}^{-3}$ that corresponds to $Kn_{0,He} \approx 0.6$. The outflow of the Ag-He mixture from the crucible occurs in the transient regime. According to the data presented in Fig. 3b the Ag mole fraction in the mixture is small. The silver mole fraction increases during expansion process and “freeze” at the distance approximately $15R$ from the crucible. For the temperature $T_0=1377$ K at a helium flow rate $Q_{He}=36$ sccm the mole fraction of silver atoms inside the crucible is near 4,5% and in the jet far field is about 12%.

The typical axial distributions of density, velocity and temperature of He and Ag atoms are presented in Fig. 4 for temperature $T_0=1377$ K. Also in Fig. 4 the additional information are shown: (i) the simulation data for the case of pure Ag outflow ($Q_{He}=0$), (ii) the analytical data [22] for the free-molecular outflow from a reservoir in vacuum through the orifice of radius R in the infinitively thin wall (parameters in the reservoir is supposed to be $n_{0,Ag}$, T_0 for the Ag jet and $n_{0,He}$, T_0 for the He jet), (iii) results of the simulation of inviscous continuum sound jet [14] (separately for Ag and He atoms). The location of the reservoir wall coincides with the plane of the crucible nozzle exit.

The presence of the He flux leads to increasing of Ag density within the jet and 60% silver vapor acceleration up to the value $1.6u_0$ ($u_0 = \{8kT_0/(\pi m_{Ag})\}^{1/2}$). Such value of the velocity is exceeding the value of the maximal stationary outflow of pure silver vapor into vacuum ($\approx 1.4u_0$). Both Ag density and velocity are greater significantly than corresponding parameters for the case of pure Ag outflow. The presence of shields affects the He axial distributions for distances $2 < X/R < 16$. Temperatures of He and Ag are very close in crucible and jet far field. Parameters both He and Ag are close to free-molecular estimations rather than parameters of the continuum viscous jet. The drastic difference is observed between calculated Ag and He temperature distributions and the same distributions obtained on the basis of the inviscid jet model (Fig. 4).

To investigate the influence of the He load on the Ag nozzle flux additional calculations with values $Q_{He}=3.6, 180, 360$ and 1080 sccm were carried out. The results for the crucible

temperature of 1377K are presented in Fig. 5a. With the rise of the He load the silver flux through the nozzle exit increases rapidly, achieves the maximum near the value $Q_{He} \approx 200$ sccm and then slowly decreases. The nozzle Ag flux determines the deposition rate and as a consequence the crucible efficiency. It can be concluded that the He load in the range of 100-200 sccm for crucible temperature near 1400K is optimal for deposition technique. The reason of efficiency decreasing for high values of Q_{He} is due to the flow behavior inside the crucible where the initial helium flux is directed towards the silver evaporating surface. The low and medium values of the He load in the crucible ($Q_{He} \approx 36$ sccm) lead to appearance of Ag density maximum near the beginning of crucible nozzle. The value of the maximum is exceeding the equilibrium density n_0 (Fig. 6a). With increasing of Q_{He} the helium gas starts to compress silver atoms toward the initial evaporating surface and restrains motion of Ag toward the nozzle. The maximum of density occurs near evaporating surface and has a value about n_0 (Fig. 6b).

Simulation values of the Ag atoms flux through the plane of the substrate is exceeding the same values estimated by experimental data on the film deposition (Fig. 7). The discrepancy between calculated and experimental data can be explained by the presence of a background gas (basically helium) in a deposition chamber. For the case of $Q_{He} = 36$ sccm the pressure of the background gas in the chamber increases up to 19 Pa. The last value depends on the efficiency of a vacuum pumping system. Under low pressures of the background gas the expansion of the supersonic jet in the surrounding occurs in the regime of scattering [23] where the jet particle (in our case Ag atoms) leave the near-axial region due to the collision process. In result the Ag flux through the substrate decreases.

The background gas scattering of Ag atoms can be estimated according [24, 25]:

$$n_{Ag}(L) = n_{Ag}^0(L) \exp(-\alpha_s L), \quad (2)$$

where n_{Ag}^0 — the density of silver vapor at the same distance L from the crucible without background gas scattering (vacuum conditions), $\alpha_s = m_{He}/m_{Ag}\lambda_s$ — the attenuation coefficient, $\lambda_s = 4/\sqrt{2n_{b,He}\pi(d_{He}+d_{Ag})^2}$ — the mean free path of Ag atoms in the background helium, $n_{b,He}$ — the density of background gas. The factor m_{He}/m_{Ag} takes into account the low efficiency of heavy Ag atom scattering by light helium atoms. For background gas parameters $p_{b,He} = 19$ Pa, $T_{b,He} = 400$ K and $L = 100$ mm we obtain $\alpha_s = 0.45$ cm⁻¹ and $n_{Ag}/n_{Ag}^0 = 0.011$. This correction factor provides very good agreement between experimental and calculated data on Ag fluxes (Fig. 7,a).

To validate the background gas scattering model the silver films were deposited at the three different distances from crucible ($L=70, 90, 100$ mm) for the temperature $T_0=1373$ K, $Q_{He}=36$ sccm, $p_{b,He}=19$ Pa and the deposition time of 30 min. The film thickness was equal 8.5, 1.8 and 1 nm correspondently. Such behavior of film thickness confirms the important role of background gas scattering because the behavior of density drop differs strongly from the relationship L^{-2} that is valid for vacuum expansion. According data presented in Fig. 7b the velocity in the far field does not depend on L and the behavior of the Ag flux is governed by density drop. With taking into account the axial distribution of free jet density in vacuum and the effect of background gas scattering (eq. (2)) the silver atom flux through the substrate plane can be presented as:

$$F_{Ag}(L) = F_{e,Ag} R^2 \exp(-\alpha'_s L) / L^2, \quad (3)$$

where $F_{e,Ag}$ — the particle flux through nozzle exit, α'_s — the effective attenuation coefficient of helium scattering which should be determined by experimental data. The data on distance dependence of the film thickness were approximated by the expression (3) with the use of values $F_{e,Ag}$ and α'_s as free parameters. According data presented in Fig. 7b the considered expression describes perfectly experimental data. The obtained best fit $\alpha'_s = 0.49$ cm⁻¹ and $F_{e,Ag} = 1.85 \cdot 10^{22}$ m⁻²s⁻¹ is in good agreement with theoretical estimation for α_s within relation

(2) and results of nozzle flux simulations (see Fig. 5a). Full match of data for considering case is not possible due to the approximate character of relation (3) which does not take into account variation of the silver atom velocity in the initial section of the jet. It can be concluded that the presence of background gas with densities from 1 to 20 Pa (typical for gas-jet method) leads to significant decreasing of the film deposition rate. Such decreasing can be estimated by the suggested scattering model.

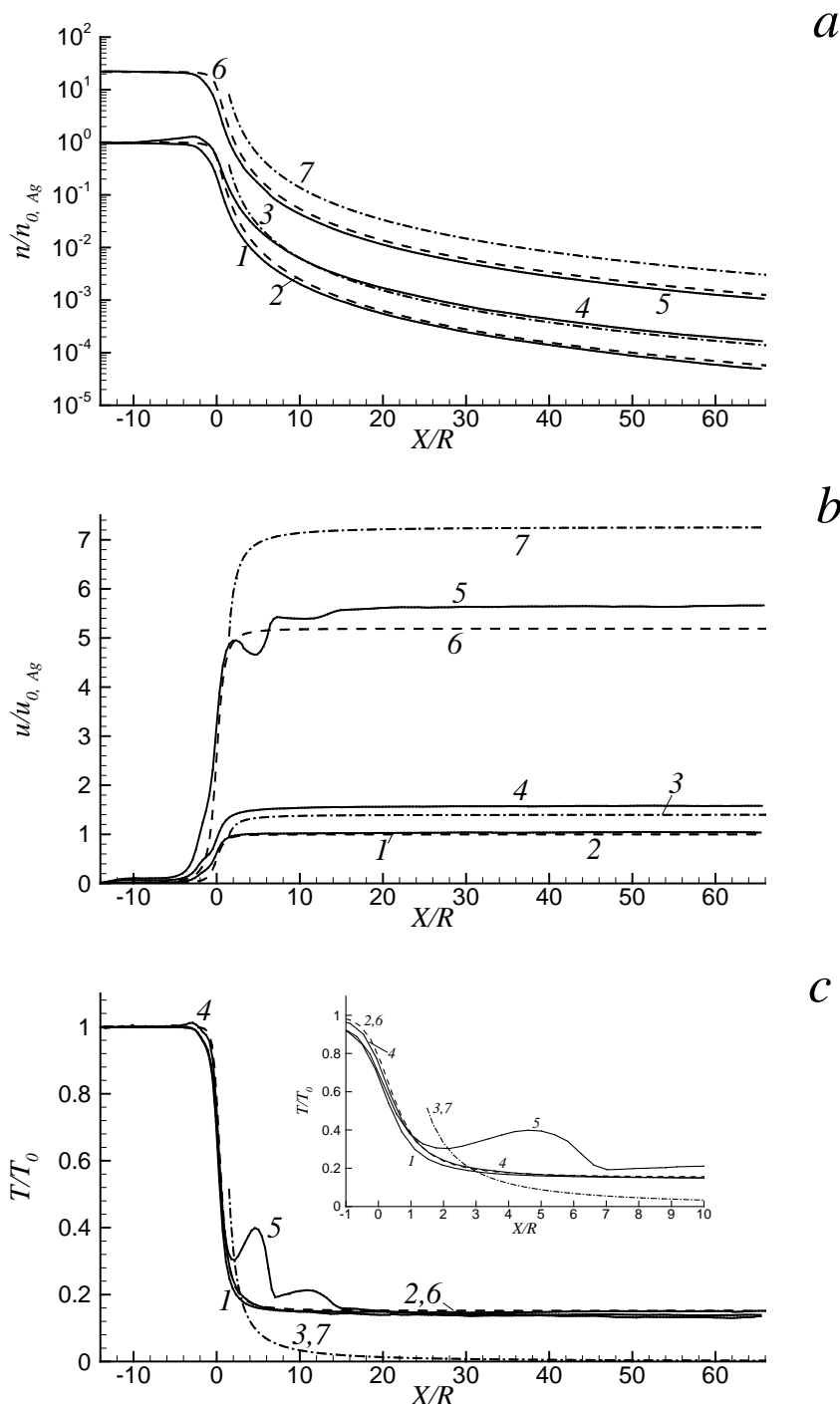


Fig. 4. The axial distributions of concentration (a), velocity (b), and temperature (c) for the pure silver jet (curve 1, $Q_{He}=0$) and gases in the Ag-He mixture ((4) silver, (5) helium, $Q_{He}=36$ sccm). $T_0=1377$ K. Curves 2 and 6 are the solution [22] for the free-molecular flow of silver and helium atoms, respectively, curves 3 and 7 are the solution [14] for the inviscous jet of silver and helium atoms, respectively.

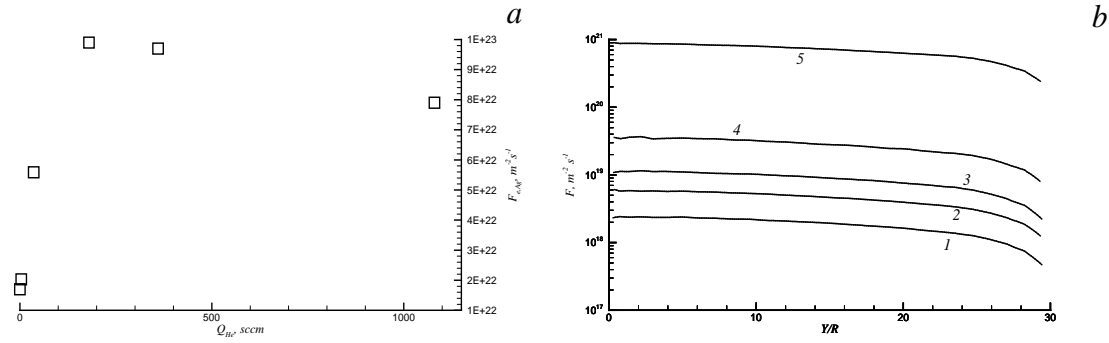


Fig. 5. (a) The dependence of the flux of silver atoms through the nozzle exit on the helium load for $T_0=1377$ K; (b) the transverse distribution of the atom flux at a distance of 100 mm from the crucible (1 — Ag, $T_0=1235$ K; 2 — Ag, $T_0=1276$ K; 3 — Ag, $T_0=1314$ K; 4 — Ag, $T_0=1377$ K; 5 — He, $T_0=1235$ K).

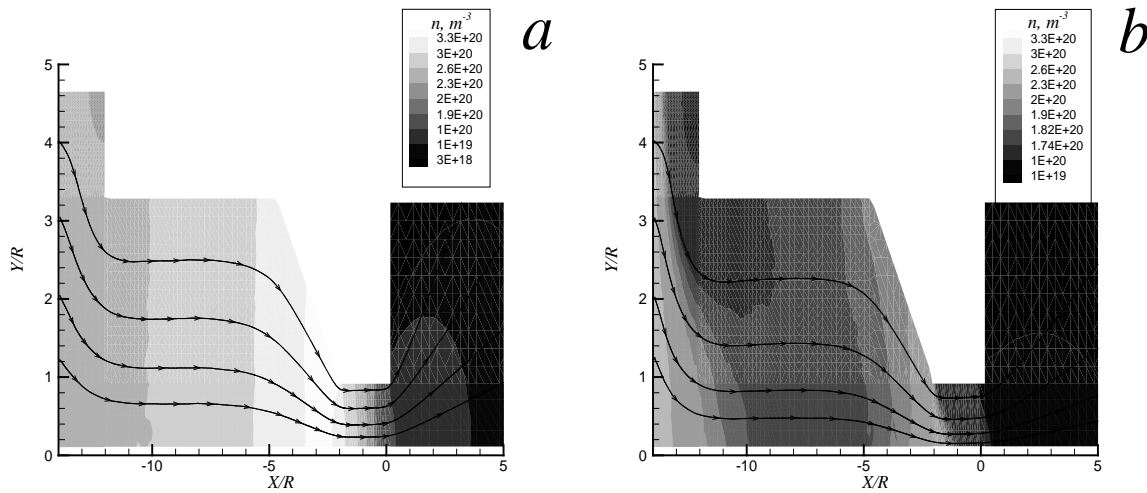
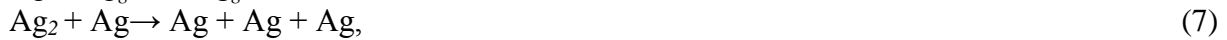


Fig. 6. The fields of the density and streamlines for silver atoms in the crucible for $T_0=1377$ K. (a) $Q_{He} = 36$ sccm, (b) $Q_{He} = 360$ sccm.

4. The direct simulation Monte-Carlo of cluster formation process in the He-Ag mixture jet

To estimate the impact of cluster formation process in the jet volume on technological parameters additional simulations were carried out. Within the DSMC method the condensation process was considered via taking into account next reactions:



Here the index 2 relates to dimers and the index g relates to clusters which consist of g -monomers. The rates of forward reactions (4), (5), (6) and reverse reactions (7), (8), (9) are denoted as $K_{I(3),Ag}$, $K_{I(3),He}$, K_{g-1} and $K_{2c,Ag}$, $K_{2c,He}$, K_g^- correspondedly. The equilibrium constant of dimerization is supposed to be $K_C = K_{2c,Ag}/K_{I(3),Ag} = K_{2c,He}/K_{I(3),He} = AT^B \exp\{-E_a/(kT)\}$ (E_a – the activation energy, A and B – constants). The rates of forward reactions are supposed to be $K_{I(3),Ag} = \alpha_{Ag} T^{\beta_{Ag}}$ for (4), $K_{I(3),He} = \alpha_{He} T^{\beta_{He}}$ for (5) and $K_{g-1} = \alpha_g T^{\beta_g}$ for (6). Within the work next values of parameters are

considered: $A=10.86 \cdot 10^{33} \text{ m}^{-3}\text{K}$, $B=-1$, $E_a=1.67\text{eV}$ according [26], $\alpha_{\text{Ag}}=0.89 \cdot 10^{-45} \text{ K}^{-0.5}\text{m}^6\text{s}^{-1}$, $\alpha_{\text{He}}=3 \cdot 10^{-45} \text{ K}^{-0.5}\text{m}^6\text{s}^{-1}$ и $\beta_{\text{Ag}}=\beta_{\text{He}}=0.5$ according the simplified model of triple collisions [19, 27], α_g is supposed to be function only of cluster size $\alpha_g(g_{\text{Ag}})$, $\beta_g=0.5$ [19]. The probabilities of all reactions were defined for DSMC method by the total collision energy (TCE) model according [15, 19].

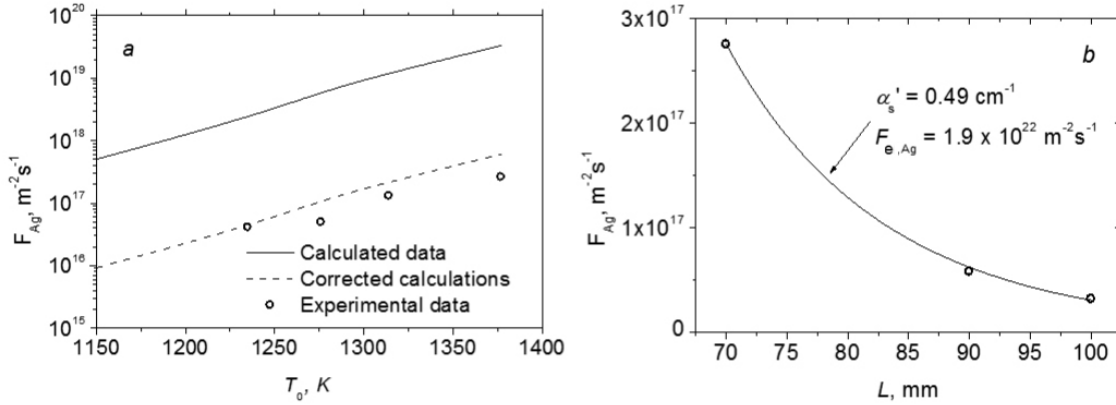


Fig. 7. (a) The simulation and experimental dependences of the silver atoms flux through the substrate on the crucible temperature. The dashed curve corresponds to the simulation results, corrected for the background gas scattering of Ag atoms by the equation (2); (b) the experimental dependence of the Ag flux on the substrate on the crucible distance, the curve is the approximation by equation (3).

Other parameters necessary for condensation process modeling [19] are the parameter that defines atom surface density of a cluster $\omega_{Zh}=0.81$ [28], coordination number for liquid silver $N_{Zh}=8.5$ [28], the radius of atom determined by density of liquid ρ : $r_{w,\text{Ag}}=(3m/(4\pi\rho))^{1/3}=1.68 \text{ \AA}$, the distance between atoms in the silver dimer $r_d=1.265 \text{ \AA}$ [29], the binding energy of a silver atom on a plate surface $\varepsilon_\infty=2.77 \text{ eV}$, the dissociation energy of a silver dimer $\varepsilon_2=1.67 \text{ eV}$ [26], the characteristic frequency of monomer vibrations inside a cluster $\nu_0=10^{12} \text{ s}^{-1}$ [30]. The energy exchange under particle collisions was described by Larsen-Borgnakke model [15]. The probability of exchange between translation and internal modes under particle collisions was 0.1. The number of vibration degrees of freedom of a silver dimer was $Z_{v,2}=1$, for other clusters with size g was $Z_{v,g}=3g-6$.

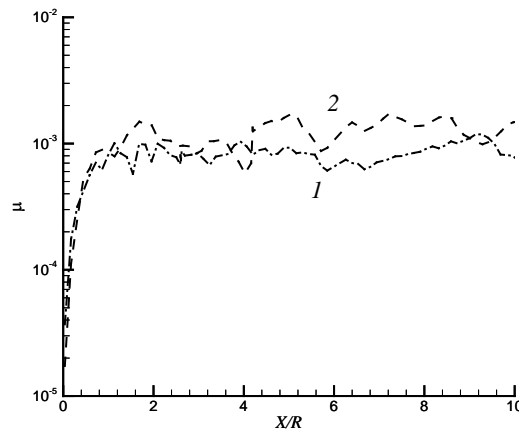


Fig. 8. Ag_2 mole fraction in the silver jet (1) and in the Ag-He jet (2).

The DSMC modeling with taking into account condensation process were carried out for the domain limited by the nozzle exit and distance $15 R$ from it in the X direction. The height of the computation domain was $10 R$. Boundary parameters at the plane of nozzle exit corresponds to parameters obtained within the computation in whole domain without taking into account the cluster formation process.

The simulation data show that there are no clusters in the jet for considered parameters of silver film deposition ($Q_{He}=36$ sccm and $T_0 < 1400$ K). Such conclusion is in agreement with estimations of [13]. In [13] for description of cluster formation process the parameter $\Gamma^* = \Gamma / \Gamma_{ch}$ was employed, where $\Gamma = n_0 d^{0.85} T_0^{-1.29}$, $d = 2R$, n_0 — the gas density inside crucible (Γ_{ch} depends on vapor properties). For considering cases $\Gamma^* < 200$ and according [12, 13] there is no cluster formation process within the jet.

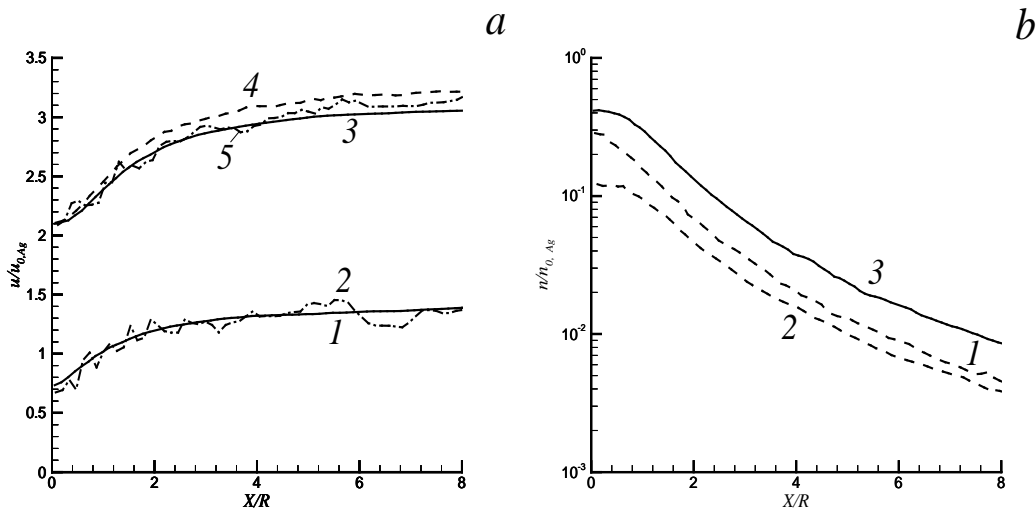


Fig. 9. (a) The velocity of particles in the silver jet (1 – Ag, 2 – Ag₂) and in the Ag-He jet (3 – Ag, 4 – He, 5 – Ag₂). (b) The dimensionless density of silver atoms in the pure silver jet (1), silver atoms in the Ag-He jet (2), helium atoms in the Ag-He jet (3). $T_0 = 2123$ K.

To define the parameters which correspond to the cluster appearance in the jet additional simulations were carried out (i) $T_0=1770$ K, $Q_{He}=0$, (ii) $T_0=1770$ K, $Q_{He}=1000$ sccm, (iii) $T_0=2123$ K, $Q_{He}=0$, (iv) $T_0=2123$ K, $Q_{He}=5000$ sccm.

The mole fractions of clusters in flowfield occur very small and less than 10^{-5} for the cases (i) and (ii). The main component of clusters is a dimer. The flow was rarefied for these cases, Knudsen numbers determined by parameters of gases in the crucible exit are in the order of 0.1. For higher value of the evaporation temperature $T_0=2123$ K mole fractions of clusters in the jet are approximately 10^{-3} (Fig. 8). Mole fractions of clusters are freezing at distance 1-2 R from the nozzle exit which is in agreement with the data of [31]. The maximal observed within simulation cluster size is 4 atoms. The helium load of $Q_{He}=5000$ sccm leads to acceleration of Ag atoms and clusters (Fig. 9a). The velocities of observed clusters are coincides approximately with the velocity of silver atoms. For such small flow clusterization degree there is no impact of condensation process on monomers parameters. The curves 1,3,4 in Fig. 9a and curves 1-3 in Fig. 9b coincide for the cases with and without taking into account cluster formation reactions.

5. Nanostructured silver film growth

Based on the set of experimental and calculated data, we can conclude that within considering experimental range of deposition parameters ($T_0 < 1400$ K, $Q_{He}=36$ sccm) the formation of

nanostructured film on the substrate surface occurs due to deposition of silver atoms only. The clusters in the jet is practically absent. The growth of the nanostructured film in this case occurs according to the Volmer-Weber mechanism [32]. The deposited atoms diffuse over the surface and nanoparticle nuclei are formed under collisions of such adatoms. The nonmonotonic dependence of the surface particle concentration (Fig. 2) proves this mechanism of nanostructure growth. After the stage of the surface nucleus formation process the next stage of particle size increasing begins. Then particle coagulation, the formation of “islands” of irregular form and transition to the percolation structure of the film are observed. The further rise of depositing mass leads to the formation of solid metal coating.

6. Conclusions

Nanostructured silver films were obtained by the gas-jet technique for the range of crucible temperatures $T = 1200-1400$ K. The direct simulation Monte Carlo method was applied for modeling the flow of a mixture of the silver vapor with a helium carrier gas inside the crucible with subsequent expansion of the mixture into vacuum as a free jet. The analysis of simulation and experimental data showed the following:

1) The increase of the helium flux for a fixed crucible temperature leads to non-monotonic behavior of the silver atom nozzle flux. Firstly the silver flux rises, reaches a maximal value and then slowly decreases. The helium gas accelerates the silver atoms that results in significant rise of the mass flow rate of silver vapor. As a result, the presence of the carrier gas promotes the rise of the silver flux to a remote substrate which is a positive factor for film deposition by the gas-jet method. The silver flux distribution along the substrate surface is found to be fairly uniform that is also an advantage of the considered deposition technique.

2) The presence of a background gas in the vacuum chamber leads to decrease of the silver atom flux onto the substrate and thus reduces the deposition efficiency. A simple scattering model can be used for estimation of the effect of background gas in the deposition process.

3) There are no clusters formed in the jet for the considered conditions (the crucible temperature is below 1400K and helium load is less or equal 36 sccm). The cluster formation process starts in the jet at sufficiently higher crucible temperatures and helium fluxes.

4) The flow estimations based on the inviscid continuum model are very rough and does not match the considered flow regimes. Estimations of silver vapor flow parameters for low temperatures of the crucible without carrier gas load may be done on the base of free-molecular relations. In general, DSMC (or other methods based on solving the Boltzmann equation) should be employed for adequate prediction of flow parameters.

5) The formation of the observed nanostructured silver films by the gas-jet deposition method for the considered parameter range is a result of nanocluster formation directly at the substrate surface due to diffusion and nucleation of the deposited silver atoms.

Acknowledgements. *This work was supported by the Russian Science Foundation (Project № 16-19-10506, experimental studies) and by the Ministry of Education and Science of the Russian Federation (Project №16.8549.2017/8.9, modeling). The computation resources were provided by the supercomputer center of Peter the Great St. Petersburg Polytechnical University.*

References

- [1] S. Jalili, E.M. Goliaei, J. Schofield // *Int. J. of Hydrogen Energy* **42(21)** (2017) 14522.
- [2] M. Haruta // *Chem. Rec.* **3** (2003) 75.

- [3] N.R. Agarwal, F. Neri, S. Trusso, A. Lucotti, P.M. Ossi // *Appl. Surf. Sci.* **258** (2012) 9148.
- [4] S.H. Cho // *Phys. Med. Biol.* **50** (2005) 163.
- [5] I. Yamada, T. Takagi // *IEEE Trans. Electron Devices* **ED-34(5)** (1987) 1018.
- [6] P. Gatz, O.F. Hagen // *Appl. Surf. Sci.* **91** (1995) 169.
- [7] K. Wagner, P. Piseri, H.V. Tafreshi, P. Milani // *J. Phys. D: Appl. Phys.* **22** (2006) R439.
- [8] M.N. Andreev, A.K. Rebrov, A.I. Safonov, N.I. Timoshenko // *Nanotechnologies in Russia* **6(9–10)** (2011) 587.
- [9] M.J. Aziz // *Appl. Phys A* **93** (2008) 579.
- [10] C. Polop, C. Rosiepen, S. Bleikamp, R. Drese, J. Mayer, A. Dimyati, T. Michely // *New J. Phys.* **9** (2007) 1.
- [11] S.V. Starinskiy, V.S. Sulyaeva, Yu.G. Shukhov, A.G. Cherkov, N.I. Timoshenko, A.V. Bulgakov, A.I. Safonov // *J. Struct. Chem.* **58(8)** (2017) 1581.
- [12] O.F. Hagen // *Surf. Sci.* **106** (1981) 101.
- [13] O.F. Hagen // *Z. Phys. D* **20** (1991) 425.
- [14] H. Ashkenas, F.S. Sherman, In: *Rarefied Gas Dynamics*, ed. by J.H. de Leeuw (N.Y.: Academic Press, 1965), p.84.
- [15] G.A. Bird, *Molecular gas dynamics and the direct simulation of gas flows* (Clarenton Press: Oxford, 1994).
- [16] G.A. Bird // *Phys.Fluids* **23** (2011) 106101.
- [17] I.B. Sebastio, A. Alexeenko // *Physics of Fluids* **28** (2016) 107103.
- [18] S. Gimelshein, I. Wysong // *Physics of Fluids* **29** (2017) 067106.
- [19] N.Y. Bykov, Yu.E. Gorbachev // *Appl. Math. Comp.* **296** (2017) 215.
- [20] <https://www.powerstream.com/vapor-pressure.htm>
- [21] https://www.webelements.com/silver/atom_sizes.html
- [22] Yu.A. Koshmarov, Yu.A. Ryzhov, *Applied Dynamics of Rarefied Gas* (Mashinostroenie, Moscow, 1977). (In Russian)
- [23] A.K. Rebrov, In: *Rarefied Gas Dynamics*, ed. by O.M. Belotserkovskii (N.Y.: Springer, 1985), p.849.
- [24] A.V. Bulgakov // *SPIE Proc.* **2403** (1995) 75.
- [25] A.V. Bulgakov, M.R. Predtechensky, A.P. Mayorov // *Appl. Surf. Sci.* **96-98** (1996) 159.
- [26] B.M. Smirnov // *Phys. Usp.* **40(11)** (1997) 1117.
- [27] *Physico-chemical processes in gas dynamics. Electronic handbook in 3 volumes. Volume I: Dynamics of physico-chemical processes in gas and plasma*, ed. by G.G. Chernyi and S.A. Losev (Moscow: publishing house of Moscow University, 1995). (In Russian)
- [28] D.I. Zhukhovitskii // *J. Chem. Phys.* **101** (1994) 5076.
- [29] B.M. Smirnov, A.S. Yatsenko // *Phys. Usp.* **39** (1996) 211.
- [30] V.N. Kondratiev, E.E. Nikitin, *Kinetics and mechanism of gas-phase reactions* (Moscow: Nauka, 1974). (In Russian)
- [31] N.Y. Bykov, Yu.E. Gorbachev, V.V. Zakharov // *AIP Conf. Proc.* **1786** (2016) 050001.
- [32] J.A. Venables, G.D.T. Spliller, M. Hanbukah // *Rep. Prog. Phys.* **47(4)** (1984) 399.

Submission of papers:

Manuscript should be submitted (**both MS Word and PDF**) by e-mail to: mpmjournal@spbstu.ru

After a confirmation of the paper acceptance, the authors should send the signed hard copy of the "Transfer of Copyright Agreement" form (available at <http://www.mpm.spbstu.ru> section "Authors") by regular post to "Materials Physics and Mechanics" editorial office:

Periodicals Editorial Office, Institute of Advanced Manufacturing Technologies, Peter the Great St.Petersburg Polytechnic University, Polytechnicheskaya, 29, St.Petersburg 195251, Russia.

The scanned copy of the signed "Transfer of Copyright Agreement" should be send by e-mail to: mpmjournal@spbstu.ru.

Filetype:

Authors are invited to send their manuscripts **as MS Word file with PDF format copy.**

MS Word file should be prepared according to the general instructions bellow; we are kindly asking the authors to look through the detail instruction at: <http://www.mpm.spbstu.ru>.

Length:

Papers should be limited to 30 typewritten pages (including Tables and Figures placed in the proper positions in the text).

Structure of the manuscript:

PAPER TITLE: CENTERED,

TIMES NEW ROMAN 14 BOLD, CAPITAL LETTERS

A.B. Firstauthor¹, C.D. Secondauthor^{2*} -Times New Roman 12, bold, centered

¹Affiliation, address, country - Times New Roman 10, centered

*e-mail: e-mail of the corresponding author - Times New Roman 10, centered

Abstract. Times New Roman 12 font, single line spacing. Abstract should not exceed 12 lines.

Keywords: please, specify paper keywords right after the abstract.

Paper organization. Use Times New Roman 12 font with single line spacing. Use *Italic* font in order to stress something; if possible, please, use **bold** for headlines only.

Page numbering. Please, do not use page numbering.

Tables, Figures, Equations. Please, see the sample file at <http://www.mpm.spbstu.ru> for more details.

References

References should be subsequently numbered by Arabic numerals in square brackets, e.g. [1,3,5-9], following the sample style below:

[1] A.K. Mukherjee // *Materials Science and Engineering: A* 322 (2002) 1.

[2] C.C. Koch, I.A. Ovid'ko, S.Seal, S. Veprek, *Structural Nanocrystalline Materials: Fundamentals and Applications* (Cambridge University Press, Cambridge, 2007).

[3] A.E. Romanov, V.I. Vladimirov, In: *Dislocations in Solids*, ed. by F.R.N. Nabarro (North Holland, Amsterdam, 1992), Vol. 9, p.191.

[4] C.K. Takemori, T.D. Müller, M.A. De Oliveira, *Numerical simulation of transient heat transfer during welding process*, In: *International Compressor Engineering Conference* (Purdue, USA 2010).

[5] W. Pollak, M. Blecha, G. Specht // *US Patent 4572848*.

[6] <http://www.mpm.spbstu.ru>

Правила подготовки статей:

Рукопись (**английский язык, MS Word и копия PDF**) должна быть направлена в редакцию журнала по электронной почте: mpmjourn@spbstu.ru.

После подтверждения принятия статьи в печать, авторы должны отправить подписанные:

1. Соглашение о передаче авторских прав (<http://www.mpm.spbstu.ru>, раздел «Авторам»);
2. Экспертные заключения о том, что материалы статьи не содержат сведений, составляющих государственную тайну, и информацию, подлежащую экспортному контролю; по адресу:

Россия, 195251, Санкт-Петербург, Политехническая, д. 29, Санкт-Петербургский политехнический университет Петра Великого, Институт передовых производственных технологий, Редакция периодических изданий.

Скан-копии подписанных документов просим направить по электронной почте: mpmjourn@spbstu.ru

Тип файла:

Редакция принимает **файлы MS Word с копией в формате PDF**. Статья должна быть подготовлена в соответствии с настоящей инструкцией, мы просим авторов также следовать более подробным инструкциям на сайте журнала <http://www.mpm.spbstu.ru> в разделе «Авторам».

Длина статьи:

Статья не должна превышать 30 страниц формата А4, включая Таблицы и Рисунки, размещенные непосредственно в соответствующих местах.

Общие правила оформления статьи:

НАЗВАНИЕ СТАТЬИ: ВЫРОВНЯТЬ ПО ЦЕНТРУ,

ШРИФТ, TIMES NEW ROMAN 14 BOLD, ЗАГЛАВНЫЕ БУКВЫ

Автор(ы): **А.Б. Первыйавтор¹, В.Г. Автор^{2*}** - шрифт Times New Roman 12, bold, по центру

¹Наименование организации, адрес, страна - шрифт Times New Roman 10, по центру

* e-mail автора, представившего статью - шрифт Times New Roman 10, по центру

Аннотация. Аннотация статьи составляет не более 12 строк. Используйте шрифт Times New Roman 12, одинарный межстрочный интервал.

Ключевые слова: укажите ключевые слова после аннотации.

Как организовать текст статьи. Используйте шрифт Times New Roman 12, одинарный межстрочный интервал. При необходимости выделить какую-либо информацию используйте *курсив*. Используйте **полужирный** шрифт только для заголовков и подзаголовков.

Номера страниц. Пожалуйста, не используйте нумерацию страниц

Таблицы, Рисунки, Уравнения. Подробные правила оформления данных элементов статьи приведены в инструкции на сайте журнала <http://www.mpm.spbstu.ru>

Литература

Ссылки приводятся в тексте в квадратных скобках [1,3,5-9]. Стиль оформления ссылок:

- [1] A.K. Mukherjee // *Materials Science and Engineering: A* 322 (2002) 1.
- [2] C.C. Koch, I.A. Ovid'ko, S.Seal, S. Veprek, *Structural Nanocrystalline Materials: Fundamentals and Applications* (Cambridge University Press, Cambridge, 2007).
- [3] A.E. Romanov, V.I. Vladimirov, In: *Dislocations in Solids*, ed. by F.R.N. Nabarro (North Holland, Amsterdam, 1992), Vol. 9, p.191.
- [4] C.K. Takemori, T.D. Müller, M.A. De Oliveira, *Numerical simulation of transient heat transfer during welding process*, In: *International Compressor Engineering Conference* (Purdue, USA 2010).
- [5] W. Pollak, M. Blecha, G. Specht // *US Patent 4572848*.
- [6] <http://www.mpm.spbstu.ru>

МЕХАНИКА И ФИЗИКА МАТЕРИАЛОВ

38 (1) 2018

Учредители: Санкт-Петербургский политехнический университет Петра Великого,

Институт проблем Машиноведения Российской академии наук

Издание зарегистрировано федеральной службой по надзору в сфере связи,
информационных технологий и массовых коммуникаций (РОСКОМНАДЗОР),

свидетельство ПИ №ФС77-69287 от 06.04.2017 г.

Редакция журнала

Профессор, д.т.н., академик РАН, А.И. Рудской – главный редактор

Профессор, д.ф.-м.н., член-корр. РАН, Д.А. Индейцев – главный редактор

Профессор, д.ф.-м.н. И.А. Овидько (1961 - 2017) – основатель и почетный редактор

Профессор, д.ф.-м.н. А.Л. Колесникова – ответственный редактор

Доцент, к.т.н. А.С. Немов – ответственный редактор

А.Ю. Зобачева, к.т.н. – выпускающий редактор

Л.И. Гузилова – редактор, корректор

Телефон редакции

+7 (812) 591-65-28

E-mail: mpmjournal@spbstu.ru

Компьютерная верстка А.Ю. Зобачева

Подписано в печать 18.06.2018 г. Формат 60x84/8. Печать цифровая
Усл. печ. л. 10,0. Тираж 100. Заказ ____.

Отпечатано с готового оригинал-макета, предоставленного автором
в Издательско-полиграфическом центре Политехнического университета Петра
Великого. 195251, Санкт-Петербург, Политехническая ул., 29.
Тел.: (812) 552-77-17; 550-40-14.

Design and manufacturing of tailored microstructure with selective laser melting	1-10
A.A. Popovich, V.Sh. Sufiiarov, E.V. Borisov, I.A. Polozov, D.V. Masaylo	
Operational characteristics of the composite aluminum - carbon nanofibers.....	11-15
T.S. Koltsova, A.D. Breki, T.V. Larionova, O.V. Tolochko	
Thermomechanical processing of steels and alloys physical foundations, resource saving technique and modelling.....	16-25
A.I. Rudskoi, G. Kodzhaspirov1, J. Kliber, Ch. Apostolopoulos	
Effect of alumina addition on weld deposits microstructure at the welding of carbon steel.....	26-32
E.V. Bobrynina, T.V. Larionova, T.S. Koltsova, S.A. Ginzburg, V.G. Michailov	
The influence of different types of mesodefets on the formation of strain induced broken dislocation boundaries at the faceted grain boundary	33-39
S.V.Kirikov, J.V. Svirina	
Technique of durability estimation for thin beryllium foils during their work in X-ray detectors.....	40-47
V.V. Mishin, I.A. Shishov, A. Minchena	
Contactless electromagnetic acoustic techniques of diagnostics and assessment of mechanical properties of steel rolled bars	48-53
V.V. Murav'ev, O.V. Murav'eva, K.V. Petrov	
Microstructure evolution of a Ti/TiB metal-matrix composite during high-temperature deformation	54-63
M.S. Ozerov, M.V. Klimova, N.D. Stepanov, S.V. Zherebtsov	
Severe plastic deformation influence on engineering plasticity of Copper	64-68
A.I. Rudskoi, A.M. Zolotov, R.A. Parshikov	
On anisotropy of mechanical properties of aluminum alloys under high temperature deformation	69-75
G.E. Kodzhaspirov, D.A. Kitaeva, Sh.T. Pazylov, Ya.I. Rudaev	
On the development of the new technology of severe plastic deformation in metal forming.....	76-81
A.I. Rudskoi, A.A. Bogatov, D.Sh. Nukhov, A.O. Tolkushkin	
Examination of hardening curves definition methods in torsion test.....	82-89
M.V. Erpalov, E.A. Kungurov	
Competition between the volume solution and the surface segregation of solved elements in α-Fe	90-110
V.P. Filippova, E.N. Blinova, A.M. Glezer, R.V. Sundeev, A.A. Tomchuk, L.F. Muradimova	
Carbide forming special features and fracture mechanisms under the austenitic chromium-nickel 304 steel post-life ageing	111-118
S.N. Petrov, O.Yu. Prokoshev, B.Z. Margolin, A.M. Shumko	
Gas-jet method of metal film deposition: direct simulation monte-carlo of He-Ag mixture flow.....	119-130
N.Y. Bykov, A.I. Safonov, D.V. Leshchev, S.V. Starinskiy, A.V. Bulgakov	